Branching ratio measurement of the π^0 Dalitz decay at NA62

by

Thomas W. Bache

A thesis submitted to the University of Birmingham
for the degree of *DOCTOR OF PHILOSOPHY*

UNIVERSITY OF BIRMINGHAM

Supervisors:
Prof. Evgueni Goudzovski
Prof. Cristina Lazzeroni

Particle Physics Group
University of Birmingham
August 2022

Abstract

An exploratory measurement of the branching ratio of the $\pi^0 \to e^+ e^- \gamma$ decay using data taken during 2018 by NA62, a fixed target kaon decay experiment based at CERN, is presented. The total number of signal events observed is 112,711 and the branching ratio was measured to be $(1.137 \pm 0.022) \times 10^{-2}$; the uncertainty is dominated by the systematic errors arising from the particle identification procedure and the limited MC sample size. Further work is required in order to complete and improve the precision measurement, details of which are given.

A crucial part of the NA62 experiment is the KTAG detector. The KTAG contains a nitrogen based Cherenkov counter known as a CEDAR detector, used to identify minority kaons in the beam. In order to reduce the number of beam particles interacting with the gas, hydrogen can be used instead and a design of a hydrogen filled CEDAR detector is presented.

To my wife, Em.

"Learning is not attained by chance, it must be sought for with ardour and attended to with diligence."

Abigail Adams, 1780

Declaration of author's contribution

Chapter 1 describes the theoretical framework to provide context to the rest of the thesis. The correction to the KTeV $B(\pi^0_{\mathrm{D}})$ measurement, described towards the end of Subsection 1.3.2, is the only part of this chapter that is my work. The NA62 experiment, detectors and, to aid the reader in understanding the main goals of NA62, a summary of the $K^+ \to \pi^+ \nu \bar{\nu}$ analysis using data taken between 2016 and 2018, are described in Chapter 2. I participated in the NA62 data-taking as a shift-worker in 2018, before the long shutdown.

Chapter 3 describes simulations of a KTAG detector that uses a CEDAR filled with hydrogen rather than nitrogen. For context and to aid understanding of the work completed, Section 3.1 gives technical details of the KTAG/CEDAR detectors and the theoretical background (neither of which are my work). Section 3.2 describes the work completed by me on the optimisation of the hydrogen filled CEDAR, in collaboration with a colleague. A detailed description of the work carried out by each party is given at the start of the aforementioned section. For completeness, Section 3.3 gives details of the work done by others since they took over the project (allowing me to carry out the work described in Chapters 4 and 5).

My contributions to the NA62 Monte Carlo simulation are described in Chapter 4. My work on the $B(\pi^0_{\mathrm{D}})$ measurement is presented in Chapter 5. Standard NA62 software tools, not developed by myself but available to members of the col-

laboration, are used in the $B(\pi_{\mathrm{D}}^0)$ measurement.

No other qualifications have been achieved with the work reported in this thesis.

Acknowledgements

A large number of people deserve recognition for their role in my PhD journey. Firstly, I would like to thank my supervisors, Cristina and in particular Evgueni, for giving me the opportunity to undertake a PhD and for guiding me throughout. Secondly, to John Fry and Michal Koval, both of whom helped the progression of my work via invaluable discussions and advice. Next, to the other students at Birmingham, thank you for all the laughs. To my family, thank you for teaching me what hard work is and to not be phased when faced with adversity (of which, a PhD is plentiful). Finally, to my wife, Em, thanks for always supporting and encouraging me, you made this journey much easier than it otherwise could have been.

Contents

List of Figures

List of Tables

Introduction

The Standard Model contains everything we currently know about particle physics and describes both the fundamental particles and the interactions between them. In its current form, the Standard Model has been experimentally confirmed to high accuracy. It was continually developed and expanded throughout the second half of the 20th century, starting with the explanation of how nuclei stay together with the strong force in the 1950s [1] and the combination of electromagnetism and the weak interaction into electroweak theory [2] and the integration of the Higgs mechanism [3] in the 1960s. Since then, its predictions have been experimentally confirmed by experiments. For example, the W and Z bosons, predicted by Glashow et al. in the 1960s, were discovered by the UA1 and UA2 experiments at CERN in 1983 [4, 5, 6, 7]. The top quark, predicted in 1973 [8], was discovered by the CDF and D∅ experiments at Fermilab in 1995 [9, 10].

However, there are phenomena that cannot be explained with current Standard Model theory or observations. Neutrino oscillations are not allowed in the Standard Model but have been observed experimentally [11]. Furthermore, it is not understood why matter is dominant over antimatter in the Universe [12] or what, as observed in cosmology observations, dark matter and dark energy are [13]. Gravity is also not included and it is unclear how this is to be done. Additional work is hence needed to improve our current understanding of the Standard Model.

Current research into beyond standard model (BSM) physics using particle accelerators is generally split into two categories. There are experiments that are

searching for new particles with high mass at very high energies, such as the experiments at CERN's Large Hadron Collider (LHC). The Higgs boson was observed using this technique [14, 15]. Then there are the experiments that are looking at very rare processes, within which large deviations from those predicted by the Standard Model could lead to observations of new physics. The search for $K^+ \rightarrow \pi^+ \nu \bar{\nu}$ ($K_{\pi\nu\bar{\nu}}$) at NA62, a decay with a Standard Model branching ratio $\sim 10^{-10}$, is an example of this.

In addition to studies of rare decays like $K_{\pi\nu\bar{\nu}}$, NA62 is able to conduct precision measurements. These are important because the more precisely something is measured, the easier it is to find deviations from what we expect. Furthermore, measurements of quantities often depend on other, externally measured quantities. This means that improvements in the precision of one measurement can lead to improvements in other measurements.

The work contained within this thesis was completed as part of the NA62 collaboration, the main part of which describes an exploratory measurement of the branching ratio of the $\pi^0 \rightarrow e^+ e^- \gamma$ decay (known as the π^0 Dalitz or π_D^0 decay). The theoretical framework is outlined in Chapter 1. Chapter 2 describes the NA62 experimental setup and software, as well as the results of the $K_{\pi\nu\bar{\nu}}$ analysis using the data taken between 2016-18. Chapter 3 describes work conducted by the author on the future upgrade of NA62's KTAG detector to convert it from a nitrogen based Cherenkov detector to a hydrogen based one. The author's contributions to the NA62 Monte Carlo simulation, in particular the pileup treatment and production method, are presented in Chapter 4. Finally, details of the π_D^0 branching ratio measurement, performed by the author, are given in Chapter 5.

Chapter 1

Theoretical framework

1.1 The Standard Model

The Standard Model (SM) encapsulates our current understanding of all the elementary particles and three of the four fundamental forces in our Universe. In terms of the theory itself, it is[1]:

- A gauge quantum field theory (QFT) driven by the local $SU(3) \times SU(2) \times U(1)$ non-Abelian symmetry.

- Self-consistent, meaning it does not contradict itself.

- Renormalisable, allowing the removal of divergences from the QFT.

Emerging from the SM, there are 12 elementary fermions (quarks, leptons plus their antiparticles), 5 vector bosons (photon, gluon, Z and $W^{\pm}$) that mediate the fundamental forces and a scalar boson (the Higgs) responsible for the mass of particles. The $SU(3)$ symmetry relates to strong interactions (i.e. quantum chromodynamics (QCD)) and the $SU(2) \times U(1)$ from electroweak interactions. Each of these has their respective gauge couplings that describe the strength of the interaction.

The $SU(2) \times U(1)$ symmetry is spontaneously broken by the Higgs field, resulting

---

[1]For a thorough introduction to QFT and the SM, see any relevant textbooks, such as [16] and [17].

in massive electroweak bosons and fermions (which then form free parameters of the SM). This symmetry breaking that gives rise to the quark masses results in the strong and weak eigenstates of the quarks diverging. The down, strange and bottom quark eigenstates (d', s', b') that interact via the weak interaction can be expressed as a function of the mass eigenstates (d, s, b) using the CKM matrix, V_{CKM} [18, 8],

$$
\begin{pmatrix} d' \\ s' \\ b' \end{pmatrix} = V_{CKM} \begin{pmatrix} d \\ s \\ b \end{pmatrix} \equiv \begin{pmatrix} V_{ud} & V_{us} & V_{ub} \\ V_{cd} & V_{cs} & V_{cb} \\ V_{td} & V_{ts} & V_{tb} \end{pmatrix} \begin{pmatrix} d \\ s \\ b \end{pmatrix},
\tag{1.1}
$$

where $|V_{ij}|^2$ gives the probability of a charged current transition from a quark of type i to type j. Equation 1.1 is expressed using (d', s', b') rather than (u', c', t') by convention only. The latter is also valid if the CKM matrix is expressed in a different way.

The CKM matrix can be parametrised using four parameters, commonly split into three matrices [19],

$$
V_{CKM} = \begin{bmatrix} 1 & 0 & 0 \\ 0 & c_{23} & s_{23} \\ 0 & -s_{23} & c_{23} \end{bmatrix} \begin{bmatrix} c_{13} & 0 & s_{13}e^{-i\delta_{13}} \\ 0 & 1 & 0 \\ -s_{13}e^{i\delta_{13}} & 0 & c_{13} \end{bmatrix} \begin{bmatrix} c_{12} & s_{12} & 0 \\ -s_{12} & c_{12} & 0 \\ 0 & 0 & 1 \end{bmatrix},
\tag{1.2}
$$

where $c_{ab} = \cos\theta_{ab}$ and $s_{ab} = \sin\theta_{ab}$. The four parameters are three Euler angles $(\theta_{12}, \theta_{23}, \theta_{13})$ that describe the coupling between the quark generations and one phase δ_{13} that is responsible for introducing CP-violation.

The values of the CKM parameters can be measured and are given by [20],

$$
\begin{pmatrix} |V_{ud}| & |V_{us}| & |V_{ub}| \\ |V_{cd}| & |V_{cs}| & |V_{cb}| \\ |V_{td}| & |V_{ts}| & |V_{tb}| \end{pmatrix} = \begin{pmatrix} 0.97401 \pm 0.00011 & 0.22650 \pm 0.00048 & 0.00361^{+0.00011}_{-0.00009} \\ 0.22636 \pm 0.00048 & 0.97320 \pm 0.00011 & 0.04053^{+0.00083}_{-0.00061} \\ 0.00854^{+0.00023}_{-0.00016} & 0.03978^{+0.00082}_{-0.00060} & 0.999172^{+0.000024}_{-0.000035} \end{pmatrix}.
\tag{1.3}
$$

Table 1.1: The 19 free parameters of the Standard Model.

Lepton masses	Electron, muon and tau masses
Quark masses	Up, down, charm, strange, bottom and top masses
CKM matrix parameters	$\theta_{12}, \theta_{23}, \theta_{13}$ and δ_{13}
Gauge couplings	U(1), SU(2) and SU(3) couplings
QCD	QCD vacuum angle, θ_{QCD}
Higgs mechanism	Vacuum expectation value, v, and Higgs boson mass

One important point to notice is that the off-diagonal elements are smaller than the on-diagonal ones. This results in processes involving, for example, a strange quark transforming into a top quark to be heavily suppressed. This is further discussed in regard to the $K^+ \to \pi^+ \nu \bar{\nu}$ decay in Section 2.5.

Including the strong (QCD) and electroweak interactions as well as the Higgs mechanism, the SM contains 19 free parameters that must be measured in experiment. These are shown in Table 1.1. The $U(1)$ and $SU(2)$ (electroweak) couplings are approximately constant whereas the $SU(3)$ (QCD) coupling depends on the interaction energy. The masses of the W and Z electroweak bosons do not appear as free parameters as they can be expressed using the two gauge constants from $U(1) \times SU(2)$. The QCD vacuum angle arises when an additional term accounting for CP violation is introduced to the QCD Lagrangian.

Precisely measuring the free parameters of the SM is the aim of a large number of experiments today. This improves the precision of theoretical calculations of quantities that use these parameters as inputs. Comparisons can then be made with experimental measurements of these quantities and any deviations from expectation hints that there is so called beyond Standard Model (BSM) physics present. As mentioned in the Introduction, there are several experimental observations that cannot currently be explained using the SM. Attempts have been made to create theories that explain these observations and for an overview of these BSM theories, see Ref. [21] and references therein.

1.2   Kaon physics

The kaon was first observed in 1947 in a cloud chamber experiment measuring cosmic ray events [22]. At the time, it was not known what this particle was, only that there was a neutral version that decayed into two charged pions and a charged version that decayed into a charged pion and a neutral particle. Two years later, a similar particle was observed decaying into three pions, leading to the tau–theta problem whereby the same particle was decaying into two different final states with different parities [23]. This led to the discovery that weak interactions do not conserve parity. More observations and measurements of this unknown particle in the early 1950s finally resulted in it being named as the K-meson (of which there were four types: K^+, K^-, K_0, $\overline{K}_0$). These measurements showed that the decay times were very long whilst the production was much faster, leading to a new quantum number, strangeness, being hypothesised [24, 25, 26, 27]. Associated production (production of a strange and anti-strange particle) was deemed the reason that the rate at which they were produced was accelerated relative to their decay. Strangeness is conserved in strong interactions but violated in weak interactions.

The neutral kaons were the subject of many studies in the mid-20th century. Despite the discovery of parity violation, it was still thought that CP symmetry was conserved. Experimental measurements showed that the weak eigenstates of the neutral kaons had different lifetimes, resulting in them being referred to as the K-long (K_L) and K-short (K_S), each having a different CP value. The K_S was observed to decay to two pions with both initial and final states having $CP = +1$, whereas the K_L was observed to decay to three pions and had $CP = -1$ (both decays hence obeying CP symmetry). However, by measuring the decay products of the weak eigenstates, it was shown in 1964 that the K_L decayed to two pions, suggesting that CP symmetry was being violated [28] (known as indirect CP violation as it occurs via neutral kaon mixing). This work was given the Physics Nobel Prize in 1980 [29]. Direct CP violation, in which the violation arises via the decay rather than mixing,

Table 1.2: Kaons and their properties [20]. The K^0 is a strong eigenstate so does not have a definite lifetime. The K_S and K_L masses are the same as the K^0 but there is a small difference $\sim 10^{-6}$ eV between them.

Particle	Antiparticle	Quark content	Mass (MeV)	Lifetime (s)
K^+	K^-	$u\bar{s}$	493.677 ± 0.013	$1.2380 \pm 0.0020 \times 10^{-8}$
K^0	$\overline{K}^0$	$d\bar{s}$	497.611 ± 0.013	N/A
K_S	Itself	$\frac{d\bar{s}-s\bar{d}}{\sqrt{2}}$	497.611 ± 0.013	$(0.8954 \pm 0.0004) \times 10^{-10}$
K_L	Itself	$\frac{d\bar{s}+s\bar{d}}{\sqrt{2}}$	497.611 ± 0.013	$(5.116 \pm 0.021) \times 10^{-8}$

Table 1.3: Main decay modes of the K^+, with their shorthand and branching ratios [20].

Decay	Shorthand	Branching ratio (%)
$K^+ \to \mu^+\nu$	$K_{\mu2}$	63.56 ± 0.11
$K^+ \to \pi^+\pi^0$	$K_{2\pi}$	20.67 ± 0.08
$K^+ \to \pi^+\pi^+\pi^-$	$K_{3\pi}$	5.583 ± 0.024
$K^+ \to \pi^0 e^+\nu_e$	K_{e3}	5.07 ± 0.04
$K^+ \to \pi^0\mu\nu_\mu$	$K_{\mu3}$	3.352 ± 0.033
$K^+ \to \pi^+\pi^0\pi^0$	$K_{3\pi^0}$	1.760 ± 0.023

also occurs in the neutral kaon system, with the first evidence being found by the NA31 experiment in the 1980s [30] followed by its discovery by the NA48 and KTeV experiments in the 1990s [31, 32].

The positively charged kaon consists of an up and an anti-strange quark, with the negatively charged kaon being the antiparticle of this. Table 1.2 gives a summary of the properties of the charged and neutral kaons. The work presented in this thesis was done as part of the NA62 experiment which uses a K^+ beam line (NA62 is described in detail in Chapter 2). Table 1.3 shows the 6 main decay modes of the K^+ and the corresponding branching ratios.

In addition to the more common decays shown in Table 1.3, K^+ mesons also undergo rare decays. One of these is the $K^+ \to \pi^+\nu\bar{\nu}$ ($K_{\pi\nu\bar{\nu}}$), a rare decay which is essentially a transformation of an anti-strange quark into an anti-down quark plus two neutrinos, leaving the up quark unchanged. This can proceed via three main
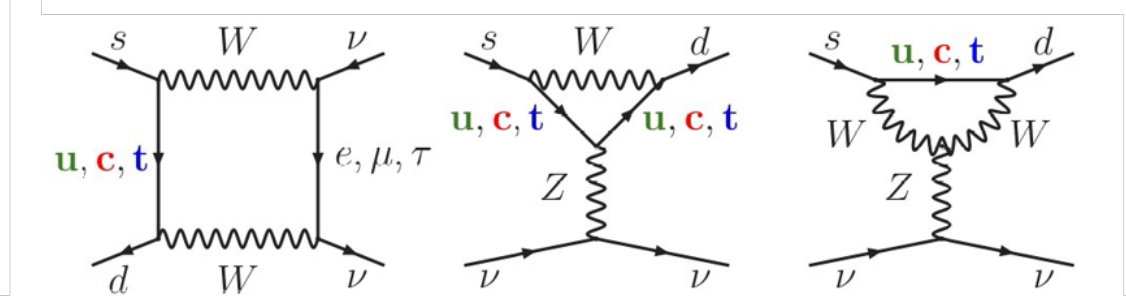
Figure 1.1: The three Feynman diagrams that $K^+ \to \pi^+ \nu \bar{\nu}$ can proceed through in the Standard Model. The first is a box diagram and the latter two are penguin diagrams. The time axis is to the right in the box diagram but downwards in the penguin diagrams.

Feynman diagrams, as shown in Figure 1.1.

All three diagrams are flavour-changing neutral current (FCNC) diagrams and the first diagram is referred to as a box diagram whilst the latter two diagrams are known as penguin diagrams. The $K_{\pi\nu\bar{\nu}}$ decay is highly suppressed via GIM and CKM suppression. Until recently, the Standard Model branching ratio (B) prediction of this decay was [33]

$$B(K^+ \to \pi^+ \nu \bar{\nu}) = (8.4 \pm 1.0) \times 10^{-11}. \tag{1.4}$$

However, a new theoretical approach that removes the dependence on certain parameters has recently reduced the error by a factor of 2.4, with the latest result being [34]

$$B(K^+ \to \pi^+ \nu \bar{\nu}) = (8.60 \pm 0.42) \times 10^{-11}. \tag{1.5}$$

Decays as rare as $K_{\pi\nu\bar{\nu}}$ are of interest because they can lead to discoveries of new physics. If the branching ratio measured in experiments such as NA62 does not agree with that given by the Standard Model, previously unseen physics could be occurring in the decay and as the branching ratio is so small, it is extremely sensitive to even very small effects. The main aim of NA62 is to obtain a measurement of $B(K^+ \to \pi^+ \nu \bar{\nu})$ at 10% precision, to match the original theoretical calculation. To

Table 1.4: Basic properties of the π^0 [20].

Quark composition	$\left(u\bar{u} - d\bar{d}\right)/\sqrt{2}$
Mass	(134.9768 ± 0.0005) MeV/c^2
Lifetime	$(8.43 \pm 0.13) \times 10^{-17}$ s

do this, ~ 100 decays are required to be observed which means that NA62 needs to obtain $\sim 10^{13}$ kaon decays. The most recent results of NA62's analysis of $K_{\pi\nu\bar{\nu}}$ are discussed in Section 2.5.

1.3   The π^0 Dalitz decay

In 1935, Hideki Yukawa hypothesised that the strong nuclear force carrier was a massive scalar particle [35]. This was extended in 1938 to a neutral meson with properties similar to that of the charged meson (what we now call the $\pi^\pm$) [36, 37] and two years later, it was suggested that this neutral meson decays to two photons and has a lifetime $\sim 10^{-16}$ s [38].

Cloud chamber experiments found cosmic-ray showers containing photons that gave the first experimental evidence of this neutral meson in 1949 [39, 40]. In 1950, it was officially discovered. Bjorklund et al. used the Berkeley cyclotron (at the University of California) to measure the gamma rays emitted when protons were incident on a nuclear target and concluded that the results could be explained by the neutral meson decaying into two photons [41].

This neutral meson is what we call today the neutral pion, a particle with quark components $\left(u\bar{u} - d\bar{d}\right)/\sqrt{2}$. The π^0 is the lightest hadron, meaning the field of hadronic physics is often influenced by its properties. Table 1.4 gives some of the basic properties of the π^0.

The π^0 decays almost always to two photons ($\pi^0 \rightarrow \gamma\gamma$, given the shorthand $\pi^0_{\gamma\gamma}$) with the next most common decay channel being the Dalitz decay, $\pi^0 \rightarrow e^+e^-\gamma$, with a branching ratio $\mathcal{O}(1\%)$ (given the shorthand π^0_{D}; see Table 1.5 for the corresponding branching ratios). It is named after Richard H. Dalitz who hypothesised, during his
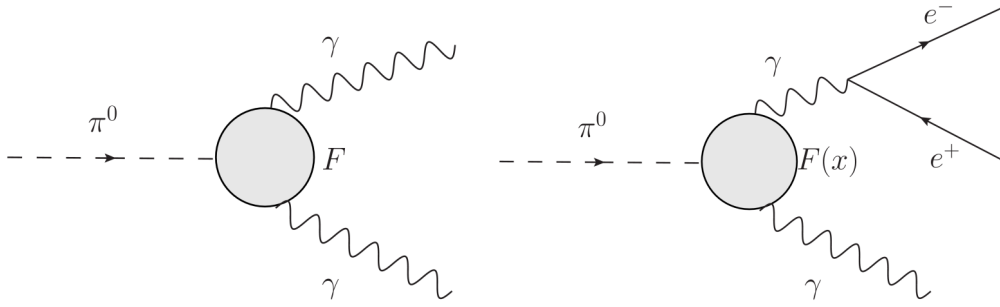
Figure 1.2: Feynman diagrams for the two most common π^0 decays. Left: $\pi^0 \rightarrow \gamma\gamma$. Right: $\pi^0 \rightarrow e^+e^-\gamma$. $F = F(0)$ and $F(x)$ are the neutral pion form factor, discussed later in this section.

Table 1.5: Decay modes of the π^0, with their shorthand and branching ratios [20]. Additional decay modes have been hypothesised but only upper limits have been set on these thus far.

Decay	Shorthand	Branching ratio
$\pi^0 \rightarrow \gamma\gamma$	$\pi^0_{\gamma\gamma}$	(98.823 ± 0.034) %
$\pi^0 \rightarrow e^+e^-\gamma$	π^0_{D}	(1.174 ± 0.035) %
$\pi^0 \rightarrow e^+e^-e^+e^-$	π^0_{DD}	$(3.34 \pm 0.16) \times 10^{-5}$
$\pi^0 \rightarrow e^+e^-$	π^0_{ee}	$(6.46 \pm 0.33) \times 10^{-8}$
$\pi^0 \rightarrow \gamma$ positronium	–	$(1.82 \pm 0.29) \times 10^{-9}$

time at the University of Birmingham (UK) in 1951, that instead of producing two real photons as in the $\pi^0_{\gamma\gamma}$ decay, the π^0 could produce one real and one virtual photon where the virtual one internally converts to an electron-positron pair [42]. The Feynman diagrams for the $\pi^0_{\gamma\gamma}$ and π^0_{D} decays are shown in Figure 1.2 (and discussed in more detail in Subsection 1.3.1). The next two most common π^0 decays are $\pi^0 \rightarrow e^+e^+e^-e^-$ (known as the double Dalitz decay) and $\pi^0 \rightarrow e^+e^-$ which have branching ratios $\sim 10^{-5}$ and $\sim 10^{-7}$ respectively. Table 1.5 shows the π^0 decay modes, their shorthand and corresponding branching ratios.

The remainder of this chapter summarises the current theoretical and experimental status of the π^0_{D} decay.

1.3.1   Theory status

The theory of quantum chromodynamics governs the interaction between quarks and gluons. At high energies or at short distances, the strong coupling constant (α_s) is small, meaning perturbation theory can be used to describe QCD interactions (as the infinite number of possible interactions can be approximated by a finite number). However, at low energies, the strength of the strong interaction increases leading to the confinement of quarks and gluons within composite hadrons (and perturbation theory no longer holds). An effective description is therefore needed to describe the internal interactions, within which the properties of the interaction between particles may be described in terms of form factors. A form factor describes the underlying physics of the interaction by providing the momentum dependence of the matrix element, allowing tests of the Standard Model and calculations to be performed that could not otherwise be done.

The circle in the centre of each Feynman diagram in Figure 1.2 represents the electromagnetic transition form factor (TFF). The quarks within the meson carry electric charge, meaning the electromagnetic interactions of the meson are affected by the internal structure. The internal structure and electromagnetic interactions of the π^0 with other particles can therefore be described using a TFF. The differential decay width, $d\Gamma$, can be factorised in to a point-like (p $-$ l) component and the TFF $(\mathcal{F}(q^2))^2$,

$$\frac{d\Gamma}{dq^2} = \frac{d\Gamma}{dq^2}\bigg|_{\text{p}-\text{l}} \left|\mathcal{F}(q^2)\right|^2, \tag{1.6}$$

where q is the four-momentum transfer [43]. The TFF can hence be measured by comparing data from experiments to quantum electrodynamic (QED) computations for point-like particles.

The most general form of $\mathcal{F}$ is the situation in which the vertex contains two off-shell photons with four-momenta q_1 and q_2, denoted $\mathcal{F}_{\pi^0\gamma^*\gamma^*}(q_1^2, q_2^2)$. If both photons

---

[2]Strictly speaking, this can only be done if only the leading order decay rate (i.e. no radiative corrections) is included. Radiative corrections are discussed later in this section.

are real and hence $q_1, q_2 \to 0$, the vertex is that of the $\pi^0_{\gamma\gamma}$ and [44]

$$\Gamma(\pi^0 \to \gamma\gamma) = \left(\frac{m_{\pi^0}}{4\pi}\right)^3 \left(\frac{\alpha}{F_\pi}\right)^2 = \frac{1}{64\pi} m_{\pi^0}^3 \, |\mathcal{F}_{\pi^0\gamma^*\gamma^*}(0,0)|^2, \tag{1.7}$$

where m_{π^0} is the π^0 mass, α is the electromagnetic fine structure constant and F_π is the π^0 decay constant[3]. The normalisation of the TFF is given by

$$\mathcal{F}_{\pi^0\gamma^*\gamma^*}(0,0) \equiv \mathcal{F}_{\pi^0\gamma\gamma} = \frac{\alpha}{\pi F_\pi}. \tag{1.8}$$

Similarly, by only taking the limit $q_2 \to 0$, the semi off-shell TFF (i.e. that corresponding to the π^0_D vertex) can be obtained:

$$\mathcal{F}_{\pi^0\gamma\gamma^*}\left(q^2\right) \equiv \mathcal{F}_{\pi^0\gamma^*\gamma^*}\left(q^2, 0\right). \tag{1.9}$$

It is convenient at this point to introduce two "Dalitz" variables that are commonly used when studying the π^0_D decay:

$$x = \left(\frac{M_{ee}}{m_{\pi^0}}\right)^2 = \frac{(p_{e^+} + p_{e^-})^2}{m_{\pi^0}^2}, \quad y = \frac{2p_{\pi^0} \cdot (p_{e^+} - p_{e^-})}{m_{\pi^0}^2 (1-x)}, \tag{1.10}$$

where the kinematically allowed region is

$$r^2 = \left(\frac{2m_e}{m_{\pi^0}}\right)^2 \le x \le 1, \quad |y| \le \beta = \sqrt{1 - \frac{r^2}{x}}, \tag{1.11}$$

where m_e is the mass of the electron, M_{ee} is the invariant mass of the electron-positron pair and p_i is the four-momentum of the particle i. The normalised semi off-shell TFF can therefore be written as

$$\mathcal{F}(x) = \frac{\mathcal{F}_{\pi^0\gamma\gamma^*}\left(xm_{\pi^0}^2\right)}{\mathcal{F}_{\pi^0\gamma\gamma}}. \tag{1.12}$$

---

[3]F_π appears in the chiral perturbation theory Lagrangian and although different normalisations exist, Peskin and Schroeder use 93 MeV [16].

Using Equation 1.6 as well as the Dalitz variables defined in Equation 1.10, the leading order (LO) differential decay width of the π^0_{D} decay can be written

$$\frac{d^2\Gamma^{\mathrm{LO}}(\pi^0_{\mathrm{D}})}{dxdy} = \Gamma(\pi^0 \to \gamma\gamma)\frac{\alpha}{4\pi}\frac{(1-x)^3}{x}\left(1+y^2+\frac{r^2}{x}\right)|\mathcal{F}(x)|^2, \tag{1.13}$$

where $\Gamma(\pi^0 \to \gamma\gamma)$ is the $\pi^0 \to \gamma\gamma$ total decay width from Equation 1.7 [44]. $\mathcal{F}(x)$ is expected to vary slowly in the π^0_{D} kinematically allowed region so a linear approximation is often used,

$$\mathcal{F}(x) = 1 + ax, \tag{1.14}$$

where a is the TFF slope parameter.

The next-to-leading order (NLO) radiative corrections to the LO π^0_{D} decay width (Equation 1.13) were studied extensively in the 1960s and 70s [45, 46, 47]. These works accounted for the virtual and bremsstrahlung radiative corrections but the one-loop one-photon-irreducible contribution was not accounted for until 2015 by Husek et al. [44][4]. The diagrams showing the respective corrections are given in Figure 1.3.

The differential decay width can be separated into LO and NLO components where the ratio between the two terms is encoded by a function δ,

$$\frac{d^2\Gamma}{dxdy} = \frac{d^2\Gamma^{\mathrm{LO}}}{dxdy} + \frac{d^2\Gamma^{\mathrm{NLO}}}{dxdy}, \quad \delta(x,y) = \frac{d^2\Gamma^{\mathrm{NLO}}}{dxdy}\bigg/\frac{d^2\Gamma^{\mathrm{LO}}}{dxdy}. \tag{1.15}$$

This leads to a correction $(1+\delta(x,y))$ to the LO term in the final differential decay width,

$$\frac{d^2\Gamma(\pi^0_{\mathrm{D}})}{dxdy} = \frac{d^2\Gamma^{\mathrm{LO}}(\pi^0_{\mathrm{D}})}{dxdy}\left(1+\delta(x,y)\right). \tag{1.16}$$

In addition, the individual radiative components can be split up depending on their origin,

$$\delta = \delta^{\mathrm{virt}} + \delta^{1\gamma\mathrm{IR}} + \delta^{\mathrm{BS}}, \tag{1.17}$$

---

[4]This additional correction was motivated by a high precision measurement of the TFF by the NA62 Collaboration using the 2007 dataset [48].
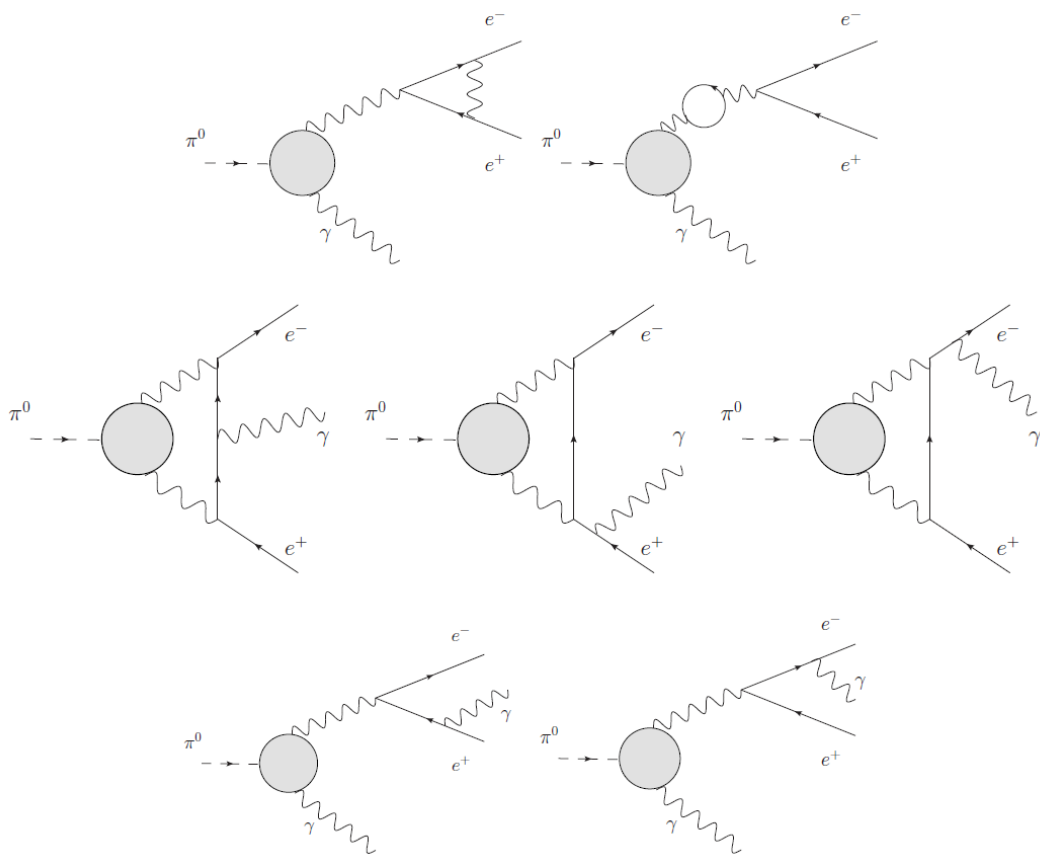
Figure 1.3: Additional Feynman diagrams that contribute to the π^0_D decay rate. 1st row: virtual radiative corrections. 2nd row: one-photon-irreducible radiative corrections. 3rd row: bremsstrahlung radiative corrections.
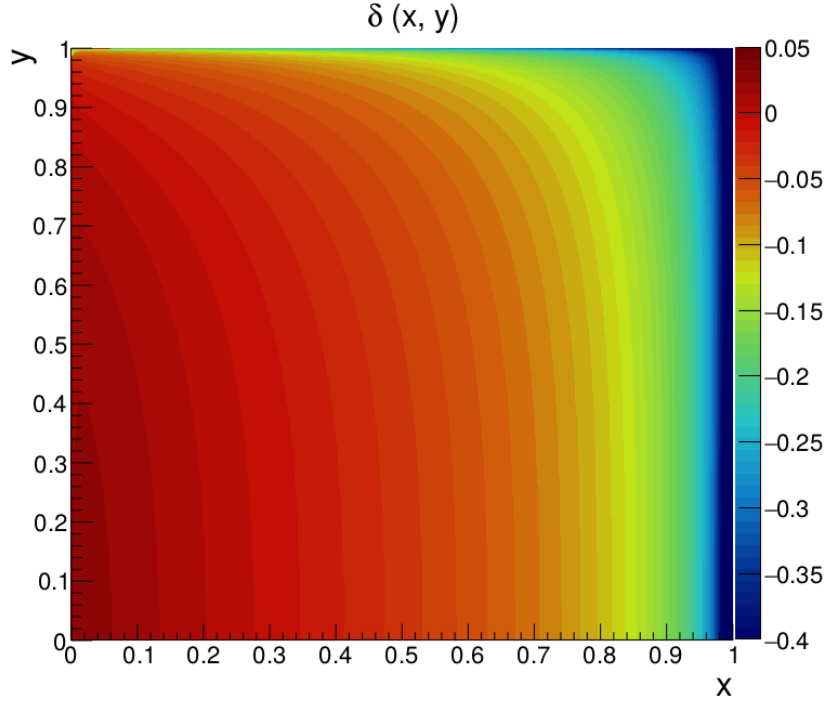
Figure 1.4: Size of the radiative corrections for the π_{D}^0 decay as a function of x and y (see Equation 1.16). This is an official NA62 plot produced as part of the TFF measurement published in Ref. [48].

where the virtual (virt), one-photon irreducible (1γIR) and bremsstrahlung (BS) contributions are accounted for. The complete calculation of each component is given in [44, 47]. The size of the radiative corrections as a function of x and y is shown in Figure 1.4. At high x and y, the radiative corrections can be up to 40% of the LO differential decay width, $d^2\Gamma^{\mathrm{LO}}(\pi_{\mathrm{D}}^0)/dxdy$.

The size of the radiative corrections as a function of x only, $\delta(x)$, can be obtained from $\delta(x, y)$ using [44]

$$\delta(x) = \frac{d\Gamma^{\mathrm{NLO}}}{dx} \bigg/ \frac{d\Gamma^{\mathrm{LO}}}{dx} = \frac{3}{8\beta} \frac{1}{\left(1 + \frac{r^2}{2x}\right)} \int_{-\beta}^{\beta} \delta(x, y) \left[1 + y^2 + \frac{r^2}{x}\right] dy, \qquad (1.18)$$

where r and β are defined in Equation 1.11. Figure 1.5 shows the size of the radiative corrections as a function of x, split into the virtual, bremsstrahlung and one-photon irreducible components. As x increases, the importance of including the one-photon-irreducible component becomes apparent.
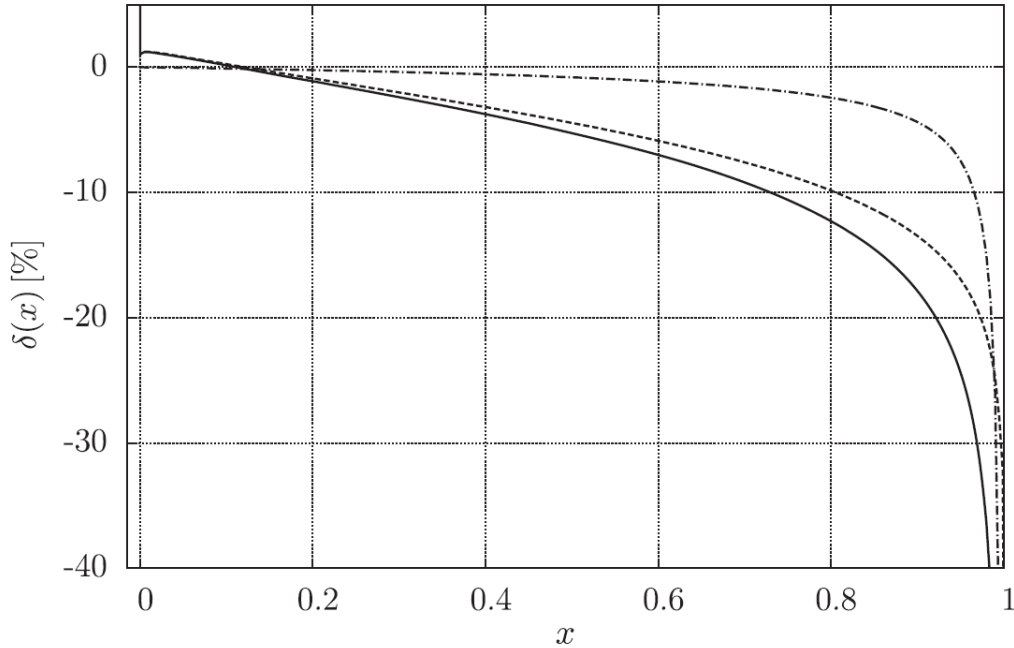
Figure 1.5: The different components of the π_{D}^0 radiative corrections as a function of x. Solid line: full δ; dashed line: $\delta^{virt} + \delta^{BS}$; dash-dot line: $\delta^{1\gamma IR}$. Figure reproduced from Ref. [44].

The decay width in Equation 1.16 can be used to calculate the branching ratio of the π_{D}^0 decay, $B(\pi_{\mathrm{D}}^0)$. The ratio of decays widths between the π_{D}^0 and $\pi_{\gamma\gamma}^0$ is defined as

$$R = \frac{\Gamma(\pi^0 \to e^+ e^- \gamma)}{\Gamma(\pi^0 \to \gamma\gamma)} = \frac{B(\pi_{\mathrm{D}}^0)}{B(\pi_{\gamma\gamma}^0)}. \tag{1.19}$$

Equation 1.14 can be used to write

$$\mathcal{F}^2(x) = 1 + 2ax + \mathcal{O}(x^2). \tag{1.20}$$

Inserting Equation 1.20 into Equation 1.13 and using the kinematically allowed limits given in Equation 1.11, the leading order value of R is given by [49]

$$R^{\mathrm{LO}} = \frac{\alpha}{\pi} \left[\frac{4}{3} \ln \left(\frac{m_{\pi^0}}{m_e} \right) - \frac{1}{3} (7 - a) + (12 - 8a) \frac{m_e^2}{m_{\pi^0}^2} + \mathcal{O} \left(\frac{m_e^4}{m_{\pi^0}^4} \right) \right]. \tag{1.21}$$

A question arises here. What if a quadratic approximation is used for $\mathcal{F}(x)$ (i.e. $\mathcal{F}(x) = 1 + ax + bx^2$) instead of a linear one? This introduces an additional term

to Equation 1.20 equal to $2bx^2 + \mathcal{O}\left(x^3\right)$. However, the region within which this additional term makes a non-negligible difference (i.e. when $x \simeq 1$) to Equation 1.21 is suppressed, as can be seen using Equation 1.13. The relative error on R^{LO} after using the linear approximation ($b = 0$) is $\simeq 10^{-5}$ which is still a good approximation when comparing to the other errors involved [49].

To obtain a precise value of R, the NLO radiative corrections need to be accounted for. Using Equations 1.13, 1.14 and 1.15, the NLO term of R is

$$R^{\mathrm{NLO}} = \frac{a}{\pi} \iint (1 + ax)^2 \, \delta(x, y) \frac{(1 - x)^3}{4x} \left(1 + y^2 + \frac{4m_e^2}{m_{\pi^0}^2 x}\right) dx\,dy. \qquad (1.22)$$

The value of R can then be found via $R \simeq R^{\mathrm{LO}} + R^{\mathrm{NLO}}$.

Due to the rarity of other decay modes (as discussed at the start of this chapter), it can be assumed that

$$B(\pi_{\gamma\gamma}^0) + B(\pi_{\mathrm{D}}^0) + B(\pi_{\mathrm{DD}}^0) \simeq 1, \qquad (1.23)$$

where $B(\pi_{\mathrm{DD}}^0)$ is the $\pi^0 \to e^+e^+e^-e^-$ (known as the π^0 double Dalitz decay). The branching ratio of the π_{D}^0 decay can hence be found using

$$B(\pi_{\mathrm{D}}^0) \simeq \frac{R}{1 + R} \left(1 - B(\pi_{\mathrm{DD}}^0)\right). \qquad (1.24)$$

The full computation was done by Husek et al. in [49] and, using a value of the FF slope[5] of $a = (3.55 \pm 0.70) \times 10^{-2}$, gave

$$B(\pi_{\mathrm{D}}^0) = (1.1836 \pm 0.0006)\,\%. \qquad (1.25)$$

A comparison of this result with experimental results is done in the following section.

For convenience, Table 1.6 shows a summary of the progress made in the radiative

---

[5]Note that $B(\pi_{\mathrm{D}}^0)$ does not vary much with a. To leading order, differentiation of Equation 1.24 gives $|dB/da| \approx 9 \times 10^{-6}$.

Table 1.6: Summary of the radiative corrections that have been calculated. The Joseph calculation differs from the rest in that he calculated corrections to the integral decay width, compared to the other calculations which also calculated corrections to the differential decay width. The Husek calculation improved on the previous virtual and bremsstrahlung calculations by including fewer approximations.

	Year	Radiative corrections included
Joseph [45]	1960	Virtual and bremsstrahlung
Lautrup and Smith [46]	1971	Virtual and bremsstrahlung (soft photon approximation)
Mikaelian and Smith [47]	1972	Virtual and bremsstrahlung (inc. hard photons)
Husek et al. [44]	2015	Virtual, bremsstrahlung and one-photon-irreducible

correction calculations over the last six decades.

1.3.2   Experimental status

Summary of previous measurements

Figure 1.6 shows an overview of the experimental $B(\pi_D^0)$ measurements, as well as the 2021 PDG average (which excludes the 2019 KTeV measurement; see later in this section). Instead of the absolute value of $B(\pi_D^0)$, the previous measurements were of $B(\pi_D^0)/B(\pi_{\gamma\gamma}^0)$ and that is the value shown when discussing each individual measurement in the rest of this section. These values were corrected, assuming $B(\pi_D^0) + B(\pi_{\gamma\gamma}^0) = 1$, in order to produce the values shown in the figure. Also shown, for comparison, are the 1972 Mikaelian and Smith and the 2019 Husek calculations (the latter improving on the former by including the $1\gamma IR$ radiative corrections and more precise TFF measurements). The relative error on the PDG average is $\sim 3\%$, much larger than the 0.05% uncertainty on the theoretical calculation.

A more detailed comparison of the experimental results is shown in Table 1.7. To help with comparison and aid the discussion of motivations for a new measurement later in this section, the NA62 exploratory measurement presented in Chapter 5 of
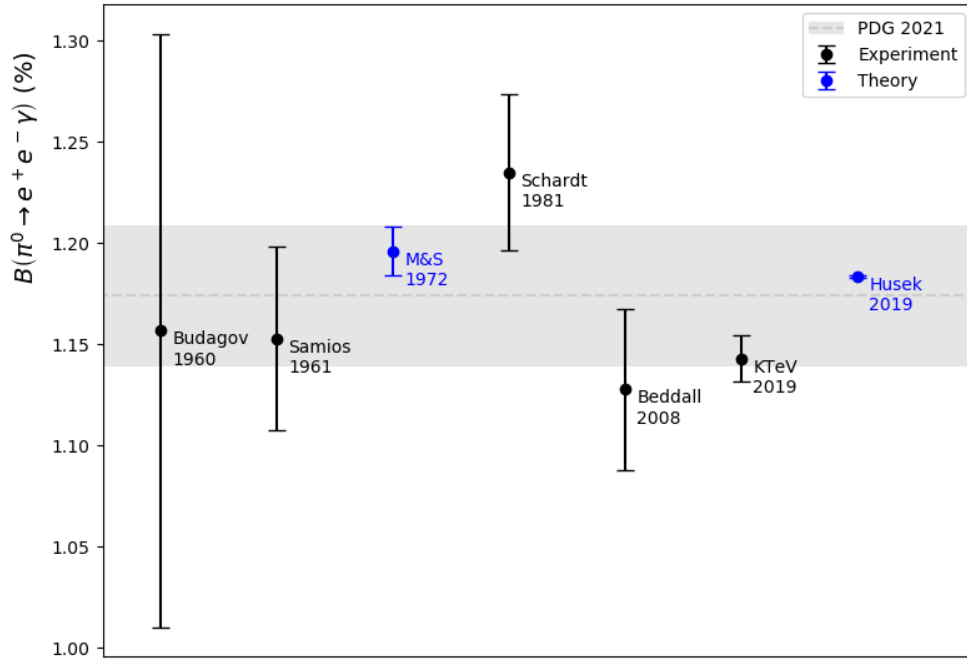
Figure 1.6: Experimental measurements and theoretical calculations of $B(\pi_{\mathrm{D}}^0)$ [50, 51, 47, 52, 53, 54, 49]. The PDG 2021 average and error is shown by the grey band [20]. The 2019 KTeV measurement was excluded when calculating the PDG average. M&S stands for Mikaelian and Smith. The 1960 Joseph theory calculation is not shown as no uncertainty was given; his calculation gave $B(\pi_{\mathrm{D}}^0) = 1.196\%$.

this thesis is also shown in the table. As in Figure 1.6, all bar the exploratory NA62 result have been converted to $B(\pi_{\mathrm{D}}^0)$ for comparison. The NA62 measurement is a direct measurement of $B(\pi_{\mathrm{D}}^0)$ and thus no correction is necessary. Furthermore, the radiative corrections used in each measurement (see Table 1.6 for a summary of the corrections) are also shown. These are inputs (via use of the form factor) into any simulation of the π_{D}^0 decay meaning that, if a measurement of $B(\pi_{\mathrm{D}}^0)$ depends on simulation results, it also depends on the radiative corrections that are used. The acceptance sensitivity is given in terms of the invariant mass of the electron–positron pair and is discussed later in this section. The remainder of this section discusses (briefly) how each measurement was conducted, followed by the motivation behind a new measurement.

Neutral pions are emitted when π^- mesons are captured at rest in hydrogen, in the process $\pi^- p \to \pi^0 n$. Y. A. Budagov conducted the first measurement of $B(\pi_{\mathrm{D}}^0)$ in 1960 using this scattering process [50]. Using 128 MeV and 162 MeV π^- beams and a hydrogen cloud chamber contained within a known magnetic field, he took $\sim 90,000$ photographs and found 27 π_{D}^0 events. An example of one of the photographs with labelled π^-, e^+ and e^- tracks is shown in Figure 1.7. By counting the number of elastic scattering events also present in the photographs and using the probability of decay vs. elastic scattering, the π_{D}^0 branching ratio was measured to be

$$\frac{B(\pi_{\mathrm{D}}^0)}{B(\pi_{\gamma\gamma}^0)} = (1.17 \pm 0.15) \times 10^{-2}, \tag{1.26}$$

where the uncertainty is statistical only (how this uncertainty was obtained is unclear).

One year later, in 1961, N. P. Samios used the same process as Budagov to measure $B(\pi_{\mathrm{D}}^0)$ with the Nevis cyclotron (Columbia University) that fired a 60 MeV π^- beam into a hydrogen bubble chamber in a known magnetic field [51]. The π^- were stopped using absorbers and then $\sim 200,000$ photographs were taken to try and observe the π^0 decay products. By using a previously measured value of the

Table 1.7: Summary of the experimental measurements of $B(\pi_{\mathrm{D}}^0)$. Where available, the statistical, systematic, total absolute and total relative uncertainties are shown. N_{signal} is the number of π_{D}^0 events observed. Cells with a dash mean the information is not publicly available. The NA62 exploratory result, which is presented in Chapter 5 of this thesis, is also shown. In all but the NA62 case, the actual measured value was $B(\pi_{\mathrm{D}}^0)/B(\pi_{\gamma\gamma}^0)$ but has been converted to $B(\pi_{\mathrm{D}}^0)$ in order to compare to the result presented in this thesis. With regard to the acceptance sensitivity, it should be noted that KTeV apply a strict cut to M_{ee} whereas the NA62 measurement is purely estimated from the acceptance.

	Year	$B(\pi_{\mathrm{D}}^0) \times 10^2$	σ_{stat}	σ_{syst}	σ_{total}	$\sigma_{\mathrm{relative}}$	N_{signal}	Radiative corrections used	Acceptance sensitivity
Budagov	1960	1.16	0.15	-	0.15	12.8%	27	-	-
Samios	1961	1.153	-	-	0.046	4.0%	3066	Joseph	-
Schardt	1981	1.24	0.04	0.01	0.04	3.2%	-	M&S	-
Beddall	2008	1.128	0.024	0.033	0.040	3.6%	12,490	Joseph	-
KTeV	2019	1.1428	0.0046	0.0105	0.0114	1.0%	63,693	M&S	$M_{ee} > 15$ MeV
NA62 (exploratory)	2022	1.137	0.003	0.022	0.022	1.9%	112,711	Husek et al.	$M_{ee} > 10$ MeV
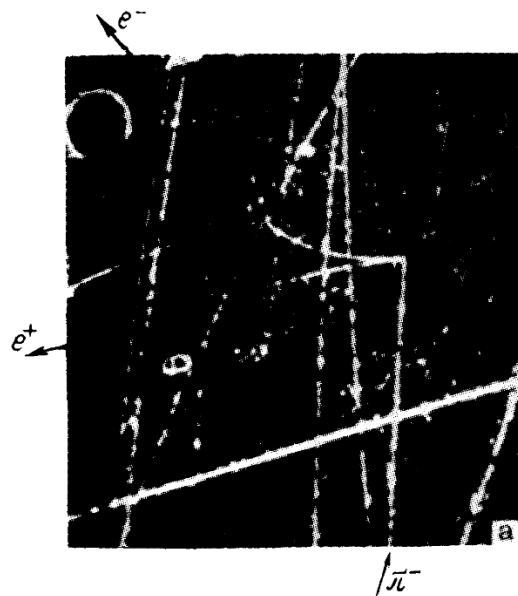
Figure 1.7: One of the $\sim$90,000 cloud chamber photographs taken by Y. A. Budagov showing a π_{D}^0 decay. The π^-, e^+ and e^- tracks are labelled. Figure reproduced from Ref. [50].

Panofsky ratio[6] and counting the number of closely spaced π^- (4.26×10^5) and electron-positron pairs (3066) in the pictures, $B(\pi_{\mathrm{D}}^0)$ was measured to be

$$\frac{B(\pi_{\mathrm{D}}^0)}{B(\pi_{\gamma\gamma}^0)} = (1.166 \pm 0.047) \times 10^{-2}. \tag{1.27}$$

Schardt et al. measured $B(\pi_{\mathrm{D}}^0)$ at LAMPF in 1981 [52]. They produced π^0s in a CH_2 target using a 300 MeV π^- beam and the same scattering process as Budagov and Samios ($\pi^- p \to \pi^0 n$). After measuring the π^0 decay products with detectors placed at two different angles relative to the beam, they exploited the number of events per target thickness to measure $B(\pi_{\mathrm{D}}^0)$ with respect to $B(\pi_{\gamma\gamma}^0)$. Their final result was

$$\frac{B(\pi_{\mathrm{D}}^0)}{B(\pi_{\gamma\gamma}^0)} = (1.25 \pm 0.04_{\mathrm{stat}} \pm 0.01_{\mathrm{syst}}) \times 10^{-2}. \tag{1.28}$$

In 2008, A. Beddall and A. Beddall used data taken by the ALEPH detector between 1991 and 1995 to measure $B(\pi_{\mathrm{D}}^0)$ [53]. The collision of 45 GeV electrons

---

[6]This is the ratio between the rates of $\pi^- p \to \pi^0 n$ and $\pi^- p \to \gamma n$, see [51] for more details.

and positrons, accelerated using the LEP Collider, produced a large number of Z bosons which then decayed hadronically to produce π^0s. The decay products of the π^0 were measured and the π^0_{D} signal region was given in terms of the $e^+e^-\gamma$ invariant mass. Based on an estimated[7] number of $12{,}490 \pm 190$ events, the measured $B(\pi^0_{\mathrm{D}})$ was

$$\frac{B(\pi^0_{\mathrm{D}})}{B(\pi^0_{\gamma\gamma})} = (1.140 \pm 0.024_{\mathrm{stat}} \pm 0.033_{\mathrm{syst}}) \times 10^{-2}, \tag{1.29}$$

where the statistical error is from the uncertainty in the fits to the signal in both data and Monte Carlo simulations. The systematic error is dominated by the uncertainty associated with the photon reconstruction (resulting in track reconstruction efficiency systematics being neglected). It is unclear from the Beddall and Beddall paper why they only compare to (and presumably use) the result by Joseph, despite the M&S result being published many years previously.

The most recent measurement of $B(\pi^0_{\mathrm{D}})$ was published in 2019, based on data taken in 1999 by the E832 KTeV experiment at Fermi National Accelerator Laboratory [54]. The experiment used a neutral kaon beam to observe $K_L \to \pi^0_{\gamma\gamma}\pi^0_{\gamma\gamma}\pi^0_{\mathrm{D}}$ (i.e. one of the three pions undergoes a Dalitz decay). The case whereby all three pions decay to $\gamma\gamma$ was used as normalisation. The measurement was conducted in the kinematic region $M_{ee} > 15$ MeV/c^2 to reduce the sensitivity to theoretical predictions. The Dalitz branching ratio was then corrected to the full e^+e^- mass range using the Mikaelian and Smith radiative corrections [47]. The final result, based on the observation of $63{,}693$ π^0_{D} events, was

$$\frac{B(\pi^0_{\mathrm{D}})}{B(\pi^0_{\gamma\gamma})} = (1.1559 \pm 0.0047_{\mathrm{stat}} \pm 0.0106_{\mathrm{syst}}) \times 10^{-2}. \tag{1.30}$$

The systematic error is dominated by the differences in the tracking efficiency between data and MC. After conversion to $B(\pi^0_{\mathrm{D}})$ in the same way as in Table 1.7, the $\sim 1\%$ relative uncertainty in Equation 1.30 means that this measurement is 3.6σ

---

[7]Estimated using fits to data taken in eight categories based on the π^0 energy relative to the beam energy.

from the most up to date SM calculation (Equation 1.25).

As mentioned at the start of this section, the PDG average excludes the KTeV measurement. The reason[8] for this was that the correction applied to the measured branching ratio (to extrapolate to the full M_{ee} range; the measurement was only conducted in the kinematic region $M_{ee} > 15$ MeV/c^2),

$$S = \frac{B(M_{ee} > 15 \text{ MeV/c}^2)}{B(\pi_{\text{D}}^0)} = 0.339128, \tag{1.31}$$

was calculated using an equation from the 1972 theoretical paper by Mikaelian and Smith which excludes important radiative corrections (see Subsection 1.3.1). The uncertainty on this correction is not mentioned, nor included in the final systematic uncertainty.

However, the $B(\pi_{\text{D}}^0)$ measured by the KTeV collaboration can be partially corrected to account for the missing radiative corrections. Table 1.8 shows the scaling factor S for the three cases of no radiative corrections, M&S radiative corrections and full radiative corrections. The first and third cases were calculated using NA62 MC generators and the second case is the KTeV scaling factor, as quoted in Equation 1.31. Also shown is the relative difference, Δ, between each case and the case with full radiative corrections. If, instead of the M&S radiative corrections, we correct the KTeV $B(M_{ee} > 15 \text{ MeV/c}^2)$ result using the full radiative corrections, the corrected $B(\pi_{\text{D}}^0)$ obtained is[9]

$$\frac{B(\pi_{\text{D}}^0)}{B(\pi_{\gamma\gamma}^0)} = (1.1749 \pm 0.0048_{\text{stat}} \pm 0.0108_{\text{syst}}) \times 10^{-2} \tag{1.32}$$

which is a relative difference of 1.6% compared with the result using M&S corrections (Equation 1.30). This also means the $B(\pi_{\text{D}}^0)$ measured by KTeV is now 1.9σ from

---

[8]The PDG do not state the reasoning in their summary tables. Thanks to A. Bettini (Istituto Nazionale di Fisica Nucleare, Italy), who was part of the group that calculated the PDG average, for explaining.

[9]Note that we can only correct the extrapolation to the full M_{ee} range, we cannot correct for any changes in MC acceptance.

Table 1.8: The scaling factor S for three types of radiative corrections.

	S	$|\Delta|$ (%)
No radiative corrections	0.340946	2.2
M&S radiative corrections	0.339128	1.6
Full radiative corrections	0.333649	0.0

the SM calculation (Equation 1.25).

Motivation for a new $B(\pi_D^0)$ measurement

Since the most recent theoretical advances of the Standard Model $B(\pi_D^0)$ calculation, there has not been an experimental branching ratio measurement that includes the most recent radiative corrections. Furthermore, $B(\pi_D^0)$ is used as normalisation for several π^0 rare decay measurements but due to the $\sim 3\%$ uncertainty on the PDG average, it often represents a limitation. For example, it dominates the uncertainty on the π^0 double Dalitz decay ($B(\pi^0 \to e^+e^-e^+e^-)$) [55] and is the largest source of uncertainty on $B(\pi^0 \to e^+e^-)$ [56]. In the rare kaon sector, it is also starting to limit measurements of the $K^+ \to \pi^+e^+e^-$ decay [57] (where a new measurement of $B(\pi_D^0)$ to 1% precision could improve the rate measurement precision by $\sim 30\%$) and the rates of the $K^\pm \to \pi^\pm\pi^0e^+e^-$ [58] and $K_{L,S} \to \pi^+\pi^-e^+e^-$ [59] decays.

One could also ask whether a precise $B(\pi_D^0)$ measurement could contribute to searches for new, beyond the Standard Model, physics[10]. However, there are currently no (known to the author) new physics (NP) models that directly depend on a precise measurement of the π_D^0 branching ratio. Furthermore, the theoretical calculation of $B(\pi_D^0)$ is very precise and does not depend on precise QCD calculations (it is mainly a QED calculation). It is hence unlikely that NP will be found in a $B(\pi_D^0)$ measurement seeing as it has not been observed already in other places.

However, precise determination of $B(\pi_D^0)$ could affect the searches for NP else-

---

[10]Thanks to T. Husek (Lund University, Sweden) for a useful discussion on new physics within the π^0 sector.

where in the π^0 sector. For example, in the measurement of the $\pi^0 \to e^+e^-$ branching ratio, the π^0_D branching ratio is used as normalisation and as explained above, is the dominant systematic uncertainty. There is currently a 3σ discrepancy between the theoretical prediction [60] and the most recent experimental measurement [56]. This may be caused by incomplete radiative corrections but several attempts have also been made to explain this discrepancy using NP. For example, Kahn et al. propose a model that uses a light vector boson produced in the annihilation of a neutral scalar dark matter candidate [61]. This model could provide both the solution to the anomalous 511 keV line that is observed being emitted from the centre of the galaxy [62], as well as (if the boson coupled to quarks in addition to electrons) explain the enhancement of the $\pi^0 \to e^+e^-$ branching ratio observed in experiment. Precise knowledge of $B(\pi^0_D)$ could therefore help in the search for beyond the Standard Model physics. A new measurement of $B(\pi^0 \to e^+e^-)$ is currently in progress at NA62.

To summarise, a new precise measurement of $B(\pi^0_D)$ is very much needed, whether it be to incorporate the latest theory improvements, compare to the latest theoretical calculation and experimental measurements or to improve the precision of other measurements/searches in the Standard Model and beyond. This forms the basis of the main work of this thesis and is presented in Chapter 5. NA62 is more sensitive to lower invariant mass values (and hence more of the M_{ee} spectrum in general) than the most recent measurement conducted by the KTeV experiment (see Table 1.7).

Chapter 2

The NA62 experiment

NA62 is a fixed target experiment, based at CERN, designed to measure rare decays of kaons using a decay-in-flight technique. The main aim is to measure the branching ratio of $K^+ \to \pi^+ \nu \bar{\nu}$, a decay with SM branching ratio $\sim 10^{-10}$. Beyond this, NA62 has a wide physics program with other precision and rare measurements as well as searches for forbidden processes and exotic particles also being conducted. Examples can be found in Refs. [48, 63, 64, 65, 66].

In order to measure kaon decays like $K_{\pi \nu \bar{\nu}}$, NA62 needs to be able to provide a high level of background rejection. The collection of $\mathcal{O}(10^{13})$ K^+ decays, accompanied by a background rejection factor $\mathcal{O}(10^{12})$, is needed to achieve the desired precision (discussed further in Section 2.5). In order to achieve this, there are several requirements:

- Particle identification of both the beam K^+ and the decay products, as well as a hermetic veto system. Both photons (from e.g. $\pi^0 \to \gamma\gamma$) and muons (from e.g. $K^+ \to \mu^+ \nu$) are produced as part of major backgrounds so detectors are needed to veto these. The required PID suppression and photon veto levels must each be $> 10^7$.

- Kinematic (momentum based) rejection at the level $\mathcal{O}(10^4 - 10^5)$. High resolution momentum measurements of both the beam K^+ and decay products

are needed to do this.

- High resolution timing at the $\mathcal{O}(100\ \text{ps})$ level. NA62 is a very high rate environment (nominal beam rate is 750 MHz) so this is needed to match the K^+ and the decay products whilst also help separate background from signal.

The rest of this chapter is mostly dedicated to how NA62 achieves the above requirements. Section 2.1 describes the beam line leading up to NA62. Each sub-detector is then described in Section 2.2, followed by a description of the trigger and data acquisition system (TDAQ) in Section 2.3. Some of the information given in these sections summarises the NA62 detector and trigger papers, available at Refs. [67, 68]. A summary of the software used within NA62 is then described in Section 2.4. Finally, the most recent results from the $K_{\pi\nu\bar{\nu}}$ analysis are shown in Section 2.5.

2.1 The beam line

The experiment uses a beam of protons from the Super Proton Synchrotron (SPS) particle accelerator[1]. These protons have a momentum of 400 GeV/c and, once extracted from the SPS, are directed towards a 40 cm long, 2 mm diameter beryllium rod that forms the fixed target (T10). The secondary beam extracted from T10 is referred to as the K12 beam and has a momentum 75 GeV/c.

The components in the K12 beam line and the NA62 detector layout are shown in Figures 2.1 and 2.2 respectively. The coordinate system is the same in both figures. "Upstream" and "downstream" are useful to define both directions and certain regions within the experiment. Upstream can either refer to the negative z-direction or to the region $z < 102.4$ m. Downstream can either refer to the positive z-direction or to the region $z > 102.4$ m.

---

[1]The SPS is the accelerator that feeds the LHC but the SPS beam is also used by NA62 and several other experiments in the CERN North Area.
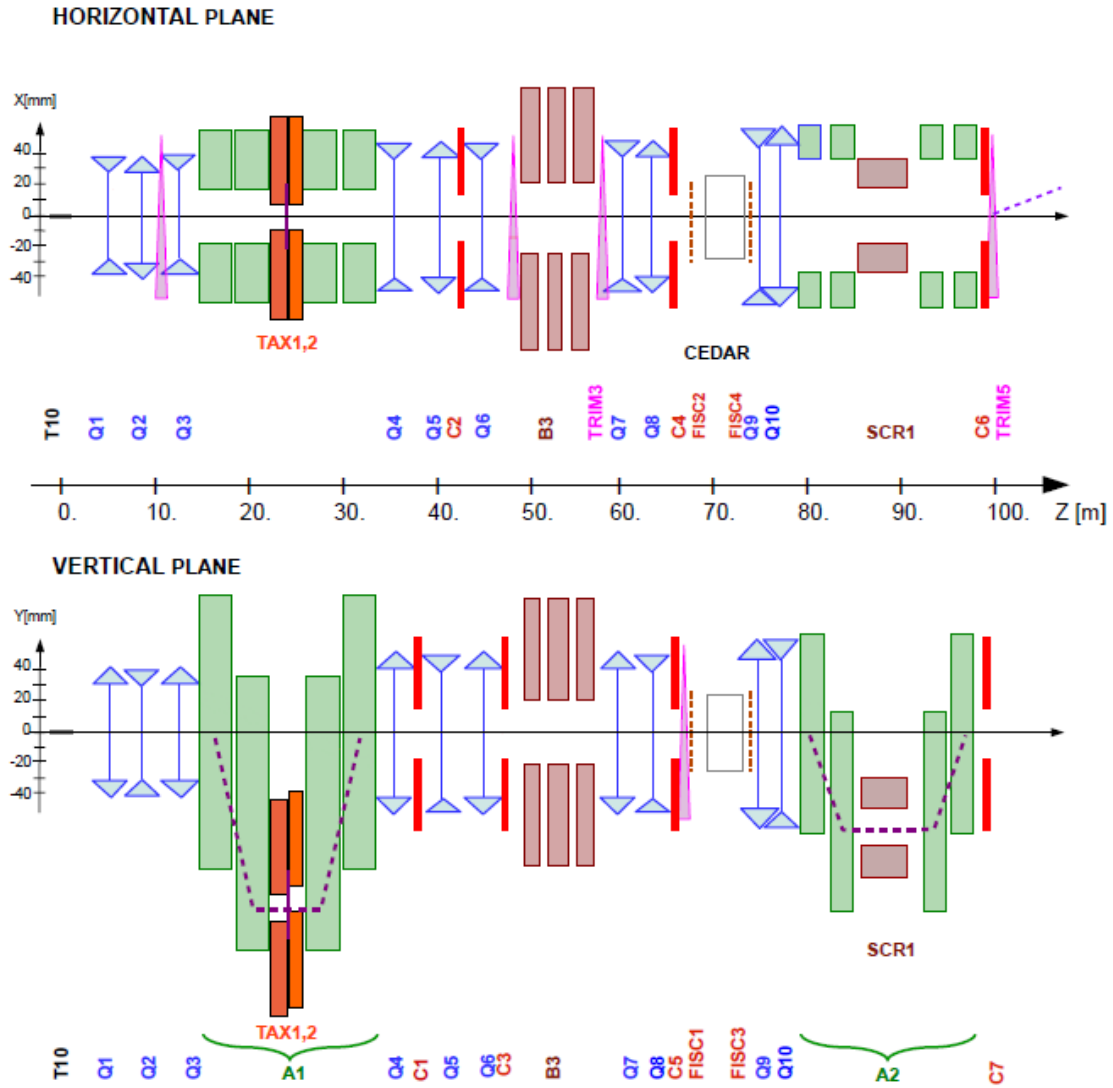
Figure 2.1: The NA62 beam line. The beam is in the positive z-direction and the dashed line shows the trajectory of an initially on-axis 75 GeV/c momentum beam particle. The notation is as follows. T10 is the target, Q represents a quadrupole magnet, TAX a beam-dump unit, C a collimator, B a dipole magnet, TRIM are steering magnets, FISC are scintillation counters, SCR are magnetic collimators and A are achromats. Figure adapted from Ref. [67].
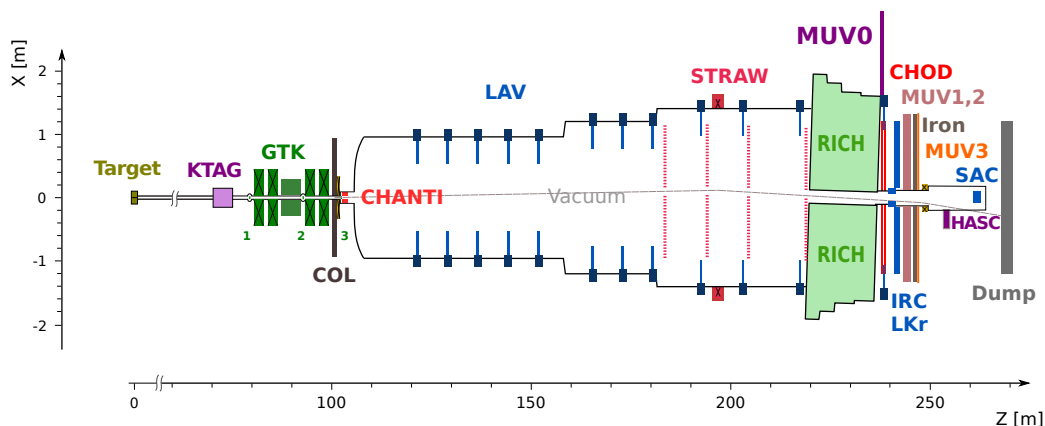
Figure 2.2: The NA62 experimental layout as observed from above. The beam is shown by the grey line (approximately along the line $x = 0$) and is in the positive z-direction. The main decay region is contained within a vacuum in order to reduce scattering of the beam and to improve the resolution on measured quantities. COL is the final collimator in the beam line, designed to absorb hadrons from upstream kaon decays. The sub-detectors are labelled and discussed further in Section 2.2. Figure reproduced from Ref. [67].

Downstream of the fixed target, a series of collimators, quadrupoles and achromats (described in detail below) ensure the desired secondary beam particles are transmitted as well as focus and select the 75 GeV/c momentum beam.

The first components of the beam line are three quadrupole magnets (Q1, Q2 and Q3) which collect a large solid angle acceptance of ± 2.7 mrad horizontally and ± 1.5 mrad vertically at 75 GeV/c central momentum. Following this, an achromat (A1) selects the beam of 75 GeV/c with a 1% rms momentum bite. The achromat is composed of four dipole magnets, the first two of which displace the beam vertically by 110 mm (while keeping the beam parallel). The following two magnets then return the beam to the original axis. Between these two sets of magnets, the beam passes through a set of holes in two beam-dump units (TAX1 and TAX2) to select the 75 GeV/c beam and absorb the remaining proton beam and unwanted secondary particles. Between TAX1 and TAX2, the beam is focused (vertically and horizontally) into a "radiator" made of tungsten plates (with thickness up to 5 mm). The thickness is optimised so that positrons in the beam lose energy via bremsstrahlung (thus causing them to be subsequently removed from the beam) whilst minimising

hadronic scattering.

Three more quadrupole magnets (Q4, Q5 and Q6) then refocus the beam in the vertical plane and ensure it is parallel to the z-axis in the horizontal plane. In between these quadrupoles are two collimators (C1 and C2) which limit the vertical and horizontal acceptance of the beam. A third collimator (C3) after Q6 absorbs positrons that had their momentum reduced by the radiator. The beam then passes through three dipole magnets (B3) that are 2 m long with iron plates placed between them. The iron plates have a 40 mm bore for the beam to pass through. The vertical magnetic field in the iron around the beam sweeps positive and negative muons aside. Two steering dipoles (TRIM2 and TRIM3) cancel any deviations of the beam due to any stray fields present inside the bore.

Two more quadrupoles (Q7 and Q8) ensure the beam is parallel so that the KTAG detector (which uses a CEDAR differential Cherenkov counter - see Subsection 2.2.3) is able to identify kaons in the beam. Proceeding the KTAG are two collimators (C4 and C5) which absorb any particles in the tails of the beam. Four filament scintillators (FISC1, FISC2, FISC3 and FISC4) are present before and after the KTAG in order to measure the mean beam divergence and tune it to zero. They also verify the remaining intrinsic beam divergence, as shown in Figure 2.3.

An additional two quadrupoles (Q9 and Q10) are present after the KTAG in order to focus the beam through the GTK detector (see Subsection 2.2.1) which measures the momentum and tracks the particles present in the beam. There are three GTK stations which are placed at different points around a second achromat (A2), as shown in Figure 2.4. A2 is composed of four dipole magnets that deflect the beam vertically by 60 mm, allowing the particle momenta to be measured (see Subsection 2.2.1 for more about the GTK). A magnetised iron collimator (SCR1) and return yokes of the third and fourth magnets remove muons which leave the beam in the momentum separated part between the second and third magnets. GTK3 is at the entrance to the decay region ($z = 102.4$ m). Two more collimators
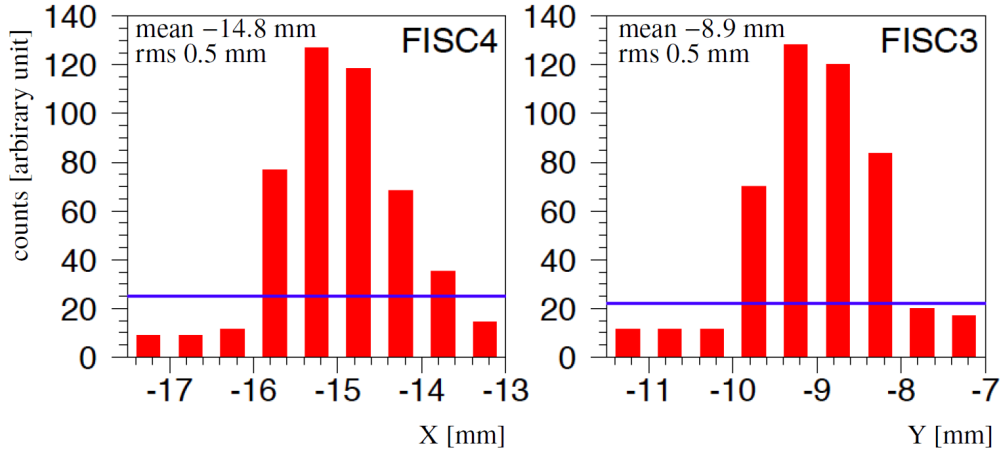
Figure 2.3: The beam divergence, as measured by the FISC scintillation counters. FISC2 and FISC4 measure in the horizontal plane and FISC1 and FISC3 measure in the vertical plane. The rms widths of 0.5 mm are equivalent to an angular divergence of 0.07 mrad. Figure reproduced from Ref. [67].
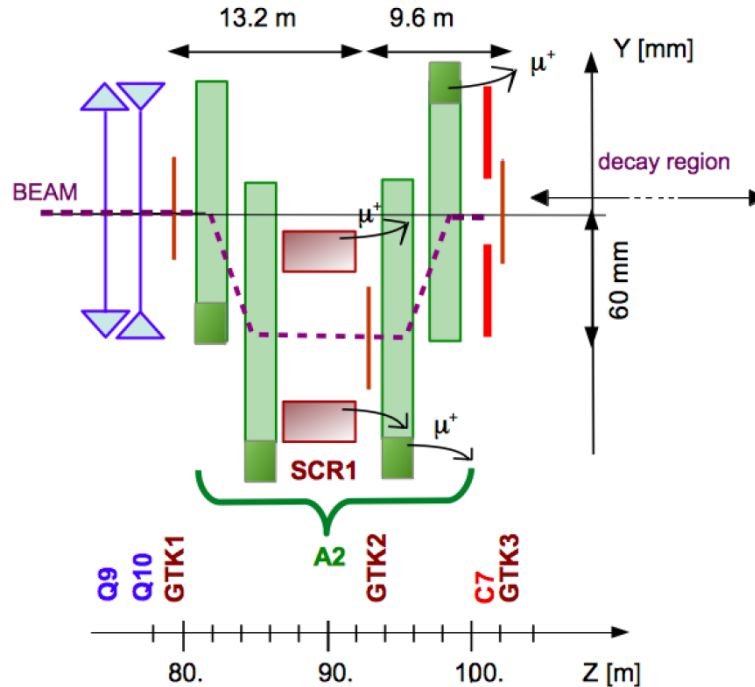
Figure 2.4: The GTK stations and second achromat in the beam line. Figure reproduced from Ref. [67].

(C6 and C7) are placed just before GTK3 to absorb beam particles (and their decay products) outside the beam acceptance. A steering magnet (TRIM5) between C6 and GTK3 deflects the beam towards positive X so that the subsequent deflection by the downstream magnet (MNP33), situated at $z \sim 200$m, directs the beam through the centre of the LKr calorimeter (see Figure 2.2 for the positions of the detectors).

The secondary beam that arrives at the decay region is at a momentum of 75 GeV/c ($\pm 1\%$) and, at full intensity, contains a total of 750 MHz of particles, of which 6% are kaons, 70% are pions, 23% are protons and <1% are muons. The defined decay region starts 102.4 m downstream of the target and is 60 m long[2]. It is contained within a 117 m long vacuum tank that also houses the STRAW and (part of the) LAV detectors and ends at the start of the RICH detector (see Section 2.2 for details regarding the individual detectors). The vessel diameter is 1.92 m at the start of the decay region, increasing to 2.8 m at the STRAW spectrometer. A 2 mm thick aluminium window separates the vacuum tank from the neon gas contained in the RICH detector. A thin-walled aluminium tube is attached to the window and passes through the RICH (and subsequent detectors), following the beam trajectory and allowing the beam to travel through vacuum until the end of the experiment.

The MNP33 magnet directs the beam so that it crosses the z-axis 2.8 m downstream of the LKr calorimeter. Two more filament scintillator counters (FISC5 and FISC6) are installed close to this crossing point to measure the beam and allow it to be steered correctly. Finally, the beam is deflected towards negative x (at an angle -13.2 mrad) by a dipole magnet (BEND) so that is misses the SAC detector which is placed inside the beam vacuum vessel. A wire chamber and ionisation chamber are placed after the vacuum exit window in order to measure the profile and intensity of the beam (the intensity measurement is often referred to as the argonian count). A beam dump at the end of the experiment is present to absorb the particles in the beam that do not decay.

---

[2]In the analysis presented in Chapter 5, 60 m is used. Other analyses use a different region size, depending on the kinematics and backgrounds present.

Table 2.1: Main parameters describing the K12 beam. Table adapted from Ref. [67].

Instantaneous proton rate per effective s of SPS spill		1.1×10^{12}
Instantaneous beam rates at decay volume entrance (MHz)	K^+	45
	π^+	525
	p	173
	μ^+	5
	Total	750
Beam acceptance (mrad)	Horizontal	± 2.7
	Vertical	± 1.5
K^+ momentum	Mean	75 GeV/c
	$\Delta p/p$	1%
Divergence at GTK (mrad; rms)	Horizontal	± 0.11
	Vertical	± 0.11
Beam size at GTK (mm; rms)	Horizontal	± 26.4
	Vertical	± 12.0
Estimated K^+ per year		5×10^{12}

The NA62 beam is received periodically from the CERN SPS. Each of these periods is known as a burst, last a few seconds and occur once every $\mathcal{O}(10 \text{ s})$. Bursts are used as the data taking unit as they give an indication as to the amount of data taken in a certain period. They are grouped into "runs" which contain bursts taken under similar data taking conditions (up to a maximum of ~ 1500 bursts, at which point a new run is started). If an intervention is needed part way though data taking for any reason, a new run is started. Note that "run" used in this context is different to when NA62 Run 1 and Run 2 are discussed. The latter are used to describe the 2016 to 2018 and 2021 to 2025 periods of data taking respectively.

Table 2.1 shows a summary of the main beam parameters.

2.2 The detectors

During the 2016 to 2018 data taking, NA62 contained 16 detectors distributed across ~ 200 m of the beam line. These are required to provide the necessary particle

identification, high-resolution timing, kinematic rejection and hermetic vetoing of photons that is needed for the $K_{\pi\nu\bar{\nu}}$ measurement as well as other measurements and searches. The detector layout is shown in Figure 2.2. To summarise:

- The GTK and STRAW detectors are responsible for the tracking of charged particles upstream and downstream respectively.

- Particle identification is done using the KTAG, RICH, LKr, MUV1, MUV2 and MUV3 detectors.

- A hermetic photon veto system is achieved using the LKr, LAV, IRC and SAC detectors.

- Two charged particle hodoscopes, NA48-CHOD and CHOD, are used for the trigger and timing measurements.

- The CHANTI, MUV0 and HASC are responsible for the rejection of certain backgrounds.

This rest of this section describes each detector in more detail. For reference, Table 2.2 shows a summary of the detectors, their primary purpose and whether they are used in the trigger.

2.2.1 GigaTracker (GTK)

The momentum and angle of the kaons needs to be measured to a precision of 0.2% and 0.016 mrad respectively in order to achieve the required level of kinematic rejection. The GTK (GigaTracker) is a silicon pixel detector that measures the time, momentum and direction of the kaons in the beam [69]. It is located inside the beam pipe and consists of three stations (GTK1, 2 and 3). The silicon is formed of pixels of size $300{\times}300$ µm^2 and is ${\sim}500$ µm thick, corresponding to 0.5% X_0. As mentioned in Section 2.1, between the three GTK stations are dipole magnets arranged as an achromat so that the beam particle momentum can be measured by

Table 2.2: Summary of the NA62 detectors. The primary purpose and the level at which they are used in the trigger are shown. The trigger is discussed in Section 2.3.

System	Detector	Primary purpose	Trigger
Tracking	GTK	Beam particle time, momentum and direction measurements.	-
	STRAW	Tracking of kaon decay products and PID when combined with information from the LKr.	L1
PID	KTAG	Kaon identification and timing	L1
	RICH	Identification and time stamping of charged downstream tracks.	L0
	MUV1/2	Identification of downstream pions and muons.	L0
	MUV3	Identification of downstream muons.	L0
Photon vetoes	LAV	Detection of photons emitted at angles $8.5 - 50$ mrad.	L1
	LKr	Detection of photons emitted at angles $1 - 8.5$ mrad and PID when combined with information from the STRAW.	L0
	IRC/SAC	Detection of photons emitted at angles $0 - 1$ mrad.	L0
Charged particle hodoscopes	NA48-CHOD	Timing of downstream charged tracks for input to L0 trigger.	L0
	CHOD	Timing of downstream charged tracks for input to L0 trigger.	L0
Other	CHANTI	Detection of upstream backgrounds, particularly inelastic interactions in GTK3.	-
	MUV0	Detection of π^- from $K_{3\pi}$ decays that are outside the STRAW acceptance.	-
	HASC	Detection of π^+ from $K_{3\pi}$ decays that are outside the STRAW acceptance.	-
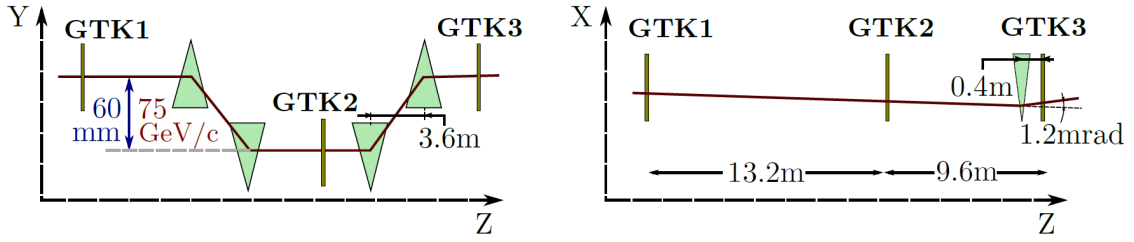
Figure 2.5: Schematic of the three GTK stations and the dipole magnets (green triangles) in the Y and X projections. The approximate centre of the beam is shown by the red line. Figure reproduced from Ref. [67].

measuring the displacement in GTK2. A schematic of the three GTK stations is shown in Figure 2.5.

The GTK was designed to achieve a timing resolution of ~ 200 ps in order to cope with the high rate environment of NA62. As the GTK has no particle identification (PID) procedure, hits must be matched with those in the KTAG as well as other PID detectors.

2.2.2 STRAW spectrometer

NA62 needs to measure the momentum of downstream tracks (i.e. those created by the beam particle decay products) to a precision of 1% and 0.060 mrad in order to obtain the required level of kinematic rejection ($\sim 10^4$) needed to suppress backgrounds. This is done by the STRAW spectrometer [70]. Four STRAW chambers, combined with a large dipole magnet referred to as MNP33, are able to track and measure the momentum to a resolution of

$$\frac{\sigma(p)}{p} = 0.30\% \oplus p \cdot 0.005\% \tag{2.1}$$

where p is the track momentum in GeV/c. The angular resolution is 60 µrad at 10 GeV/c and 20 µrad at 50 GeV/c.

The spectrometer starts at $z = 183$ m and is placed inside the vacuum vessel. The chambers are 10–14 m apart and each chamber has a circular active area of

outer diameter 2.1 m and is composed of four "views" which are orientated 45° to each other (see Figure 2.6a). Each view contains 448 straws split into 4 layers (see Figure 2.6b), meaning the track of a charged particle can be found as it is guaranteed to pass through at least two straws. A 12 cm gap without any straws is present in each view so that, upon combination of the four views, an octagon shaped gap of 6 cm apothem is left for the beam to pass through.

The straws themselves are tubes of 9.82 mm diameter and 2160 mm length, coated with 50 nm of copper and 20 nm of gold on the inside (forming the cathode) and filled with a gaseous mixture of 30% argon and 70% carbon dioxide. The straws are composed of a light material (PET) so as to reduce multiple scattering within them. The total amount of material in the whole STRAW detector corresponds to 1.8% X_0. Each straw also has an anode wire threaded through the middle of the tube. When charged particles pass through one of the straws, the gas is ionised and a signal is detected within the wire. Due to the variation in drift times that can occur, the track time resolution is ~ 5 ns.

The MNP33 magnet is between the second and third chambers. It delivers a known momentum kick to the charged particles (270 MeV/c towards the negative X-axis for positively charged particles) which allows their momentum to be measured.

2.2.3 KTAG

As the beam is only 6% K^+, a high timing resolution detector is needed to detect and differentiate the kaons from the pions and protons present in the beam. This is done using the first detector along the beam line, the KTAG [71], situated at $z = 69.3$ m and composed of a ~ 5 m long vessel filled with nitrogen gas at 1.7 bar as well as a readout system external to the vessel. The vessel is a CERN CEDAR-West detector [72, 73] and is aligned in the longitudinal direction. The KTAG is an upgrade of a CEDAR-West, a differential gas Cherenkov counter designed in the 1970s to discriminate between kaons, pions and protons in charged particle beams.
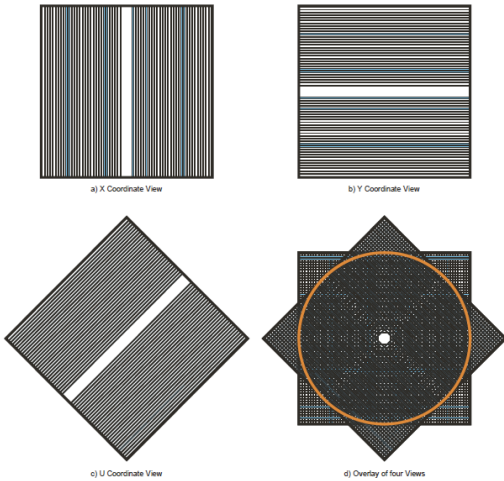
(a) Three of the four STRAW views (X, Y and U) plus the overlay of all four.
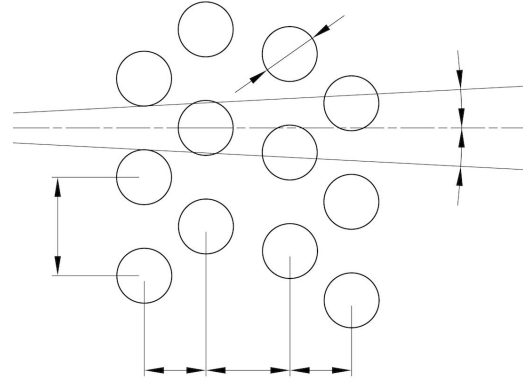
(b) The four layers within a STRAW view. A charged track will always pass through at least two straws.

Figure 2.6: The STRAW spectrometer layout. Figures reproduced from Ref. [67].

In order to do this, the CEDAR exploits the dependence of Cherenkov emission angle on particle mass. The gas pressure is tuned so that Cherenkov light from kaons is focused by a series of mirrors and lenses onto arrays of photomultiplier tubes (PMs) whereas light from pions and protons is not. This allows kaons in the beam to be identified and time-stamped. A schematic of the original CEDAR is shown in Figure 2.7.

The high timing resolution requirements (< 100 ps) meant that the original CEDAR readout system was replaced for use in NA62. Instead of 8 individual PMs as was in the original CEDARs, 8 sectors of 48 PMs are used. Each set of 48 PMs is arranged in a lightguide. Figure 2.8 shows a schematic of the KTAG photon detection system, as well as the CEDAR optics after the diaphragm. Coincidence (usually at least 4 or 5) of signals between these 8 sectors are used to define a kaon hit. The time resolution of a single channel is ~ 300 ps meaning that, as ~ 18 photons are detected per kaon, the overall kaon time resolution is ~ 70 ps. The KTAG is able to identify K^+ in the beam with $> 98\%$ efficiency when requiring at least 5 sectors are in coincidence.

The KTAG, in particular its future upgrade, is discussed extensively in Chap-
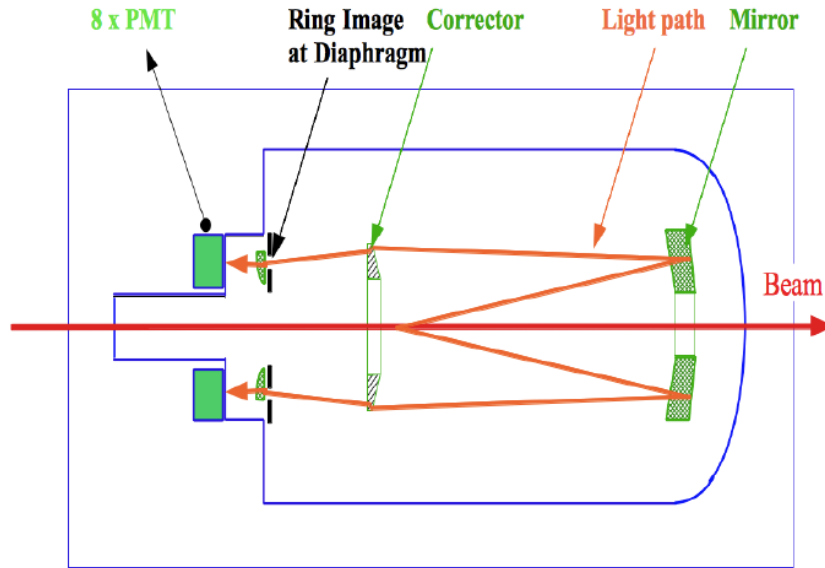
Figure 2.7: The CEDAR vessel. The paths of two Cherenkov photons, emitted by a K^+, are shown. Note that in the current NA62 setup, the 8 PMs have been replaced with 8 sectors of 48 PMs due to the higher intensity beam, as shown in Figure 2.8. Figure reproduced from Ref. [74].

ter 3.

2.2.4   RICH

The RICH detector (ring imaging Cherenkov detector) is used for the identification and time-stamping of electrons, muons, pions and scattered kaons [75]. It is particularly important for identifying muons and pions in the $15 - 35$ GeV/c range in the $K_{\pi\nu\bar{\nu}}$ analysis. It is composed of a 17 m long radiator vessel, aligned in the longitudinal direction and filled with neon at atmospheric pressure, with the beam passing through the centre. A mosaic of mirrors at the downstream end reflects the Cherenkov cone emitted by particles passing through the neon towards two PM arrays. Each of these arrays contain 976 PMs. Figure 2.9 shows a schematic of the RICH detector with the mirror mosaic at the far right and a zoom of one of the PM arrays on the left.

The RICH in Figure 2.2 is tilted with respect to the beam axis so that the beam
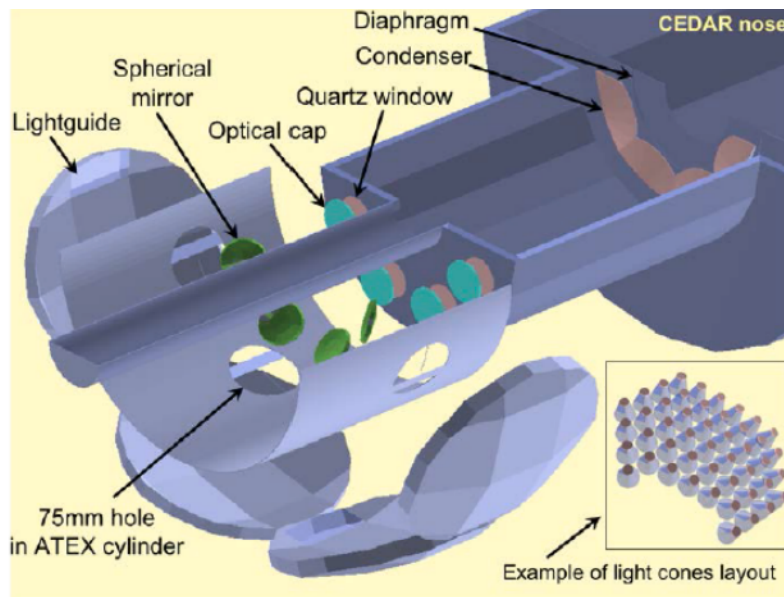
Figure 2.8: The KTAG photon detection system. The upper half of the detector has been removed from the schematic for clarity. Cherenkov light passes through the CEDAR quartz windows and is then reflected by spherical mirrors in the transverse direction into 8 lightguides. Figure produced internally by NA62; more figures are available in Ref. [71].
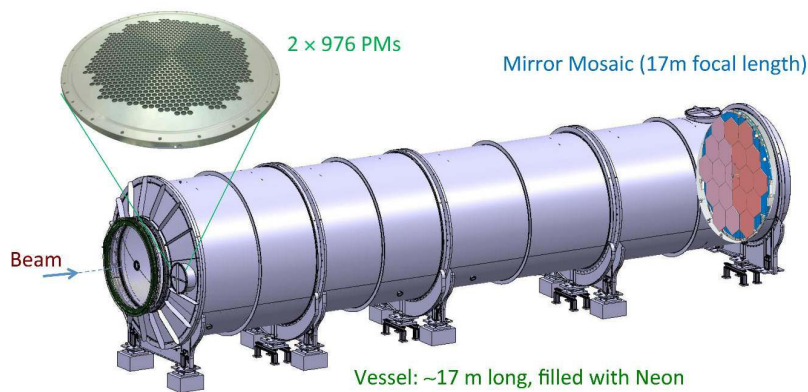
Figure 2.9: Schematic of the RICH detector. A zoom of the PM array is shown on the left and the mirror mosaic is shown on the right. Figure reproduced from Ref. [67].

passes through the middle of the RICH after deflection by the MNP33 magnet. For the $K_{\pi\nu\bar{\nu}}$ measurement, it is more important to identify positively over negatively charged particles. The RICH mirrors are hence tilted with respect to the beam axis so as to better align with the positive particles that were deflected in the opposite direction to the negative particles by the MNP33 magnet. This allows more light from positive particles to be collected, thus increasing the identification efficiency.

As in the KTAG, the Cherenkov emission angle (and hence the Cherenkov ring radius) depends on the particle mass. However, unlike the KTAG where all particles have approximately equal momenta, the particles passing through the RICH can have different momenta and the ring radius depends on this. The dependence of ring radius on momentum can be seen in Figure 2.10. The regions occupied by different particles are labelled and show that particles can be distinguished at lower momenta (< 35 GeV/c). At higher momenta however, the separation in ring radius between particles is lost. Hence, in analyses such as $K_{\pi\nu\bar{\nu}}$, a cut requiring the π^+ momentum to be < 35 GeV/c is applied.

The RICH is also used for high resolution (~ 70 ps) timing and as the reference detector when taking timing measurements. It complements other PID systems in achieving an overall muon suppression factor $\sim 10^7$, of which $\sim 10^2$ is given by the RICH.

2.2.5   HAC (MUV1 and MUV2)

The hadronic calorimeter (HAC) is composed of two detectors, MUV1 and MUV2 (see Figure 2.2), which are able to distinguish between pions and muons by the energy deposited within them [67]. Both detectors are made from alternating layers of iron and scintillator. MUV2 was originally the NA48 hadronic calorimeter [76] whereas MUV1 was designed for NA62. MUV1 has a finer transversal segmentation to better distinguish between hadronic and electromagnetic shower components (hadronic shower profiles are more spread out in the transverse direction whereas
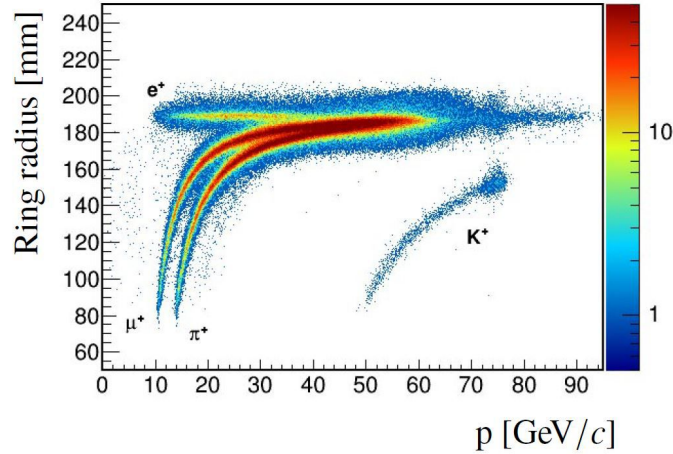
Figure 2.10: The Cherenkov ring radius vs. particle momentum. Below 35 GeV/c, e^+, μ^+ and π^+ can be distinguished. Figure reproduced from Ref. [67].

electromagnetic showers are more concentrated).

When combined with the NA48-CHOD detector (see Subsection 2.2.7), the MUV1/2 timing resolution is 0.9 ns for muons. The energy resolution is

$$\frac{\sigma(E)}{E} = 0.115 \oplus \frac{0.38}{\sqrt{E}} \oplus \frac{1.37}{E} \tag{2.2}$$

where E is in GeV. This can be improved using information from the LKr calorimeter (see Subsection 2.2.8).

2.2.6 Muon detector (MUV3)

The MUV3 detector is designed to detect muons with high time resolution and consists of two main components [67]. Firstly, there is a 80 cm thick iron wall (with a hole for the beam pipe) that attempts to absorb non-muon particles that pass through the calorimeters further upstream. The second component is the actual detector, comprised of 148 scintillator tiles arranged as shown in Figure 2.11 and placed downstream of the iron wall. Of the 148 tiles, 140 are 220×220 mm^2 and the remaining 8, which lie next to the beam pipe, are smaller due to the high particle rate there. The hit rate (computed from MC simulations) in each tile is also shown
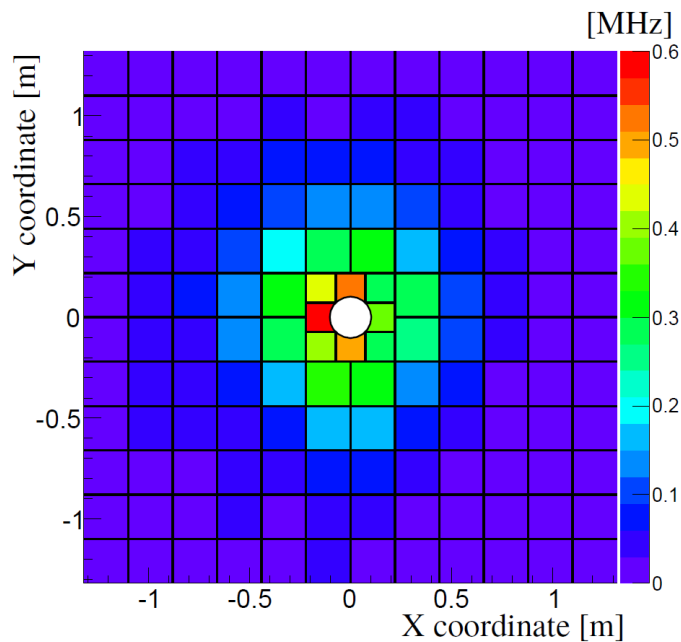
Figure 2.11: The layout of the MUV3 scintillator tiles and the corresponding hit rates per tile. The hot tile on the negative X side of the beam pipe has a rate of 3.2 MHz and is caused by beam pions decaying to muons (which are deflected towards negative X by the MNP33 magnet). Figure reproduced from Ref. [67].

in the figure.

The MUV3 time resolution is ~ 0.5 ns and the identification efficiency is $> 99.5\%$ for muons with > 15 GeV/c momentum. The efficiency drops to $\sim 96\%$ at 5 GeV/c.

2.2.7 Charged particle hodoscopes (NA48-CHOD and CHOD)

The charged particle hodoscopes are scintillation detectors with the main function of providing an input to the L0 trigger when at least one charged particle crosses their acceptance (Section 2.3 covers details of the trigger). The system is composed of two detectors: NA48-CHOD from NA48 (the predecessor of NA62) and a new CHOD detector designed specifically for the higher particle rate within NA62. They cover the lateral region downstream of the RICH and upstream of the LKr which is an annulus between the LAV12 inner radius (1070 mm) and the IRC outer radius (145 mm). The CHOD is placed on the upstream face of the LAV12 station and the NA48-CHOD is ~ 1.4 m downstream of this.

Note that in certain literature, the NA48-CHOD and CHOD are instead referred to as the CHOD and NewCHOD respectively. However, in this thesis, only the former will be used. In Figure 2.2, NA48-CHOD and CHOD are both shown by the "CHOD" label.

NA48-CHOD

The NA48-CHOD (charged particle hodoscope) [76] is mainly used for timing and provides an input for the L0 trigger. As shown in Figure 2.12a, NA48-CHOD consists of two consecutive planes of vertical and horizontal, 20 mm thick, plastic scintillator slabs (only half sections are shown in the figure). Each plane contains 64 slabs. The 128 slabs are split into 4 quadrants with each slab read out with PMs at the outside end. Due to the octagonal shape, the slabs vary in length from 600 mm at the outer edges to 1210 mm at the centre. The slabs closer to the beam pipe are also narrower than those at the outer edges due to the higher particle flux present there.

The coincidence of two signals from each plane is used to provide a track time (with precision 200 ps) and approximate track hit position (with precision 6.5 cm close to the beam pipe and 9.9 cm further out). The time measurement is corrected for the hit impact point position along the detector slabs.

CHOD

The CHOD detector [77] is used to complement the timing measurements from the NA48-CHOD but instead of long scintillator slabs, it is composed of 152 plastic scintillator tiles meaning that it is able to cope with the high intensity conditions of NA62. Rows of tiles placed alternatively on the upstream and downstream sides of a central support, with a 1 mm overlap between the tiles, are used to ensure there are no gaps for particles to pass through undetected. As with some of the other detectors, the tiles nearer the beam pipe are smaller due to the higher particle flux.

Figure 2.12b shows the CHOD tile geometry and the hit rates (obtained from

(a) Technical drawing of the NA48-CHOD detector.

(b) Tile geometry and hit rates (in MHz) in the CHOD detector.
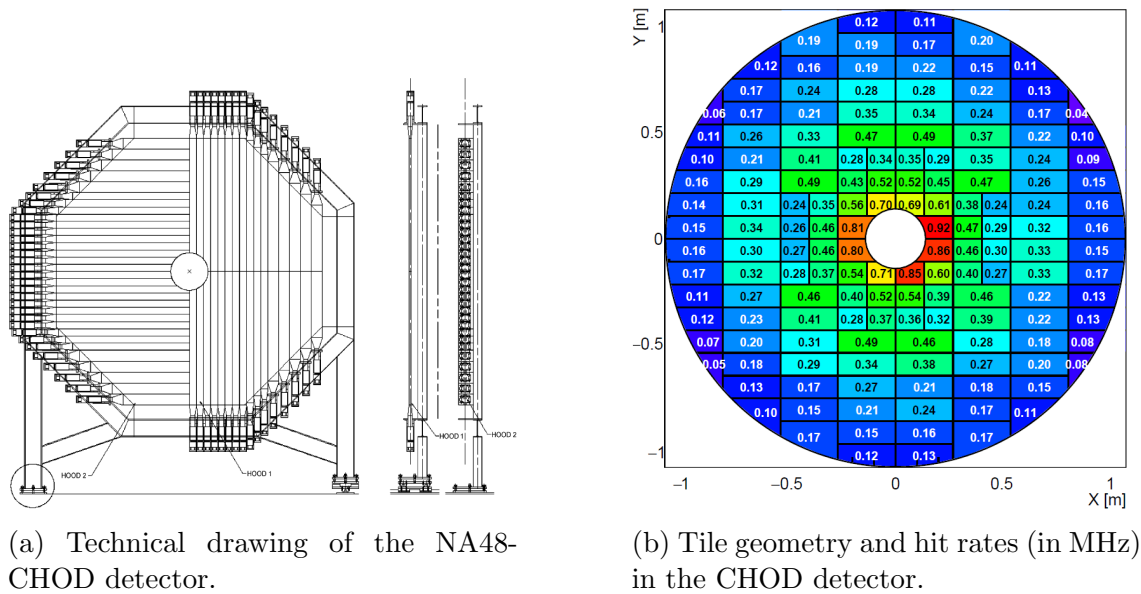
Figure 2.12: The two charged particle hodoscopes. The beam pipe passes through the centre of each. Figures reproduced from Ref. [67].

MC simulations) in each tile. 304 silicon PMs (SiPMs) are used to detect the signals from the tiles. The time resolution of the CHOD signals is ~ 1 ns.

2.2.8   Photon vetoes (LAV, LKr, IRC and SAC)

As explained at the start of this chapter, a π^0 (mainly originating from $K^+ \to \pi^+ \pi^0$) suppression factor $\sim 10^8$ is needed to accompany the kinematic rejection factor $\sim 10^4$. Due to the requirements (< 35 GeV/c) made on the π^+ momentum in the $K_{\pi\nu\bar{\nu}}$ analysis, the π^0 energy will be at least 40 GeV/c. It is important that the photons in the $\pi^0 \to \gamma\gamma$ decay have high energy in order to obtain high detection efficiency. Rejection of $\pi^0 \to \gamma\gamma$ events is then done by the photon veto system. Four different calorimeters are used within this system. They are placed in positions along the beam line such that the angular coverage is between 0 and 50 mrad. For angles between 8.5 and 50 mrad, the LAV detector is used. The LKr detector then covers angles of 1 to 8.5 mrad followed by the IRC and SAC detectors which cover $0 - 1$ mrad. Due to the anti-correlation between emission angle and energy in the two body $\pi^0 \to \gamma\gamma$ decay, each detector is optimised for the range of energies most

likely to be present in each region.

LAV

Twelve ring-shaped LAV (large angle veto) photon veto stations were designed for NA62 in order to cover angles outside of the LKr acceptance [78]. Each station is an annulus and is composed of radially aligned lead glass blocks. Eleven of the stations are placed around the perimeter of the vacuum vessel and the final station is ~ 0.6 m downstream of the RICH and operated in air. One of these stations is shown in Figure 2.13. Photons produce electromagnetic showers in the lead glass and the resulting Cherenkov light is then detected by a PM. One PM is used per lead glass block and in total, there are 896 blocks across all 12 stations.

The angular coverage is $8.5 - 50$ mrad (with respect to the z-axis) which, in the $K_{\pi\nu\bar{\nu}}$ analysis because of the momentum cut on the π^+, is large enough to make it impossible for both photons in the $\pi^0 \to \gamma\gamma$ (where the π^0 is from a $K^+ \to \pi^+\pi^0$ decay) to have angles larger than 50 mrad. Although it is possible for one photon to be at such an angle, this only occurs in 0.2% of events.

The photon detection inefficiency is $< 10^{-4}$, helping contribute to the overall photon rejection power of NA62 of 10^8. Furthermore, to keep the accidental rate to $\sim 1\%$, the time resolution of the LAV, which depends on the photon energy, is ~ 1 ns for a 1 GeV photon. In addition to this, in order to apply a precise veto energy threshold, the energy resolution is $< 10\%$.

LKr

The NA48 LKr (liquid krypton electromagnetic calorimeter) [76] was reused in NA62. The main part of the detector was left unchanged but part of the cryogenic system had to be replaced to ensure it was capable of lasting another decade of data taking. In addition, the readout system needed replacing in order to cope with the high intensity nature of NA62 [79].

Figure 2.13: The first LAV station before placement in the vacuum vessel. Image reproduced from Ref. [67].

The LKr is a quasi-homogeneous calorimeter, placed ~ 240 m downstream of the target. It has an inner radius of 8 cm and an outer radius of 128 cm. It is filled with liquid krypton at 120 K and the sensitive area is divided into 13248 longitudinal cells. These cells have a cross section $\sim 2 \times 2$ cm^2 and length 127 cm ($27X_0$) and are formed by zig-zagged electrodes (alternating cathode and anode strips - see Figure 2.14). Particles crossing the LKr produce a shower and thus a signal within these electrodes.

The angular coverage of the LKr is $1 - 8.5$ mrad and the photon-veto inefficiency varies from 10^{-3} at 1 GeV photon energies to 10^{-5} at > 10 GeV. The amount of energy deposited by particles in the LKr can be measured as it is directly proportional to the charge deposited on the electrodes. If two shower clusters overlap, corrections are applied to each cluster energy based on the energy deposited in the cell that is in the centre of each cluster. With E in GeV, the energy resolution is given by

$$\frac{\sigma_E}{E} = \frac{0.032}{\sqrt{E}} \oplus \frac{0.09}{E} \oplus 0.0042, \tag{2.3}$$

meaning the energy resolution is $\sigma_E/E = 0.8\%$ for a 25 GeV energy deposit. The spatial and time resolutions (in cm and ns respectively; E is still in GeV) are:

$$\sigma_{X,Y} = \frac{0.42}{\sqrt{E}} \oplus 0.06, \tag{2.4}$$

48
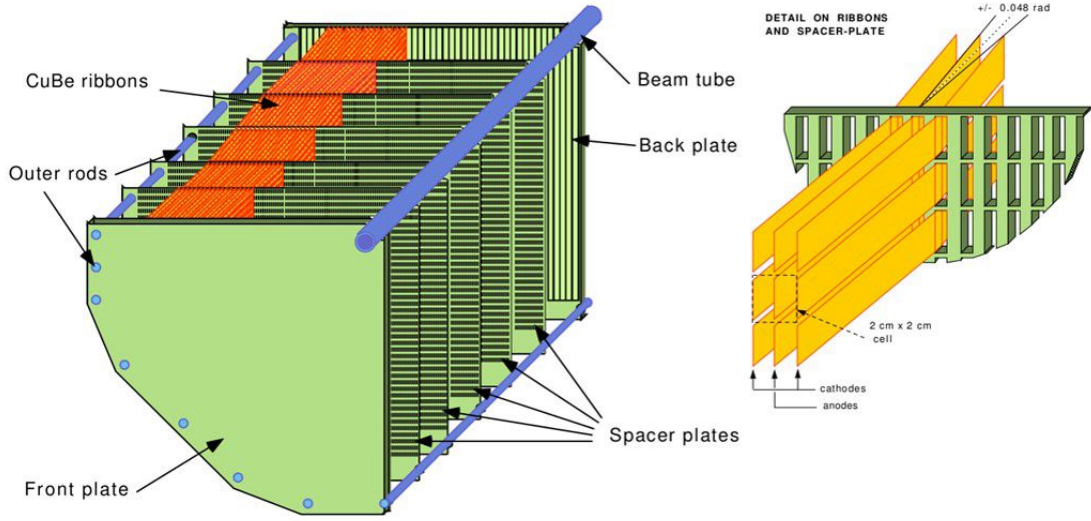
Figure 2.14: Left: A single quadrant that forms the LKr calorimeter. Right: The electrodes and cells within the LKr. Figure reproduced from Ref. [67].

$$\sigma_t = \frac{2.5}{\sqrt{E}}. \tag{2.5}$$

For a 25 GeV deposit, these are equal to 1 mm and 0.5 ns respectively.

Due to the fundamental differences between particles and their interaction with matter at different energies, the LKr can be used together with the STRAW as a PID system. For example, the ratio of energy deposited in the LKr to the total momentum (measured by the STRAW), E/p, for muons and pions will typically be less than 0.2 and 0.8 respectively. On the other hand, electrons and positrons result in electromagnetic showers within the LKr, deposit all their energy and have $E/p \sim 1$. This is the main PID system used in the π^0_D analysis, discussed in Chapter 5.

SAV (IRC and SAC)

The small angle veto (SAV) system is composed of two detectors, the IRC (intermediate ring calorimeter) and SAC (small angle calorimeter) which are able to detect photons between 0 and 1 mrad [67]. Both detectors are Shashlyk calorimeters (i.e. alternating lead and plastic scintillator plates) and are used to detect the high en-

ergy photons (> 5 GeV) that would otherwise be lost down the beam pipe. The inefficiency of the SAV is 7×10^{-4}. The time resolution for muons is < 2 ns for the SAC and < 1.6 ns for the IRC. For photons, the time resolution of the SAC and IRC together is < 1 ns.

2.2.9 Other detectors

CHANTI

Inelastic scattering can occur in the third GTK station (as the beam passes directly through the silicon) and the Charged Anti-coincidence detector (CHANTI) is used to detect this [80]. This aids the vetoing of backgrounds as particles produced in these interactions can enter the downstream detectors. Scattering from the first two stations is not a problem due to the collimator and magnet yokes removing these backgrounds (see Section 2.1).

The CHANTI is formed of 6 square hodoscope stations, each composed of triangular cross section scintillator bars. Figure 2.15 shows one of the stations as well as 5 of the 6 CHANTI stations within the vacuum vessel (picture was taking during assembly). The positions of each station is such that particles generated in GTK3 that could be within the acceptance of the downstream detectors are within the CHANTI acceptance. A time resolution of ~ 1 ns is achieved with the CHANTI which is enough to keep the random veto to within a few percent.

MUV0

The MUV0 detector is used to detect π^-, particularly those with momentum < 10 GeV/c, from $K^+ \rightarrow \pi^+\pi^+\pi^-$ that are outside the lateral acceptance of the STRAW chambers [67]. It is a scintillator hodoscope, composed of two layers of 48 plastic scintillator tiles ($200{\times}200{\times}10$ mm^3), read out using PMs.
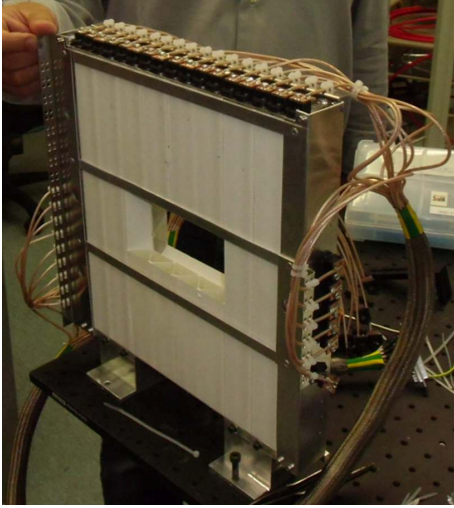
(a) A single station.
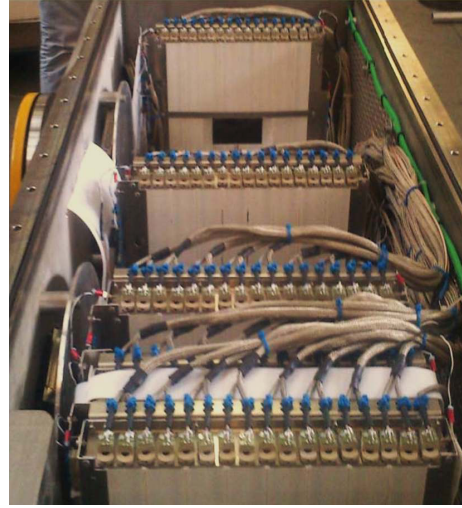
(b) Inside the vacuum vessel.

Figure 2.15: The CHANTI detector during assembly. Images reproduced from Ref. [67].

HASC

The MUV0 detector is used to detect the π^- in $K^+ \to \pi^+\pi^+\pi^-$ that are outside the lateral acceptance of the STRAW chambers. However, the π^+ also need detecting which is done with the HASC (hadronic sampling calorimeter, reused from a NA61 prototype detector [81]), in particular those with > 50 GeV/c that pass through the beam holes in the STRAW chamber centres. A dipole magnet upstream of the HASC sweeps these pions out of the K^+ beam, allowing them to be identified separately. The detector is composed of alternating lead - scintillator plates, read out using SiPMs.

2.3 The TDAQ system

As mentioned at the start of this chapter, it is necessary to collect $\mathcal{O}(10^{13})$ kaon decays to achieve the required precision on the $K_{\pi\nu\bar{\nu}}$ measurement, accompanied by a rejection factor $\mathcal{O}(10^{12})$. A trigger is hence required in the experiment that contributes to this level of suppression and limits the amount of data being stored and analysed. The NA62 trigger and data acquisition system (TDAQ) is composed

of a Level 0 (L0) hardware trigger, followed by a software based Level 1 (L1) trigger. The L1 trigger is often referred to as the High Level Trigger (HLT). Table 2.2 summarises which detectors are used at each trigger level.

The beam particle decay rate means that the particle rate in the detectors is > 10 MHz which is too high to be read or stored. The L0 trigger is designed to reduce this rate by a factor of 10, to $\sim$ 1 MHz (the maximum readout rate of most detectors). Each detector system that participates in the L0 trigger (generally the detectors which are faster) is programmed to generate data, known as L0 trigger primitives, that encode the trigger conditions that were satisfied as well as the time of the event. These are collected, time-matched and processed by the L0 trigger processor (L0TP) which makes a decision based on the full L0 trigger criteria. The detectors all use the same 40 MHz clock, allowing timestamps to be compared (and also allowing checks of time-alignment between detectors to be carried out). If a trigger condition is satisfied, the readout of the detectors' data to an online PC farm is then started for processing by the HLT.

The latency of the L0 system is 1 ms and data from detectors that can be read out and have a trigger decision made within this time window are used at L0 in order to achieve the factor 10 data reduction required. A minimum deadtime of 75 ns between consecutive triggers is needed due to the trigger transmission logic of NA62. This allows for 3 clock cycles to occur (the clock frequency is 40 MHz) which is required by the trigger hardware in order to receive, register and deliver a trigger signal to the detectors [82, 83].

The L1 trigger algorithms work on information from single detectors and cut the rate by another factor of 10 to 100 kHz as well as, if a positive L1 trigger signal is obtained, prompt the readout of data from the data-heavy detectors (STRAW and calorimeters[3]). If an event passes the L1 trigger, it is saved to disk for offline analysis.

---

[3]Despite being data-heavy overall, some coarse-grained data from the LKr, MUV1 and MUV2 calorimeters is used at L0.

NA62 took data between 2016 and 2018 (known as Run 1), each year at a higher intensity. Full intensity corresponds to a beam rate of 750 MHz (which itself corresponds to a kaon decay rate in the decay region of ~ 4 MHz). The data taking during these years wasn't conducted at full intensity (45% in 2016, 50–55% in 2017 and 60% in 2018) due to hardware limits associated with the L0 trigger as well as problems with the beam stability (spikes in intensity at the start of burst would overwhelm the readout). Upgrades to the the firmware and beam stability during the 2018–2021 long shutdown meant that NA62 could run at 100% intensity during the 2021 data taking however. A total of 205k, 301k and 525k bursts were collected in 2016, 2017 and 2018 respectively. This corresponds to a total of $\sim 2.2 \times 10^{18}$ protons on target ($\sim 1.9 \times 10^{12}$ protons impact upon the target per SPS spill) and a total number of K^+ decays of $\sim 6 \times 10^{12}$.

Within the TDAQ system, a minimum-bias (otherwise known as control or CTRL) trigger is present so that the efficiency of each trigger can be measured. The only trigger condition is the coincidence of two hits in a NA48-CHOD quadrant (one hit from each plane) and a downscaling of 400 is used in order to limit the amount of data that is recorded. In addition to trigger efficiency measurements, the minimum-bias trigger is used for analysis (see Section 2.5 and Chapter 5).

More details on the TDAQ system and its performance in Run 1 can be found in Refs. [68, 82, 84].

2.4 The NA62 software

NA62 uses a software framework (NA62fw) which is open for use by members of the collaboration. This section briefly describes the framework but full details can be found in Ref. [85]. The author made several contributions to both NA62MC and NA62Analysis which are detailed in other parts of the thesis.

NA62MC

The NA62 Monte Carlo (NA62MC) is a Geant4 based code that allows the simulation of all parts of the experiment. Geant4 is a toolkit that simulates particle-matter interactions [86] and each detector in NA62 can be created within it to be geometrically accurate and composed of the correct material. Particle interactions within each detector/material are fully simulated by Geant4. This includes hadronic, electromagnetic and optical processes. The NA62 beam and beam line is simulated using the TURTLE package [87] and particles and their decay products are then tracked through the detectors and are allowed to decay according to either NA62 or Geant4 defined generators. Generators simulate the decay kinematics and output the daughter four-momenta. NA62 defined particle decay generators are used where possible over Geant4 ones so that appropriate matrix elements and form factors are used. The main topic of this thesis is a measurement of the π_D^0 decay and an up to date generator that includes the most recent advances in the calculation of the radiative corrections (from Husek et al. [44]), discussed in Section 1.3, is used when simulating this decay mode.

MC samples containing large numbers of events[4] are often needed in order to obtain the required statistical precision. These are centrally produced using NA62MC on the computing GRID for use by NA62fw users. The MC samples can either be of a specific beam particle forced to decay to a certain mode (e.g. only $K^+ \rightarrow \pi^+\pi^0$), a beam particle forced to decay to a mixed set of decay modes (e.g. the six most common K^+ decays, known as mixed MC) or beam particles that are not forced to decay. When the beam particle is forced to decay, it is done so in a certain z-range (usually 102.425 m to 180.0 m).

---

[4]In this context, an event is the simulation of one beam particle plus its decay products.

NA62Reconstruction

NA62Reconstruction is a ROOT [88] based code that carries out the reconstruction of both raw MC simulations (from NA62MC) and raw data in a similar way. This is done in a modular fashion for each detector. Hits from the detectors are analysed and if appropriate, combined to form a "reconstructed candidate" (the decision to combine hits is based on spatial and timing information from each detector). A candidate represents the detection (which is not the same as identification) of a single particle by a detector. This allows the conversion of the raw data and MC outputs into a readable format for analysis (by NA62Analysis, see below). The digitisation of signals in the MC is simulated as part of the reconstruction. As with NA62MC, NA62Reconstruction is run centrally by the collaboration so that each user has access to reconstructed data and MC.

In standard MC samples, an "event" contains a single beam particle decay (and the subsequent daughter interactions). However in real life, with NA62 being a high intensity experiment, decays are occurring at the same time, leading to inefficiencies in the detectors (due to for example, the read-out deadtime). In order to simulate this, so-called "overlaid" MC is often used whereby MC events are injected into the MC sample of interest at the beginning of the reconstruction, resulting in additional hits in each detector. The MC events being injected are picked at random from MC samples in which the beam particles are not forced to decay. These samples are hence mainly composed of beam particles that do not decay or interact. For example, a standard $K^+ \to \pi^+ \pi^0$ MC sample normally only contains kaons that are forced to decay to $\pi^+ \pi^0$. However, an overlaid $K^+ \to \pi^+ \pi^0$ MC sample contains kaons that are forced to decay to $\pi^+ \pi^0$ but also contains kaons, pions and protons passing through the experiment without interacting/decaying, kaons that scatter, kaon decays to e.g. $\mu^+ \nu$, pion decays to e.g. $\mu^+ \nu$ etc. The rate at which events are injected is calculated using the probability that, in real life, two events will occur in a certain time window. This time window is calculated using the beam rate as

well as the read-out window. Overlaid MC leads to an improved simulation of what occurs in data compared to standard MC. It is a must in non-rare decay analyses, such as that described in Chapter 5 and studies detailing the improvements are presented there.

Due to the presence of overlays in the MC samples, the decay type from which a reconstucted particle track originated from is unknown. However, the reconstructed track can be "matched" to a true MC track using position and momentum information, allowing the decay type to be found. This is how the different decay modes are separated in the MC samples used in Chapter 5. However, this matching can sometimes fail meaning the true decay type cannot be found (this occurs in $\mathcal{O}(0.1\%)$ of cases). These decays are thus labelled "unknown", as will be seen in the figures shown later in this thesis.

Some additional nomenclature associated with the reconstruction should be defined. In MC, an event is the simulation of a single decay as well as the overlaid decays in a ±200 ns time window if it is overlaid MC. The former will be referred to as the original event whereas the latter the overlaid event(s). In data, an event is usually defined as the data that is readout before/after the firing of a trigger. A track is a collection of reconstructed STRAW hits that are associated with a single particle (mis-reconstruction can however merge hits from different particles). It can of course be extrapolated forwards/backwards to obtain the approximate path that the particle took. The track fitting is done using a Kalman filter method [89]. The association between hits in different detectors can be done by extrapolating the STRAW track to the detector plane(s) and checking for geometrical and temporal association using the hit position and time. A vertex is formed when multiple tracks pass through approximately the same point in space. A least-squares fit is used to build the vertices present in an event [90].

NA62Analysis

NA62Analysis provides users with a number of tools that are both necessary and useful for analysis of data and MC (post-reconstruction by NA62Reconstruction). For example, associations between STRAW tracks and other detector candidates as well as MC truth data can be accessed. Calibrations and corrections for both data and MC are also available for users. In data, this is done to correct for differing data-taking conditions. In MC, it is done to fine-tune parameters that are already present in the simulation but may need adjusting to simulate a certain data taking period. For example, corrections are needed to STRAW track momenta in order to account for slight variations in the MNP33 magnetic field and for any residual misalignments of the detector. Corrections are also needed, in both data and MC, to clusters in the LKr calorimeter in order to account for e.g. spatial dependence of the measured energy due to electric field variations and charge collection efficiency near the anode. Additional corrections are needed in MC to fine-tune the total cluster energy.

The measurement described in Chapter 5 was conducted using NA62Analysis.

2.5 The $K^+ \to \pi^+ \nu \bar{\nu}$ decay

This section contains a brief summary of the analysis conducted in Ref. [91] and is given for completeness only. See Section 1.2 for the theory and motivation behind the measurement.

The decay signature for $K_{\pi\nu\bar{\nu}}$ is one incoming kaon and one downstream pion with mass missing from the decay due to the two un-detected neutrinos. The missing mass is given by

$$M^2_{\text{miss}} = (P_K - P_\pi)^2 \tag{2.6}$$

where P_K is the kaon four-momentum and P_π is the pion four-momentum. The reconstructed M^2_{miss} vs the π^+ momentum, obtained from minimum-bias triggered

data, is shown in Figure 2.16. Each of the main three K^+ background decays (labelled by the corresponding decay products - see Table 1.3 for a summary of the decays) are shown and due to kinematics, are mostly constrained to specific areas of the diagram, as shown by the black boxes surrounding the "hot" areas of the figure and the respective labels. It is therefore beneficial to define two signal regions, Region 1 and Region 2, which kinematically favour the $K_{\pi\nu\bar{\nu}}$ decay and reduce the amount of background coming from other K^+ decays. These signal regions are shown by the hatched boxes in Figure 2.16. Region 2 can extend to higher momentum than Region 1 because the $K_{\mu2}$ background is larger at higher momentum. It should also be noted that Region 2 was only defined up to a pion momentum of 35 GeV/c in the 2016 and 2017 data analyses. Various improvements to the selection allowed it to be extended for the analysis of 2018 data.

Figure 2.16 also shows five control regions. The analysis was performed blinded, meaning that the signal and control regions were hidden until the selection and background studies were finalised. This was done so as to avoid introducing bias when optimising the signal selection. The control regions were unblinded first to ensure that the expected background was understood. Once confirmed that this was the case, the signal regions were unblinded.

A dedicated trigger was used to collect data for the $K_{\pi\nu\bar{\nu}}$ analysis, known as the PNN trigger. The L0 and L1 trigger conditions were chosen so as to select $K_{\pi\nu\bar{\nu}}$ events whilst reducing background from the three K^+ decays shown in Figure 2.16. The L0 trigger requirements were:

- A signal in the RICH to tag a charged particle. The time of this signal, referred to as the trigger time, is used as a reference time. The remaining L0 requirements in this list must all be within 6.3 ns of the trigger time (the LKr data transfer clock frequency is 160 MHz, hence the specific cut value).

- A signal in one to four CHOD tiles.

- No signals in opposite CHOD quadrants to suppress $K^+ \to \pi^+\pi^+\pi^-$ decays.
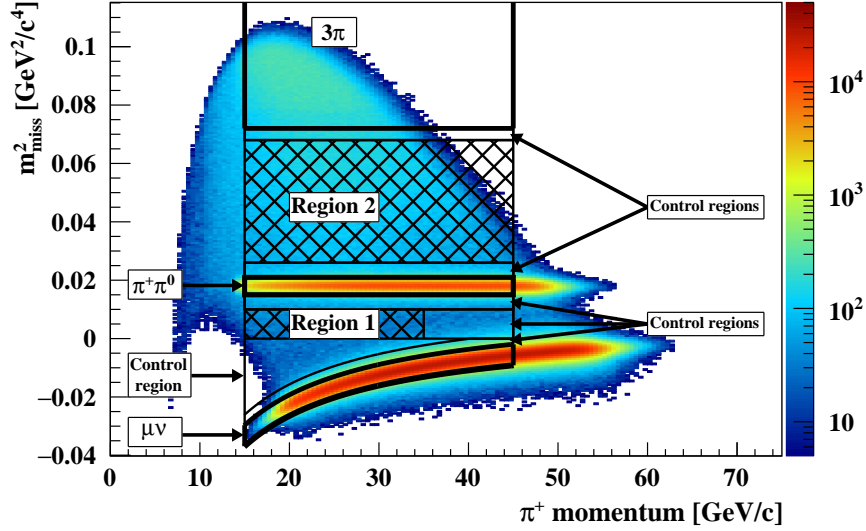
Figure 2.16: The reconstructed M^2_{miss} vs the π^+ momentum for kaon decays in NA62. The three main K^+ decay background regions as well as the $K_{\pi\nu\bar{\nu}}$ signal region are shown. For the $K_{\pi\nu\bar{\nu}}$ measurement, the π^+ momentum is restricted to 15-35 GeV/c (15-45 GeV/c in 2018) so that the RICH detector can be used for particle identification and so that, in the $K^+ \to \pi^+\pi^0$ decay, the π^0 has a large amount of energy and is thus easier to detect. Figure reproduced from Ref. [91].

- No signals in MUV3 to reject $K^+ \to \mu^+\nu$ decays.

- Less than 30 GeV deposited energy and no more than one cluster in the LKr to reject $K^+ \to \pi^+\pi^0$ decays.

The L1 trigger requirements were:

- A kaon identified in KTAG.

- Signals within 10 ns of the trigger time in at most two blocks of each LAV station.

- At least one STRAW track corresponding to a particle with momentum below 50 GeV/c and forming a vertex with the nominal beam axis upstream of the first STRAW chamber.

In addition to the PNN trigger, the minimum-bias trigger (using the NA48-CHOD detector) was used at analysis level to measure the K^+ flux, efficiencies
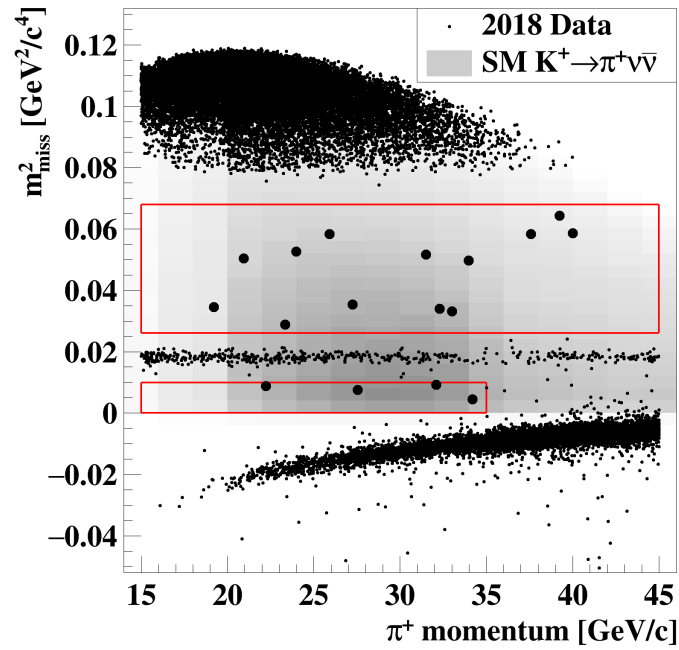
Figure 2.17: The reconstructed M^2_{miss} vs the π^+ momentum after the $K_{\pi\nu\bar{\nu}}$ 2018 analysis has been completed. 17 events were observed. The three sets of main background can also be seen, similar to that in Figure 2.16. The SM acceptance is shown by the intensity of the grey shaded area. Figure reproduced from Ref. [91].

and for background estimations. The downscaling factor used by the minimum-bias trigger was 400 and the trigger time, in this case, was defined as the time of the NA48-CHOD signal.

A total of three $K_{\pi\nu\bar{\nu}}$ events were observed in the 2016 [92] and 2017 [93] datasets. In 2018, 17 events were observed and Figure 2.17 shows the unblinded results of the 2018 analysis.

In order to calculate $B(K_{\pi\nu\bar{\nu}})$, the single event sensitivity was used. This is defined as the branching ratio that would be measured if one signal event was observed:

$$SES = \frac{1}{N_K \epsilon_{\pi\nu\bar{\nu}}} \tag{2.7}$$

where N_K is the number of K^+ decays in the fiducual volume and $\epsilon_{\pi\nu\bar{\nu}}$ is the signal selection efficiency. The signal selection efficiency depends on the signal acceptance, the trigger efficiency and the random veto efficiency. The normalisation is done

relative to $K^+ \to \pi^+ \pi^0$, selected from minimum-bias data and also used in the computation of N_K. The branching ratio can then be extracted with a binned log-likelihood fit using the signal acceptance and background expectation. After combining the 2016–2018 results, a signal significance of 3.4 standard deviations was obtained from a background-only hypothesis test. The measured branching ratio (again from 2016–2018 data), at 68% CL, was

$$B(K^+ \to \pi^+ \nu \bar{\nu}) = (10.6^{+4.0}_{-3.4}|_{\text{stat}} \pm 0.9_{\text{syst}}) \times 10^{-11}, \tag{2.8}$$

which is consistent with respect to the SM expectation within 1 standard deviation and is the most precise measurement to date.

Chapter 3

Hydrogen filled CEDAR

3.1   The KTAG detector

In order for NA62 to measure decays of kaons, the kaons themselves need to be tagged. As kaons only make up $\sim 6\%$ of the beam (a rate of 45 MHz, compared with the total particle rate of 750 MHz), the pion/proton mis-tag should also be kept to a minimum. This is achieved using the KTAG detector[1] [71], a gas Cherenkov detector that is composed of a CEDAR Cherenkov counter [72, 73] and a photodetector system external to the CEDAR. The CEDAR is filled with nitrogen gas and is designed to identify minority kaons in a beam (or more precisely, it identifies kaons and excludes pions/protons) by detecting the Cherenkov light emitted. The dependence of Cherenkov angle on particle velocity is exploited in order to do this. The CEDAR is a ~ 6 m long vessel which contains several optical instruments which are finely tuned so that the Cherenkov light emitted by the kaons in the beam is focused to sets of photomultiplier tubes (PMs) upstream of the CEDAR[2]. There are two types of CEDAR: a type West (CEDAR-W) and a type North (CEDAR-N).

---

[1]Note that, for completeness, some information from the description of the KTAG in Subsection 2.2.3 is repeated here.

[2]As in previous Chapters, upstream refers to the negative z-direction and downstream refers to the positive z-direction. Hence, when the photons are initially emitted, they are travelling in the downstream direction.

The former was designed for use with nitrogen (N_2) and a lower momentum beam while the latter was designed for use with helium (He) and a higher momentum beam. They contain the same optical components but with slightly different geometrical parameters. The current NA62 KTAG uses a CEDAR-W. Table A.2 in Appendix A.2 shows the geometrical parameters used in each type of CEDAR, as well as other information that will be explained later in this chapter.

A beam particle, with velocity $\beta = v/c$, passing through a gaseous medium of refractive index n, emits Cherenkov light in the shape of a cone of semi-aperture θ_C, with

$$\cos\theta_C = \frac{1}{\beta n}. \tag{3.1}$$

The optical components of the CEDAR detector focus this cone of light to give a ring of light. The velocity of the beam particle is given by [73]

$$\beta = \left[1 + \left(\frac{m^2}{p^2}\right)\right]^{-0.5} \tag{3.2}$$

where m and p are the beam particle mass and momentum respectively. In practice, the beam particle momenta have an RMS spread of $\Delta p/p \approx 1\%$. The difference in velocity between two beam particles can be written as (assuming $\beta \approx 1$)

$$\frac{\Delta\beta}{\beta} \approx \beta_2 - \beta_1 = \left[1 + \left(\frac{m_2}{p}\right)^2\right]^{-0.5} - \left[1 + \left(\frac{m_1}{p}\right)^2\right]^{-0.5} \approx \frac{m_2^2 - m_1^2}{2p^2}. \tag{3.3}$$

If we assume that n is constant and that the small angle approximation holds[3], Equation 3.1 can be differentiated to give the difference in Cherenkov angle between two beam particles,

$$\Delta\theta = \frac{1}{\tan\theta}\frac{\Delta\beta}{\beta} \approx \frac{1}{\theta}\frac{\Delta\beta}{\beta}, \tag{3.4}$$

which means the difference in Cherenkov ring radius at the focal length of the system,

---

[3]The Cherenkov angle for particles in the NA62 beam is ~ 30 mrad so it is safe to assume θ_C is small.

f, is

$$\Delta R = f\Delta\theta = \frac{f}{\theta}\frac{m_2^2 - m_1^2}{2p^2}. \tag{3.5}$$

A diaphragm with variable annular opening can hence be placed at the correct radius in the focal plane of the system to select the kaons in the beam, whilst ignoring the pions and protons. The effective focal length of the NA62 CEDAR is 3.24 m. Hence, the separations at the diaphragm plane between light from kaons and pions/protons are:

$$\Delta R_{K\pi} = 2.1 \text{ mm}; \quad \Delta R_{Kp} = 6.0 \text{ mm}. \tag{3.6}$$

An aperture of 2 mm will hence distinguish kaons from other particles in the beam. Furthermore, by differentiating Equation 3.5, the effect of the momentum RMS spread of 1% on ΔR can be calculated to be 0.02 mm and hence does not affect the CEDARs ability to distinguish kaons from other particles.

As well as differentiating kaons from other particles in the beam, the photons themselves must be detected. The intensity of the Cherenkov radiation (number of photons, N, per unit length, x, of particle path per unit wavelength, λ), for beam particles passing through a gas with refractive index n is given by [94, p. 638]

$$\frac{d^2N}{dxd\lambda} = \frac{2\pi\alpha}{\lambda^2}\left(1 - \frac{1}{\beta^2 n^2}\right) = \frac{2\pi\alpha}{\lambda^2}\sin^2\theta_C \tag{3.7}$$

where α is the fine structure constant. Furthermore, for a gas with constant chemical composition [95],

$$(n-1) \propto density, \tag{3.8}$$

meaning that for an ideal gas at constant temperature,

$$(n-1) \propto pressure. \tag{3.9}$$

Equations 3.7 and 3.9 show that if the pressure is increased, the number of Cherenkov
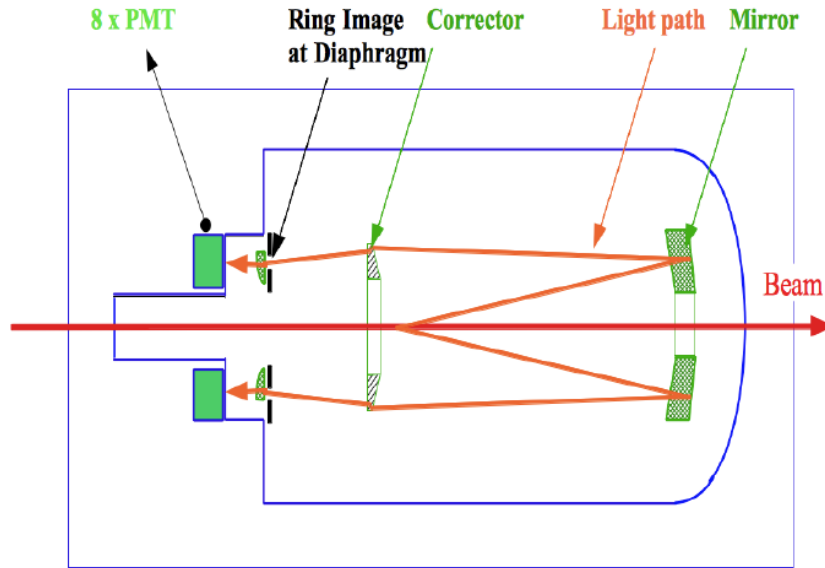
Figure 3.1: Schematic drawing of the original CEDAR vessel and its optical components. The PMs in the original CEDAR shown are placed just upstream of eight quartz windows. Figure reproduced from Ref. [74]. A more detailed diagram of the optical components, as well as a photograph of an opened CEDAR vessel, are given in Appendix A.1.

photons per unit length also increases. The kaon-tagging efficiency of the CEDAR increases if more photons from a single kaon can be detected, meaning the higher the gas pressure, the better the efficiency. However, higher pressures result in more safety concerns so a balance between the two must be found.

3.1.1   The CEDAR optics

Cherenkov photons emitted by particles in the beam travel through four optical components in the CEDAR. The original CEDAR layout and the paths of two Cherenkov photons are shown in Figure 3.1. Note that for NA62, the original CEDAR was adapted; the eight PMs were removed and replaced with the KTAG photon detection system, as will be explained in Subsection 3.1.2.

The first optical component Cherenkov photons pass through is the Mangin mirror which consists of a diverging spherical lens with its downstream surface silvered to act as a converging spherical mirror [96]. The Mangin mirror reduces spherical

65

aberration when the radius of curvature of the reflective surface is greater than that of the refractive surface. The focal length, f_M of the Mangin mirror is given by,

$$\frac{1}{f_M} = \frac{2\left(1 - n_g\right)}{r_1} - \frac{2n}{r_2},$$ (3.10)

where n_g is the glass refractive index (equal to 1.48 for a photon of wavelength 300 nm) and $r_1 = 6.615$ m and $r_2 = 8.613$ m are the radii of curvature of the refractive and reflective surfaces respectively. The Mangin mirror has a focal length 5.034 m (for a photon of wavelength 300 nm) which is approximately equal to the distance between it and the diaphragm.

The second optical component is the Chromatic Corrector which is a plano-convex lens (the upstream surface being the planar one) designed to reduce chromatic aberration (i.e. counteracts the wavelength dependence of refraction, resulting in light of all wavelengths being focused to the same radius in the diaphragm plane). This is needed to negate the chromatic aberration caused by refraction of photons of different wavelength in the first surface of the Mangin mirror. The focal length, f_C of the Chromatic Corrector is given by,

$$\frac{1}{f_C} = \frac{n_g - 1}{r_C},$$ (3.11)

where $r_C = 1.385$ m is the radius of curvature of the convex surface. For a photon of wavelength 300 nm, $f_C = 2.89$ m.

After focusing by the Mangin mirror and Chromatic Corrector, photons emitted by kaons then pass through the diaphragm aperture which is at a radius of 100 mm[4]. The aperture is adjustable and set to 2 mm wide. Photons emitted by pions/protons reach the diaphragm plane at a different radius and hence do not pass through the aperture (technically some do pass through and this is quantified

---

[4]The coordinate system used in this section is as before i.e. cylindrical polar coordinates where the positive z-direction is in the direction of the beam.

later in this chapter).

There are several effects that can cause the size of the lightspot at the diaphragm to increase [74], causing fewer photons from kaons being measured as well as increased contamination from pions. However, some of these can be mitigated by the detector design.

- Beam divergence can have a large effect but in NA62, due to the beam line components upstream of the CEDAR (see Section 2.1), is limited to an RMS angle of 70 µrad in each plane. This translates to a lightspot broadening of 0.2 mm.

- Beam multiple scattering (causes beam particles to be non-parallel) can be reduced by the choice of gas. In the NA62 CEDAR filled with N_2, the lightspot broadening is 0.09 mm [73]. This is discussed extensively later in this chapter.

- Pressure and temperature gradients can cause an inhomogeneous refractive index [73],

$$\frac{\Delta n}{n} = \frac{(n-1)}{n} \left(\frac{\Delta P}{P} - \frac{\Delta T}{T} \right), \tag{3.12}$$

leading to a variation in θ_C (see Equation 3.1). To mitigate this, the pressure is fixed and temperature gradients are reduced by thermal insulation and by having the experiment underground with a naturally stable temperature. By differentiating Equation 3.1 and substituting Equation 3.12, the spread of photons at the diaphragm caused by this effect is limited to 0.05 mm for a (conservative) temperature variation of 1 K. Variations in pressure are negligible.

- Noise and halo particles can produce scintillation light in the gas. This has a negligible effect on the size of the lightspot.

Once photons pass through the diapragm aperture, they are focused through eight quartz windows by a set of eight condensers. The condensers are lenses that have one spherical surface and one planar surface and the system of eight condensers

transforms a ring of light (which is what emerges from the aperture) into eight light spots by reducing the ϕ-spread (ϕ is the cylindrical polar angle) of the photons that pass through the lens.

3.1.2 The KTAG optics

For NA62, the photon detection system of the CEDAR had to be upgraded due to the high beam intensity. A kaon tagging efficiency $> 95\%$ (although $> 99\%$ is achieved in reality), a pion mis-tag caused by Cherenkov light from pions passing through the aperture (hereinafter referred to as contamination) $\leq 10^{-4}$ and a time resolution of 100 ps were required in order to conduct the $K_{\pi\nu\bar{\nu}}$ measurement and handle the increased rate within the CEDAR. Hence, the PMs shown in Figure 3.1 were replaced by a more complex photodetector, shown in Figure 3.2. For clarity, only half of the diaphragm , condensers, quartz windows and optical caps (placed on the quartz windows) are shown. Only half the plane holding the quartz windows in place is also shown. Once photons emerge from the eight quartz windows and thus leave the CEDAR vessel, they pass through eight "optical caps" which are simple plano-convex lenses, slightly upstream of the eight quartz windows, designed to focus the photons onto eight spherical mirrors while also reducing the size of the lightspot by the time the photons reach the lightguide. The spherical mirrors reflect the photons radially outwards, to eight light guides, each of which contains 48 PMs. The photons are directed radially outwards so that there is room for the large light guides and also to reduce radiation damage inflicted onto the PMs by the beam particles.

There are two types of PMs used in the KTAG and they are distributed as in Figure 3.3[5]. Due to the higher intensity of light at the centre of the lightguide, the PMs used in the centre are the higher quantum efficiency (QE) ones (Hamamatsu

---

[5]Two types of PMs are used due to historical reasons. Some R7400-03 PMs were already available (they are the same as that used by the RICH detector) but were no longer in production. Hence, the R9880U-110 PMs are used as well.
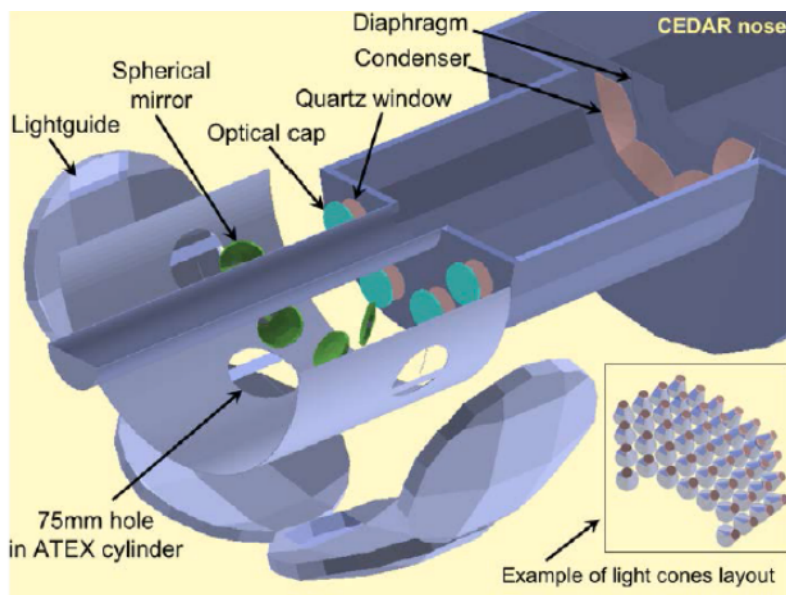
Figure 3.2: Visualisation of the KTAG photodetection system. The upper half of the detector has been removed so that the inner components can be seen. Figure produced internally by NA62; more figures are available in Ref. [71].
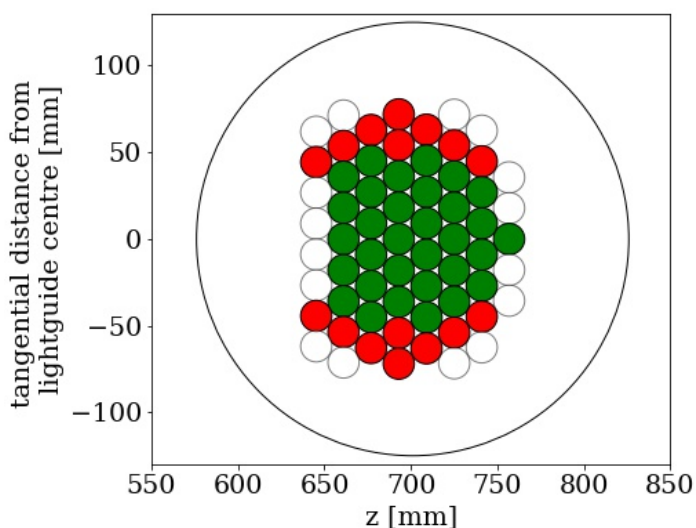
Figure 3.3: Distribution of PMs in the KTAG lightguides. The higher QE PMs (R9880U-110) are shown in yellow and the lower QE PMs (R7400U-03) are shown in red. The outline of the lightguide is also shown.
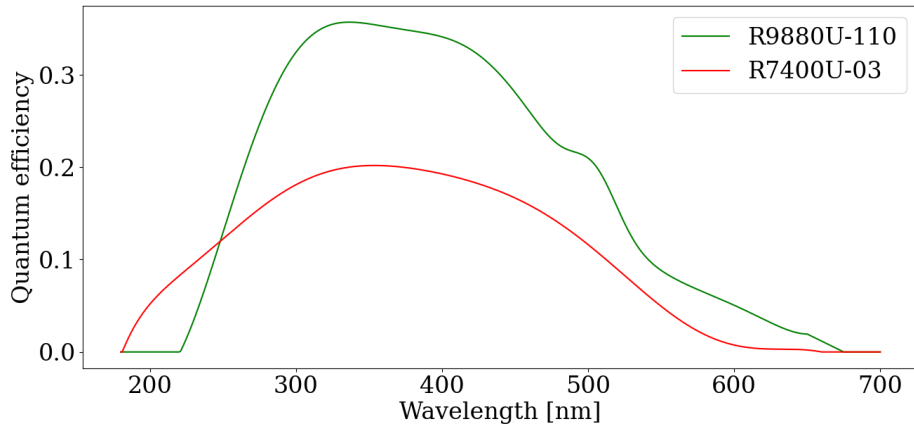
Figure 3.4: Quantum efficiency of the two types of PM used in the KTAG.

R9880U-110; yellow), with the lower QE PMs at the edge (Hamamatsu R7400U-03; red). The positions shown in white are currently un-instrumented but PMs could be placed there in the future. The quantum efficiency of the two types of PMs is shown in Figure 3.4.

The time that a kaon passes through the KTAG can be measured if the photons produced by the kaon arrive at the PMs in coincidence and the CEDAR and KTAG optics are designed so that this happens. The time resolution for a single photon per PM, σ_γ is ~ 300 ps. The time resolution for a single kaon is thus

$$\sigma_K = \frac{\sigma_\gamma}{\sqrt{N_\gamma}}, \tag{3.13}$$

where $N_\gamma \sim 18$ is the number of photons detector per kaon. Hence, a kaon time resolution of ~ 70 ps is achieved.

3.1.3   The CEDAR with hydrogen

The CEDAR currently used in the NA62 KTAG is designed for use with N_2. However, if H_2 was to be used, the total thickness of the detector would be reduced from 3.7% to 0.7% of X_0, reducing the number of interactions between the beam and the gas [74] and hence improving the quality of the beam as well as reducing potential

upstream backgrounds.

The Cherenkov photon wavelength against the radial spread of photons at the diaphragm, in the CEDAR-W (which is currently used with N_2 in the NA62 KTAG) with both a nitrogen filled and hydrogen filled CEDAR, is shown in Figure 3.5. These distributions were created using a NA62MC simulation of 1000 kaons, resulting in a total of $\sim 10^6$ Cherenkov photons being produced. Also shown (in the right hand distribution of each sub-figure) are the distributions of photons from pions using either N_2 or H_2 (same simulations, just with a pion beam instead of a kaon beam). The counts are weighted using the quantum efficiency of the PMs (which depends on each individual photons wavelength). As mentioned in Subsection 3.1.1, the diaphragm aperture is centred on a radius of 100 mm and is 2 mm is diameter.

As Figure 3.5 shows, the distribution of photons emitted by kaons using nitrogen is centred on 100 mm, is almost entirely contained within the aperture diameter and the photon distribution from pions is also well separated from the kaon distribution. On the other hand, the distribution of photons emitted by kaons using hydrogen has a much larger radial spread and there is a large overlap between the kaon and pion distributions, unlike when using nitrogen. Hence, if H_2 was used in the current KTAG, the diaphragm aperture would need widening meaning the pion contamination would have a non-negligible effect on the pion mis-tag.

Furthermore, the actual number of photons detected per kaon in the hydrogen case is $\sim 30\%$ lower than when using N_2 (if the diaphragm aperture is kept at 2 mm) because the radial spread in photons is wider than the diaphragm aperture so many photons do not pass through. The diaphragm aperture cannot be increased beyond 2 mm because more light from pions would pass through (see Equation 3.6).

Two questions are therefore raised about using hydrogen in the CEDAR:

- Can the $\sim 30\%$ light loss be recuperated by re-designing the CEDAR optics?

- Can hydrogen provide the $> 95\%$ kaon-tagging efficiency and pion contamination $\leq 10^{-4}$ that is required?

(a) Nitrogen
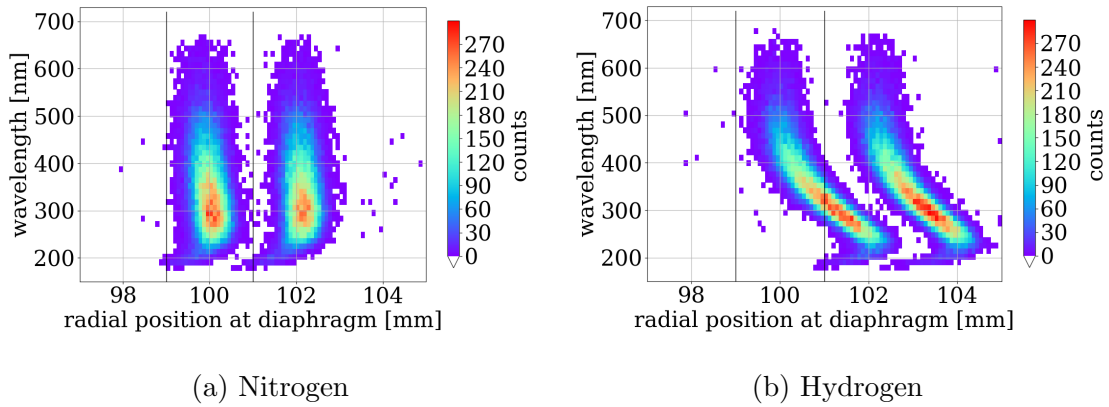
(b) Hydrogen

Figure 3.5: Photon wavelength against radial distribution at the diaphragm for the CEDAR-W with nitrogen and hydrogen. The kaon distribution is the one on the left of each figure. The diaphragm aperture is between the lines at 99 and 101 mm. The counts are weighted by the PM quantum efficiency.

3.2   Adaptations needed

As the current KTAG uses a CEDAR-W and is therefore better understood than the CEDAR-N, it was originally decided that work should be focused on optimising a CEDAR-W for the use of hydrogen. In the following, Subsection 3.2.1 describes the simulations completed to optimise the CEDAR-W for use with hydrogen. For reasons that will be explained, work was then switched to optimising a CEDAR-N, the results of which are shown in Subsection 3.2.2. Finally, Subsection 3.2.3 describes simulations completed on what will be called a Custom CEDAR (as all the main optical components are changed so is no longer related to the West or North CEDARs). Both Subsections 3.2.2 and 3.2.3 present a solution for using hydrogen in a CEDAR. The CEDAR-N optimisation was completed under the boundary condition of keeping the Mangin mirror unchanged. On the other hand, the Custom CEDAR optimisation was completed under a different set of boundary conditions.

This work was completed in collaboration with John Fry (University of Birmingham). More specifically, John focused on finding the radii of curvature and axial position of the Mangin mirror and Chromatic Corrector that were required in order to focus the Cherenkov light through the diaphragm when using hydrogen at a cer-

tain pressure. He did this using an analytical ray-tracing program which gave the "ideal" scenario (hence did not include optical effects such as chromatic abberation). The radii of curvature and axial positions described in Subsections 3.2.2 and 3.2.3 were found by John. The author of this thesis then verified (and in some cases made adjustments to certain parameters to correct the "ideal" simulation) these results using the full optical simulation contained within NA62MC, as well as carried out the optimisation of the KTAG optics (i.e. external to the CEDAR). Improvements to the NA62MC code were also implemented in places in order to carry out this work and this was done by the author.

The CEDAR simulations described in this chapter were conducted using NA62MC (see Section 2.4), meaning optical processes such as transmittance, absorption and reflection were all parametrised and taken into account correctly. Every Cherenkov photon (with wavelengths from 180 nm to 700 nm) was traced through the KTAG optics by NA62MC. Although Cherenkov light is emitted on a continuous spectrum, this range of wavelengths is used because the QE of the KTAG PMs is zero outside of these points (see Figure 3.4). As is standard for NA62MC simulations, the 75 GeV/c K^+ (or π^+) beam was simulated using TURTLE [87] which conducts a full simulation of the beam[6]. In order to carry out the studies presented below, the NA62MC code had to be changed so that different CEDAR types and gases could be created within Geant4 and used interchangeably. This was done in such a way so as to not affect the "standard" simulation that is used to generate the official MC samples but could be used by those doing future KTAG studies. The CEDAR-N geometrical parameters were obtained from the original CEDAR papers [72, 73].

There are two important results that should be compared when analysing the KTAG and CEDAR simulations. The first is the spread in photons (emitted by kaons) at the diaphragm. It should ideally be entirely contained within the diaphragm aperture and there should be as few photons from pions as possible trav-

---

[6]It should be assumed that a TURTLE beam is used in each simulation unless explicitly stated that a pencil beam is used.

elling through. The second is the number of photons that can be detected per kaon (and hence the kaon-tagging efficiency). In the current NA62 experimental setup using a KTAG with a nitrogen filled CEDAR-W, a mean of approximately 18 photons are detected per kaon, the kaon-tagging efficiency is $> 99\%$ and the pion mis-tag is at the 10^{-2} level. A CEDAR designed for use with hydrogen should be at least as good as this. The pion mis-tag is dominated by the high intensity at which NA62 runs; the probability of having a kaon and pion in the same time window is much higher than the probability of identifying a pion as a kaon in the KTAG. The latter effect is at the level $\sim 10^{-4}$.

Throughout this chapter, the beam axis, CEDAR axis and z-axis are identical and used interchangeably. The origin of the coordinate system used is 69.278 m downstream of the T10 fixed target. This is 1251 mm upstream of the diaphragm centre.

3.2.1   CEDAR-W optimisation

As described in Subsection 3.1.3, the CEDAR-W requires some adaptations to be made if it is to be filled with hydrogen. For practical reasons, the smaller the number of optical components that are changed the better. Due to this, it was decided that only the Chromatic Corrector, being a simple plano-convex lens, should be changed and the Mangin mirror should remain as it is because it is a more complex and more expensive lens with two curved surfaces. There are two changes that can be made to the Chromatic Corrector - its position along the z-axis and the radius of curvature of the curved surface. Both of these parameters were independently scanned using NA62MC simulations with a pencil beam for simplicity (a pencil beam, having no width or divergence, results in more ideal results than that of a proper beam simulation) and it was found that by only changing one parameter, the RMS spread in photons at the diaphragm was always too large and could not be improved, see for example, Tables 3.1 and 3.2. For reference, the current CEDAR-W with N_2,

Table 3.1: RMS radius with varying Chromatic corrector axial position in a CEDAR-W filled with H_2. The current Chromatic Corrector axial position is underlined. The current CEDAR-W with N_2, using the same axial pencil beam, has an RMS spread of 0.12 mm.

Z_{CC} (mm)	2183	2203	2223	<u>2234</u>	2243	2263	2283	2303
RMS radius (mm)	0.94	0.87	0.83	0.80	0.79	0.75	0.76	0.77

Table 3.2: RMS radius with varying Chromatic corrector radius of curvature in a CEDAR-W filled with H_2. The current Chromatic Corrector radius of curvature is underlined. The current CEDAR-W with N_2, using the same axial pencil beam, has an RMS spread of 0.12 mm.

R_{CC} (mm)	1206	1246	1286	1326	1366	<u>1385</u>	1406	1446
RMS radius (mm)	0.63	0.61	0.64	0.70	0.76	0.80	0.84	0.92

using the same axial pencil beam, has an RMS spread of 0.12 mm.

Another option would be to change the material of the Chromatic Corrector (whilst leaving the geometric properties of the Chromatic Corrector unchanged). This would alter the refractive index vs. wavelength relation and therefore could reduce the spread in photons at the diaphragm. Using the standard CEDAR-W geometrical parameters, the required refractive index to focus light of a range of wavelengths onto a radius of 100 mm at the diaphragm was found[7]. A χ^2 fit was then performed[8] to find the optimal refractive index vs. wavelength relationship. The fit was based on a two-term Sellmeier formula,

$$n(\lambda) = \sqrt{1 + \frac{B_1 \lambda^2}{\lambda^2 - C_1^2} + \frac{B_2 \lambda^2}{\lambda^2 - C_2^2}}, \tag{3.14}$$

where n is the refractive index, λ is the wavelength and B_1, C_1, B_2 and C_2 are the fit parameters. A comparison of the refractive index given by this fit ("New material") and the quartz (Suprasil 1) refractive index currently used in the Chromatic

---

[7]Note that this data was not found by the author, see the start of Section 3.2. All other work in this section was.

[8]The fitting was done with the python based SciPy optimize package. SciPy is python software designed for science and computing.
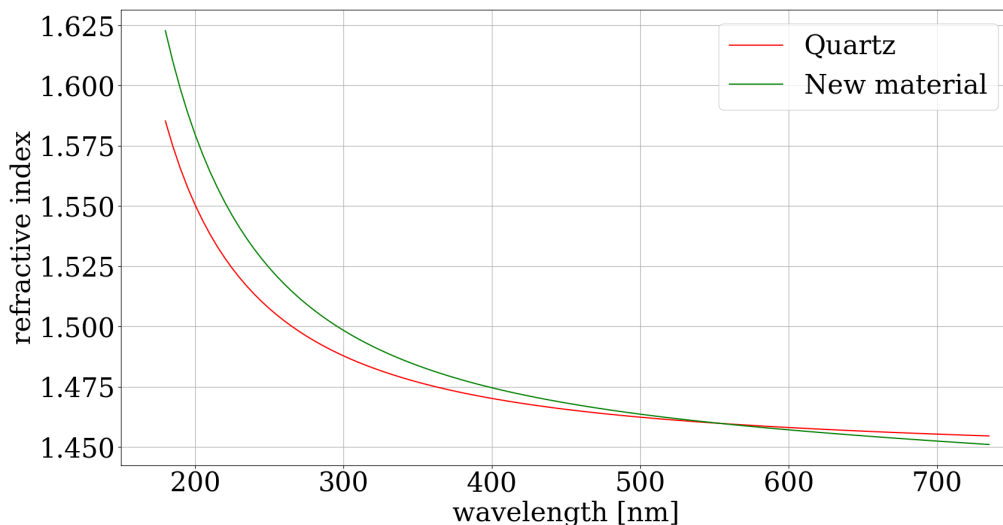
Figure 3.6: Refractive index vs wavelength for the current Chromatic Corrector material (Suprasil 1 quartz) and the new, hypothetical, type of quartz.

Corrector is shown in Figure 3.6.

This thus provided an ideal, hypothetical material with a refractive index that would focus light of all wavelengths through the aperture. NA62MC simulations of 1000 kaons (this time using a Turtle beam) in the CEDAR-W with H_2 were carried out using this hypothetical material in the Chromatic Corrector (for simplicity, the transmittance was kept the same as in the quartz currently used) and the QE-weighted distribution of photons at the diaphragm can be seen in Figure 3.7. The photons are now centred on a radius of 100 mm and have a spread similar to that seen when using the standard Chromatic Corrector with N_2.

However, there is one obvious question raised here. Does a material with the above properties actually exist? A large number of NA62MC simulations each using the refractive index of different glass produced by Schott (a glass manufacturing company) were conducted and a material similar to the hypothetical material discussed above could not be found. Furthermore, discussions with a member of the National Institute of Optics (Florence, Italy) revealed that the material currently used in the Chromatic Corrector (Suprasil 1) is one of the best when both refractive index and transmittance are taken into account. It was hence concluded that a
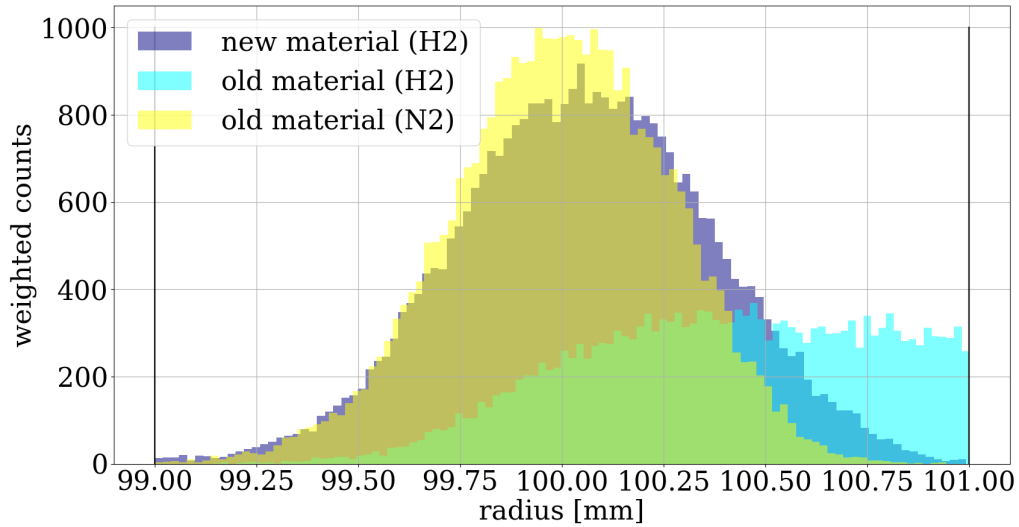
Figure 3.7: Radial distribution at the diaphragm for the current KTAG with N_2 and H_2, as well as with H_2 and the new Chromatic Corrector material.

change in material could not provide the necessary requirements in order to optimise the CEDAR-W for the use of H_2.

Another question raised is whether changing both the position and radius of curvature of the Chromatic Corrector (rather than changing one at a time as was discussed above) can provide the solution. However, at this point in the project, CERN made a CEDAR-N detector available. It was hence decided to, instead of adapting the CEDAR-W currently used at NA62, focus on adapting the CEDAR-N for use with hydrogen as any necessary engineering work could be completed on that whilst the CEDAR-W was in operation at NA62.

3.2.2 CEDAR-N optimisation

The original CEDAR-N detectors were designed for use with helium (He) at a large pressure (~ 10 bar). The Mangin mirror and Chromatic corrector are at the same axial locations but their radii of curvature are different to that in the CEDAR-W so that the photons are still focused onto the diaphragm at a radius of 100.0 mm. It is unclear, from the original CEDAR papers [73, 72], what the exact pressure should be when using helium. Hence, the pressure used is 10.74 bar as that focused
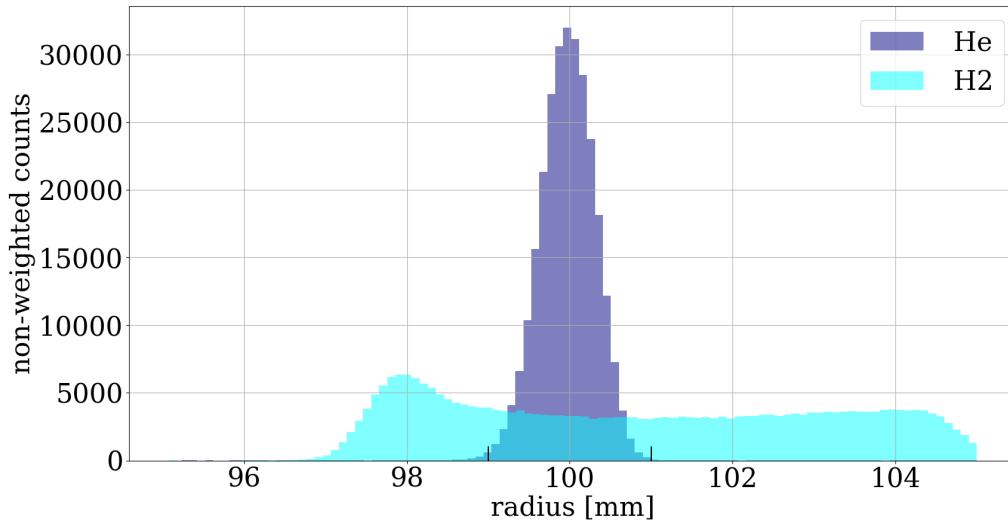
Figure 3.8: Distribution of photons at the diaphragm. Two CEDAR-N cases (with default geometrical parameters) are shown, one with helium at 10.74 bar and one with hydrogen at 2.58 bar. The counts are not QE-weighted but the wavelength is restricted to > 220 nm only.

the photons into the diaphragm aperture in the simulation of the CEDAR-N. For comparison purposes, the hydrogen pressure used was 2.58 bar so that the number of photons emitted in each simulation was approximately equivalent[9].

Simulations of 1000 kaons in a CEDAR-N filled with both He and H_2 were conducted. The distribution of photons at the diaphragm, in both cases, is shown in Figure 3.8. Note that, although the counts in this case are not weighted by the quantum efficiency, photons with wavelengths < 220 nm are not included as the quantum efficiency is almost zero below this range. The He distribution is centred on 100.0 mm and is almost contained within the aperture (99 to 101 mm). The H_2 distribution however, has an extremely large spread, with a peak at $\sim$ 98 mm. The wavelengths are well corrected for with He (Figure 3.9a) whereas this isn't the case with H_2 (Figure 3.9b).

Hence, it is clear that a CEDAR-N with default geometrical parameters cannot be used with hydrogen (which is to be expected as it was not designed for this). An optimisation is thus needed. A similar approach to that taken for the CEDAR-W

---

[9]The pressure mainly changes the radius at which the photons reach the diaphragm so is, in some ways, almost arbitrary in this comparison.

(a) Helium   (b) Hydrogen
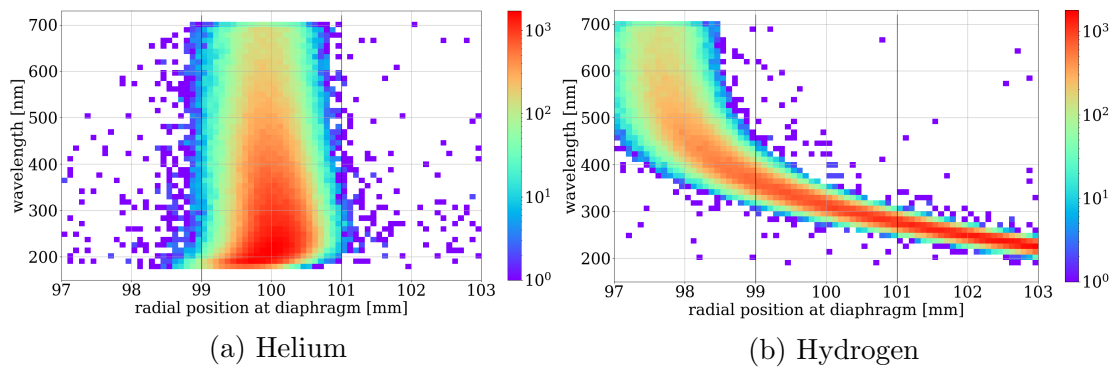
Figure 3.9: Wavelength vs radius distributions at the diaphragm, for the two CEDAR-N cases (with default geometrical parameters). The counts are not QE-weighted but the wavelength is restricted to > 220 nm only.

was initially used for the CEDAR-N with similar constraints - i.e. the Mangin mirror and the actual CEDAR vessel should remain unaltered.

It was first investigated whether changing a single parameter in the Chromatic Corrector (either the axial position or radius of curvature) can successfully optimise the CEDAR-N for the use of H_2, obtaining the desired radial position (of 100mm) and spread at the diaphragm. However, as with the CEDAR-W, this could not be done. It was then investigated whether changing both the position and radius of curvature of the Chromatic Corrector could optimise the CEDAR-N and this turned out to be successful. The remainder of this section describes both the internal adaptations made to optimise the CEDAR-N optics for the use of H_2 as well as the adaptations needed external to the CEDAR-N (i.e. the KTAG optics). A summary of the results using this solution is then presented. A list of the optimised CEDAR-N/KTAG parameters is given in Table A.2 in Appendix A.2.

Adaptations made to the CEDAR-N optics

To focus the Cherenkov photons through the diaphragm aperture in the solution shown here, only the Chromatic Corrector and the radiator gas pressure are changed. A H_2 gas pressure of 4.10 bar was used, chosen so that more photons are emitted compared to the CEDAR-W with N_2 case while being low enough to be considered

safe. The Chromatic Corrector is replaced by another plano-convex lens of the same material but with the downstream surface radius of curvature reduced to 583.0 mm. To accommodate the larger Cherenkov angle at this large pressure and the reduced radius of curvature, the Chromatic Corrector outer radius is increased to 165 mm while the inner radius of 75 mm is kept the same. The thickness of the Chromatic Corrector at its outer radius, is set to 5.0 mm, meaning the central thickness is 23.5 mm. Furthermore, it is moved upstream so that the planar surface is at an axial position of 1651 mm[10]. The diaphragm aperture, condensers and quartz windows are kept the same.

The Chromatic Corrector is now 583 mm closer to the diaphragm (it was previously at an axial position of 2234 mm). This causes the light to leave the diaphragm aperture at a much larger angle meaning the light does not pass through the quartz windows, as shown in Figure 3.10. It was investigated whether the Condensers could be adapted to fix this. Reducing the radius of curvature of the Condensers did direct the photons through the quartz windows. However it also resulted in a large increase in the spread in the ϕ-direction (in cylindrical polar coordinates where the z-axis points in the same direction as the beam) as the focus was moved much further away (upstream) from the quartz windows. The ϕ-spread by the time the photons reached the light guides was thus too large. It was hence decided that, instead of adapting the Condensers in a more complicated way (as it would require a complete re-design of the 8-lens array), it would be simpler to introduce a new lens, hereinafter referred to as the post-condenser lens.

This post-condenser lens is a plano-concave lens introduced upstream of the Condensers which focuses the photons through the quartz windows. The upstream surface is concave with a radius of curvature 420 mm. The downstream surface is planar and is at an axial position of 1170 mm. The inner and outer radii are equal to 65.0 mm and 130.0 mm respectively and the thickness, at the outer radius, is equal

---

[10]The radius of curvature and axial position were not found by myself, see Section 3.2.
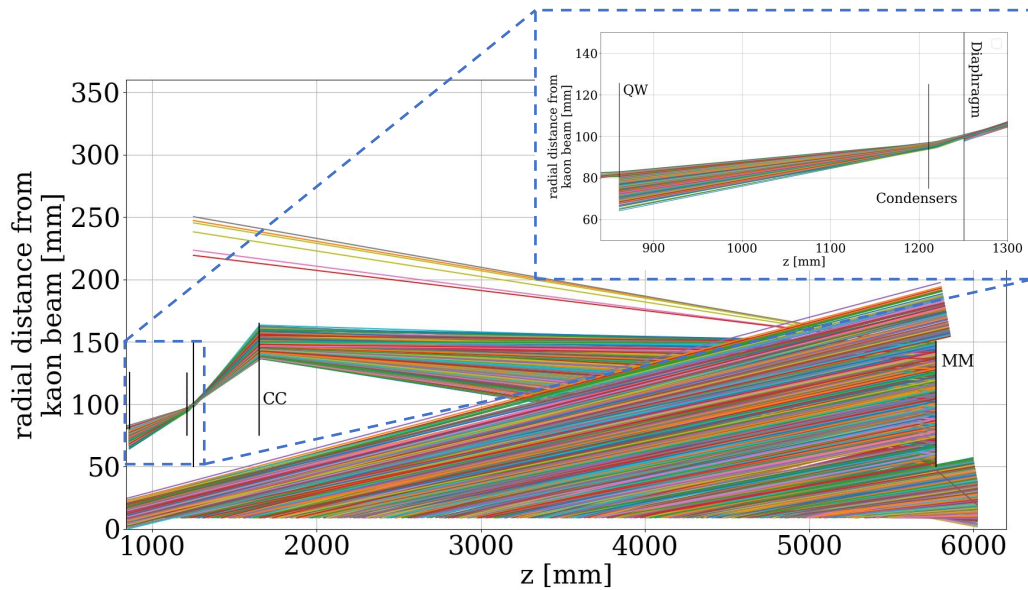
Figure 3.10: Paths taken by photons (in the radius-z projection) in the CEDAR-N with the optimised Chromatic Corrector (CC). The Mangin mirror is labelled by MM. A zoomed in image of the photon paths after the diaphragm is also shown. The majority of photons do not pass through the quartz windows (QW) due to the larger angle at which they leave the diaphragm. The approximate locations of each optical component are shown by the vertical black lines.

to 20.0 mm. A visualisation of the post-condenser lens (and the KTAG optics) within the CEDAR vessel is shown in Figure 3.11. Figure 3.12 shows the path taken by photons between the diaphragm and quartz windows after the introduction of the post-condenser lens. The majority of photons now pass through the quartz windows.

Adaptations made to the KTAG optics

Once the photons pass through the quartz windows, they are focused onto eight spherical mirrors by eight lenses known as the optical caps. The optical caps are plano-convex lenses and the downstream curved surface currently has a radius of curvature of 114.62 mm. To account for the increased spread of photons when using hydrogen gas in the CEDAR-N, the radius of curvature should be reduced to 91.69 mm. This value was chosen as it is a lens currently produced by Edmund Optics.

The spherical mirrors, ATEX cylinder and lightguides are left unchanged. There
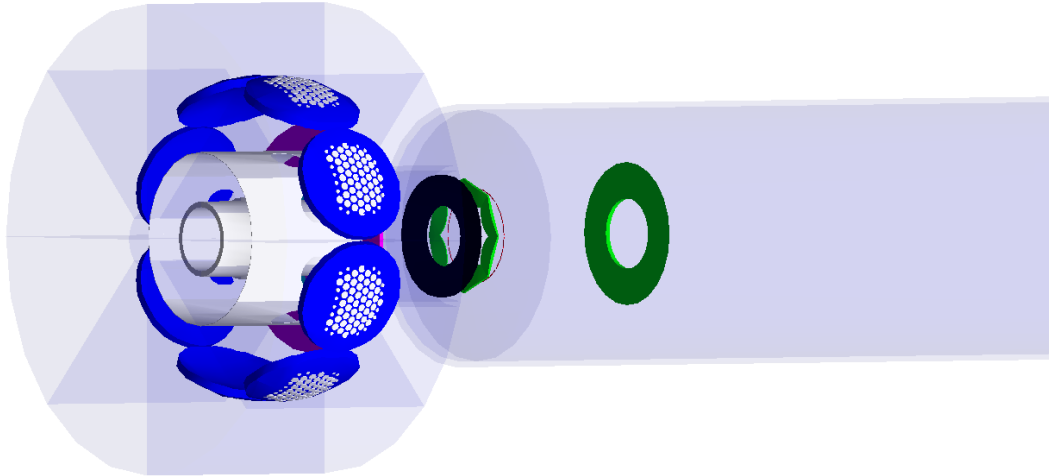
Figure 3.11: The KTAG optics (with the new concave lens in black) and the upstream end of the CEDAR vessel. From right to left, the Chromatic Corrector (green), diaphragm (red) condensers (green), new concave lens (black), quartz window mount (pink), beam pipe (white), ATEX cylinder (white; the holes can just be seen) and light guides/PMTs (blue/white) can be seen. The CEDAR vessel (transparent blue) is also shown. The quartz windows, optical caps and spherical mirrors are hidden.
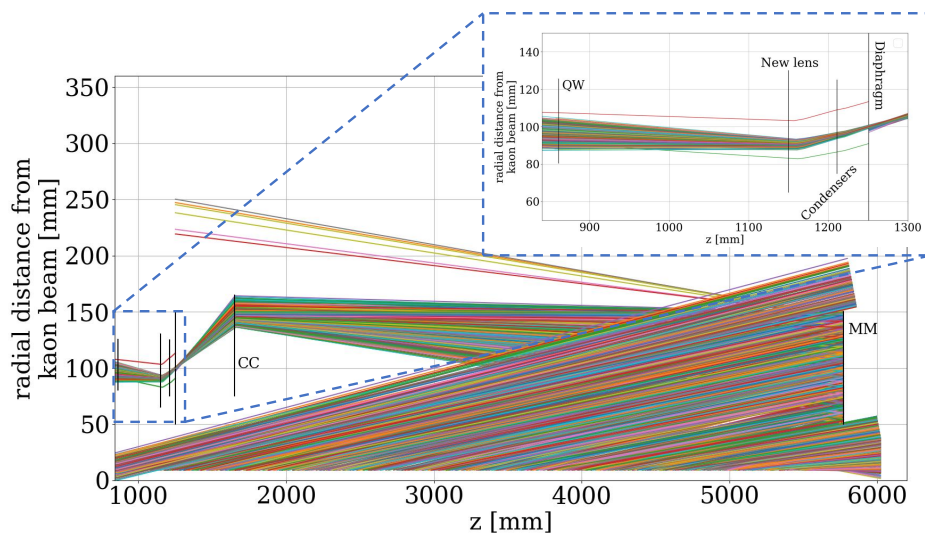
Figure 3.12: Paths taken by photons (in the radius-z projection) in the CEDAR-N with the optimised Chromatic Corrector and introduction of the post-condenser lens. A zoomed in image of the photon paths after the diaphragm is also shown. The approximate locations of each component are shown by the black lines.

are two types of PMs used in the KTAG lightguides (R7400U-03 (lower QE) and R9880U-110 (higher QE)) and these are also left unchanged.

Ray-tracing results

The paths taken by photons (between wavelengths 180 nm and 700 nm) in the radius vs z projection through the optimised CEDAR-N and KTAG optics using H_2 are shown in Figure 3.13. Approximately 1200 photons are shown (emitted by a single kaon). Due to the nature of the CEDAR, a large number of photons are outside of the acceptance range of the Mangin mirror. Furthermore, due to the increased gas pressure, the Cherenkov angle is larger (see Section 3.1) which, as can be seen in the figure, is part of the reason the Chromatic Corrector (the component at $z = 1651$ mm) diameter had to be increased. Note that Geant4 (see Section 2.4) only stores the particle positions at boundaries between different materials/volumes. Hence, in these ray-tracing figures of radius vs z, the majority of photons appear as though they are only emitted towards larger radius. This is not the case, it is just that only the start and end points of each trajectory can be accessed. At low and high z, the photons can be seen travelling towards lower radii - this is because the photons are traversing different volumes in these regions (i.e. the quartz windows at the ends of the vessel) so the points at which the photons cross these boundaries is saved.

The distribution of photons, emitted by both 1,000 K^+ and 1,000 π^+, at the diaphragm plane is shown in Figure 3.14. Each distribution is weighted using the PM QE. To do this, the QE was applied at the diaphragm under the assumption that 25% of photons reach R7400U-03 PMs (lower QE), 50% reach R9880U-110 PMs (higher QE) and 25% do not reach active PMs. These percentages were chosen as each light guide is made up of 32 R9880U-110 PMs, 16 R7400U-03 PMs and 16 positions which are currently unused/inactive. In reality, there are more photons hitting the centre of each light guide than the outer edges so more than 50% will be reaching the higher QE R9880U-110 PMs. The weighted counts in each bin will
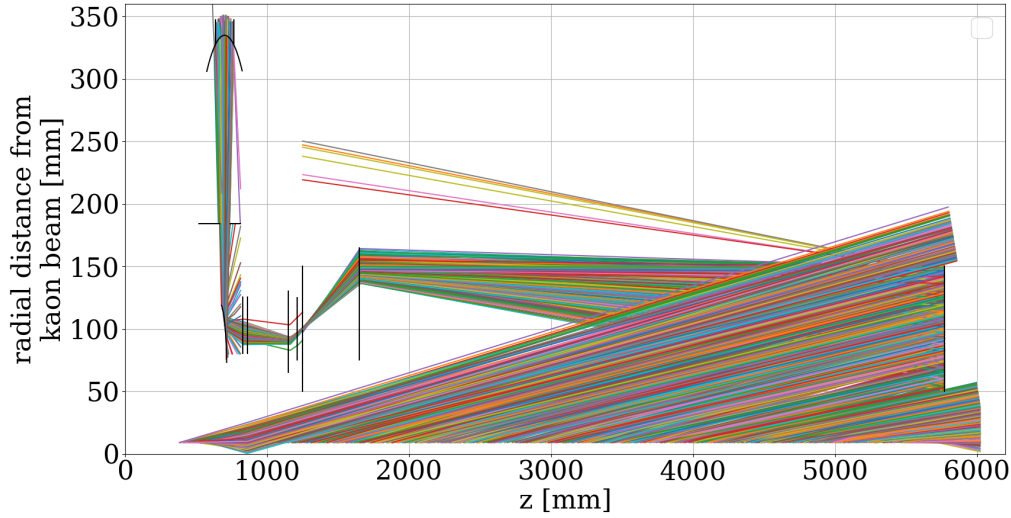
Figure 3.13: The paths taken by photons throughout the hydrogen optimised CEDAR-N and KTAG detectors. The (approximate) locations of the optical components are shown by the vertical black lines. Note that the colour of the photon lines (showing the ray-tracing path) has no meaning.

therefore be higher than those shown in Figure 3.14. Weighting the distribution using the QE excludes low wavelength ($\lesssim$ 220 nm) photons which the PMs are not sensitive to. The proportions of "weighted" photons that pass through the diaphragm aperture, relative to the number that reach the diaphragm, are 99.1% and 0.7% for photons emitted by kaons and pions respectively. The pre-diaphragm optics therefore do a good job at excluding light emitted by pions.

The paths shown by photons (emitted by a single kaon for clarity) that pass through the diaphragm are shown in Figure 3.15 (essentially a zoomed in version of Figure 3.13). Now that the new concave lens has been introduced, the photons pass through the quartz windows. This can be seen more clearly in Figure 3.16 which shows the x-y distribution (i.e. perpendicular to the beam) of photons, emitted by 1,000 kaons, passing through the quartz windows (where $x = 0$, $y = 0$ is the centre of each quartz window; the 8 distributions have been combined). Furthermore, the optical caps (which have had their radius of curvature reduced) and spherical mirrors (which are unchanged) focus the photon beam onto the PM array which
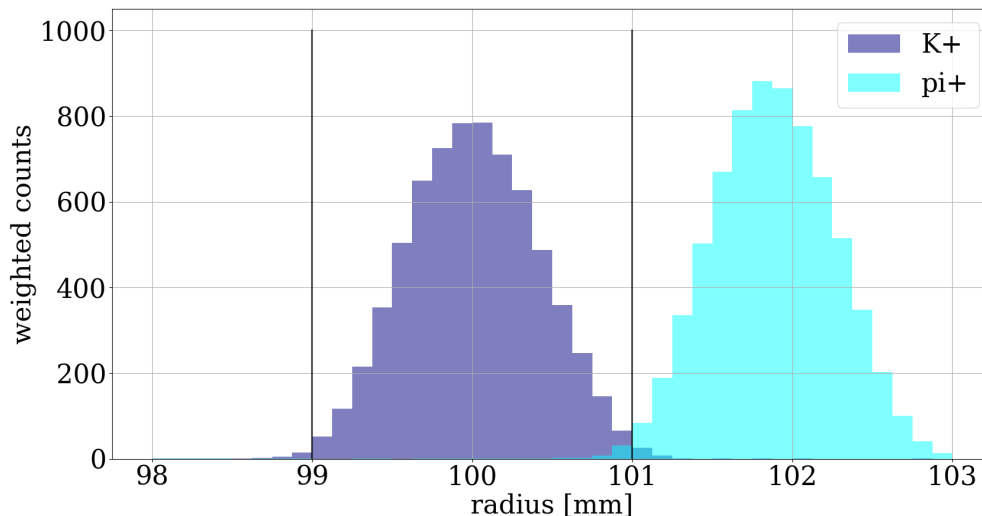
Figure 3.14: The weighted distribution of photons at the diaphragm in the optimised CEDAR-N with H_2 in two cases, one with a beam containing 1,000 K^+ and the other with a beam containing 1,000 π^+. The vertical black lines show the edges of the diaphragm aperture. A small amount (quantified later in this section) of pion contamination can be seen.

again can be seen in Figure 3.15. The PM array contains light collection cones that guide the photons into the PM windows. Photons can reflect radially inwards off these cones and then can be either absorbed by the ATEX cylinder or reflect off the spherical mirrors and then be absorbed elsewhere in the detector. Figure 3.17 shows the distribution of the photons (emitted by 1,000 kaons) at the light guide (large black circle), as well as the PM cones (small black circles) and the unused PM positions (small grey circles). It can be seen that the solution discussed results in well illuminated PMs, even at the edges where the PMs are either not instrumented or have low QE.

The number of kaon candidates detected is a measure of the efficiency of the detector. A kaon candidate is defined as a particle that emits photons that are detected in at least five sectors (i.e. at least five different light guides). This was calculated in two cases: (i) a simulation with 1,000 kaons and (ii) a simulation with 10,000 pions. The numbers of kaons/pions was chosen as it represents the approximate NA62 beam composition ratio. Table 3.3 shows a comparison of the number of kaon candidates in the CEDAR-W N_2 case and the optimised CEDAR-N
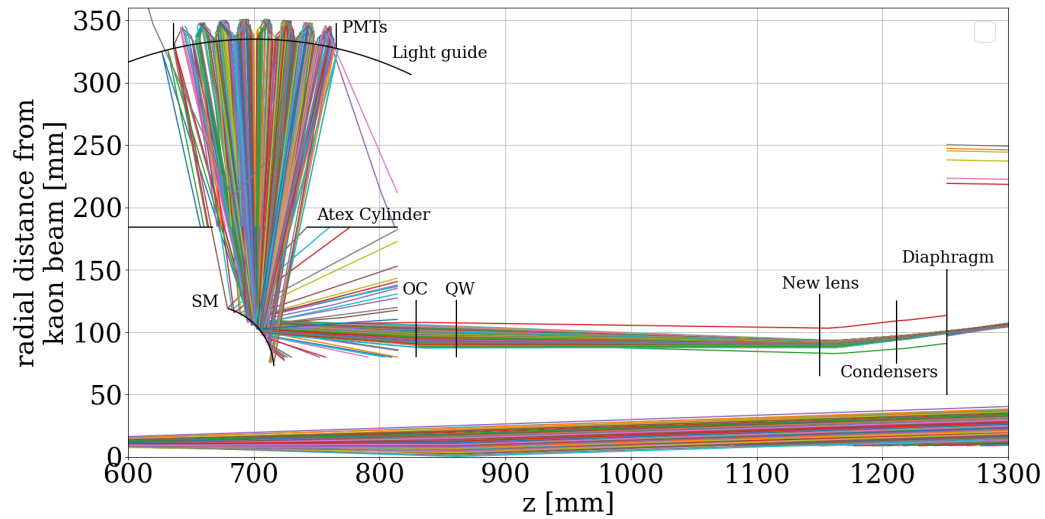
Figure 3.15: The paths taken by photons after passing through the diaphragm in the CEDAR-N. The name of each component is shown. Note that the line colour has no meaning.
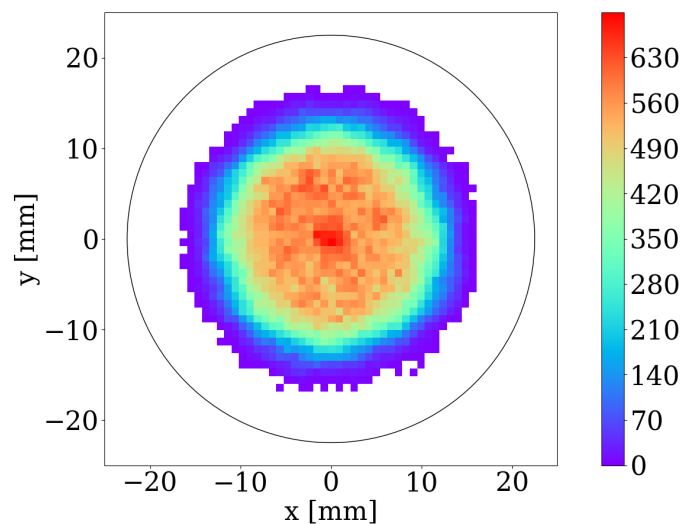
Figure 3.16: Intensity distribution of photons at the quartz windows in the optimised CEDAR-N. The black circle shows the shape of the quartz windows.
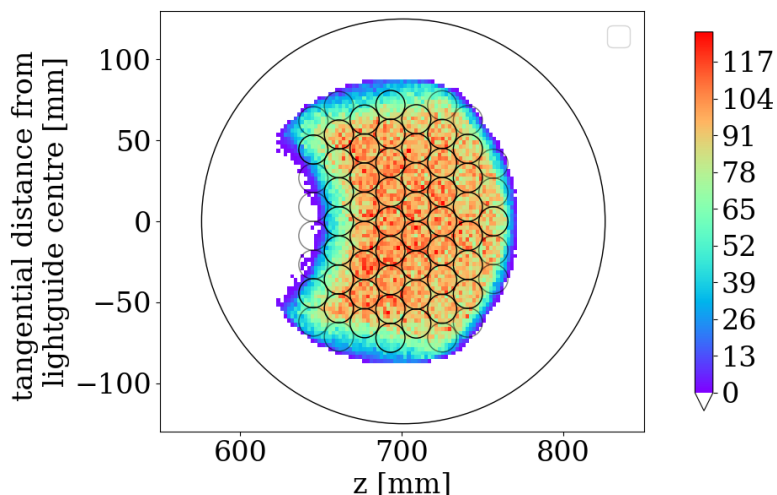
Figure 3.17: The shape of the lightspot at the light guide in the optimised CEDAR-N. The PMs are shown as black circles while the unused positions (i.e. no PM present) are shown in grey. This could possibly be optimised in the future to improve the light yield.

Table 3.3: Number of kaon candidates in simulations of 1,000 kaons and 10,000 pions for both the CEDAR-W with N_2 and optimised CEDAR-N with H_2.

Number of kaon candidates in...	CEDAR-W N_2		Optimised CEDAR-N H_2	
	1,000 K^+	10,000 π^+	1,000 K^+	10,000 π^+
...at least 5 sectors	990	0	993	0

H_2 case. The numbers are very similar in both cases ($\geq 99\%$ efficiency) and the contamination from pions is at the 10^{-4} level in the optimised CEDAR-N with H_2. It will hence have a negligible effect on the pion mis-tag.

3.2.3 Custom CEDAR optimisation

The work described in Subsection 3.2.2 was discussed with members of the CERN beam and engineering departments. The conclusions from the meeting were that although the optimisation of the CEDAR-N we found most likely would work, it would be too complex (and thus expensive) to implement in reality. This is because the mechanical supports for the lenses would either need to be changed (in the case of the Chromatic Corrector as it is moved to a different position along the

z-axis) or made from scratch (in the case of the post-condenser lens but could also apply to the Chromatic Corrector). In addition, the structure holding the supports would potentially need to be changed if the Chromatic Corrector outer diameter was changed (this relies on the mechanical supports allowing some degree of flexibility and it is unclear, without opening an actual CEDAR vessel and examining the components, whether this is possible - see Section 3.3 for more on this). It would thus be simpler (and cheaper) to keep the supports and structure of the vessel the same and only change the lenses. It would hence be desirable to:

- keep the lenses at the same axial position;

- keep the diameter of the lenses the same as they are at present, if possible.

This would mean that the mechanical supports and structure can be kept the same as much as possible.

Furthermore, it was stated that the Mangin mirror radii of curvature could be changed if needed (more expensive than only changing the Chromatic Corrector but could save introducing a post-condenser lens and changing the supports). The work described in this section therefore focuses on changing both the Mangin mirror and the Chromatic Corrector in the CEDAR, under the boundary conditions mentioned above.

It was decided that, initially at least, a pressure of ~ 4 bar was to be used in order to increase the number of photons emitted. The three radii of curvature (two from the mirror, one from the corrector) were then varied until the Cherenkov photons were focused at a radius of 100 mm on the diaphragm plane with a desirable spread. As before, the diaphragm aperture is kept at 2 mm.

Table 3.4: Parameters required to adapt the optical components in the Custom CEDAR for use with H_2 at 4.060 bar. MM stands for Mangin mirror.

	MM refractive surface	MM reflective surface	Chromatic corrector
Radius of curvature (mm)	6080	8470	1185

The Custom CEDAR optics

The new geometrical parameters are shown in Table 3.4[11]. The material for the Chromatic Corrector and Mangin mirror was kept as Suprasil 1 quartz and the H_2 pressure used was 4.060 bar. A full list of parameters, compared with both the CEDAR-N and CEDAR-W parameters, are shown in Table A.2 in Appendix A.2.

Ray-tracing results for the Custom CEDAR

The paths taken by photons up to the diaphragm in the Custom CEDAR, emitted by a single kaon, are shown in Figure 3.18. The diaphragm can be seen on the far left, the chromatic corrector at 2234 mm and the Mangin mirror at 5732 mm. A large number of photons reach the diaphragm at a radius of 100.0 mm (see next paragraph) but a large number also miss the Chromatic Corrector entirely. This is caused by the larger pressure and thus the larger Cherenkov angle.

The radial distributions of photons at the diaphragm, from a simulation of 1,000 kaons and ~ 1.2 million photons, are shown in Figure 3.19. The counts are weighted using the QE of the PMs. The photons are focused, by the adapted optics, to be centred on a radius of 100.0 mm and are almost entirely contained within the 2 mm diameter of the diaphragm aperture. Also shown is the pion distribution using the same setup and the two distributions are well separated.

Due to the increased pressure and hence increased Cherenkov angle, some photons pass the Chromatic Corrector at a radius larger than its outer radius and

---

[11]Note that these parameters were found in a preliminary analytical study by John Fry (see Section 3.2) and then confirmed by the author using NA62MC.
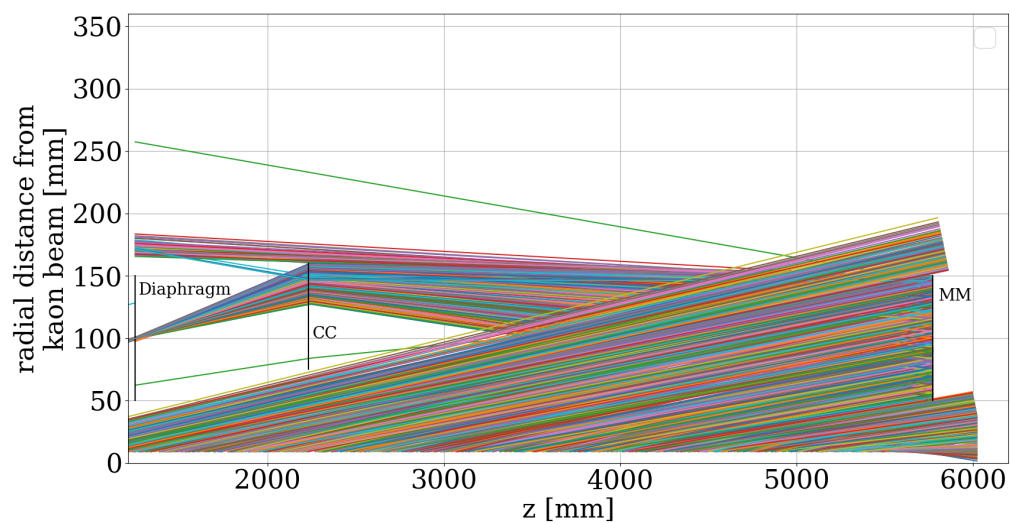
Figure 3.18: The paths taken by photons in the Custom CEDAR. About 1200 photons are shown, emitted by a single kaon.
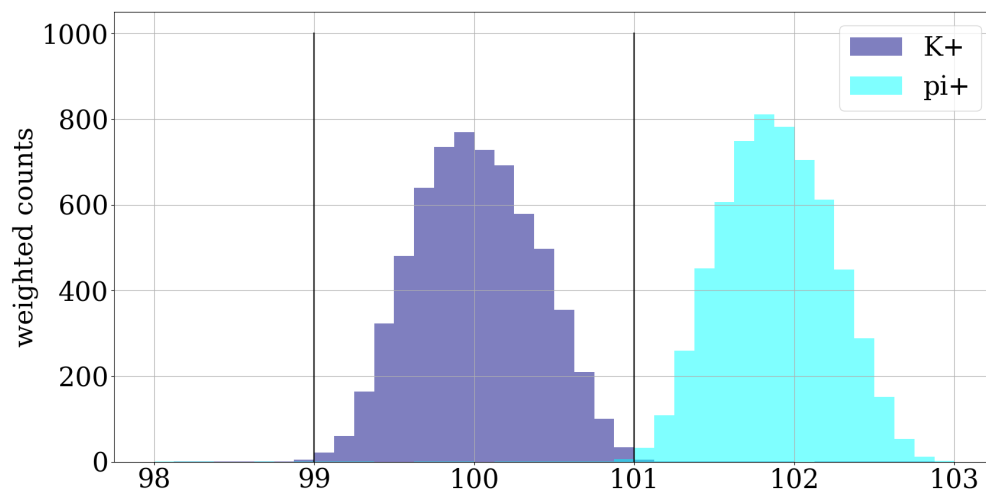
Figure 3.19: The QE-weighted distribution of photons at the diaphragm for the Custom CEDAR.

hence are not refracted towards the diaphragm aperture. If it was possible to increase the Chromatic Corrector outer diameter (as previously mentioned, it is not known whether this is possible[12]), the numbers of photons detected would increase. Figure 3.20 shows the effective number of photons detected per kaon as a function of the Chromatic Corrector outer diameter. The effective number of photons is calculated by weighting the counts of photons that pass through the diaphragm aperture using the QE. The effective number of photons detected per kaon is larger than that actually detected in experiment because post-diaphragm losses are not taken into account. Each simulation was repeated 3 times and the mean (and standard deviation as the error bars) in each case is shown. The CEDAR-W with nitrogen (which is the current NA62 detector) results are shown in black and the adapted CEDAR results, with different corrector outer diameters, in red. Even when the outer diameter is the default value (320 mm) and thus a large number of photons miss the corrector in the Custom CEDAR, the effective number of photons detected is still larger when compared to the CEDAR-W. This is due to there being more photons emitted in the first place as the pressure is larger. As the figure shows, an increase by 10-20 mm in the corrector outer diameter could increase the light yield by $\sim 10\%$.

Finally, once the photons pass through the diaphragm, they are directed through the quartz windows by the condensers. The CEDAR-N condensers were used in the simulation as there is a spare CEDAR-N available at CERN. The QE-weighted $x - y$ distribution of photons at the quartz windows is shown in Figure 3.21a. As before, the distributions from the 8 windows has been combined into a single window. All the photons pass through the quartz windows but not through the centre, hence why photons from each of the eight sectors can be distinguished. For comparison, another simulation was conducted using the CEDAR-W condensers (inside the Custom CEDAR) and the distribution of photons at the quartz windows

---

[12]Note that work on this has progressed since the author conducted this project, see Section 3.3.
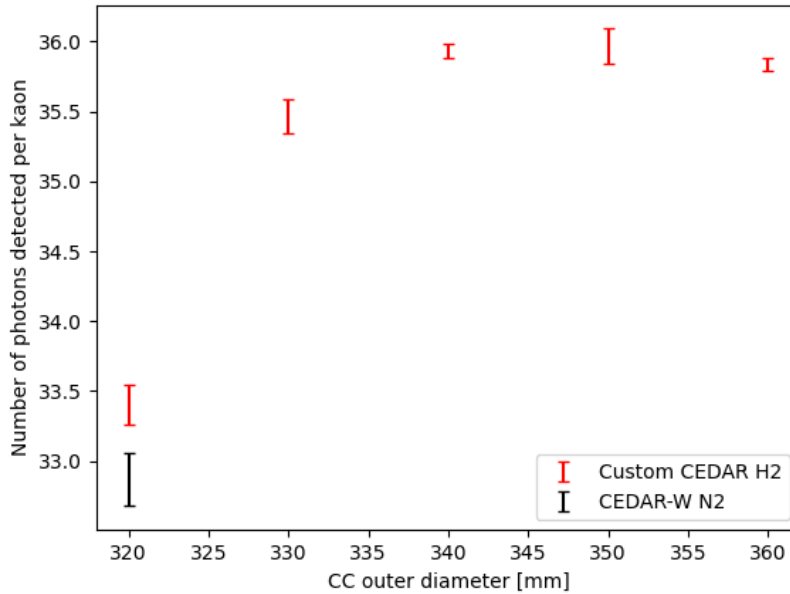
Figure 3.20: The number of photons detected per kaon, applying the QE at the diaphragm, in the CEDAR-W with N_2 and the Custom CEDAR with H_2 and for varying corrector outer diameters.

using these is shown in Figure 3.21b. When using the CEDAR-W condensers, the photons are centred at each quartz window. The radius of curvature of the CEDAR-W condensers is larger, meaning the photons are not over-focused past the centre of the quartz windows. Condensers similar to that of the CEDAR-W would hence be required.

Ray-tracing results in the KTAG

Finally, a study was done on whether the KTAG optics (external to the CEDAR) can be adapted for use with the Custom CEDAR solution discussed above.

It is not clear from the photon distributions at the quartz windows (Figure 3.21) whether the shape of the distributions will affect the number of photons reaching the lightguides. Figure 3.22 shows the radius vs z projection of the photons once they pass through the quartz windows when using the CEDAR-N condensers. The spherical mirrors have been moved radially inwards by 9 mm so that the photons

(a) Using CEDAR-N condensers   (b) Using CEDAR-W condensers
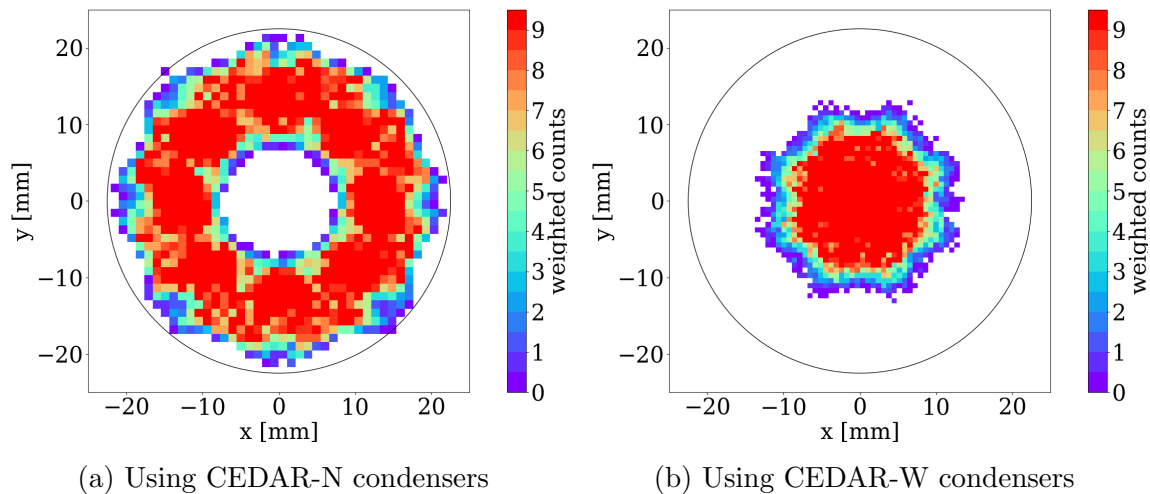
Figure 3.21: The QE-weighted distribution of photons at the quartz windows in the Custom CEDAR with the two types of condensers. This was produced using a simulation of 1,000 kaons.

are approximately directed towards the lightguides. The black line at a radius of 183 mm is the atex cylinder which is a cylinder designed for structural support and it contains eight circular holes (with diameter ~ 75 mm) for the photons to pass through. The hole can be seen in the figure as a gap between the two black lines at radius 183 mm (it can also be seen in the visualisation in Figure 3.11; it is the cylinder radially inwards of the lightguides). A large number of the photons are absorbed by the atex cylinder because the spread in the ϕ-distribution is too large and these photons cannot therefore pass through the hole.

The next approach was to try the CEDAR-W condensers, which as shown in Figure 3.21, focused the light through the centre of the quartz windows. In this case, the spherical mirrors have been moved radially inwards by 2 mm to focus the photons onto the lightguides. The ϕ-distribution is small enough in this case that photons are not stopped by the atex cylinder, as was the case when using the CEDAR-N condensers. The distribution of photons, at the lightguides, is shown in Figure 3.23 and it can be seen that the lightguide is well illuminated. This was produced using a simulation of 1,000 kaons.
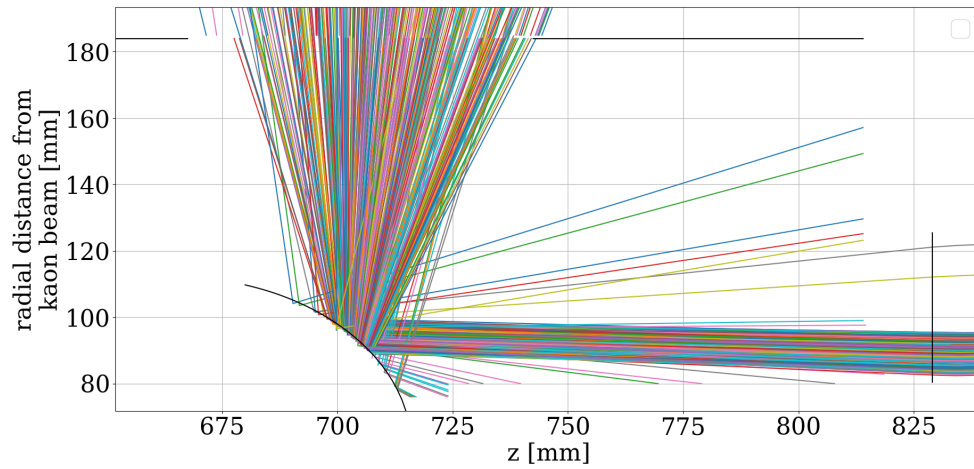
Figure 3.22: The paths taken by photons once they pass through the quartz windows in the Custom CEDAR using the CEDAR-N condensers. The component on the far right is the optical caps, the photons then reflect off the spherical mirror and onto the atex cylinder where they either pass through the hole or are absorbed.
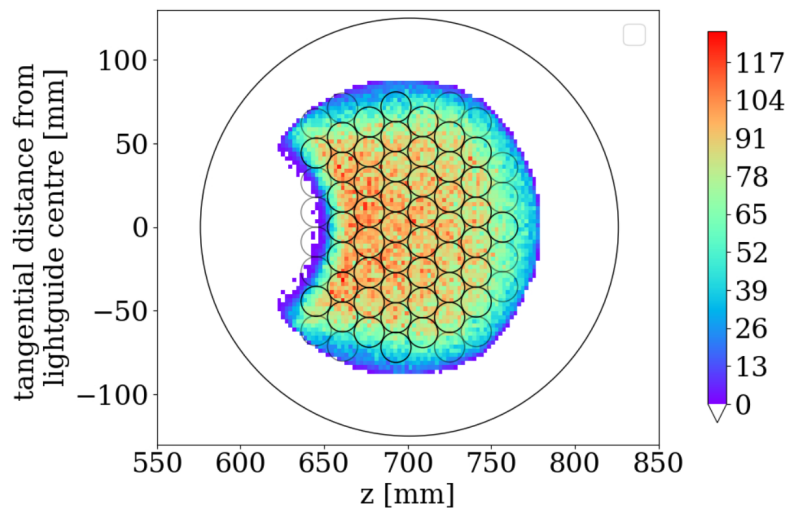
Figure 3.23: Shape of the lightspot at the lightguide when using the CEDAR-W condensers in the Custom CEDAR. The PMs are shown as the small black circles. The currently inactive PM positions are shown as grey circles.

Table 3.5: Number of kaon candidates in simulations of 1,000 kaons and 10,000 pions for both the CEDAR-W with N_2 and Custom CEDAR with H_2. The CEDAR-W condensers have been used in the Custom CEDAR.

Number of kaon candidates in...	CEDAR-W N_2		Custom CEDAR H_2	
	1,000 K^+	10,000 π^+	1,000 K^+	10,000 π^+
...at least 5 sectors	991	0	994	0

The number of kaon candidates was calculated using simulations of 1,000 kaons and 10,000 pions using the Custom CEDAR filled with H_2 with the CEDAR-W condensers. The results are shown in Table 3.5. The K^+ tagging efficiency is 0.3% (absolute) higher than that of the CEDAR-W with N_2 and the π^+ mis-ID is still at the $< 10^{-4}$ level. These numbers could potentially be optimised by tuning the diaphragm aperture or the PM layout.

3.3 Summary

A summary of the two solutions presented (optimised CEDAR-N and the custom CEDAR) is given in Subsection 3.3.1. The progress made on the design of the H_2 filled CEDAR since the author left the project is given in Subsection 3.3.2.

3.3.1 Summary of this work

The KTAG detector plays a vital role in NA62's measurements of kaon decays and in this report, two potential solutions for a hydrogen gas filled CEDAR (as opposed to the current detector which uses nitrogen) have been presented.

The first solution, an optimisation of a CEDAR-N, was completed without changing the Mangin mirror. A H_2 pressure of 4.10 bar was required. The geometrical changes made were:

- a new Chromatic Corrector was introduced with a smaller radius of curvature and an axial position that is closer to the diaphragm;

- a new plano-concave lens, known as the post-condenser lens, was introduced upstream of the Condensers which ensured the light was directed out of the quartz windows;

- the optical caps were replaced with similar lenses that had a smaller radius of curvature which reduced the spread of photons at the lightguides.

The second solution, referred to as the Custom CEDAR, was a re-design of the CEDAR internal optics whilst attempting to keep the mechanical supports (which hold the lenses in place) the same as at present. This meant the lens diameters or axial positions could not be changed. A H_2 pressure of 4.06 bar was required. The geometrical changes made were:

- a new Mangin mirror was introduced (both radii of curvature were changed);

- a new Chromatic Corrector was introduced (still plano-convex but with a different radius of curvature);

- condensers identical to that of the CEDAR-W were used;

- the KTAG spherical mirrors were moved radially inwards by 2 mm.

Both solutions, although starting from different boundary conditions, produce similar results that are at least comparable to the current nitrogen filled KTAG/CEDAR.

3.3.2   Summary of work done since leaving the project

This section contains a description of work not carried out by the author but is included for completeness.

John Fry continued work on the hydrogen filled CEDAR project with the role of the author being taken over by a colleague to allow the author to move onto the π_D^0 analysis presented in Chapter 5. It was decided at this point that further effort should be made to find a H_2 KTAG solution at a lower pressure to ensure there were

no safety concerns[13]. This motivated research into a different analytical approach which allowed another solution to be found, with different optimal geometrical parameters and a reduced pressure (compared to the solutions presented in this thesis) of 3.8 bar. The Mangin mirror, Chromatic Corrector and spherical mirrors still had to be replaced. The CEDAR-N condensers were also still replaced with ones from a CEDAR-W.

CERN engineering department have checked that the spare CEDAR-N is in good condition as well as designed the required safety, gas and optical alignment systems. Once the CEDAR-N was opened (see Appendix A.1 for a photograph of the opened CEDAR), it was confirmed that the Chromatic Corrector outer diameter could not be increased. After receipt of the new optical components from the manufacturers, the H_2 CEDAR is currently being built and the plan is to install, test and commission the new CEDAR with H_2 using a test beam line at CERN in October 2022. Following this, it will be installed into the NA62 beam line in January 2023, ready for the start of data taking in spring/summer 2023.

---

[13]Part of the operation of the KTAG involves pressure scans to ensure the kaon, pion and proton peaks are well separated. This means the pressure would get close to the 5 bar limit if the running pressure was above 4 bar.

Chapter 4

Contributions to the NA62 Monte Carlo simulation

The $B(\pi^0 \to e^+ e^- \gamma)$ measurement described in Chapter 5 involved the development and understanding of two aspects of the NA62 Monte Carlo (MC) simulation: the treatment of pileup/accidental coincidences and the MC production method. The technical aspects and the author's contributions to these two features are discussed in this chapter. However, to fully understand the reasons why they are important for the $B(\pi^0 \to e^+ e^- \gamma)$ measurement, some context around the analysis is required. Some discussion is hence postponed until Chapter 5.

4.1   Overlaid Monte Carlo

Overlaid MC is a method of simulating the effect of pileup as well as accidental coincidences (hereinafter referred to as accidentals). This is achieved during the reconstruction stage[1] by adding beam particles to MC events where the beam particles are allowed to decay, scatter or do neither and just propagate along the beam axis. While in non-overlaid MC, the original decay makes up the entirety of the MC event, overlaid MC events contain both the original decay mode and overlaid beam

---

[1] See Section 2.4 for more details regarding the reconstruction.

particles. As discussed in Section 2.4, in both non-overlaid and overlaid MC, the original decay is forced to occur within the decay volume. Overlaid beam particles are not forced to decay but if they do (the decay probability is determined by the particle lifetime), the decay mode is chosen based on the branching fractions.

Overlaid beam particles are added to the original event at a certain time within the so-called overlaid time window. This time window is -200 ns $< t < 200$ ns, where the original decay is at time $t = 0$ ns and overlaid beam particle times are uniformly distributed across it. The rate at which overlaid beam particles are added to the original event is based upon the instantaneous beam intensity as well as the overlaid time window. The instantaneous intensity is measured on data by counting the number of hits in the GTK over a 45 ns time window; the intensity distribution is then sampled to obtain the overlay intensity. This is an approximate simulation of what happens in data whereby a decay causes the firing of a trigger, with read-out from detectors occurring in a certain time-window around this trigger time (see below for why it is only approximate). Both the original and overlaid events result in responses from the detectors; hence within the reconstruction, coincident hits are merged. For example, in the LKr calorimeter, the energy deposits of nearby coincident showers are combined. This is the same as in real life data.

The probability, averaged across intensity, of finding an overlaid kaon decay, occurring within ± 5 m and ± 10 ns with respect to the original kaon decay, is 2.4%. This probability, as a function of the instantaneous beam intensity, is shown in Figure 4.1. As mentioned above, in the MC simulation, the overlay intensity is taken from GTK intensity measurements on data.

Using overlaid MC results in better agreement between data and MC due to it simulating the effects of both pileup and accidental tracks. This improvement arises because:

- The effects of detector deadtime are simulated, resulting in the removal of hits within the detectors.
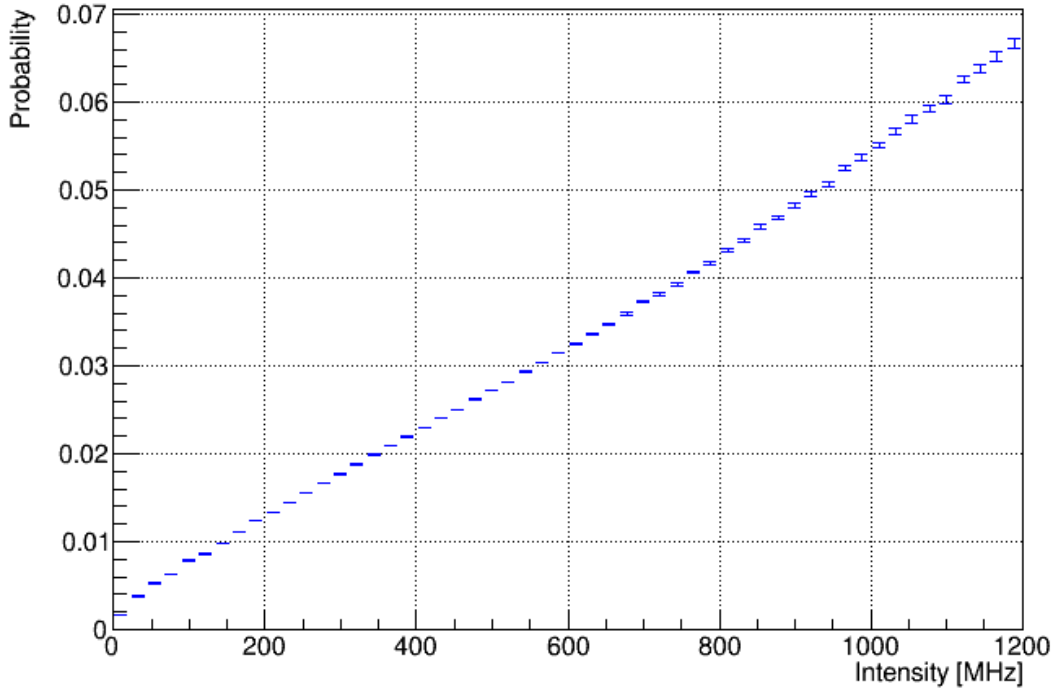
Figure 4.1: Probability of finding an overlaid kaon decay, within ± 5 m and ± 10 ns of an original kaon decay, as a function of the instantaneous beam intensity.

- Detector resolutions in the MC better match that of data. For example, the additional hits in the STRAW that arise from accidentals results in a STRAW resolution that better matches data.

- Backgrounds that emerge as a result of two close in space and time decays are simulated. For example, if a $K^+ \to \pi^+\pi^0$ $[\pi^0 \to \gamma\gamma]$ decay and a $K^+ \to \pi^0 e^+\nu$ $[\pi^0 \to e^+e^-\gamma]$ decay occur at almost the same position in space and time, the combination can appear to look like a $K^+ \to \pi^+\pi^0$ $[\pi^0 \to e^+e^-\gamma]$ decay.

See Chapter 5 for a comparison of non-overlaid and overlaid MC and a discussion of the above improvements in the context of the $B(\pi^0 \to e^+e^-\gamma)$ measurement.

The one issue with simulating pileup/accidentals in this manner is that we assume the original event to be at $t = 0$ and thus assume it is the event that caused the firing of the trigger. This is not necessarily true because, for example, it could be

the case that no secondary particles from the original decay actually passed through the detector(s) responsible for said trigger. Despite this, the overlaid MC reproduces data very well, as will be shown later. A trigger emulator can also be used to ensure the original decay is that which caused the trigger. This is not however used in the $B(\pi^0 \to e^+e^-\gamma)$ measurement and this is discussed in Section 5.12.

The contributions, by the author, to the overlaid MC simulation were as follows:

- Studies were conducted with the aim of understanding the improved agreement between data and overlaid MC (relative to non-overlaid), in particular the simulated NA48-CHOD and MUV3 hit timing distributions. This is discussed further, in the context of the $B(\pi_{\mathrm{D}}^0)$ measurement, in Chapter 5.

- During the hit time distribution studies above, it was noticed that the detector digitisers in the NA62 reconstruction code were incorrectly treating close-in-time overlaid events and the wrong hits were being removed if two hits were within the detector deadtime of each other. The correct treatment was found, in collaboration with a colleague, and a fix was deployed by said colleague.

- Methods were developed to extract the overlaid decay type during the analysis of the MC sample. Previously, there was no way of obtaining this but it is useful to have when splitting analysis results/studies by decay mode. In addition to this, changes were made to the way decay types were encoded within the simulation in order to improve the handling of neutral pions. This allowed decay modes with more than one neutral pion to be distinguished. Both of these features were included within the NA62 software framework.

4.2   Mixed Monte Carlo development

The standard NA62 MC samples (before any overlaid decays are added) are composed of a number of events, each containing the same K^+ or π^+ decay mode that

is forced to occur within the decay volume of the experiment (see Figure 2.2 for the decay volume definition). Secondary neutral pions are also forced to decay to a certain decay mode. These single decay mode samples can be combined by weighting the MC events based on the branching ratio and the sample sizes.

As will be explained when describing the $B(\pi^0 \to e^+e^-\gamma)$ measurement in Chapter 5, it was necessary to be able to vary the value of $B(\pi^0 \to e^+e^-\gamma)$ within the MC simulation. If the analysis used non-overlaid MC samples, the traditional approach above could be used with adjusted MC event weights to account for the new branching fraction value. However, overlaid MC samples were required, meaning each single decay mode sample would need to be overlaid separately. Hence, from the MC sample production/processing point of view, in order to avoid generating/overlaying a large number of samples with an altered $B(\pi^0 \to e^+e^-\gamma)$, it made sense to generate and overlay a single MC sample containing all the required decay modes with the new π^0 branching fractions. In other words, this MC sample contains original beam particles that are forced to decay within the decay volume but the mode by which they decay is not forced (and it can then be overlaid in the usual way). The decay mode is chosen based on the branching fractions. It was decided that this MC sample should be composed of the six most common K^+ decay modes[2] which range from branching fractions of 63.6% to 1.8%; see Table 1.3 for a full list of these with their respective branching fractions. Only these are included as the combined branching fraction of the remaining decay modes is $\sim 10^{-4}$. This MC sample is hereinafter referred to as a mixed MC sample. Note that, unless otherwise specified, a mixed MC sample uses the PDG central $B(\pi^0_{\mathrm{D}})$ value.

To summarise, the advantages of the standard approach are:

- A large number of rare decay events can be simulated, resulting in a small MC statistical uncertainty. This is not the case in mixed MC due to the decays being in proportion to the branching fractions (this is discussed further below).

---

[2]The π^+ decay modes enter when the MC sample is overlaid. They are not needed as "original" decays due to the small KTAG mis-tag rate. See Chapter 3 for more on the KTAG detector.

- Analysts can use only the decay modes they require, rather than running on decay modes that have no impact on their measurement.

On the other hand, the advantages of using mixed MC are:

- It allows parameters, such as $B(\pi^0 \rightarrow e^+e^-\gamma)$, to be varied without the need to generate or re-process a number of overlaid MC samples.

- Being a single MC sample, it can be used to do exploratory tests and searches for potential backgrounds without analysing a large number of samples.

As mentioned above, the disadvantage of using mixed MC is it can result in a limited number of signal decays being generated. For example, the signal decay chain measured in Chapter 5 has a combined branching fraction of $\sim 0.2\%$. Hence, in a mixed MC sample, only 0.2% of original decays will be signal decays. This leads to a small signal sample and thus a large MC statistical uncertainty. Despite this, it was decided that for the exploratory measurement discussed in Chapter 5, mixed MC would be used due to the practical advantages it offers. This is discussed further, along with steps to improve this procedure, at the end of said chapter.

The contributions, by the author, to the mixed MC simulation were as follows:

- Adapted the NA62MC software, allowing mixed MC to be generated. This involved creating a new production method whereby decays are forced to occur in the decay volume but the decay mode is not forced.

- Adapted the NA62MC software so that a user-defined $B(\pi^0 \rightarrow e^+e^-\gamma)$ could be used as an input into the MC simulation.

Both the above contributions were included in the official NA62 software framework.

Chapter 5

Branching Ratio Measurement of the Neutral Pion Dalitz Decay

5.1 Analysis overview

The aim of the analysis is a measurement of the branching ratio of the $\pi^0 \to e^+ e^- \gamma$ (π^0 Dalitz or π^0_{D}) decay. The neutral pions are obtained from a sample of $K^+ \to \pi^+ \pi^0$ ($K_{2\pi}$) decays. There are three other K^+ decay channels that include neutral pions (K_{e3}, $K_{\mu 3}$ and $K_{3\pi^0}$ - see Table 1.3) but the $K_{2\pi}$ channel was chosen over the others as it has the largest branching fraction (21% compared with the next largest of 6%) and because strong kinematic constraints can be applied due to the absence of neutrinos. In addition, the sample of $K_{2\pi}$ decays, with no requirements on the π^0 decay, is used as normalisation. The chain of a $K_{2\pi}$ decay followed by a π^0_{D} decay is hereinafter referred to as a $K_{2\pi^0_{\mathrm{D}}}$ decay.

The amount of data taken by NA62 between 2016 and 2018 means it is likely that the uncertainty on this measurement will be dominated by systematic errors. Two conditions were therefore decided upon when outlining the analysis strategy in order to minimise the systematic uncertainties:

- as few detectors as possible should be used;

- the criteria used to select signal $(K_{2\pi_{\mathrm{D}}^0})$ and normalisation $(K_{2\pi})$ events should be as similar as possible so as to achieve cancellation of systematic uncertainties in the ratio.

Accounting for the above conditions, the normalisation decay signature is given by a single π^+ track and missing mass from the decay equivalent to that of the π^0 mass. The signal decay signature is similar except for the presence of two additional tracks, an e^+ and an e^-, which due to the short lifetime of the π^0, originate from the same vertex as the $K_{2\pi}$ decay. No attempt is made to measure the γ's from the $\pi^0 \to \gamma\gamma$ $(\pi_{\gamma\gamma}^0)$ or π_{D}^0 decays so as to reduce the systematic uncertainty.

This chapter starts with a description of the calculation procedure used for the measurement, described in Section 5.2. Details regarding the data sample and trigger are given in Section 5.3. Next, Section 5.4 outlines the event selections for both the normalisation and signal channels and then the MC samples used and the studies of the MC simulation are described in Section 5.5. The properties of the normalisation and signal samples and a comparison between data and simulation are then shown in Section 5.6. The background mechanisms and treatment of the background are described in Section 5.7, followed by a discussion of the trigger efficiency measurements in Section 5.8. The $B(\pi_{\mathrm{D}}^0)$ results and statistical uncertainty are given in Section 5.9 with the systematic uncertainties described in Section 5.10. A summary of the $B(\pi_{\mathrm{D}}^0)$ result, statistical and systematic error budget and a comparison with previous measurements and theoretical calculations is given in Section 5.11. Finally, the next steps for the analysis are outlined in Section 5.12.

5.2 $B(\pi_{\mathrm{D}}^0)$ calculation procedure

The ratio between the number of π^0 (N_{π^0}) and π_{D}^0 ($N_{\pi_{\mathrm{D}}^0}$) events observed in the normalisation and signal samples respectively is defined as

$$\epsilon = \frac{N_{\pi_{\mathrm{D}}^0}}{N_{\pi^0}}, \tag{5.1}$$

where ϵ depends on $B(\pi_{\mathrm{D}}^0)$. The value of ϵ measured from data will be referred to as the data/measured ϵ (ϵ_{data}) whereas the value from MC will be referred to as the MC ϵ (ϵ_{MC}).

In the Monte Carlo (MC) simulation, the π_{D}^0 branching ratio, $B(\pi_{\mathrm{D}}^0)_{\mathrm{MC}}$, can be varied, allowing us to calculate the expected value of ϵ_{MC} as a function of $B(\pi_{\mathrm{D}}^0)_{\mathrm{MC}}$. A linear fit can be performed,

$$\epsilon_{\mathrm{MC}} = \alpha \cdot B(\pi_{\mathrm{D}}^0)_{\mathrm{MC}} + \beta, \tag{5.2}$$

where α and β are the slope and intercept respectively.

The ϵ measured on data can then be used with the linear fit parameters to calculate the measured $B(\pi_{\mathrm{D}}^0)$,

$$B(\pi_{\mathrm{D}}^0) = \frac{\epsilon_{\mathrm{data}} - \beta}{\alpha}. \tag{5.3}$$

Corrections to ϵ_{data}, due to downscalings and trigger efficiencies, are also required and described later in this chapter. The statistical error on ϵ_{data} is used to find the statistical error on $B(\pi_{\mathrm{D}}^0)$, again using the linear fit.

The method is demonstrated pictorially in Figure 5.1 (this figure is only to aid the explanation of the method, it is not a result). Each data point corresponds to an independent MC sample.
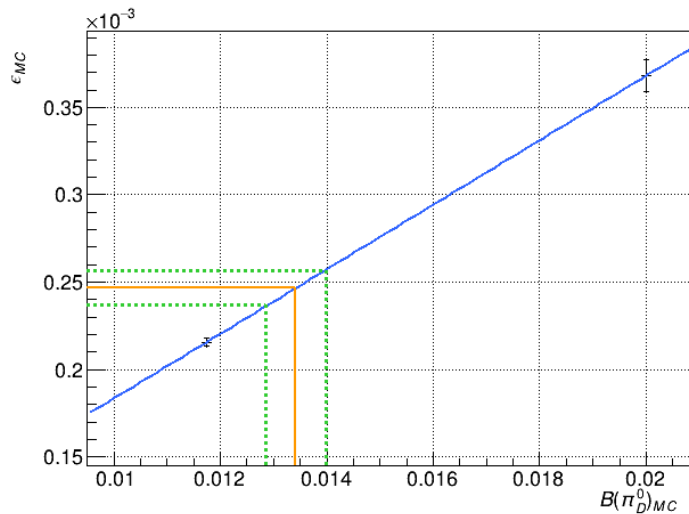
Figure 5.1: Demonstration of the method used to calculate the measured $B(\pi_D^0)$. Two data points are used and the linear fit is shown in blue. The measured ϵ and $B(\pi_D^0)$ are shown by the orange lines. The corresponding data statistical uncertainties are shown by the green dashed lines. This figure is only to aid the explanation of the method, it is not a result.

5.3 Data sample and trigger

The $B(\pi_D^0)$ measurement is conducted using the data collected by NA62 during the 2018 run. The data collected between 2016 and 2017 could also be included but as the statistical uncertainty provided by the 2018 sample is expected to be sub-dominant compared to the systematic uncertainties, it was decided to only use this sample for this thesis. The 2018 data sample corresponds to 1.4×10^{18} protons extracted from the SPS in $\sim 5 \times 10^5$ spills and directed on to the T10 target. This is equivalent to $\sim 4 \times 10^{12}\ K^+$ decays within the decay volume. The 2016 and 2017 samples are smaller than 2018 and contain a combined total of 0.8×10^{18} protons on T10. The MC simulations used within this analysis are tuned to the data taking conditions in 2018.

The trigger used for both the normalisation and signal channels is a minimum-bias trigger, otherwise known as the Control (CTRL) trigger. The only trigger condition requirement is the coincidence of two hits in a NA48-CHOD quadrant (one hit from each plane), akin to asking that at least one charged particle is present. The

CTRL trigger has a downscaling equal to 400 (i.e. 1 out of every 400 events that pass the trigger condition is kept). The downscaling has to be large because the relaxed trigger criteria mean too much data would otherwise be read out. See Section 2.3 for more information on the NA62 trigger system. The same trigger is used for both normalisation and signal channels in order to reduce the systematic uncertainties associated with the trigger. However, full cancellation of trigger efficiency systematics cannot be achieved due to the different number of charged particles present in the final state of each channel. This is discussed further in Sections 5.8 and 5.10.

Centrally run filtering is performed by NA62 and there are a variety of filters available; the ones used in this analysis are the CTRL filter and the restricted positron (RESPOS) filter. The CTRL filter is used for the normalisation channel and applies an additional downscaling factor of 25 on top of that already applied by the CTRL trigger, bringing the total downscaling to a factor of 10,000. On the other hand, the RESPOS filter is used for the signal channel. It asks for at least one track in the event that has the properties of a positron. This track must satisfy the following conditions:

- Positively charged.

- Track momentum < 70 GeV/c.

- Ratio between the energy deposited in the LKr and the STRAW track momentum, $E/p > 0.8$; this value is chosen as 98.0% of electrons and positrons lie within this region as they usually deposit most of their energy within the LKr.

- Vertex formed between the track and the nominal beam axis must be between $Z = 90$ m and $Z = 180$ m.

- Track $\chi^2 < 40$. The χ^2 is from the fitting algorithm used to define a track and is a measure of the track quality.

- The track must pass through the active regions of all four STRAW chambers.

No additional downscaling is applied in the RESPOS filter on top of that applied in the CTRL trigger, meaning the overall downscaling remains a factor 400.

In addition to filtering, a number of data quality checks are also run centrally. These check for issues in all the systems present in the experiment (detectors and read-out) and any bursts or events that have issues are referred to as bad bursts or bad events. As part of the π_D^0 analysis, these checks are performed in the systems used and if found, are not included as part of the data sample. These systems are the KTAG, NA48-CHOD, CHOD, LKr, MUV3, STRAW, TDAQ and the post-processing system.

5.4 Event selection

As both signal and normalisation decay channels are based on the $K_{2\pi}$ decay, the selection criteria for each channel are kept as similar as possible so that systematic errors cancel in the ratio. The normalisation selection finds events with a π^+ candidate track and missing mass equivalent to the π^0 mass. The signal selection is then applied on top of the normalisation selection in order to find π_D^0 events. The first part of the signal selection is hence the same as that used for the normalisation channel (hereinafter referred to as the normalisation or common selection), shown diagrammatically in Figure 5.2.

The initial studies into a signal selection that was as simple as possible are discussed in Subsection 5.4.1. However, for reasons that will be explained, a stricter signal selection was required. The common selection is then detailed in Subsection 5.4.2, followed by a description of the additional cuts made by the signal selection to select the e^+ and e^- in Subsection 5.4.3. Finally, the data-driven particle identification (PID) procedure and the beam momentum fine-tuning (as well as the reasons for using such procedures) are described in Subsections 5.4.4 and 5.4.5 respectively.
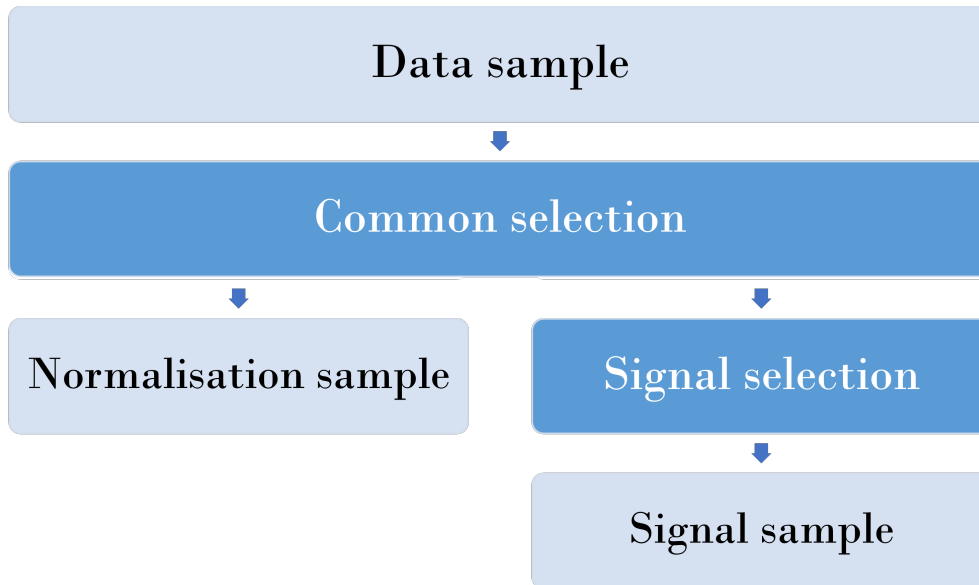
Figure 5.2: Selection workflow used to select signal and normalisation samples.

5.4.1 One track signal selection studies

As mentioned at the start of this chapter, the measurement is expected to be dominated by systematic uncertainties. Keeping the signal selection as simple as possible would thus be preferable. Under this premise, a signal selection was created that only required the identification of the π^+ track and one of the $e^\pm$ tracks from the π_D^0 decay (as opposed to the π^+ and both the electron and positron), hereinafter referred to as the "simple selection". If more than one $e^\pm$ candidate was found, the track with the smallest closest distance of approach (CDA) with the π^+ track was chosen.

The $K_{2\pi}$ and $K_{2\pi_D^0}$ MC acceptances (calculated with non-overlaid MC), defined as the number of events passing the selection relative to the number of kaon decays in the region $105\,\mathrm{m} < Z < 180\,\mathrm{m}$, using this simple selection, are shown in Table 5.1 and demonstrate the problem with using such a simple selection. There is a factor ~ 100 between the two acceptances which is approximately the same as the ratio between the effective branching ratios[1] of $K_{2\pi}$ and $K_{2\pi_D^0}$. This means that half of the events passing the simple signal selection were actually $K_{2\pi}$ background events.

---

[1]Effective branching ratio means the product of both the K^+ and the π^0 branching ratios.

Table 5.1: The non-overlaid MC acceptances after application of the simple signal selection. The difference between non-overlaid and overlaid MC was discussed in Chapter 4.

	$K_{2\pi}$	$K_{2\pi_D^0}$
Acceptance	$(8.93 \pm 0.12) \times 10^{-4}$	$(9.38 \pm 0.01) \times 10^{-2}$

The background arises from the decay of $\pi^0 \to \gamma\gamma$ followed by photon conversion to $e^+ e^-$.

A stricter version of the aforementioned simple selection, whereby the single $e^\pm$ lepton that was chosen was required to be separated from all other tracks by a transverse distance of 30 mm at the first STRAW chamber, was also tested but only reduced the $K_{2\pi}$ acceptance by a factor 1.3. However, including the requirement into the selection for both the e^+ and e^- to be identified (and separated at the first STRAW chamber) reduced the $K_{2\pi}$ acceptance by approximately 4 orders of magnitude. It was thus decided to proceed with this selection, as outlined in the following two sections.

5.4.2   Common selection

The common selection is designed to select $K_{2\pi}$ events. The following cuts are applied:

- The event must contain exactly one "good" π^+ STRAW track. The event is rejected if more than one good track is found. A good track satisfies the following conditions:

  - The extrapolated track must pass through the active regions of the STRAW (all four chambers), LKr, NA48-CHOD, CHOD and MUV3 detectors. It also must not pass through the LAV12 material (as this affects the E/p measurement described below).

  - Track time within ± 10 ns of the trigger time. The track time is given

by the time of a NA48-CHOD hit that is associated (geometrically and in-time) with the track. If a NA48-CHOD hit time does not exist[2], the CHOD hit time is used instead. Whichever is used here is also used as the track time in the remainder of the selection.

– Track $\chi^2 < 30$. The χ^2 is from the fitting algorithm used to define a track and is a measure of the track quality.

– The nominal beam axis vertex, $Z_{\text{vtx}}^{\text{nominal}}$, should satisfy 90 m $< Z_{\text{vtx}}^{\text{nominal}} <$ 180 m. This is the vertex formed between the track and the nominal beam axis and is done for consistency with the RESPOS filter used for the signal selection. However, in practice, performing this cut has little effect due to the below requirement on $Z_{\text{vtx}}^{beam\ axis}$.

– The vertex formed between the beam axis and the track must have a Z-position that satisfies 115 m $< Z_{\text{vtx}}^{\text{beam axis}} <$ 175 m. The beam axis is calculated on a run-by-run basis.

– The closest distance of approach (CDA) between the beam axis and the track must be less than 30 mm.

– The amount of energy deposited by the track within the LKr, relative to the track momentum measured by the STRAW, E/p, must satisfy $E/p < 0.85$. This is the range within which the majority of pions lie. For MC, E/p is obtained from measurements performed on data, as explained in Subsection 5.4.4.

– Charge of the track must equal +1.

– Muon veto requiring no association (spatial association within ± 4 ns of the track time) between the track and a MUV3 candidate.

– Track momentum must satisfy 10 GeV $< p_{\text{track}} <$ 44 GeV. These values were chosen for consistency with the selection used to take E/p measurements on data.

---

[2]This occurs rarely but can arise from, for example, inefficiencies in the read-out system.

– The track time must be within ± 2 ns of a KTAG candidate. The KTAG candidate must have been created from hits in at least 5 octants.

- The square of the missing mass, defined as

$$M_{\text{miss}}^2 = (P_K - P_\pi)^2 \,, \tag{5.4}$$

where P_K and P_π are the four-momenta of the incoming K^+ and outgoing good π^+ track respectively, should satisfy $0.005 \ \text{GeV}^2/\text{c}^4 < M_{\text{miss}}^2 < 0.036 \ \text{GeV}^2/\text{c}^4$. The average beam momentum (calculated on a run-by-run basis) is used for the kaon three-momentum. Fine tuning of the average beam momentum is described in Subsection 5.4.5.

After application of the common selection described above, a normalisation sample of $K_{2\pi}$ events is obtained.

5.4.3 Signal selection

The signal selection begins with the application of the common selection in order to obtain a sample of $K_{2\pi}$ events. It then proceeds with a search for the positron and electron tracks from the π_D^0 decay. As previously mentioned, the γ is not searched for. The remaining steps of the signal selection are as follows.

The event must contain exactly one "good" vertex with the following properties (if more than one good vertex is found, the event is rejected):

- Exactly three tracks.

- One of the tracks is the good π^+ track found in the common selection.

- The vertex Z-position must satisfy $115 \ \text{m} < Z_{\text{vtx}} < 175 \ \text{m}$.

- The vertex χ^2 must satisfy $\chi^2 < 25$. This is a measure of the quality of the vertex and is output by the least-squares fit in the reconstruction.
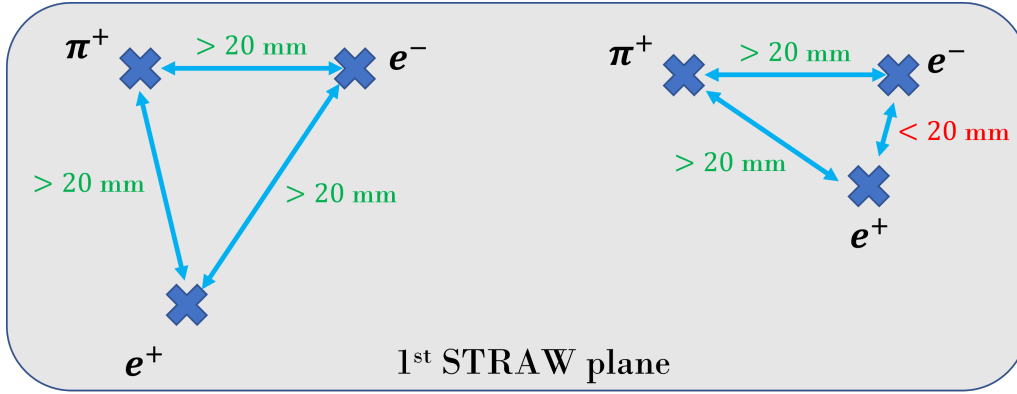
Figure 5.3: Schematic illustrating the cut on the separation between each of the three tracks originating from the three track vertex. Left: an event that would pass the cut. Right: an event that would fail the cut. The intersection points between each track and the first STRAW plane are shown by the crosses.

- The vertex time must be within ± 10 ns of the trigger time. The vertex time is obtained using an average of the track NA48-CHOD/CHOD times. As with the track time in the common selection, the time used is that from the NA48-CHOD unless it does not exist, in which case the CHOD time is used.

- Separation between each pair within the three tracks, at the first STRAW chamber, must be > 20 mm. This is to remove the events in which a photon undergoes conversion in the first STRAW chamber and the resulting $e^{\pm}$ tracks are reconstructed as the π_D^0 decay products. This is shown diagrammatically in Figure 5.3.

- The two tracks that are not the π^+ track must be:

    - Oppositely charged.

    - Must pass through the active regions of the STRAW (all four chambers), LKr, NA48-CHOD, CHOD and MUV3 detectors. It also must not pass through the LAV12 material (as this affects the E/p measurement described below).

    - The nominal beam axis vertex, $Z_{\mathrm{vtx}}^{\mathrm{nominal}}$, should satisfy $90 \text{ m} < Z_{\mathrm{vtx}}^{\mathrm{nominal}} < 180$ m. This is done for consistency with the RESPOS filter but in prac-

tice has little effect due to the above requirement on Z_{vtx}.

– Track time within ± 10 ns of the trigger time. The track time is given by the track NA48-CHOD time or the track CHOD time if the NA48-CHOD time does not exist. Whichever is used here is also used as the track time in the remainder of the selection.

– The π^+ and $e^\pm$ track times must be within ± 4 ns of each other.

– The amount of energy deposited by the track within the LKr, relative to the track momentum measured by the STRAW, E/p, must satisfy $0.9 < E/p < 1.1$. This range is chosen as electrons and positrons usually deposit all their energy in the LKr. E/p is obtained from measurements on data rather than MC, as explained in Subsection 5.4.4.

– Track momentum must satisfy 6 GeV $< p_{\mathrm{track}} < 46$ GeV. These values were chosen for consistency with the selection used to take E/p measurements on data.

– Track $\chi^2 < 30$. The χ^2 is from the fitting algorithm used to define a track and is a measure of the track quality.

After the above signal selection is applied, a sample of $K_{2\pi_{\mathrm{D}}^0}$ events is obtained.

5.4.4 PID using E/p

Due to the limited precision of the simulation of hadronic showers and their reconstruction, the probability of correctly identifying particles using the LKr is not the same between data and MC. This is demonstrated in Figure 5.4 which shows the E/p distribution of tracks in MC[3], after applying the common selection without any PID criteria (to show the full distribution and the different regions occupied by each particle). Furthermore, measurements on $K_{3\pi}$ events show that the probability of a pion track having E/p between 0.9 and 1.1 is 0.010 in MC but 0.017 in

---

[3]The MC sample used is a mixture of the six main K^+ decay modes and is discussed further in Section 5.5.
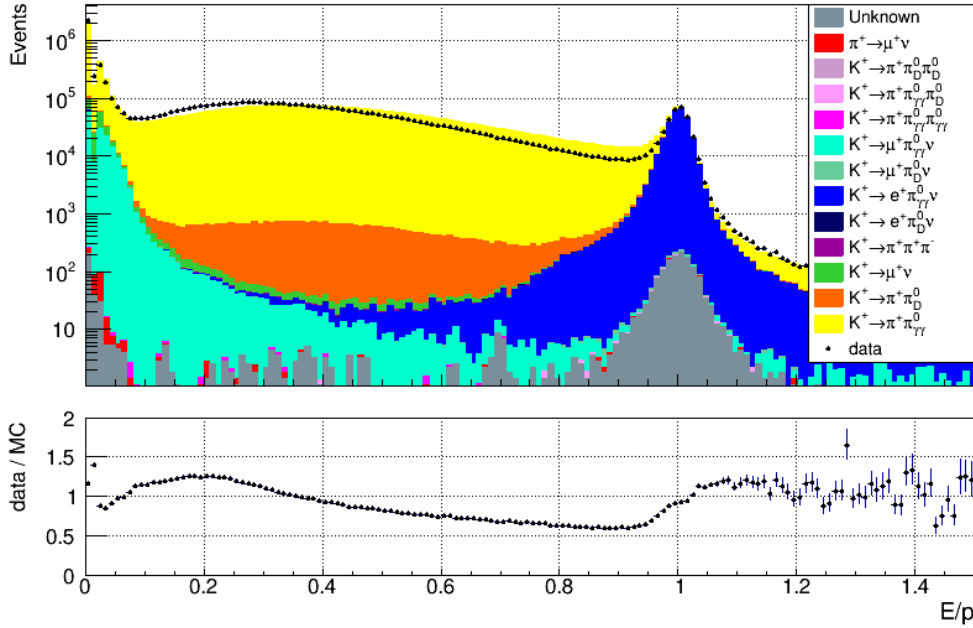
Figure 5.4: E/p distribution for tracks passing the common selection with no PID applied (LKr or MUV3), showing the limited simulation of hadronic showers. The histogram in grey is "unknown" reconstructed decays that could not be matched to the true MC decays, as explained in Section 2.4. The PDG central value for $B(\pi_D^0)$ is used in the MC shown here.

data. Therefore, instead of using the E/p values obtained from the MC simulation, a combination of the true MC information and the measured particle identification (PID) probabilities from data are used to perform PID using the LKr. The rest of this section describes this procedure.

There are four PID phenomena important within the π_D^0 analysis. The first two are identification of the π^+ and $e^\pm$ tracks which, due to the potential for overlap between E/p values for $\pi^+/e^\pm$ tracks (see Figure 5.4), have a certain efficiency associated with identifying them, despite non-overlapping definitions within the selection. The second two are mis-identification of π^+ and e^+ tracks as e^+ and π^+ tracks respectively. Again, due to the potential for overlap between the two E/p distributions, there is a certain probability for each of these mis-identification phenomena to occur. All four of these PID processes depend on the track momentum due to the dependence of energy deposited in the LKr detector on momentum. The phenomena

Table 5.2: PID mechanisms that allow certain decays to pass the common and signal selections. Only a collection of example decays and PID mechanisms are shown, the full background mechanisms (e.g. including photon conversion) are discussed in Section 5.7.

| Example decays | PID mechanism by which decay can pass selection | |
	Common selection	Signal selection
$K_{2\pi}$ $(K^+ \rightarrow \pi^+\pi^0)$	π^+ ID	-
$K_{2\pi_D^0}$ $(K^+ \rightarrow \pi^+\pi_D^0)$	π^+ ID	$e^\pm$ ID
$K_{3\pi}$ $(K^+ \rightarrow \pi^+\pi^+\pi^-)$	π^+ ID	Double $\pi^\pm \rightarrow e^\pm$ mis-ID
K_{e3} $(K^+ \rightarrow \pi^0 e^+\nu)$	$e^+ \rightarrow \pi^+$ mis-ID	-

important within the common selection, where a π^+ track is being searched for, are π^+ identification and $e^+ \rightarrow \pi^+$ mis-identification. On the other hand, in the signal selection, $e^\pm$ identification and $\pi^\pm \rightarrow e^\pm$ mis-identification are required. Table 5.2 shows some example decays and the PID mechanisms required in order for them to pass the common and signal selections.

Two additional mis-identification mechanisms are left out of the discussion above, that being $\mu^+ \rightarrow \pi^+$ and $\mu^\pm \rightarrow e^\pm$ mis-identification. However, in reality, these are not required within the π_D^0 analysis. In the former case, as can be seen by comparing, for example, the $K^+ \rightarrow \mu^+\nu$ and $K^+ \rightarrow \pi^+\pi^0$ distributions in Figure 5.4, the E/p distributions for muon and pion tracks cannot be distinguished (note that the figure was produced without the MUV3 veto). This is why the MUV3 detector is used to veto decays containing muon tracks which it does with high efficiency. In the latter case, as the figure again shows, the probability of $\mu^\pm \rightarrow e^\pm$ mis-identification is negligible (even when no muon veto is applied) and hence does not contribute.

The π^+ and e^+ identification efficiencies as well as the $\pi^\pm \rightarrow e^\pm$ and $e^+ \rightarrow \pi^+$ mis-identification probabilities were obtained from samples of $K_{3\pi}$ and K_{e3} events using selections that are part of NA62Analysis[4]. Within these selections, a π^+ is defined as having $E/p < 0.85$ whereas a $e^\pm$ is defined as having $0.9 < E/p < 1.1$.

---

[4]The identification efficiency and mis-identification probability measurements and fits subsequently described in this subsection are part of the NA62 software framework and were completed as part of a recently published NA62 search for $K^+ \rightarrow \pi^-(\pi^0)e^+e^+$ decays, available at Ref. [97].

The same conditions are used in the common and signal selections in the π_D^0 analysis.

These measurements are shown in Figure 5.5 as a function of track momentum. The MC measurements are shown only for comparison with data, they are not used in the π_D^0 analysis PID procedure. Also shown in the figure are the polynomial fits to the data measurements. Third order polynomials are used for the π^+ identification efficiency and mis-identification probabilities; seventh and fifth order polynomials are used for the $e^\pm$ identification efficiency and mis-identification probabilities respectively. It is assumed that the electron and positron identification probabilities are equivalent which has been shown to be true to a good approximation in other NA62 analyses [97]. The difference in the efficiencies/probabilities between data and MC can be seen in the figure and shows why this procedure is required. For example, in the case of the $e^+ \to \pi^+$ mis-identification probability (Figure 5.5b), the difference is at least a factor of two in places, resulting in approximately double the number of positrons passing the common selection in data compared to MC.

An accept-reject method is applied within the common and signal selections to use the aforementioned identification efficiencies and mis-identification probabilities for particle identification. Firstly, the reconstructed tracks in each MC event are matched to true tracks. This matching is performed using charge, position and momentum information. If the matching fails (which occurs in $\mathcal{O}(0.1\%)$ of cases), the data-driven procedure cannot be performed so the PID is applied using the E/p value from simulation and the rest of the procedure below is ignored. If the matching is successful, the true identity of each reconstructed track is used to apply the correct PID procedure.

The (mis-)identification probability measurements in Figure 5.5 can be used to define two equations[5],

$$P(\pi \text{ ID}) + P(\pi \to e \text{ mis-ID}) + P_1(\text{unknown}) = 1 \qquad (5.5)$$

---

[5]As mentioned previously, a π^+ is defined as having $E/p < 0.85$ whereas a $e^\pm$ is defined as having $0.9 < E/p < 1.1$.

(a) π^+ ID efficiency.

(b) $e^+ \to \pi^+$ mis-ID probability.

(c) $e^\pm$ ID efficiency.

(d) $\pi^\pm \to e^\pm$ mis-ID probability.
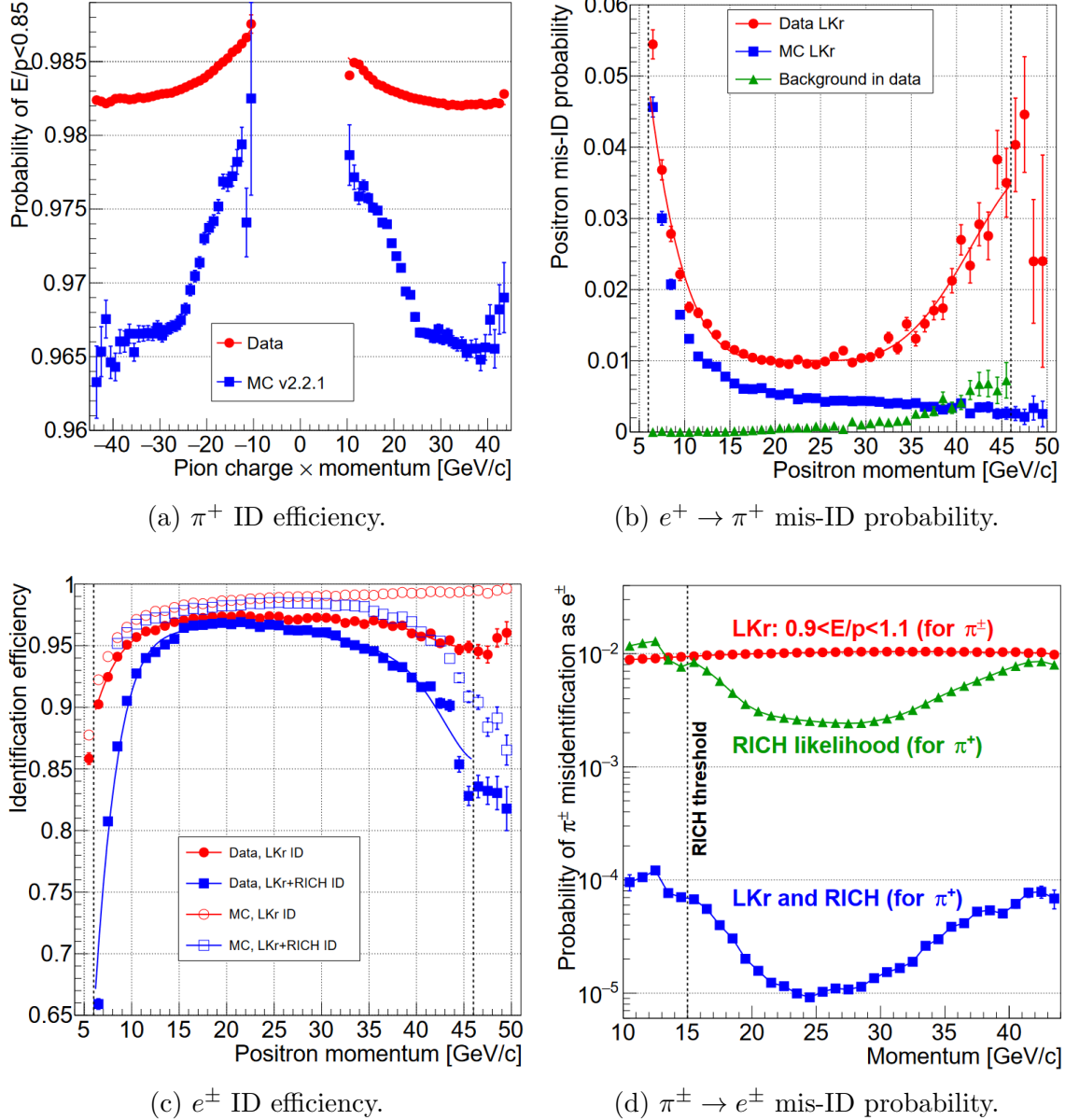
Figure 5.5: Identification efficiencies and mis-identification probabilities from E/p measurements on data and MC. Polynomial fits to the data measurements, which are used for the PID in the analysis, are shown. Note that these plots were centrally produced by NA62 (as part of the analysis described in Ref. [97]) and hence also include measurements conducted with the RICH detector. These are not used within the π_D^0 analysis so can be ignored.

and

$$P(e \to \pi \text{ mis-ID}) + P(e \text{ ID}) + P_2(\text{unknown}) = 1, \qquad (5.6)$$

where P represents a probability and the former is for true $\pi^\pm$ tracks and the latter for true $e^\pm$ tracks. The particle charges have been dropped for brevity. The variable $P(\text{unknown})$ accounts for the regions in the E/p distribution not covered by the $\pi^\pm$ and $e^\pm$ regions (the subscripts 1 and 2 are used to show the two variables are not equivalent).

To determine whether a true track is identified correctly, mis-identified as a $\pi^\pm/e^\pm$ or neither of the two, a random number (r) drawn from a uniform distribution between 0 and 1 is used with one of Equations 5.5 or 5.6. For example, if the true track is a π^+, Equation 5.5 is used and there are three possible outcomes, depending on the value of r:

- $r < P(\pi \text{ ID})$: the true π^+ is correctly identified as a π^+.

- $P(\pi \text{ ID}) < r < (P(\pi \text{ ID}) + P(\pi \to e \text{ mis-ID}))$: the true π^+ is mis-identified as a e^+.

- $r > P(\pi \text{ ID}) + P(\pi \to e \text{ mis-ID})$: the identity of the true π^+ is unknown.

If the true track is a $e^\pm$, Equation 5.6 is used instead. The above procedure is repeated for each true track in the MC event in order to assign an identity to each reconstructed particle track for use in the common and signal selections when searching for good π^+ and $e^\pm$ tracks respectively.

The effect of implementing the above PID procedure is demonstrated in Figures 5.6a and 5.6b which show the M_{miss}^2 distributions without and with the procedure respectively (produced after application of the common selection). The main difference is in the region $0.03 \text{ GeV}^2/\text{c}^4 < M_{\text{miss}}^2 < 0.06 \text{ GeV}^2/\text{c}^4$ which is dominated by $K_{2\pi}$ and K_{e3} decays. The increase (approximately double) in the e^+ to π^+ mis-identification probability results in an increase in the number of e^+ from K_{e3} events being selected as the good π^+ track, improving the agreement between

data and MC. This shows the importance of using this data-driven procedure within the $B(\pi_D^0)$ analysis. The systematic uncertainty associated with this procedure is discussed in Section 5.10.

5.4.5   Corrections to beam momentum

The beam momentum, used in both the common and signal selections, is the average momentum across a certain data-taking period (known as a run, see Section 2.1). Due to limitations associated with the simulation of the beam, a weighting algorithm is used for MC to fine-tune the beam momentum resolution (particularly the transverse components) in order to improve the agreement between data and MC. This algorithm is part of NA62Analysis and computes weights for MC events based on the difference between the true beam particle (kaon or pion) momentum and the run-dependent beam momentum. The beam particle used is that which produced the π^+ candidate track (so can be an original or overlaid beam particle). The weights are calculated for each momentum component (p_x, p_y, p_z) from eighth order polynomial fits to $p_i^{\text{vtx}} - p_i^{\text{beam}}$ data/MC ratios, where p_i^{vtx} is the vertex momentum (sum of the track momenta), p_i^{beam} is the average beam momentum and $i \in (x, y, z)$. The total weight is the product of the three component weights. The distribution of weights is shown in Figure 5.7. A comparison of the M_{miss}^2 data/MC ratios without and with the weighting procedure (after applying the common selection) is shown in Figure 5.8. Systematic uncertainties associated with this weighting procedure are discussed in Subsection 5.10.4.

5.5   Monte Carlo samples

5.5.1   Pileup treatment

Due to the high intensity nature of NA62 and the relatively (compared to other measurements conducted) large branching ratio of the $K_{2\pi}$ and π_D^0 decays, pileup
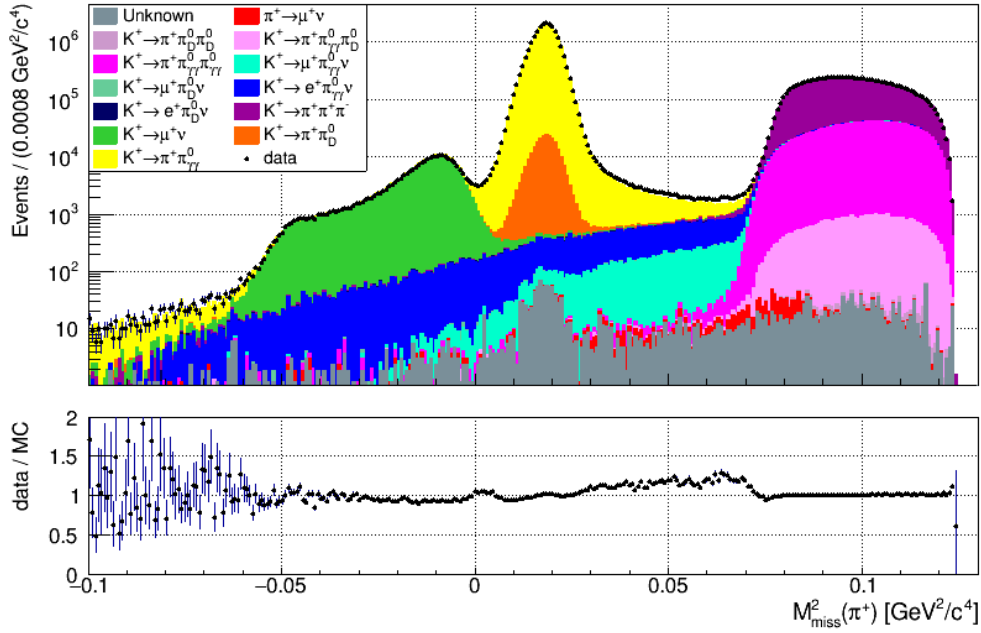
(a) Using E/p from MC simulation for PID.
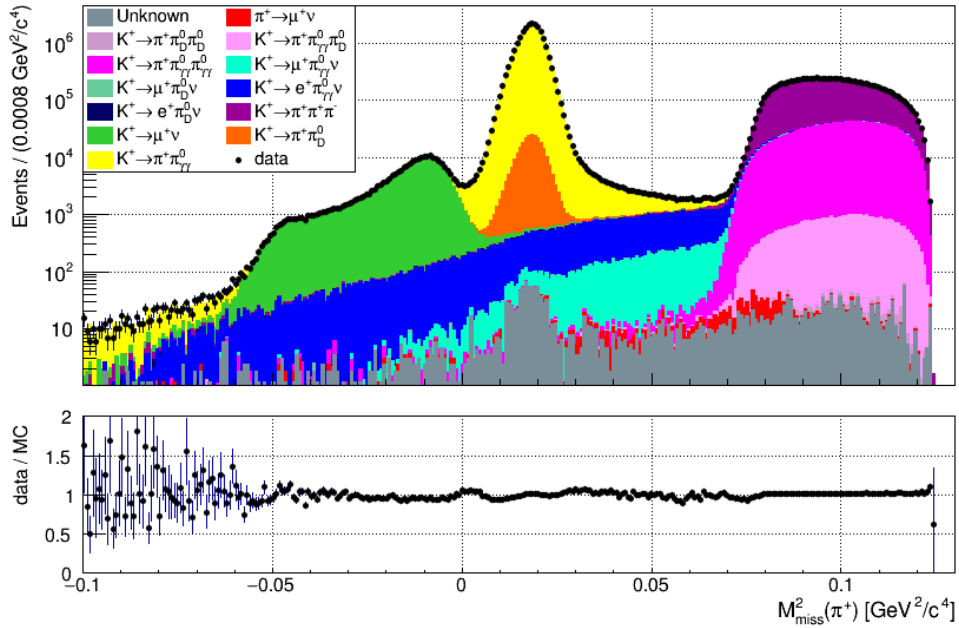
(b) Using E/p from data measurements for PID.

Figure 5.6: M_{miss}^2 comparison of the two E/p PID methods after the application of the common selection. The PDG central value for $B(\pi_D^0)$ is used in the MC shown here.
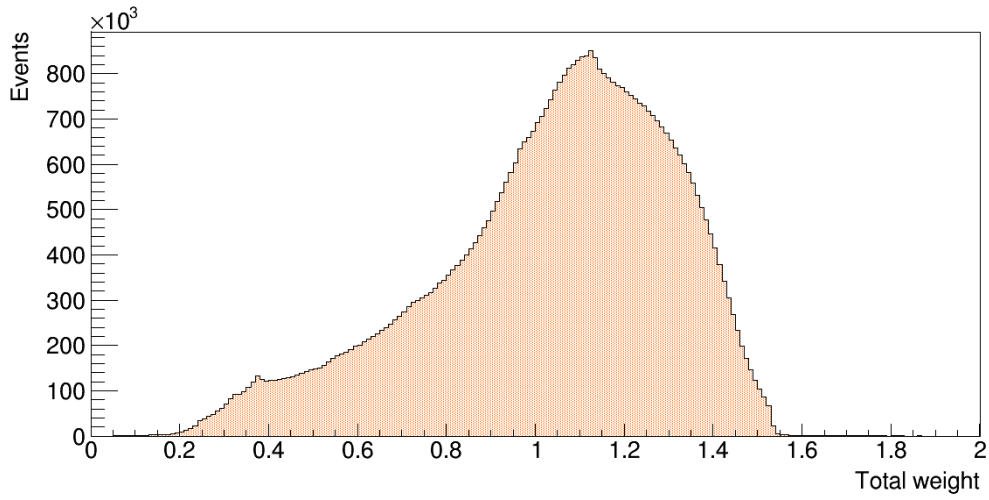
Figure 5.7: Distribution of weights applied to MC events to correct the simulation of the beam.
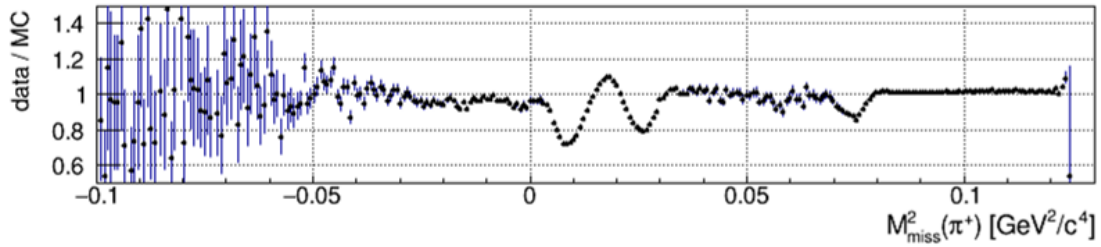
(a) Without momentum weighting procedure.
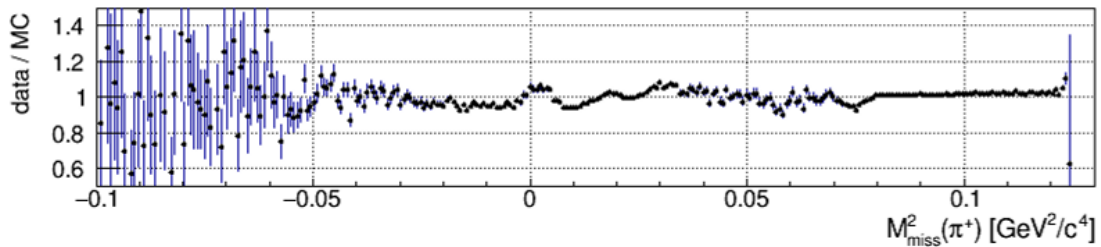
(b) With momentum weighting procedure.

Figure 5.8: M_{miss}^2 data/MC ratio before and after applying the beam momentum weighting procedure. This was produced after applying the π^0 selection.

plays a very important role in the analysis due to a non-negligible chance of a decay occurring at the same time and place as the decays being measured. Overlaid MC is used to simulate the pileup, resulting in each MC event being composed of an "original decay" plus a collection of "overlaid decays". These overlaid decays can be beam particle decays, inelastic interactions or beam particles that pass through the experimental setup without interacting. Chapter 4 covered the technical aspects of, as well as a summary of the author's contributions towards, overlaid MC. This subsection describes the latter in more detail, in the context of the $B(\pi_D^0)$ measurement.

The effects of using overlaid MC can be seen in the M_{miss}^2 plots in Figure 5.9, produced after applying the common selection[6]. The main effect can be seen in the negative M_{miss}^2 region where the $K_{\mu 2}$ decay is dominant. A smaller but also substantial improvement can be seen in the region $0.03 \text{ GeV}^2/\text{c}^4 < M_{\mathrm{miss}}^2 < 0.06 \text{ GeV}^2/\text{c}^4$.

With overlaid MC being a relatively new concept within NA62, the reason for such a large improvement in the data/MC ratio in the $K_{\mu 2}$ dominated region was the subject of a thorough investigation. Without any pileup treatment, $K_{\mu 2}$ events pass the common selection, despite applying a muon veto, mainly due to inefficiencies in the MUV3 detector. These MUV3 inefficiencies account for approximately 75% of the $K_{\mu 2}$ events that are present in the $K_{\mu 2}$ dominated region in Figure 5.9a, with the main causes being the 0.8 mm gap present between the two halves of the MUV3 detector as well as the beam pipe. Muons that pass through these regions are not vetoed (as they do not actually enter the active region of the MUV3) but can be mis-reconstructed such that the extrapolated track appears to be within the MUV3 active region. The mis-reconstructed track therefore looks like a particle that did not make it to MUV3 (and thus unlikely to be a muon), allowing it to pass the selection. The gap and beam pipe effects can be seen in Figure 5.10 which shows the true and reconstructed track positions at the MUV3 for $K_{\mu 2}$ MC events (the common selection

---

[6]The distribution with pileup is the same as that shown in Figure 5.6b but is also shown here for ease of comparison.
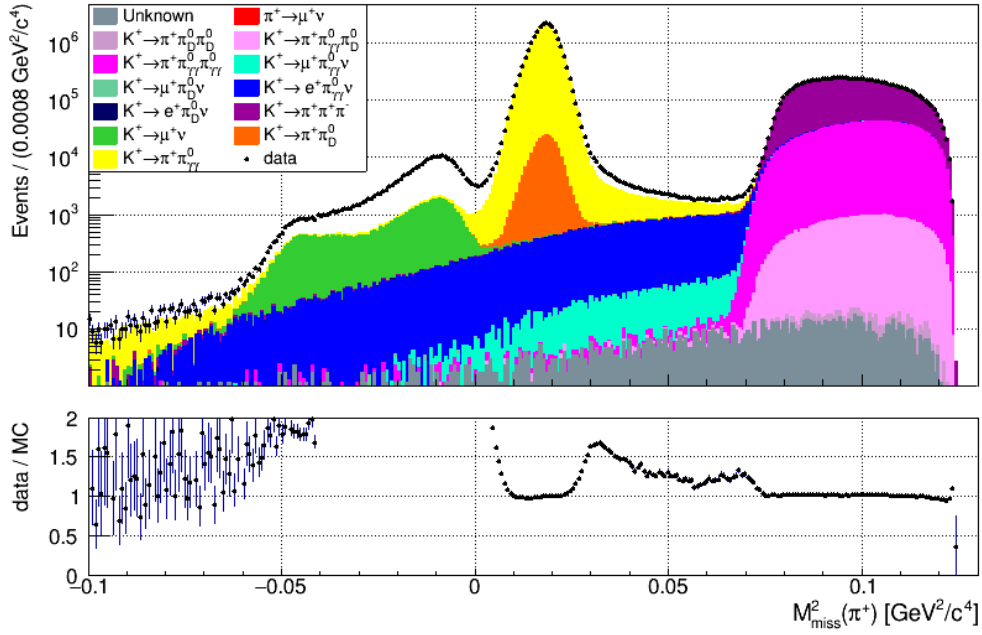
(a) Without pileup.
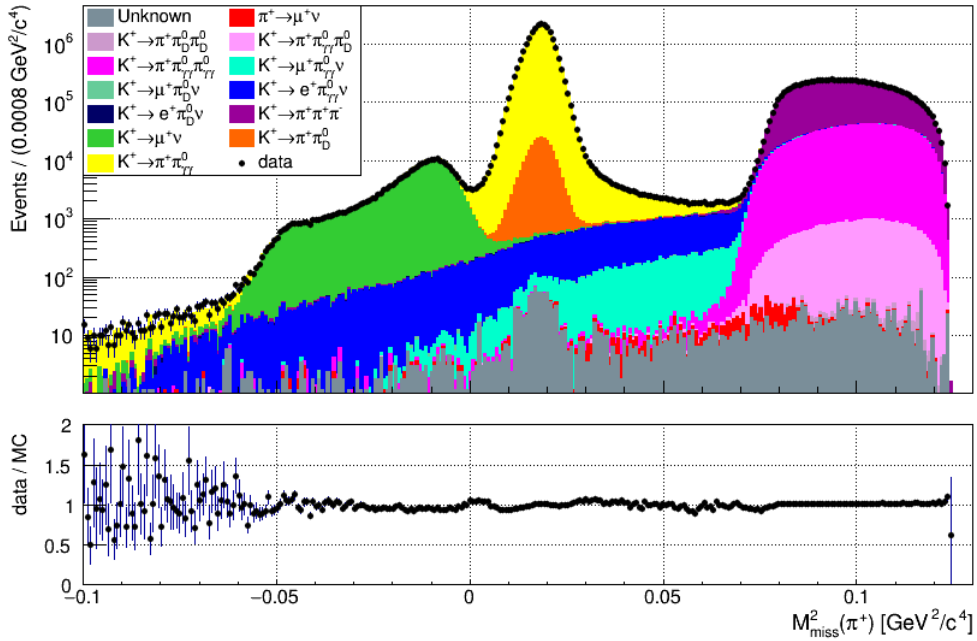
(b) With pileup.

Figure 5.9: M_{miss}^2 distribution without and with the pileup treatment, after application of the common selection (except the M_{miss}^2 cut). The PDG central value for $B(\pi_D^0)$ is used in the MC shown here.

is applied except for the M^2_{miss} cut which is changed to $M^2_{\text{miss}} < 0.002$ GeV^2/c^4). Inefficiencies also arise due to muons crossing the boundaries between MUV3 tiles which can be seen in the square structures in Figure 5.10a. In addition to MUV3 inefficiencies, muons that decay before they reach the MUV3 detector also cannot be vetoed; this is the second largest (approximately 25%) source of $K_{\mu 2}$ events in Figure 5.9a.

The phenomena that lead to $K_{\mu 2}$ events entering Figure 5.9a (i.e. with no pileup treatment) only account for 23% of the $K_{\mu 2}$ events when pileup is included (Figure 5.9b). The remaining 77% of events arise due to detector deadtime which is only accounted for properly when overlaid MC is used. Figure 5.11 shows the time difference between the track NA48-CHOD time and the time of the track MUV3 association(s) for $K_{\mu 2}$ events in the $M^2_{\text{miss}} < 0.002$ GeV^2/c^4 region of Figure 5.9b. The number of events is reduced between -4 and 4 ns due to the in-time MUV3 veto applied (with respect to the track NA48-CHOD time) during the selection. However, a large number of events are outside of this region and it is these events that are present in the M^2_{miss} distribution (Figure 5.9b).

On the positive side of Figure 5.11, there are a large number of events forming a "block" up to 35 ns. The deadtime of the MUV3 detector is 35 ns and is the cause of this block of events. To understand this, consider the following example whereby an event has two tracks (A, B) that hit the same MUV3 tile. The hit of A happens before that of B, so the hit of B falls within the deadtime. If B is the selected track and A is not selected (for whatever reason), B normally would have been vetoed because if A didn't exist, it would have an in-time hit. As A does exist and B is associated to the hit of A (which occurs outside the ± 4 ns veto region), B is allowed to pass the selection. When calculating the time of the MUV3 association(s) of B, as it is associated to the earlier hit of A, it appears in the large block of events. This only happens up to the point at which the hits of B and A are separated by the deadtime, when B would produce its own hit and hence be vetoed. The deadtime
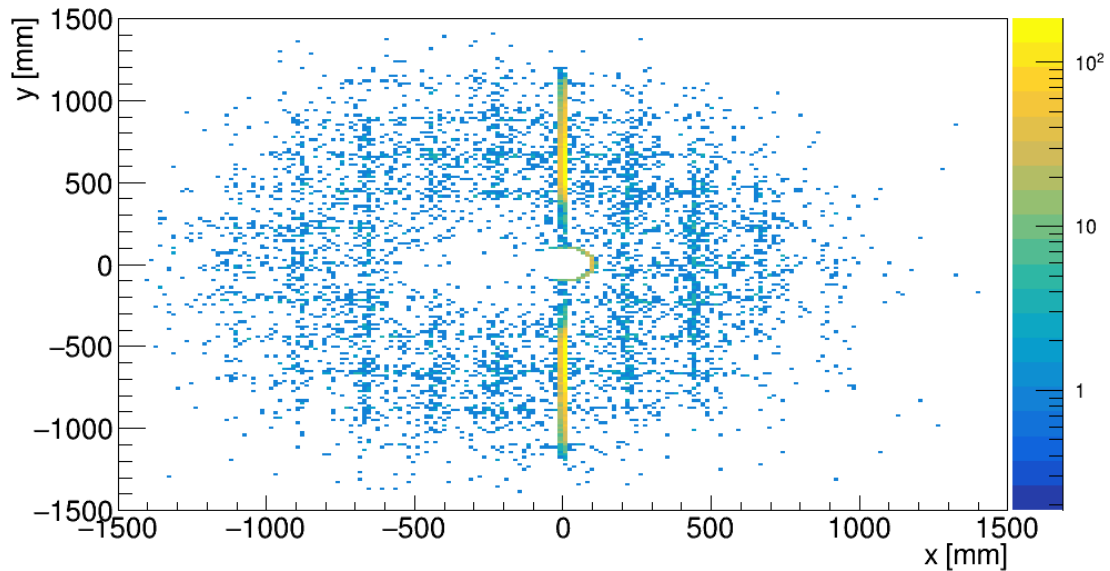
(a) True position.
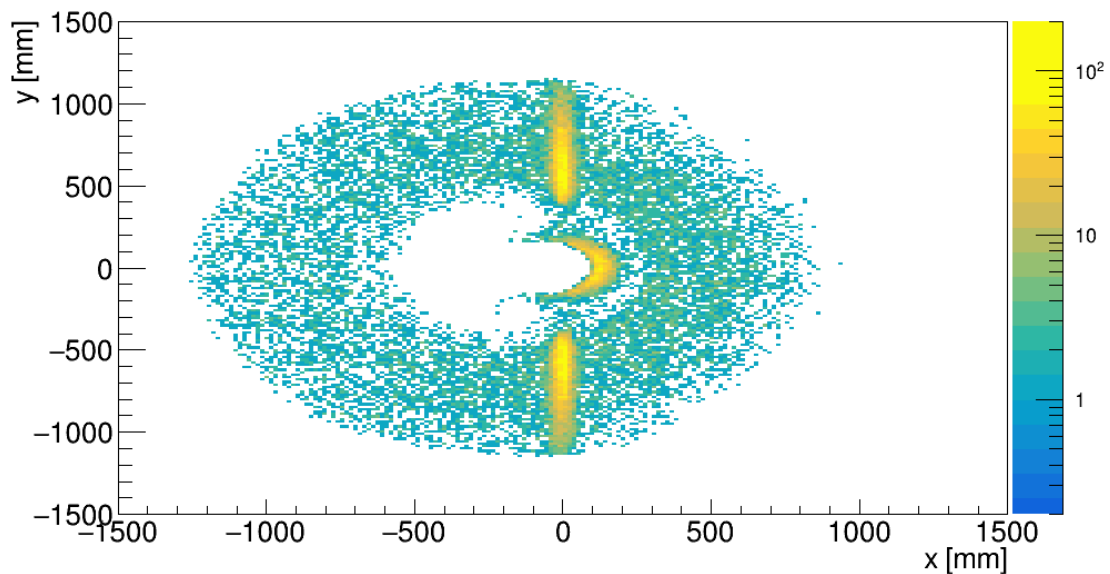
(b) Reconstructed position.

Figure 5.10: The true and reconstructed positions, in the transverse plane at the MUV3 detector, of the track in (mainly) $K_{\mu2}$ MC events with no pileup treatment. Both figures were produced using the common selection with the M_{miss}^2 cut changed to $M_{\mathrm{miss}}^2 < 0.002 \ \mathrm{GeV}^2/\mathrm{c}^4$. The effects of the beam pipe, MUV3 gap and MUV3 tile edges can be seen.
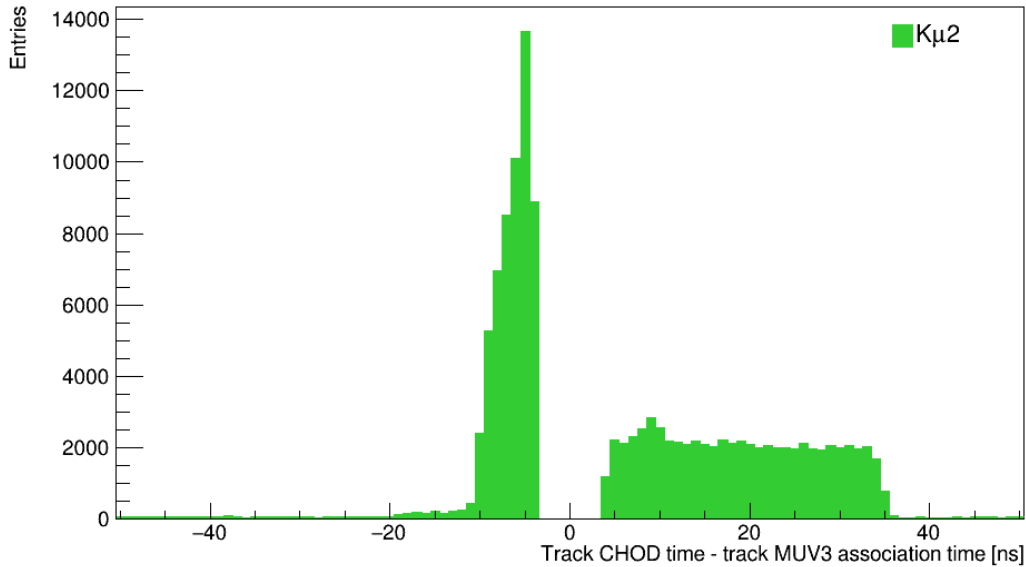
Figure 5.11: Track MUV3 association time(s) with respect to the track NA48-CHOD time for $K_{\mu 2}$ events in the region $M_{\mathrm{miss}}^2 < 0.002$ GeV^2/c^4. The region between -4 ns and 4 ns is empty as a cut on the variable plotted is applied in the analysis.

hence allows $K_{\mu 2}$ events to escape the MUV3 in-time veto.

The peak of events on the negative side of Figure 5.11 is caused by a similar effect as in the positive region but instead occurring in the NA48-CHOD which has a deadtime of 10 ns. The NA48-CHOD is composed of long slabs, compared to the MUV3 which is made up of tiles. In the NA48-CHOD case, the most likely scenario is for two hits to be near the beam pipe due to the spatial distribution of tracks (see the CHOD hit rates in Figure 2.12b); hence the reconstructed time will appear very close to $t_{\mathrm{CHOD}} - t_{\mathrm{MUV3}} = 0$. It is less likely to get two hits where the overlaid is in the outer region of the NA48-CHOD and the original is near the beam pipe; hence the reconstructed time will appear further away from the main peak. This results in a sloping shoulder of events rather than a block of events as in the MUV3 case.

The phenomena described above also lead to improvement in the data/MC region around 0.03 GeV^2/c$^4 < M_{\mathrm{miss}}^2 < 0.06$ GeV^2/c^4 of Figure 5.9b due to an increase (approximately a factor of 4) in the number of $K_{\mu 2}$ and $K_{\mu 3}$ events. An additional (more minor) contribution to the improvement in this region is also present however.
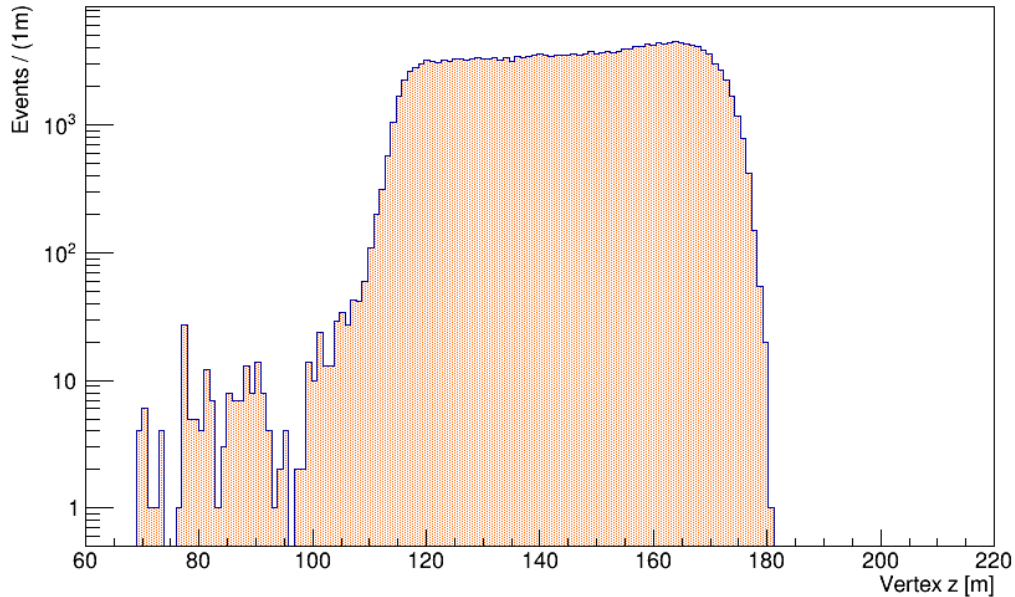
Figure 5.12: True Z_{vtx} for MC events in the region 0.03 GeV^2/c^4 < M_{miss}^2 < 0.06 GeV^2/c^4 of Figure 5.9b. A number of events in the upstream region (< 102.4 m) can be seen.

The sample used for overlaying includes decays within the so-called upstream region, that is the region upstream of the decay volume. The sample that is being overlaid does not contain these upstream events as the majority of the time, they are not needed due to the analysis selection removing them (as there is a requirement for a K^+ candidate in the KTAG). Part of the improvement in the region 0.03 GeV^2/c^4 < M_{miss}^2 < 0.06 GeV^2/c^4 comes about because of the presence of these upstream events. If these events cross the beam axis (via scattering or deflection by the beam line magnets upstream of the decay volume) within the decay volume, the cut on the Z_{vtx} applied during the selection cannot remove them. The true Z_{vtx} of events in the 0.03 GeV^2/c^4 < M_{miss}^2 < 0.06 GeV^2/c^4 region is shown in Figure 5.12. A number of decays occurring upstream can be seen. In addition, the reconstructed Z_{vtx} for events with true Z_{vtx} < 102.4 m (i.e. classified as upstream) is shown in Figure 5.13. One can see that despite the decay occurring upstream, it is reconstructed to occur in the decay volume due to the track crossing the beam axis.
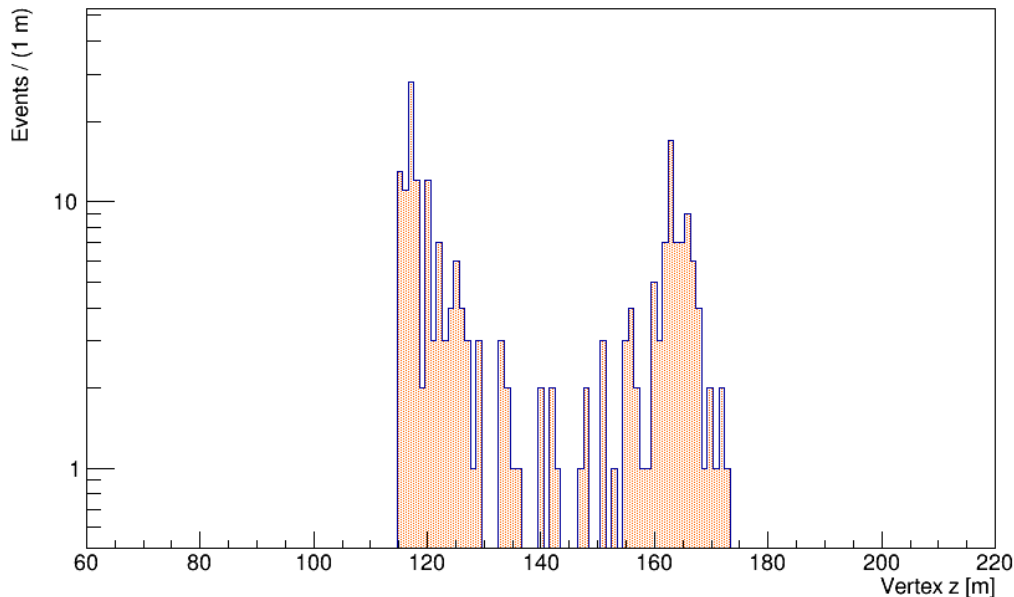
Figure 5.13: Reconstructed $Z_{\mathrm{vtx}}^{\mathrm{beam\ axis}}$ for MC events in the region 0.03 GeV^2/c^4 < M_{miss}^2 < 0.06 GeV^2/c^4 of Figure 5.9b that have a true Z_{vtx} originating upstream (< 102.4 m). Due to crossing of the beam axis, these events pass the cut on the reconstructed $Z_{\mathrm{vtx}}^{\mathrm{beam\ axis}}$ applied during the common selection.

One final difference between Figures 5.9a and 5.9b is the distribution of "unknown" events (see Subsection 2.4). The probability of failing to match a reconstructed track with a true particle track increases when pileup is included because of the large increase in the number of tracks present. This explains the increase in unknown events between the two figures.

5.5.2   Mixed MC

The calculation procedure described in Section 5.2 requires the $B(\pi_D^0)$ used in the MC to be varied. As discussed in Chapter 4, mixed MC was developed for this due to the practical advantages it offers over the standard MC production approach.

To briefly summarise, a mixed MC sample is a single sample containing the six most common K^+ decay modes. The main advantage is that it allows the $B(\pi_D^0)$ used in the simulation ($(B(\pi_D^0)_{\mathrm{MC}})$) to be varied without requiring a large number of samples to be reprocessed/regenerated. The disadvantage is the suppression of

130

the signal decay by its branching fraction resulting in a small number of signal MC events. This is discussed in more detail in Subsection 5.5.4.

Mixed MC is overlaid in the usual way except if a different value for $B(\pi_D^0)_{MC}$ is used, the overlaid events must also use that same value. It should be assumed that all MC samples are overlaid unless explicitly stated otherwise.

The studies conducted, using the mixed MC, to find the optimal $B(\pi_D^0)_{MC}$ values, the required sample sizes as well as the possibility of using additional MC samples to improve the linear fit uncertainties are discussed in the rest of this section.

5.5.3   MC sample with altered $B(\pi_D^0)$

As discussed in Section 5.2, in order to conduct the $B(\pi_D^0)$ measurement, at least two MC samples are needed that use a different $B(\pi_D^0)_{MC}$ to each other. The $B(\pi_D^0)_{MC}$ values can technically be any value $\in [0, 1]$. However there are some constraints that should be applied, based on the fact the relationship between ϵ_{MC} and $B(\pi_D^0)_{MC}$ is assumed to be linear:

- Minimise the difference between the $B(\pi_D^0)_{MC}$ used in the two MC samples. If the two $B(\pi_D^0)_{MC}$ values chosen are orders of magnitude apart, the non-linear effect from situations with multiple π_D^0 present could become non-negligible[7].

- Minimise the amount of extrapolation between the two $B(\pi_D^0)_{MC}$ values. The two points should not be orders of magnitude away from what we expect the $B(\pi_D^0)$ result to be (somewhere around the PDG central value).

Under these constraints, it was decided that one of the samples should use the PDG central $B(\pi_D^0)$ value (1.174% [20]) as a large number of additional MC sample productions would not be required (due to already being available and in use by others in the NA62 collaboration) and to minimise the extrapolation that is needed. Using only two samples, this leaves the question of what $B(\pi_D^0)$ should be used in the

---

[7]This effect is quantified and discussed in detail in Section 5.9.

second MC sample. A mixed MC sample using the PDG central $B(\pi_D^0)$ value and containing 10^8 events was produced at this stage in order to validate the production procedure and to enable the studies discussed in the rest of this section.

To improve the statistical precision, it makes sense to increase the $B(\pi_D^0)$ in the second sample, rather that decrease it. To determine the $B(\pi_D^0)$ that should be used for the second MC sample, the effect of the linear fit parameters' (see Equation 5.2) uncertainties[8] on the final $B(\pi_D^0)$ measurement was estimated by scaling the number of π_D^0 events observed in the mixed MC sample that uses the PDG central $B(\pi_D^0)$ value. The scaling factor used depends linearly on the $B(\pi_D^0)$ being tested. After this scaling, the measured $B(\pi_D^0)$ and its partial error (only including the data statistical error and the systematic error from the fit uncertainties) can be recalculated using the method described in Section 5.2.

Figure 5.14 shows the partial error on the measured $B(\pi_D^0)$ as a function of the $B(\pi_D^0)$ used for the second MC sample. The uncertainty stops reducing after $B(\pi_D^0) = 0.02$. Hence, in order to minimise the difference between the two $B(\pi_D^0)$ values used in the two MC samples, this is the value that was chosen for the second MC sample, hereinafter referred to as the mixed-002 sample.

5.5.4 MC sample sizes

As discussed in Subsection 5.5.2, due to the usage of mixed MC, the signal sample statistics are limited due to the small signal decay branching ratio. For the preliminary studies (and validation of the mixed MC production procedure), a mixed MC sample containing 10^8 events was produced. The suppression by the branching ratio and signal acceptance meant that only $\mathcal{O}(1000)$ π_D^0 events were observed in this sample, leading to a statistical error $\mathcal{O}(3\%)$. Hence, to reach a statistical error of 1% on the number of events observed in the mixed MC sample, a sample size of 10^9 events is required. Due to the larger $B(\pi_D^0)$ in the mixed-002 sample, a factor

---

[8]The fit uncertainty systematics are discussed further in Section 5.10.
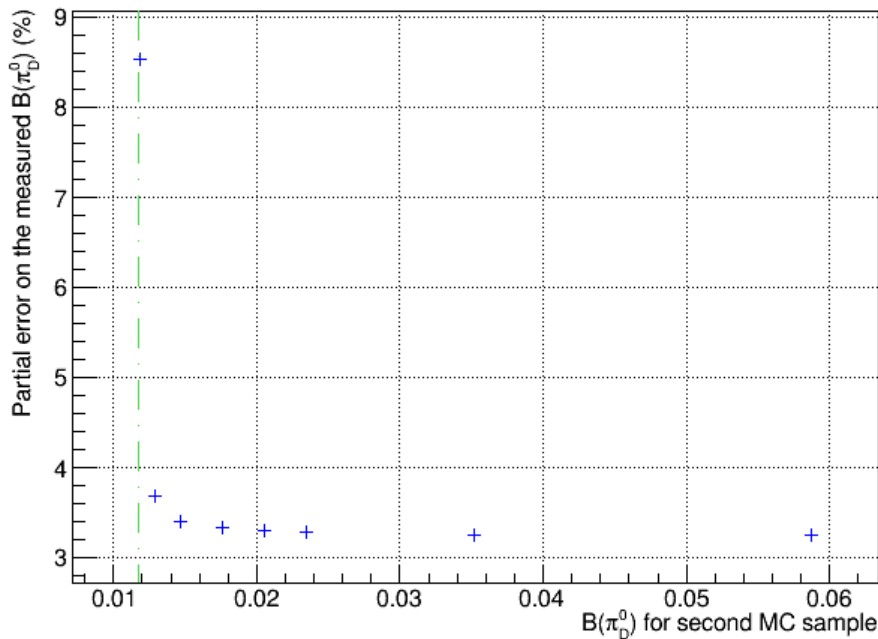
Figure 5.14: Partial relative error on the measured $B(\pi^0_D)$ as a function of the $B(\pi^0_D)$ used in the second MC sample (blue points). The PDG central $B(\pi^0_D)$ value is shown by the green dashed line and is the value used for the first MC sample. The MC samples are assumed to each contain 10^8 events. The point closest to the green line, with a partial error of $\sim 8.5\%$, uses a $B(\pi^0_D)$ value 1% (relative) larger than the central PDG value.

1.3 fewer generated events would be required to reach the same 1% precision.

However, the error on the measured $B(\pi^0_D)$ arising from the fit uncertainties (which in turn depend on the size of the MC samples) does not depend equally on each data point (the data points referred to are those in Figure 5.1). The partial relative error on $B(\pi^0_D)$ (including statistical error from data and the fit uncertainty systematic only), as a function of the size of the two mixed MC samples, is shown in Figure 5.15. The partial error was estimated by scaling the number of π^0_D and π^0 events observed in each MC sample linearly with the sample size. This shows that the error on $B(\pi^0_D)$ does not vary much with the size of the mixed-002 sample but does heavily depend on the size of the standard mixed sample. In other words, there is approximately a 1:1 ratio between the statistical uncertainty on the latter and the error on the $B(\pi^0_D)$ due to the fit uncertainties.

The reason why this error only depends on the size of the mixed sample is
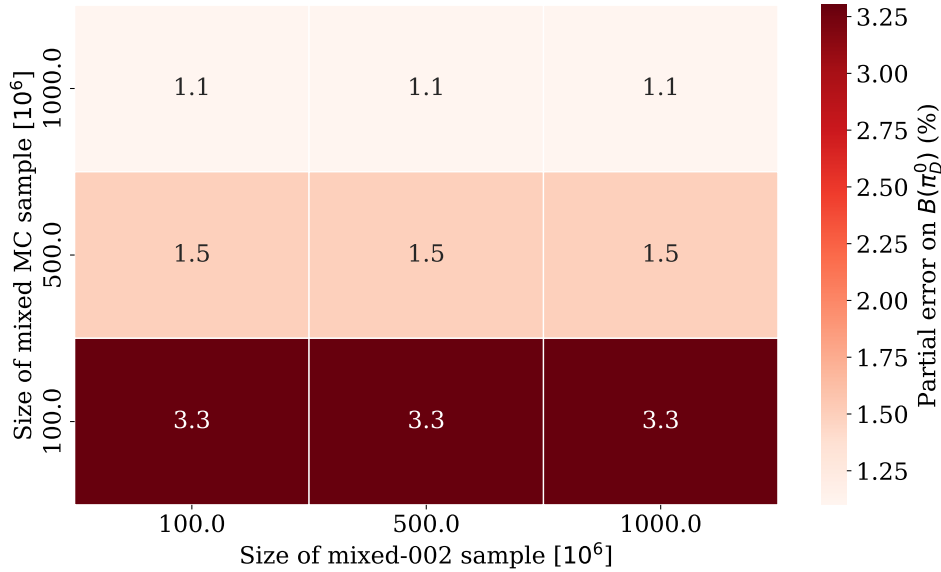
Figure 5.15: Partial relative error on $B(\pi_D^0)$ as a function of the two MC sample sizes.

due to the measured $B(\pi_D^0)$ being closer to the mixed sample data point. This is demonstrated in the schematic shown in Figure 5.16[9]. The top plot shows the case of the mixed and mixed-002 samples having equal sizes; the lower left shows the case with a larger mixed sample; the lower right shows the case with the larger mixed-002 sample. The red band shows some of the possible linear fit lines that would come about if each data point underwent a shift up to the size of its error. The horizontal green dashed line shows the measured value of ϵ_{data}. The vertical green dashed lines show the minimum and maximum $B(\pi_D^0)$ that could be obtained at the fixed value of the measured ϵ_{data}, based on the range of linear fits shown by the red band.

As Figure 5.16 shows, the case that uses a larger mixed sample (lower left) results in a smaller error on the measured $B(\pi_D^0)$ due to the measured $B(\pi_D^0)$ being closer to the $B(\pi_D^0)$ used in the mixed sample. The same argument can be made if the red band was replaced with one showing a collection of possible fit lines of equal gradient and varying intercept (as opposed to Figure 5.16 which shows lines

---

[9]For clarity and to aid the explanation, the values used in these plots are not real values.
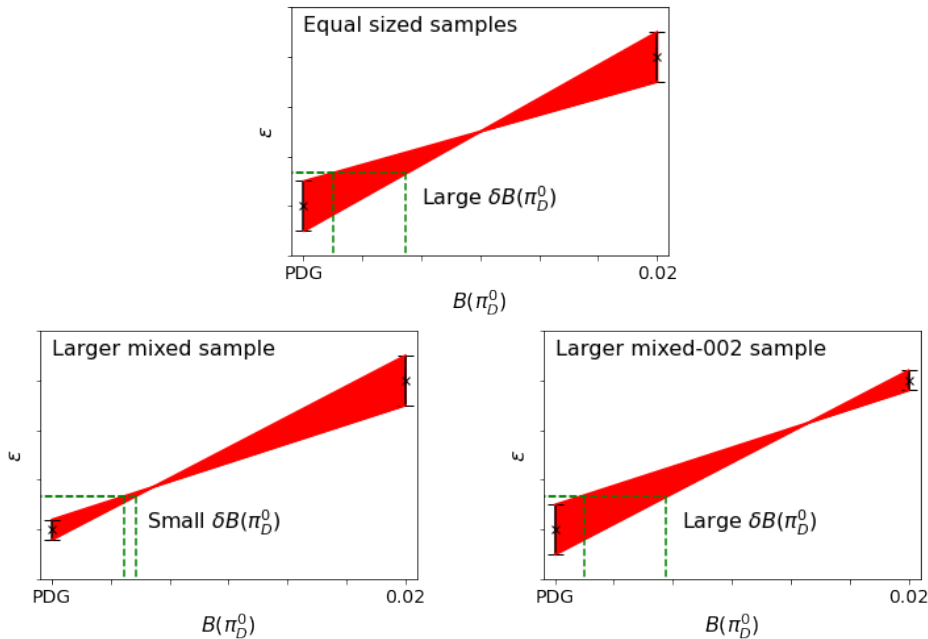
Figure 5.16: Effect of different sample sizes on the linear fit and subsequently the measured $B(\pi_{\mathrm{D}}^0)$. Three cases are looked at: equal sample sizes, larger mixed sample and larger mixed-002 sample. The red band shows some of the possible linear fits that could arise depending on the errors on each data point (which in turn depend on the sample sizes). The green dashed lines show the measured ϵ and minimum/maximum $B(\pi_{\mathrm{D}}^0)$ depending on the fit line used.

of varying gradient and intercept).

5.5.5 MC sample production

One point not mentioned in Chapter 4 was the two methods by which mixed MC can be produced. The first is by producing a single sample whereby the kaons are forced to decay but the decay mode is not forced. This method can be used to produce both mixed MC with the PDG central $B(\pi_{\mathrm{D}}^0)$ value, as well as mixed MC using $B(\pi_{\mathrm{D}}^0) = 0.02$. The second method combines the standard, single decay mode MC samples (which are produced for other NA62 analyses) and the number of events used per single decay mode sample depends on the decay modes branching ratio[10].

---

[10]Instead of running only on a certain number of events, a weighting procedure could also be used. This is discussed in Section 5.12.

This second method is the same as generating additional mixed MC events because mixed MC is simply a reshuffle of single decay mode MC events in the correct proportions, albeit without the additional MC generation/processing time as the samples already exist and are in use by other members of the collaboration. Due to the presence of overlays, for practical reasons, this second method can only be used when the PDG central $B(\pi_D^0)$ value is used (otherwise, a large number of samples would require reprocessing, see Section 4.2). However, this suits the requirements of the $B(\pi_D^0)$ measurement due to the uncertainty on the measured $B(\pi_D^0)$ being almost independent of the size of the mixed-002 sample, as discussed in Subsection 5.5.4.

For the mixed sample that uses the PDG central $B(\pi_D^0)$ value, both methods were used due to the large statistics required and the single decay mode samples being already available. For the $B(\pi_D^0)$ measurement, 3×10^8 events came from a dedicated mixed MC sample and 4.7×10^8 from the standard samples. The total of 7.7×10^8 mixed events is hereinafter collectively referred to as the mixed MC sample. For the mixed-002 sample, once NA62MC was adapted so that the simulated $B(\pi_D^0)$ could be varied (see the author's contributions in Chapter 4), the first method was used to generate 10^8 events.

5.5.6   MC sample summary

To summarise, there are two MC samples used within the π_D^0 analysis. Both contain K^+ beam particles that are not forced to decay to a certain mode (i.e. they decay according to the corresponding branching ratios) but are forced to decay within the 105 m to 180 m decay volume. Both samples are overlaid. One sample, the mixed sample, uses the $B(\pi_D^0)$ given by the PDG central value and is the sample that will dominate the systematic uncertainty on the measured $B(\pi_D^0)$ as a result of the MC statistical uncertainty. This sample contains 7.7×10^8 events which is as much as currently available. The second sample, the mixed-002 sample, uses $B(\pi_D^0) = 0.02$ and contains 10^8 events.

Table 5.3: The effective branching ratio of each decay mode present in the two MC samples used in the π_{D}^0 analysis. The π^0 decay modes and any combinatorics, for each π^0 present in the K^+ decay, are included within each branching ratio where appropriate. The precision of each is given by that quoted in the PDG.

Decay mode	Effective branching ratio	
	Mixed	Mixed-002
$K_{2\pi};\ \pi_{\gamma\gamma}^0$	0.2043	0.2026
$K_{2\pi};\ \pi_{\mathrm{D}}^0$	2.427×10^{-3}	4.134×10^{-3}
$K_{3\pi}$	0.05583	0.05583
$K_{3\pi^0};\ \pi_{\gamma\gamma}^0,\ \pi_{\gamma\gamma}^0$	0.01719	0.01690
$K_{3\pi^0};\ \pi_{\gamma\gamma}^0,\ \pi_{\mathrm{D}}^0$	4.084×10^{-4}	6.899×10^{-4}
$K_{3\pi^0};\ \pi_{\mathrm{D}}^0,\ \pi_{\mathrm{D}}^0$	2.426×10^{-6}	7.040×10^{-6}
$K_{\mu2}$	0.6356	0.6356
$K_{\mu3};\ \pi_{\gamma\gamma}^0$	0.03313	0.03285
$K_{\mu3};\ \pi_{\mathrm{D}}^0$	3.935×10^{-4}	6.704×10^{-4}
$K_{e3};\ \pi_{\gamma\gamma}^0$	0.0501	0.0497
$K_{e3};\ \pi_{\mathrm{D}}^0$	5.95×10^{-4}	1.01×10^{-3}

Table 5.3 shows the effective branching ratio of each decay channel present in the two MC samples (it is effective as the π^0 branching ratio is included wherever neutral pions are present).

5.5.7   Additional MC samples

A question that arises from the studies presented in this section is whether having more than two MC samples would be beneficial. Using a similar method to that used to estimate the $B(\pi_{\mathrm{D}}^0)$ to be used and the size of the mixed-002 sample, that is by scaling the number of π_{D}^0 and π^0 events observed in MC, the effect of introducing a third MC sample can be estimated. The partial error on the measured $B(\pi_{\mathrm{D}}^0)$ (i.e. only including statistical error from data and systematic error from the fit), as a function of the $B(\pi_{\mathrm{D}}^0)$ used in the third simulation, is shown in Figure 5.17. This study was done for two sizes of the third MC sample: 1.0×10^8 events and 7.7×10^8
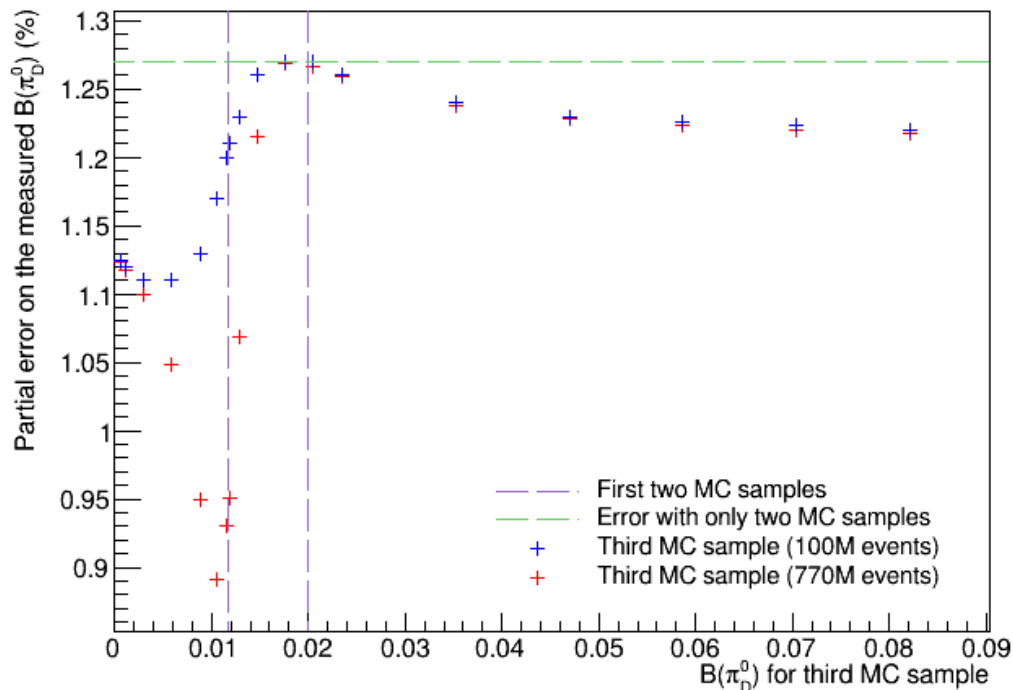
Figure 5.17: Partial relative error on $B(\pi_D^0)$ as a function of the simulated $B(\pi_D^0)$ used in the third MC sample, for two sample sizes of 1.0×10^8 and 7.7×10^8 events. The vertical dashed purple lines show the two values of the $B(\pi_D^0)$ used in the two MC samples discussed in Subsection 5.5.3. The horizontal dashed green line shows the partial relative error obtained using only two MC samples.

events. The best result that can be achieved is a 31% relative decrease in the error arising from the fit uncertainties, obtained using a third MC sample that uses a simulated $B(\pi_D^0)$ of 0.0106 (equivalent to a 10% reduction with respect to the PDG central value) and a size of 7.7×10^8 events. It may be possible to produce a sample similar to this in the future; however, given the marginal improvement relative to the other uncertainties involved in the $B(\pi_D^0)$ measurement (see Section 5.10 on systematic errors later), it was not done for this thesis.

5.6 Analysis samples

Figures 5.18a and 5.18b show the M_{miss}^2 distributions for the normalisation and signal samples respectively[11]; the signal region in each case is defined as $0.005 \text{ GeV}^2/\text{c}^4 < M_{\text{miss}}^2 < 0.036 \text{ GeV}^2/\text{c}^4$ and both figures use the PDG central value for $B(\pi_D^0)$ in the MC simulation. The data and MC agree very well after the common selection and inside the signal region after the signal selection. However, the lack of MC statistics results in a poor data/MC agreement with the signal selection outside of the signal region.

Similarly, Figures 5.19a and 5.19b show the M_{miss}^2 distributions, for the normalisation and signal samples respectively, but using the mixed-002 MC sample (i.e. with $B(\pi_D^0) = 0.02$). Apart from the difference in MC statistics (which causes fluctuations in the MC distribution due to the smaller size of the mixed-002 sample), the only noticeable difference in the normalisation sample is the number of $K_{2\pi_D^0}$ events which has increased by a factor 1.7, as one would expect due to the increased value of $B(\pi_D^0)$ used. As will be discussed later (in Section 5.7), the number of $K_{2\pi}$ (with $\pi_{\gamma\gamma}^0$) events also changes but is not noticeable here. Again, this is as expected. Furthermore, in the signal sample, there is very little difference observed between the mixed-002 and standard mixed samples, other than that caused by the difference in MC statistics[12]. The altered $B(\pi_D^0)$ thus has very little effect on the M_{miss}^2 distributions. This is aided by the negligible amount of background present in each case.

The remainder of this section shows a comparison of data and MC after application of the common and signal selections. All plots use the PDG central value for $B(\pi_D^0)$ in the MC simulation. Note that due to the design of the selections (more specifically, the requirement of only one good π^+ track or one good vertex in an

---

[11]Figure 5.18b is the same as Figure 5.6b but is also shown here for ease of comparison.

[12]Note that, the MC events are normalised using the respective numbers of events passing the selection in the data and MC samples, hence why the data and MC distributions agree in the signal region despite the different $B(\pi_D^0)$ values present.
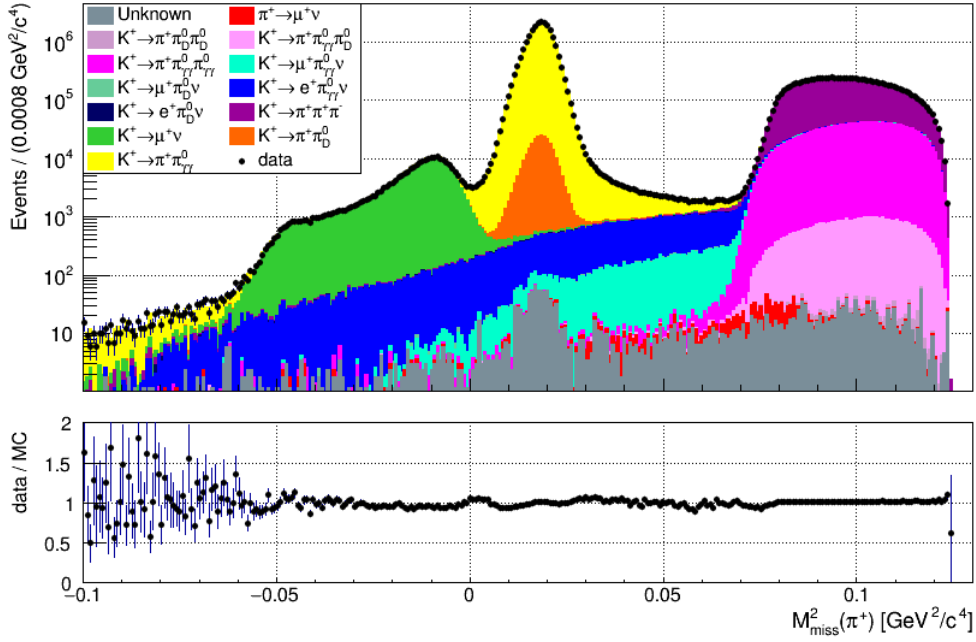
(a) Common selection.
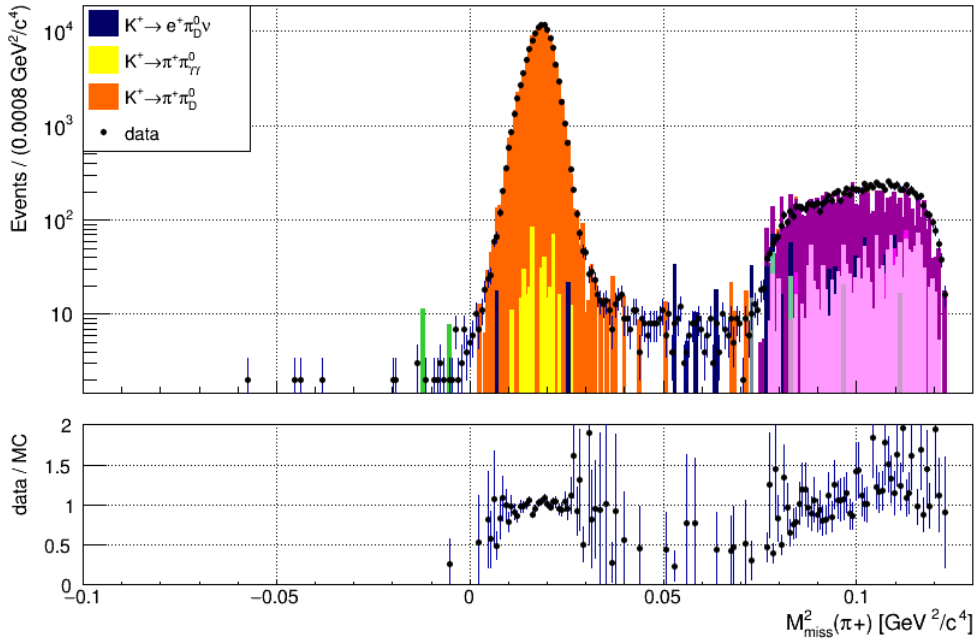
(b) Signal selection.

Figure 5.18: M_{miss}^2 distributions after application of each selection. The PDG central value for $B(\pi_D^0)$ is used in the MC shown here. The MC decay mode shown by each colour is that of the selected decay. This may be the original or an overlaid decay.
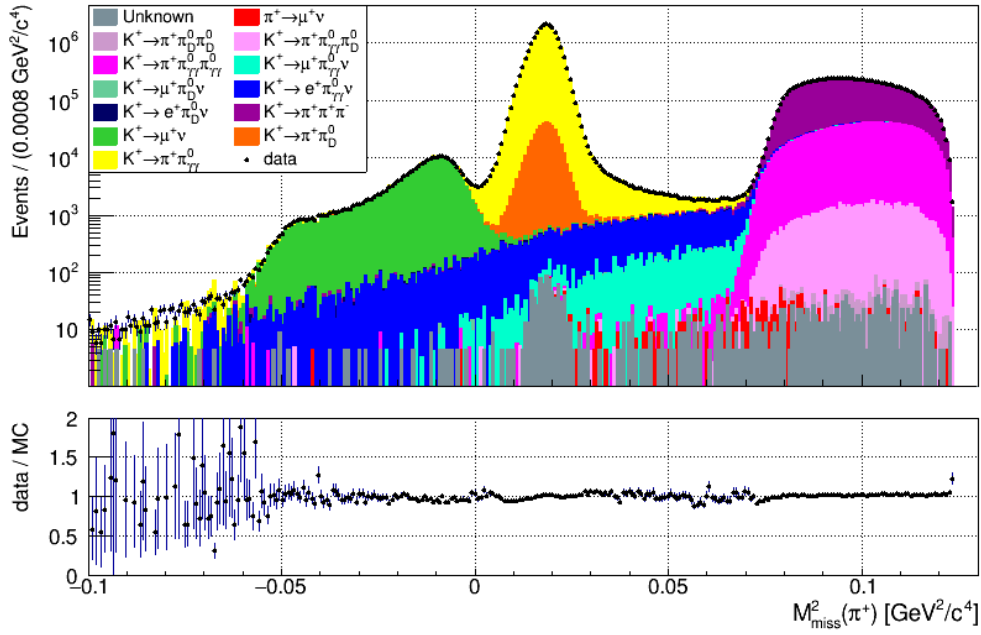
(a) Common selection.
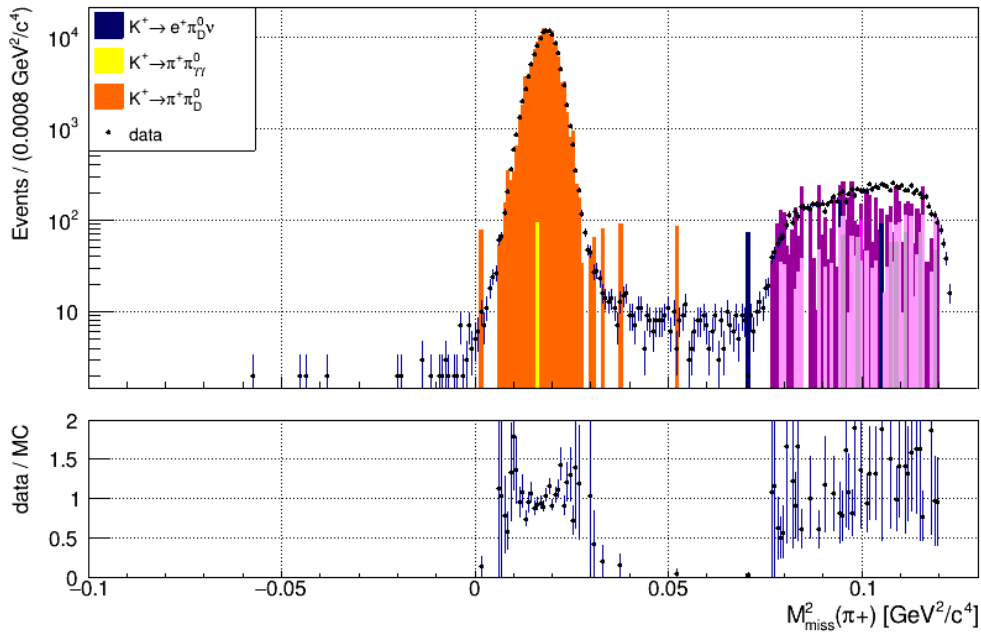
(b) Signal selection.

Figure 5.19: M_{miss}^2 distributions after application of each selection using the mixed-002 MC sample $(B(\pi_D^0) = 0.02)$. The MC decay mode shown by each colour is that of the selected decay. This may be the original or an overlaid decay.

event), plots of variables outside of their respective cut regions is not possible[13]. For example, the pion momentum plot is cut off at 10 and 46 GeV/c as that is where the cut is applied. The pion momentum is one of the variables used to define a "good" pion track so there is no way of plotting this whilst also applying the cut on the number of good pion tracks.

All figures in this section contain weighted MC events, as discussed in Subsection 5.4.5.

Normalisation sample

Figures 5.20 to 5.22 show the data and MC comparisons across a variety of variables after application of the common selection. Data and MC are in good agreement in Figure 5.21 whereas small discrepancies arise at low momentum in Figure 5.20 and high CDA in Figure 5.22. The cause of these discrepancies is unknown but are both in regions of low statistics and will also cancel in the ratio of signal and normalisation so are not expected to result in a sizeable systematic uncertainty (with respect to the other systematic errors involved in the analysis).

Signal sample

Figures 5.23 to 5.28 show the data and MC comparisons across a variety of variables after application of the signal selection. In general, data and MC agree well. There appears to be a downward trend at low π^+ momentum in Figure 5.23. However, as mentioned above, this also occurs in Figure 5.20 and the two are expected to cancel to first order. A similar disagreement arises to that seen in Figure 5.22 in the CDA distribution (Figure 5.26); again, these will cancel to first order.

---

[13]The exceptions are the M_{miss}^2 distributions shown previously. These are different as the definition of a good pion or good vertex does not include the M_{miss}^2 cut.
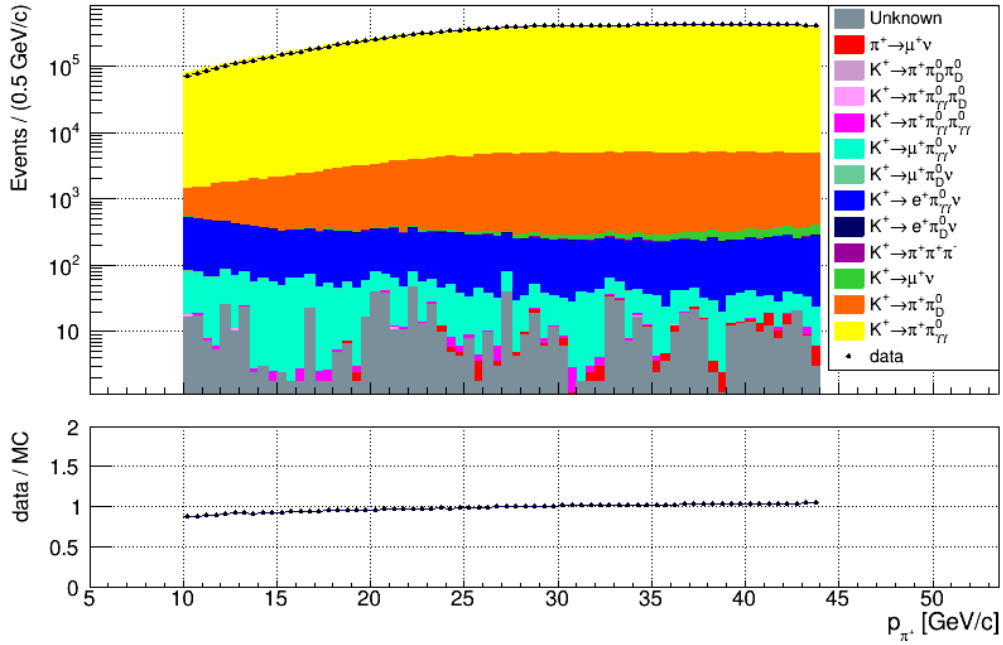
Figure 5.20: Pion track momentum after application of the common selection.
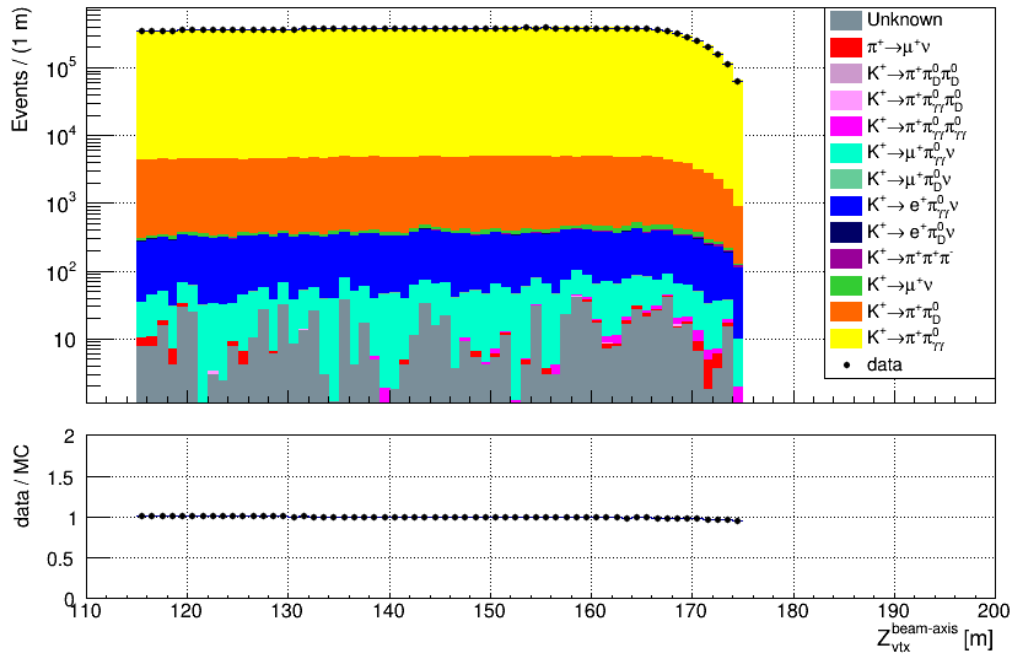
Figure 5.21: Vertex between the pion track and the beam axis after application of the common selection.
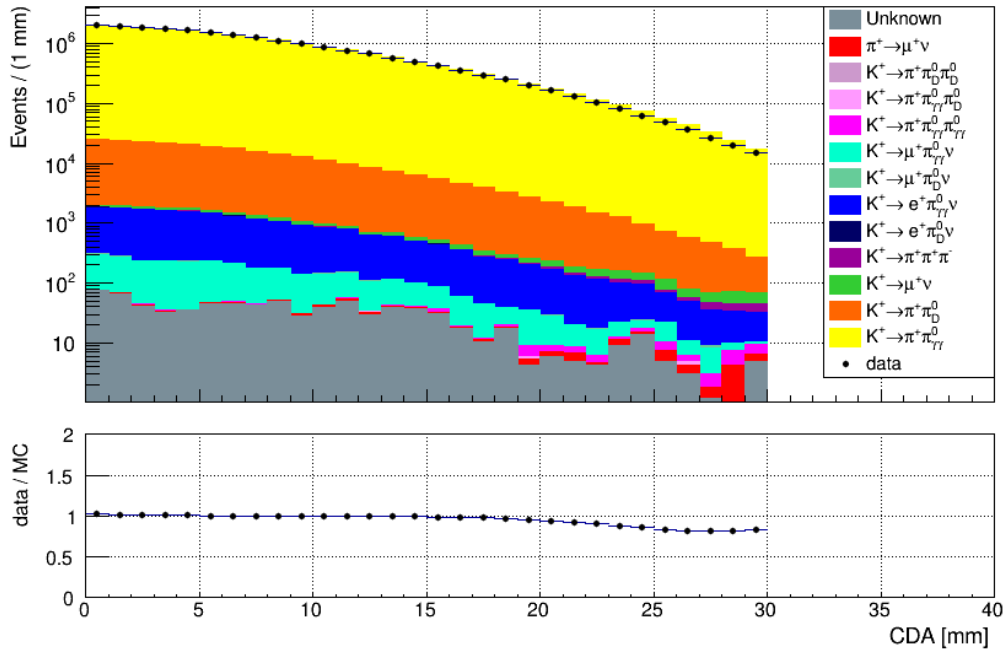
Figure 5.22: Closest distance of approach between the pion track and the beam axis after application of the common selection.
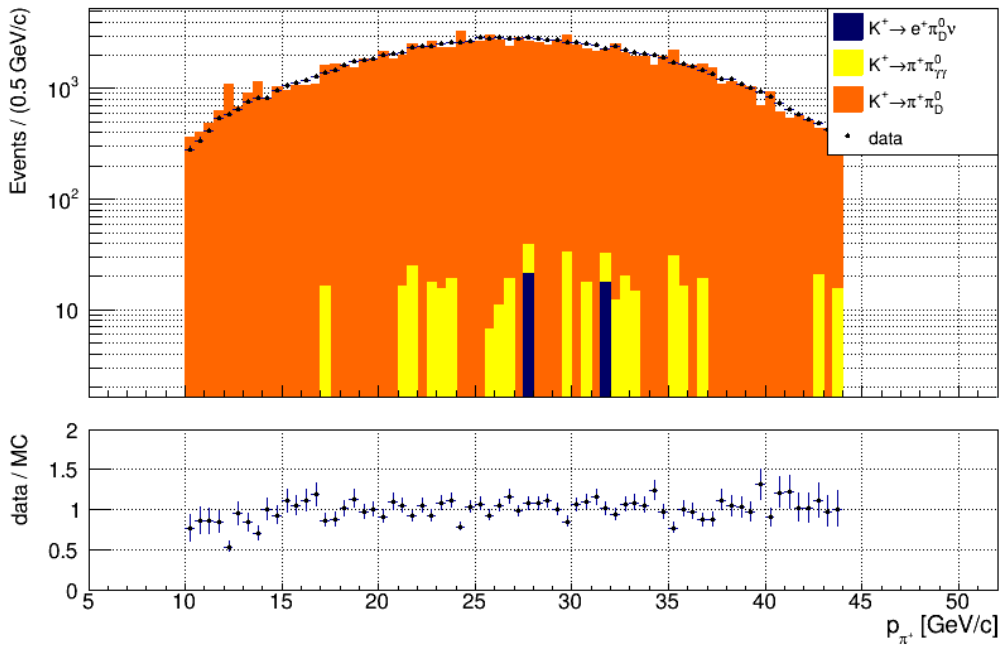
Figure 5.23: Charged pion momentum after application of the signal selection.
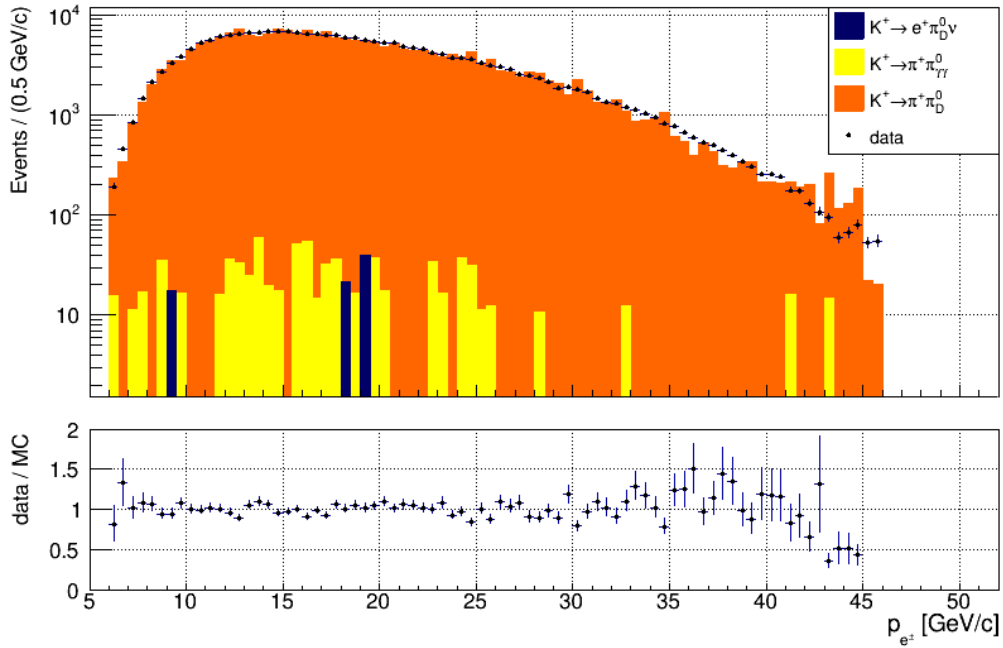
Figure 5.24: $e^\pm$ momentum after application of the signal selection. Both particles are included in the figure meaning there are two entries per event.
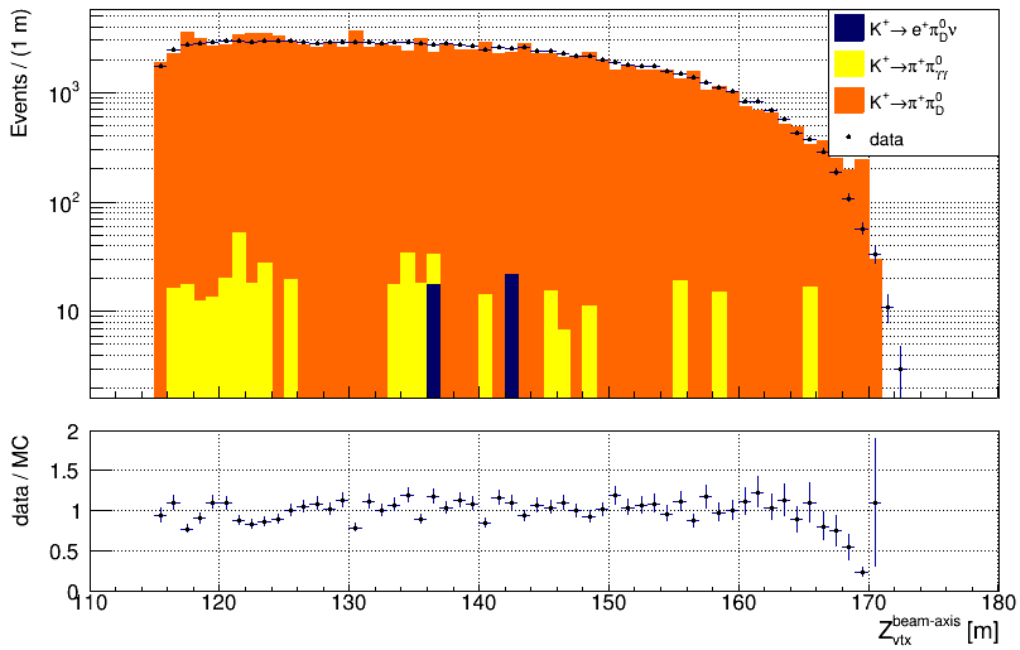
Figure 5.25: Z-coordinate of the vertex between the pion track and the beam axis ($Z_{vtx}^{\text{beam-axis}}$) after application of the signal selection.
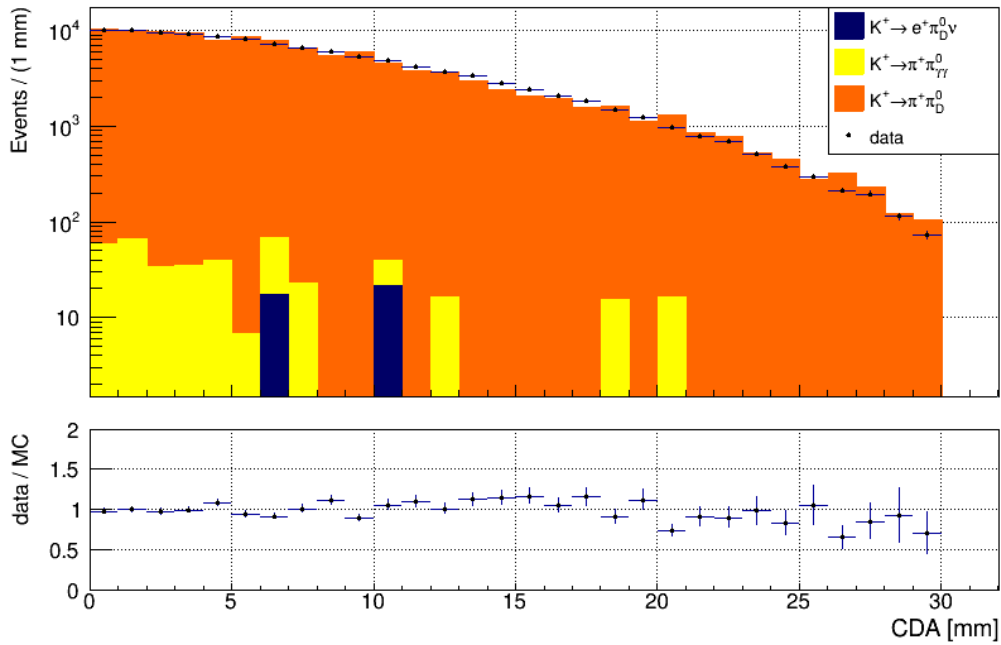
Figure 5.26: Closest distance of approach between the pion track and the beam axis after application of the signal selection.
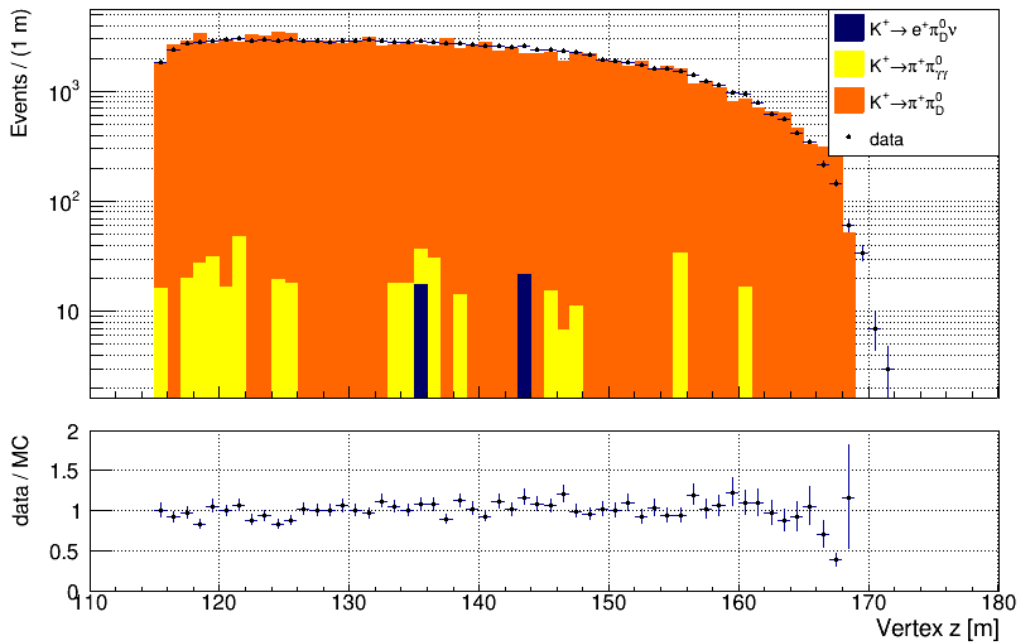
Figure 5.27: Z-position of the vertex formed between the π^+, e^+ and e^- tracks after application of the signal selection.
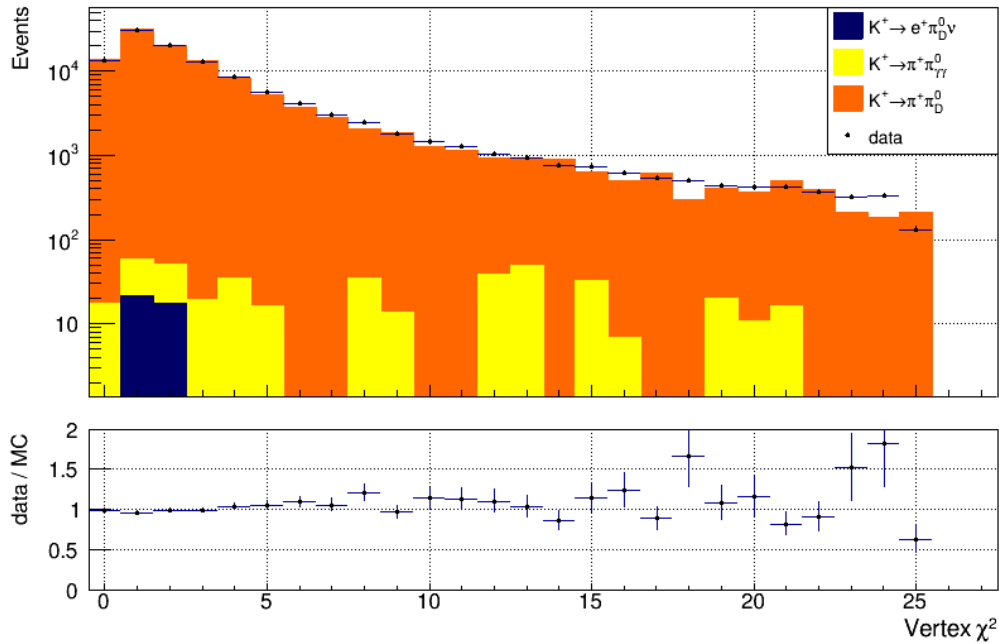
Figure 5.28: χ^2 of the vertex formed between the π^+, e^+ and e^- tracks after application of the signal selection.

Cut flow analysis

The number of tracks/vertices that pass each stage of the common and signal selections can be used to give an idea as to the effect each cut has. It should be noted that the figures referred to in the remainder of this section are all bar charts, not histograms. The area of each bar thus has no meaning and is aesthetic only. Figure 5.29 shows the number of tracks that pass each successive cut in the common selection when searching for a good π^+ track (see Subsection 5.4.2 for the definition of "good") in the data sample. The order in which the cuts are applied in the selection is the same as the order they are listed in the figure. The black bar shows the total number of tracks in the sample. The cut with the largest effect, relative to the previous cuts, is the requirement that the track has no associated hit in the MUV3 detector, removing approximately two thirds of tracks that pass previous cuts. This cut removes a large number of muon tracks that come from $K_{\mu 2}$ decays, as discussed in Subsection 5.5.1.
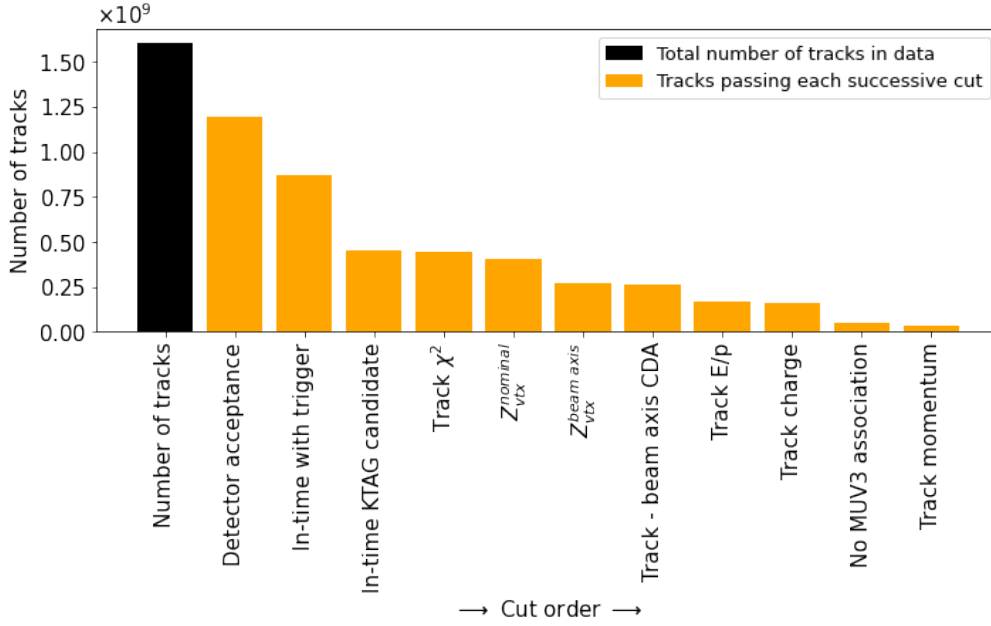
Figure 5.29: Number of tracks passing each successive cut in the common selection, when searching for a good π^+ track, in the data sample. Also shown (black bar) is the total number of tracks present in the data sample. The exact cuts are described in Subsection 5.4.2.

Figure 5.30 shows the total number of good π^+ tracks per event in the data sample. The common selection requires exactly one good π^+ track per event (orange bar); the M_{miss}^2 cut is then applied on top of this and the number of events passing both these cuts is shown by the green bar. Of the events passing the cut on the number of good π^+ tracks, 33.1% fail the M_{miss}^2 cut. As can be seen in Figure 5.18a, the events that fail the M_{miss}^2 cut are mostly $K_{\mu 2}$ and $K_{3\pi}$ and hence pass the cut on the number of good π^+ tracks due to $\mu^+ \to \pi^+$ mis-identification and a missing π^+ track respectively.

Figure 5.31 shows the number of vertices that pass each cut in the signal selection when searching for a good π_D^0 vertex (see Subsection 5.4.3 for the definition of "good") in the data sample. This is after the application of the common selection. The black bar shows the total number of three track vertices present in the sample after the common selection has been applied. The cuts that have the largest effect are the E/p cut used for PID and the requirement to have all three of the $K_{2\pi_D^0}$ tracks
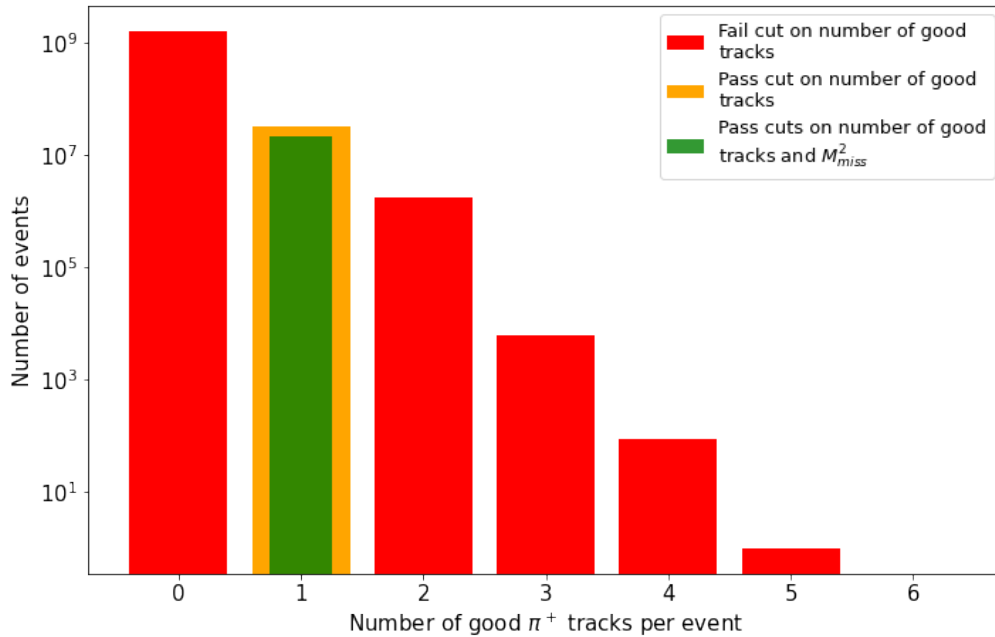
Figure 5.30: Total number of good π^+ tracks per event in the data sample. The orange bar represents the number of events passing the cut; the green bar represents the number of events passing the cut as well as passing the M_{miss}^2 cut. Note that the bar area has no meaning.

identified as good tracks (as opposed to only, for example, the π^+ and e^-). The figure shows that less than 2% of the three track vertices present after the common selection are selected as π_D^0 vertices.

Figure 5.32 shows the number of good π_D^0 vertices per event in the data sample. The signal selection requires exactly one good π_D^0 vertex (green bar). However the majority of events do not have a good π_D^0 vertex present.

5.7 Backgrounds

The M_{miss}^2 plots in Figures 5.18a and 5.18b show that neither the normalisation or signal samples are completely background free, although the backgrounds are below the 10^{-3} level. However, due to the method used to measure $B(\pi_D^0)$ (see Section 5.2), the background cancels between data and MC and thus does not need to be subtracted. To show this is true, take the simple case of only one MC sample
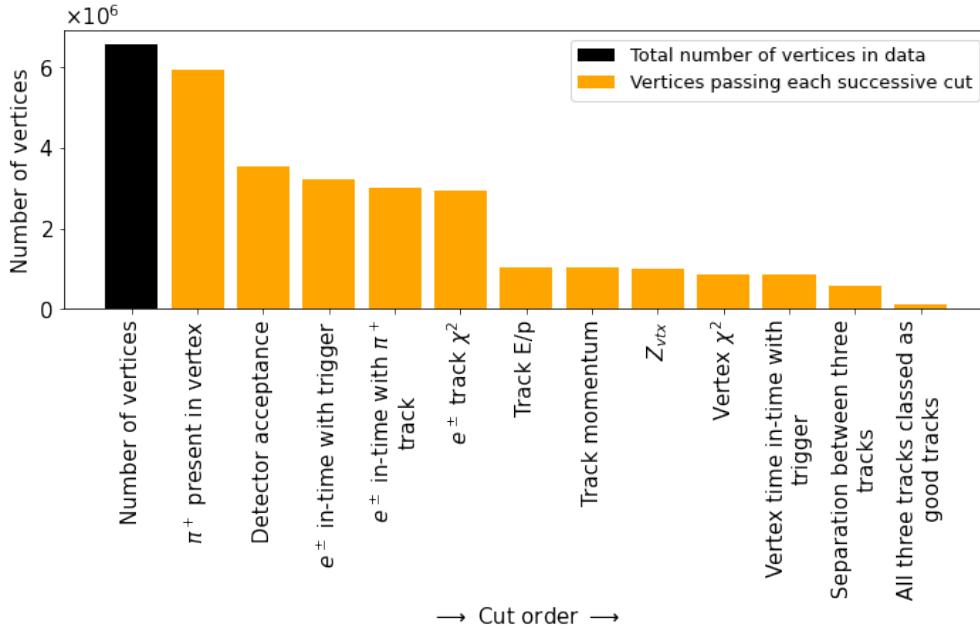
Figure 5.31: Number of vertices passing each successive cut in the signal selection, when searching for a good π_D^0 vertex, in the data sample. Also shown (black bar) is the total number of three track vertices present in the data sample. This is after the application of the common selection. The exact cuts are described in Subsection 5.4.3.
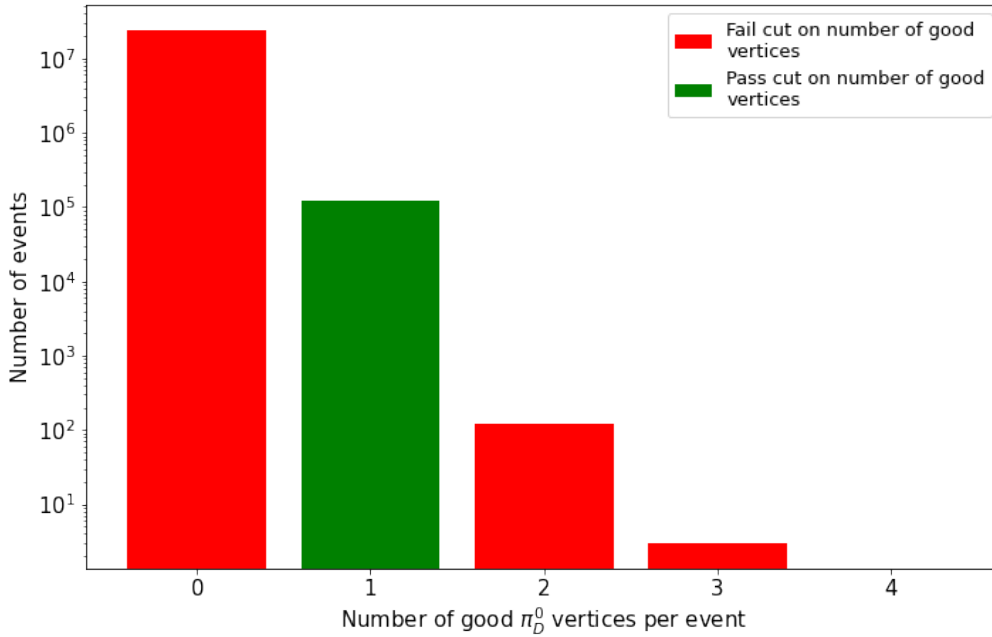
Figure 5.32: Total number of good π_D^0 vertices per event in the data sample. The green bar represents the number of events passing the cut.

which we can use to calculate the measured $B(\pi_{\mathrm{D}}^0)$ by comparing the measured values of ϵ in data and MC. If $N_{\mathrm{sig.}}^{\mathrm{MC}}$ and $N_{\mathrm{norm.}}^{\mathrm{MC}}$ are the true numbers of signal and normalisation events observed in the MC sample and $B_{\mathrm{sig.}}$ and $B_{\mathrm{norm.}}$ are the numbers of background events present in the signal and normalisation samples in MC, the expected value of ϵ in the MC is given by

$$\epsilon_{\mathrm{MC}} = \frac{N_{\mathrm{sig.}}^{\mathrm{MC}} + B_{\mathrm{sig.}}}{N_{\mathrm{norm.}}^{\mathrm{MC}} + B_{\mathrm{norm.}}}. \tag{5.7}$$

The backgrounds in data are in the same proportions as that in MC (shown to be the case by the very good data/MC agreement), meaning the measured value of ϵ in data can be expressed as a function of the background in MC,

$$\epsilon_{\mathrm{data}} = \frac{N_{\mathrm{sig.}}^{\mathrm{data}} + B_{\mathrm{sig.}}\left(\frac{N_{\mathrm{sig.}}^{\mathrm{data}}}{N_{\mathrm{sig.}}^{\mathrm{MC}}}\right)}{N_{\mathrm{norm.}}^{\mathrm{data}} + B_{\mathrm{norm.}}\left(\frac{N_{\mathrm{norm.}}^{\mathrm{data}}}{N_{\mathrm{norm.}}^{\mathrm{MC}}}\right)}, \tag{5.8}$$

where $N_{\mathrm{sig.}}^{\mathrm{data}}$ and $N_{\mathrm{norm.}}^{\mathrm{data}}$ are the true numbers of signal and normalisation events observed in the data sample. After rationalising this expression, one obtains,

$$\epsilon_{\mathrm{data}} = \frac{N_{\mathrm{sig.}}^{\mathrm{data}}(N_{\mathrm{sig.}}^{\mathrm{MC}} + B_{\mathrm{sig.}})/N_{\mathrm{sig.}}^{\mathrm{MC}}}{N_{\mathrm{norm.}}^{\mathrm{data}}(N_{\mathrm{norm.}}^{\mathrm{MC}} + B_{\mathrm{norm.}})/N_{\mathrm{norm.}}^{\mathrm{MC}}} = \frac{N_{\mathrm{sig.}}^{\mathrm{data}}}{N_{\mathrm{norm.}}^{\mathrm{data}}} \frac{N_{\mathrm{norm.}}^{\mathrm{MC}}}{N_{\mathrm{sig.}}^{\mathrm{MC}}} \epsilon_{\mathrm{MC}}, \tag{5.9}$$

where ϵ_{MC} arises after use of Equation 5.7. This is the same expression one obtains with zero background, showing no subtraction is necessary.

For completeness, Table 5.4 shows the number of each decay mode present in the final normalisation and signal samples (before normalising to data) in each of the two MC samples. The difference between the two MC samples can be explained by the factor 1.7 increase in the simulated $B(\pi_{\mathrm{D}}^0)$ (which results in a decrease of $B(\pi_{\gamma\gamma}^0)$ by a factor 1.008) and the factor 7.7 increase in the size of the mixed sample relative to the mixed-002 sample. For decays that include a π^0, the K^+ decay modes are split based on whether the π^0 undergoes a $\pi_{\gamma\gamma}^0$ or π_{D}^0 decay. The mechanisms by which all these backgrounds enter the final samples are explained in the remainder

Table 5.4: Breakdown of the number of events passing the normalisation and signal selections per decay mode in the two MC samples which use different $B(\pi_D^0)$ values. The π^0 decay modes are also shown. The total number of events passing each selection is shown at the bottom of the table. Non-integer values are given due to the beam momentum MC weighting procedure used, as described in Subsection 5.4.5.

Decay mode	Mixed Normalisation	Signal	Mixed-002 Normalisation	Signal
$K_{2\pi}$; $\pi_{\gamma\gamma}^0$	35148084.0	25.5	4509207.5	1.4
$K_{2\pi}$; π_D^0	411134.0	7648.9	91113.0	1694.3
$K_{3\pi}$	475.5	0.0	68.1	0.0
$K_{3\pi^0}$; $\pi_{\gamma\gamma}^0$, $\pi_{\gamma\gamma}^0$	77.0	0.0	12.2	0.0
$K_{3\pi^0}$; $\pi_{\gamma\gamma}^0$, π_D^0	6.1	0.0	6.4	0.0
$K_{3\pi^0}$; π_D^0, π_D^0	0.0	0.0	0.0	0.0
$K_{\mu2}$	4330.1	0.0	550.1	0.0
$K_{\mu3}$; $\pi_{\gamma\gamma}^0$	3957.0	0.0	449.6	0.0
$K_{\mu3}$; π_D^0	79.7	0.0	4.5	0.0
K_{e3}; $\pi_{\gamma\gamma}^0$	28056.8	0.0	3596.8	0.0
K_{e3}; π_D^0	390.8	2.7	84.0	0.0
$\pi_{\mu2}$	92.6	0.0	13.0	0.0
Unknown	1508.4	0.0	179.3	0.0
Total	**35,598,192.0**	**7,677.1**	**4,605,284.5**	**1,695.7**

of this section.

Backgrounds in the normalisation sample

$\boldsymbol{K^+ \to \pi^0 e^+ \nu}$ (K_{e3}). Decays of this type enter the signal selection via $e^+ \to \pi^+$ mis-identification. If the ν is low energy (in the lab frame), the e^+ can have momentum such that the M_{miss}^2 lies within the signal region. This is the most common decay within the normalisation sample that does not originate from a $K_{2\pi}$ decay. The mis-identification procedure used in the π_D^0 analysis is described in detail in Subsection 5.4.4.

$\boldsymbol{K^+ \to \mu^+ \nu}$ ($K_{\mu2}$). Similar to the normalisation channel, this is also a single

track decay. It enters as a background via $\mu^+ \to \pi^+$ mis-identification as a result of inefficiencies in the MUV3. These processes are discussed in detail in Subsection 5.5.1. The majority of $K_{\mu 2}$ events are removed by the MUV3 veto as well as the M_{miss}^2 cut due to the different pion and muon masses.

$\boldsymbol{K^+ \to \pi^0 \mu^+ \nu}$ ($K_{\mu 3}$). This background has a similar mechanism to that of the $K_{\mu 2}$ background, albeit with a different M_{miss}^2 distribution due to the presence of the π^0.

$\boldsymbol{K^+ \to \pi^+ \pi^+ \pi^-}$ ($K_{3\pi}$). This is a three track decay with three pions in the final state meaning the probability of this decay passing the selection is low and the majority of events are removed by the requirement for a single good π^+ track and the M_{miss}^2 cut. $K_{3\pi}$ decays can enter the final sample if one of the π^+ tracks is not considered a good pion. If the π^+ that is selected has momentum such that the event lies in the tail of the $K_{3\pi}$ M_{miss}^2 distribution (see Figure 5.18a) then it can enter the final sample.

$\boldsymbol{K^+ \to \pi^+ \pi^0 \pi^0}$ ($K_{3\pi^0}$). This decay becomes a background if the π^0 daughters (either $\pi_{\gamma\gamma}^0$ with γ conversion or through π_D^0 decays) are not reconstructed as good π^+ candidates. As with the $K_{3\pi}$ background, if the momentum of the π^+ is such that the event lies in the tail of the M_{miss}^2 distribution, it can enter the signal region.

$\boldsymbol{\pi^+ \to \mu^+ \nu}$ ($\pi_{\mu 2}$). Beam pions, if in-time with a beam kaon when propagating through the KTAG, cannot be distinguished from beam kaons. Similarly to the $K_{\mu 2}$ background, if the muon is not vetoed by the MUV3 leading to it being mis-identified as a π^+, $\pi_{\mu 2}$ decays enter the M_{miss}^2 signal region if the μ momentum allows it. However, due to the probability of an in-time pion combined with the probability of the MUV3 being inefficient and the M_{miss}^2 cut, this background is highly suppressed. It should also be noted that the branching ratio of the $\pi_{\mu 2}$ is 99.99%. The next most common decay channel is the $\pi^+ \to e^+ \nu$ which, due to its rarity and the analysis selection conditions, does not enter as a background.

Unknown. As mentioned in Sections 2.4 and 5.4, due to the MC sample used

in the analysis and the fact that the matching of reconstructed particles to true particles fails in $\mathcal{O}(0.1\%)$ of cases, some events are labelled as "unknown" in the M_{miss}^2 plots. These events may be background but are more likely to be signal events, as can be seen from the peak in the "unknown" distribution in Figure 5.18a. Very few "unknown" events pass the common selection due to the high efficiency with which reconstructed tracks are matched to true MC particles.

Backgrounds in the signal sample

Due to the lack of statistics in MC, a complete understanding of which backgrounds are present is difficult. However, the two present in Figure 5.18b are discussed here.

$\boldsymbol{K^+ \to \pi^+\pi^0;\ \pi^0 \to \gamma\gamma}$ ($K_{2\pi_{\gamma\gamma}^0}$). This arises via two mechanisms. The first is double photon conversion, whereby both photons (produced by the $\pi_{\gamma\gamma}^0$ decay) undergo conversion in the first STRAW chamber, producing two e^+e^- pairs. The π^+ from the $K_{2\pi}$ decay forms the π^+ candidate whilst one lepton from each e^+e^- conversion pair form the e^+ and e^- candidates, making the event look like a Dalitz event. The photons undergoing conversion are high energy meaning the e^+ and e^- tracks point back to the $K_{2\pi}$ vertex. This background cannot be removed by the cut on the separation between the e^+ and e^- tracks at the first STRAW chamber, introduced to reduce the background when only one photon undergoes conversion.

The second mechanism is a $K_{2\pi}$ decay occurring at almost the same point in space and time as another decay that contains an e^+e^- pair in the final state (meaning the two decays cannot be distinguished and are merged). For example, the second decay could be a K_{e3D} (K_{e3} followed by a π_{D}^0 decay).

Of the 24 (non-weighted) $K_{2\pi_{\gamma\gamma}^0}$ events that pass the signal selection in the mixed MC sample, 15 are from double photon conversion and 9 are from merged decays.

$\boldsymbol{K^+ \to \pi^0 e^+\nu;\ \pi^0 \to e^+e^-\gamma}$ (K_{e3D}). This arises via $e^+ \to \pi^+$ mis-identification. The e^+e^- pair from the π_{D}^0 decay forms a vertex with the mis-identified e^+ from the K_{e3} decay. The mis-identification procedure used in the analysis is discussed in

detail in Subsection 5.4.4.

5.8   Trigger efficiency

Despite using the minimum-bias CTRL trigger for both the signal and normalisation channels, the trigger efficiency does not cancel exactly in the ratio due to the different numbers of tracks in the two final states. As described in Section 5.3, the minimum-bias (CTRL) trigger requires the coincidence of two hits in a NA48-CHOD quadrant (one hit from each plane). It is hence expected that the three track trigger efficiency will be higher than the single track efficiency. There are two ways to account for the trigger efficiency, either using an emulator or by measuring it directly. An emulator is available within NA62 but is known to have issues so it was decided to proceed with a direct measurement. Trigger emulators are further discussed in Section 5.12.

To measure the single track (normalisation) and three track (signal) CTRL trigger efficiencies, the same trigger can be used. At L0 (hardware), this trigger (hereinafter referred to as Mask0) requires:

- a signal in the RICH to tag a charged particle (the RICH signal also defines the trigger time);

- a signal in the CHOD within 6.3 ns of the RICH time;

- no signal in the MUV3 within 6.3 ns of the RICH time.

Additionally, two L1 (software) requirements are present:

- a signal in the KTAG within 5 ns of the RICH time;

- one track present in the STRAW.

The NA48-CHOD is not used in the Mask0 trigger, allowing the latter to be used for the CTRL trigger efficiency measurements.

The efficiency for each channel was measured for Mask0 triggered data events that passed the selections described in Section 5.4. Both the three track and single
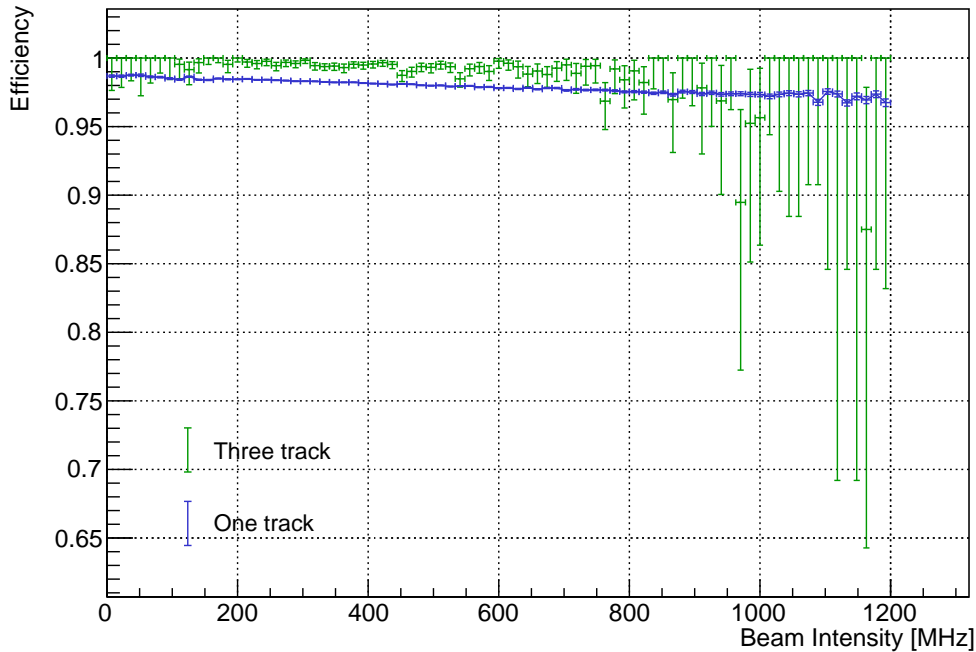
Figure 5.33: The three track and single track CTRL trigger efficiencies as a function of the instantaneous intensity. Both efficiencies were measured using Mask0 triggered data.

track CTRL trigger efficiencies are shown as a function of the beam instantaneous intensity (measured by the GTK) in Figure 5.33. The total efficiencies are shown in Table 5.5. As expected, the three track efficiency is close to 100% with the one track efficiency being slightly lower.

The ratio between the two efficiencies,

$$\frac{\eta_{1T}}{\eta_{3T}} = 0.9868, \tag{5.10}$$

is used to correct ϵ_{data} in the $B(\pi_D^0)$ calculation. This is further discussed in Section 5.9 and the uncertainty on this correction, treated as a systematic error on the measured $B(\pi_D^0)$, is described in Subsection 5.10.5.

Table 5.5: Measured CTRL trigger efficiencies.

	Measured efficiency (%)
Single track (η_{1T})	98.099 ± 0.004
Three track (η_{3T})	99.412 ± 0.042

5.9 Calculation results

The method used to calculate $B(\pi_D^0)$ is described in Section 5.2. However, before presenting the results, one aspect of the procedure should be addressed. There are two phenomena that break the assumption that the relationship between ϵ_{MC} and $B(\pi_D^0)_{MC}$ is linear. The first is events where a pileup π_D^0 event is present alongside another π_D^0 event. The second is kaon decays that contain more than one π_D^0 decay in the final state. The only decay with multiple neutral pions relevant to this measurement is the $K^+ \to \pi^+\pi^0\pi^0$ ($K_{3\pi^0}$) decay which has a branching ratio $(1.760 \pm 0.023)\%$. All other K^+ decays with two neutral pions in the final state have branching ratios $\lesssim 10^{-5}$ meaning they are highly suppressed. In both the pileup and double π_D^0 decay cases, there are two π_D^0 present meaning any increase by a factor C in $B(\pi_D^0)$ will result in an increase in the frequency with which these events appear by C^2. However, in reality, the M_{miss}^2 cut in the signal selection removes the majority of $K_{3\pi^0}$ events where both π^0 undergo a Dalitz decay ($K_{3\pi_{2D}^0}$), resulting in an acceptance of 2.0×10^{-7} (measured on non-overlaid $K_{3\pi_{2D}^0}$ MC). Furthermore, none of these events pass the signal selection in the mixed MC used in this analysis or the mixed MC with $B(\pi_D^0) = 0.02$ (due to a combination of suppression by both the branching ratio and acceptance). With regard to the pileup effects, the probability of a π_D^0 decay, originating from an overlaid event, passing the selection when the original event also contained a π_D^0 decay is 3×10^{-4} (measured on overlaid $K_{2\pi_D^0}$ MC) and hence also highly suppressed. Therefore, in practice, these phenomena do not affect the assumption that the relationship between ϵ_{MC} and $B(\pi_D^0)^{MC}$ is linear.

As previously mentioned, the measured ϵ must be corrected for the different

Table 5.6: Parameters required to calculate the measured value of ϵ in data. The value of ϵ_{data} is also shown.

Parameter	Value
N_{π^0}	21,305,632
$N_{\pi_{\text{D}}^0}$	112,711
D	25
η_{1T}/η_{3T}	0.9868
ϵ_{data}	$(2.088 \pm 0.006) \times 10^{-4}$

trigger downscalings and efficiencies between the signal and normalisation channels. The additional downscaling factor (D) of 25, present in the CTRL filter (used for the normalisation channel), must be accounted for when calculating the measured ϵ by multiplying N_{π^0} by 25. Including these corrections, the measured value of ϵ can be calculated using,

$$\epsilon_{\text{data}} = \frac{N_{\pi_{\text{D}}^0}}{N_{\pi^0}} \frac{1}{D} \frac{\eta_{1T}}{\eta_{3T}}, \tag{5.11}$$

where η_{1T} and η_{3T} are the measured trigger efficiencies (see Section 5.8). Table 5.6 shows the results observed in the data sample. The numbers of events observed in the data sample, after application of the respective selections, the values of D and η_{1T}/η_{3T} as well as the final value of ϵ_{data} are all shown. The uncertainty on ϵ_{data} is statistical, emanating from the size of the data sample[14].

Table 5.7 shows the numbers of normalisation and signal events and the corresponding value for ϵ_{MC} observed in each of the two MC samples:

$$\epsilon_{\text{MC}} = \frac{N_{\pi_{\text{D}}^0}^{\text{MC}}}{N_{\pi^0}^{\text{MC}}} \tag{5.12}$$

The numbers of events observed in the two MC samples are consistent with each other when the different sample sizes and $B(\pi_{\text{D}}^0)$ used are accounted for. As expected, due to the respective MC sample sizes, the error on ϵ_{MC} is a factor 3.6

---

[14]The trigger efficiency uncertainty is not included here as it is treated as a systematic error. This is discussed in Section 5.10.

Table 5.7: Numbers of normalisation and signal events and the value of ϵ_{MC} observed in the two MC samples. The numbers observed in MC are weighted, as described in Section 5.4.5, and in the mixed sample case, are equivalent to those shown in the "Total" row of Table 5.4.

MC sample	Sample size	$N_{\pi^0}^{\mathrm{MC}}$	$N_{\pi_D^0}^{\mathrm{MC}}$	ϵ_{MC}
Mixed	7.7×10^8	35,598,192.0	7,677.1	$(2.156 \pm 0.025) \times 10^{-4}$
Mixed-002	1.0×10^8	4,605,284.5	1,695.7	$(3.682 \pm 0.089) \times 10^{-4}$

Table 5.8: Parameters used for and produced by the linear fit. The correlation between the gradient and intercept is also shown.

Parameter	Value
Gradient α	$(1.847 \pm 0.112) \times 10^{-2}$
Intercept β	$(-0.117 \pm 1.403) \times 10^{-5}$
Fit correlation	-0.986

smaller for the mixed MC sample than the mixed-002 MC sample. This is consistent with the sample sizes and the increased number of π_D^0 events observed in the mixed-002 sample as a result of the increased $B(\pi_D^0)$.

Using the ϵ_{MC} values in Table 5.7 and the method described in Section 5.2, a linear fit was performed[15][16],

$$\epsilon_{\mathrm{MC}} = \alpha \cdot B(\pi_D^0)_{\mathrm{MC}} + \beta, \tag{5.13}$$

and the fit parameters, as well as the correlation between them, are shown in Table 5.8. The linear fit and the extrapolation of the measured ϵ to the measured $B(\pi_D^0)$ are shown in Figure 5.34.

The value of the intercept, β, is consistent with zero. In the absence of background (which is almost the situation here), this is expected because if $B(\pi_D^0)$ is reduced to zero, the number of π_D^0 events and hence ϵ_{MC} also reduces to zero[17]. In

---

[15]The linear fit performed is a χ^2 fit using the TMinuit package from the ROOT Data Analysis Framework [88].

[16]This is the same as Equation 5.2 but is repeated for clarity.

[17]This would not be the case if the "simple" one-track selection described in Subsection 5.4.1 was used due to the large background from conversions.
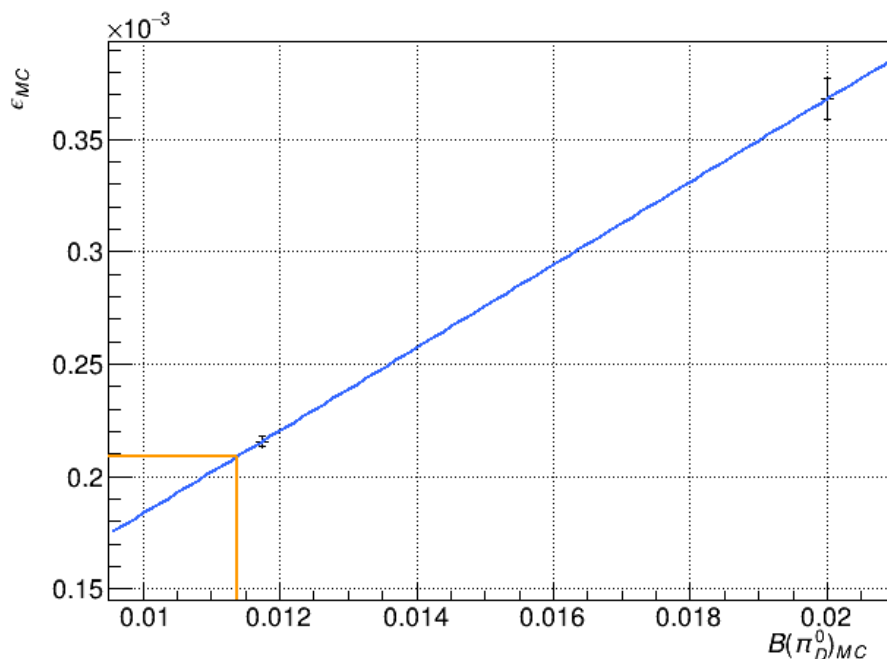
Figure 5.34: Values of ϵ_{MC} for each MC sample, as a function of the $B(\pi_D^0)_{\text{MC}}$ used. A linear fit is performed (blue line) and used to calculate the measured $B(\pi_D^0)$ using the measured value of ϵ (orange lines). The statistical errors are too small to be shown on this scale.

addition, the gradient, α, represents a factor that accounts for the signal acceptance with respect to the π^0 acceptance (this is separate from the $B(\pi_D^0)$). The signal selection thus collects 1.8% of π_D^0 events that were present after the common selection. This can be seen in the cut-flow plot shown in Figure 5.31; less than 2% of the vertices present after the common selection is applied are selected as π_D^0 vertices by the signal selection.

Using the method described in Section 5.2, the measured value of ϵ, combined with the linear fit produced using MC, results in a $B(\pi_D^0)$ measurement and statistical uncertainty equal to

$$B(\pi_D^0) = (1.137 \pm 0.003_{\text{stat}}) \times 10^{-2}. \tag{5.14}$$

The statistical uncertainty is calculated from the statistical uncertainty on ϵ_{data} and corresponds to a relative uncertainty of 0.30%.

5.10   Systematic uncertainties

This section details the dominant systematic uncertainties associated with the $B(\pi_{\mathrm{D}}^0)$ measurement.

5.10.1   MC statistical error

The errors on the linear fit parameters (α and β), obtained during the fit of ϵ_{MC} vs. $B(\pi_{\mathrm{D}}^0)_{\mathrm{MC}}$, depend on the size of the MC samples used. In other words, the statistical uncertainty arising from the size of the MC samples results in a systematic uncertainty on $B(\pi_{\mathrm{D}}^0)$. As described in Subsection 5.5.4, the statistical uncertainty arising from the size of the mixed sample (as opposed to that on the mixed-002 sample) dominates the error on $B(\pi_{\mathrm{D}}^0)$. The systematic error on $B(\pi_{\mathrm{D}}^0)$, associated with the errors on the fit parameters (see Table 5.8), is obtained via standard error propagation, accounting correctly for the -98.6% correlation between α and β. With sizes 770M and 100M events for the PDG $B(\pi_{\mathrm{D}}^0)$ and $B\left(\pi_{\mathrm{D}}^0\right) = 0.02$ mixed MC samples respectively, the systematic error on the measured $B(\pi_{\mathrm{D}}^0)$ as a result of the MC sample statistical uncertainty is

$$\delta B(\pi_{\mathrm{D}}^0)\big|_{\mathrm{MC\ stat.}} = 1.45 \times 10^{-4}, \tag{5.15}$$

corresponding to a relative uncertainty of 1.3%.

5.10.2   STRAW track reconstruction efficiency

This analysis is unusual in that the signal and normalisation channels have different numbers of charged tracks in the final state. This means that the STRAW track reconstruction efficiency will be different in each case and thus won't cancel between the signal and normalisation channels.

The true three-track reconstruction efficiency is the probability of reconstructing all three tracks in the vertex given that all three tracks pass through the STRAW

active region. This is impossible to measure on data so a probe-based tool has been developed within NA62 for systematic estimates associated with the track reconstruction efficiency for three-track decays. This tool measures the probability of reconstructing a third vertex track given that all three tracks pass through the STRAW active region and two tracks have already been reconstructed. This is not the same as the true three-track reconstruction efficiency. However, the probability of reconstructing a STRAW track for a particle that passes through the STRAW active region is approximately 0.95. Hence, the probability of reconstructing at least two of the three tracks in a three-track vertex (where all three pass through the STRAW active region) is equal to 0.993. This is almost 1, meaning to first order, the efficiency measured by the probe-based tool and the true three-track reconstruction efficiency should be similar. Furthermore, the true reconstruction efficiency can be measured on MC and comparing efficiencies computed using the probe method and the true three-track efficiency gives agreement within 1%[18]. Note that, for the rest of this subsection, the efficiency measured by the probe tool will be referred to as the three-track reconstruction efficiency.

To conduct the efficiency measurement, $K_{3\pi}$ decays are selected from minimum-bias triggered data and from MC (the MC sample used was an overlaid mixed MC sample). Two-track vertices are built and a selection is applied:

- Vertex $\chi^2 < 20$. This is a measure of the quality of the vertex and is output by the least-squares fit in the reconstruction.

- Z-position of the vertex satisfies 110 m $< Z_{\mathrm{vtx}} < 180$ m.

- Total momentum of the vertex, $p_{\mathrm{vtx}} < 70$ GeV/c.

- $|t_{\mathrm{vtx}} - t_{\mathrm{trigger}}| < 6$ ns where the vertex time, t_{vtx}, is the average of the two-track times, given by the NA48-CHOD.

- Both tracks must pass through the active regions of the STRAW (all four

---

[18]This comparison was done as part of a $K^+ \to \pi^+ \mu^+ \mu^- (\gamma)$ measurement at NA62 [98].

chambers), LKr, NA48-CHOD, CHOD and MUV3 detectors. They must not pass through the LAV12 material.

- At least one good KTAG candidate within 6 ns of the vertex time and the trigger.

- The K^+ time (measured by the GTK) and the vertex time satisfy: $dT = |t_{\text{GTK}} - t_{\text{vtx}}| < 1.5$ ns. The distance between the extrapolated GTK track and the vertex in the $x - y$ plane < 15 mm. If more than one K^+ track is found, the one with smallest dT is chosen.

If at least one two-track vertex with the above properties is found in the event, a probe is built. This probe is a track with properties calculated based on the properties of the two tracks in the vertex (position, momentum and charge). It is checked that the probe has a mass within 10 MeV/c of the $\pi^{\pm}$ mass, passes through the active regions of the STRAW (all four chambers and at least two views in the first two chambers), LKr, NA48-CHOD, CHOD and MUV3 detectors and does not pass through the LAV12 material. A search is then conducted for a track in the event that matches the properties (position, momentum and charge) of the probe.

The three-track reconstruction efficiency is thus defined as the number of events with a compatible two-track vertex that have a compatible probe, relative to the total number of events with a compatible two-track vertex. The efficiency is calculated in bins of the probe momentum and the number of views that the third track (i.e. the one that was not in the two-track vertex) passes through in the first and second STRAW chambers. This is shown in Figure 5.35, with the efficiency being measured separately for positive and negatively charged probes. Plots for both data and MC are shown.

To evaluate the systematic uncertainty on $B(\pi_D^0)$ from the three-track reconstruction efficiency, a weight is applied to MC events based on the efficiencies shown

(a) Data, positive probe.

(b) Data, negative probe.

(c) MC, positive probe.

(d) MC, negative probe.
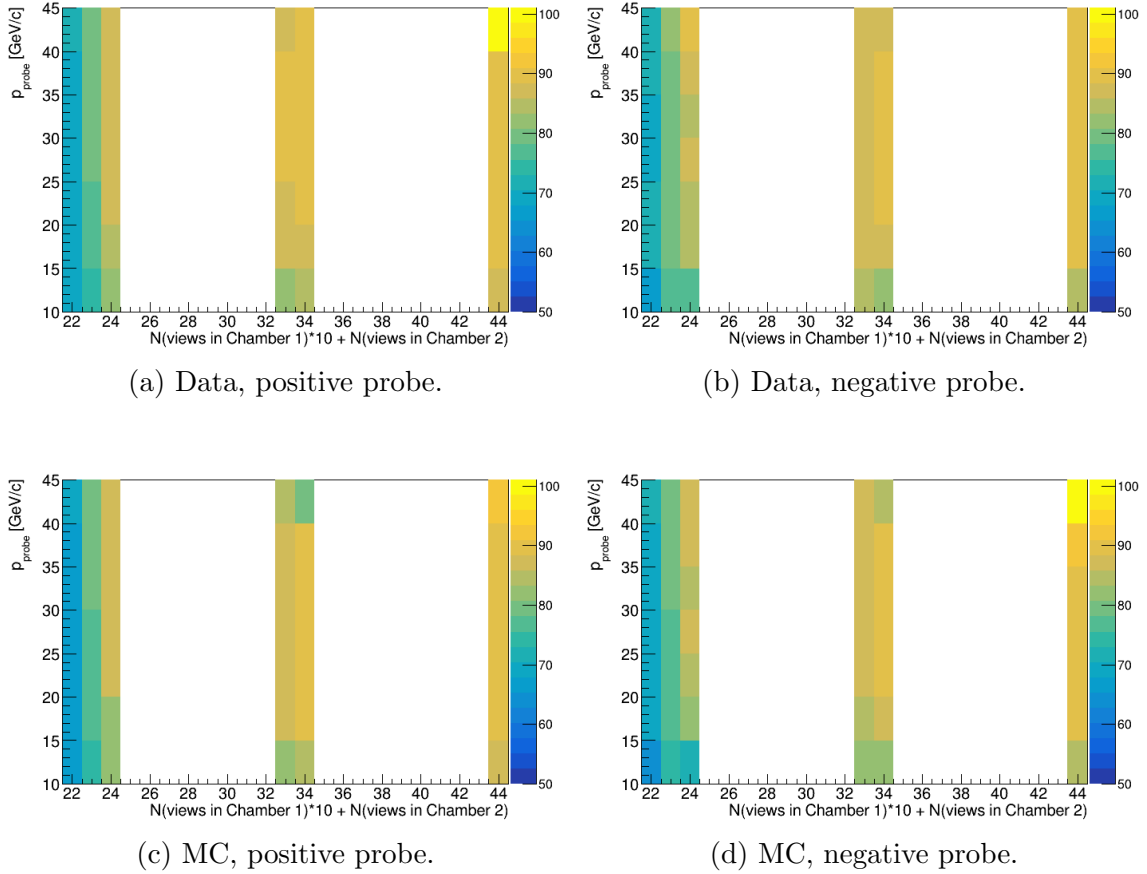
Figure 5.35: Track reconstruction efficiency as a function of the probe momentum and the number of STRAW views the third track travels through in the first and second chambers. First row: data. Second row: MC. First column: positive probes. Second column: negative probes. This is an NA62 internal figure, produced as part of a $K^+ \to \pi^+ \mu^+ \mu^- (\gamma)$ measurement at NA62 [98].

in Figure 5.35. This weight is equal to

$$w = \frac{\xi_{Data}(q, p_{\mathrm{probe}}, N(\mathrm{views}))}{\xi_{MC}(q, p_{\mathrm{probe}}, N(\mathrm{views}))} \tag{5.16}$$

where ξ_{Data} and ξ_{MC} are the three-track reconstruction efficiencies for data and MC respectively (i.e. those in Figure 5.35). These are both functions of the probe charge, q, probe momentum, p_{probe}, and an encoded value describing the number of STRAW views traversed by the probe, $N(\mathrm{views}) = 10N(\mathrm{views\ in\ Ch1}) + N(\mathrm{views\ in\ Ch2})$. The number of views traversed in STRAW chambers 1 and 2 and the track momentum are that of one of the three tracks (i.e. one of π^+, e^+ or e^- in the π_{D}^0 analysis), with the track chosen at random for each event.

The difference between the $B(\pi_{\mathrm{D}}^0)$ with and without these weights applied to the MC is taken as the systematic uncertainty on $B(\pi_{\mathrm{D}}^0)$ as a result of the three-track reconstruction efficiency. This uncertainty is equal to

$$\delta B(\pi_{\mathrm{D}}^0)\big|_{\mathrm{track\ reco.}} = 4.9 \times 10^{-5}. \tag{5.17}$$

5.10.3 Particle identification

Due to the design of the selections described in Section 5.4, the systematic errors associated with the π^+ identification and $e^+ \to \pi^+$ mis-identification cancel to first order in the ratio between signal and normalisation. However, the systematic errors that arise from the $e^\pm$ identification and $\pi^\pm \to e^\pm$ mis-identification, applied in the signal selection only, do not cancel. The $e^\pm$ identification is expected to produce the largest uncertainty because the only way $\pi^\pm \to e^\pm$ mis-identification can enter the signal sample is through $K_{3\pi}$ decays or a combination of two or more decays occurring at similar points in space and time. No $K_{3\pi}$ decays pass the signal selection due to the application of the M_{miss}^2 cut and the probability of two events combining to form a signal-like event that passes the selection, although difficult to calculate,

is expected to be rare. It is hence assumed that $e^\pm$ identification dominates the systematic uncertainty associated with the PID procedure and the uncertainty associated with the $\pi^\pm \to e^\pm$ mis-identification is expected to be negligible. The procedure used to conduct particle identification is discussed in Subsection 5.4.4.

Due to the dependence of the $e^\pm$ identification efficiency on the $e^\pm \to \pi^\pm$ mis-identification probability, as described in Subsection 5.4.4, the two cannot be decoupled when evaluating the systematic uncertainty. We hence have to evaluate the systematic uncertainty that arises from both procedures. To do this, a comparison between the $B(\pi_D^0)$ obtained using E/p from simulation and that obtained from fits to the probability/efficiency measured on MC can be performed. The latter is the same method as used in the actual PID procedure within the π_D^0 analysis except measured on MC rather than data. This hence evaluates the systematic uncertainty associated with the PID method used, rather than that associated with the probability measurements themselves which is assumed to be negligible in comparison. This assumption is valid as the uncertainty on the (mis-)identification probability measurements (see for example, Figure 5.5c) is ~ 0.001 which, as shown later in this section, is negligible.

Unlike in the data case discussed in Section 5.4.4, fits have not already been performed on the MC probability measurements. Fits to these MC measurements thus need to be conducted for both processes. The measurements[19] and fits are shown in Figure 5.36. As before, the probabilities are measured as a function of the reconstructed particle momentum. In the $e^\pm$ identification case, a 9th order polynomial was used to conduct the fit. In the $e^\pm \to \pi^\pm$ mis-identification case, a function given by

$$P_{\text{mis-ID}} = C_0 + \frac{C_1}{p} + \frac{C_2}{p^2} + \frac{C_3}{p^3} \tag{5.18}$$

was used, where p is the momentum of the particle and C_i are the fit parameters.

---

[19]The $e^\pm$ identification and $e^\pm \to \pi^\pm$ mis-identification MC measurements are part of the NA62 software framework. The fits however were conducted by the author.
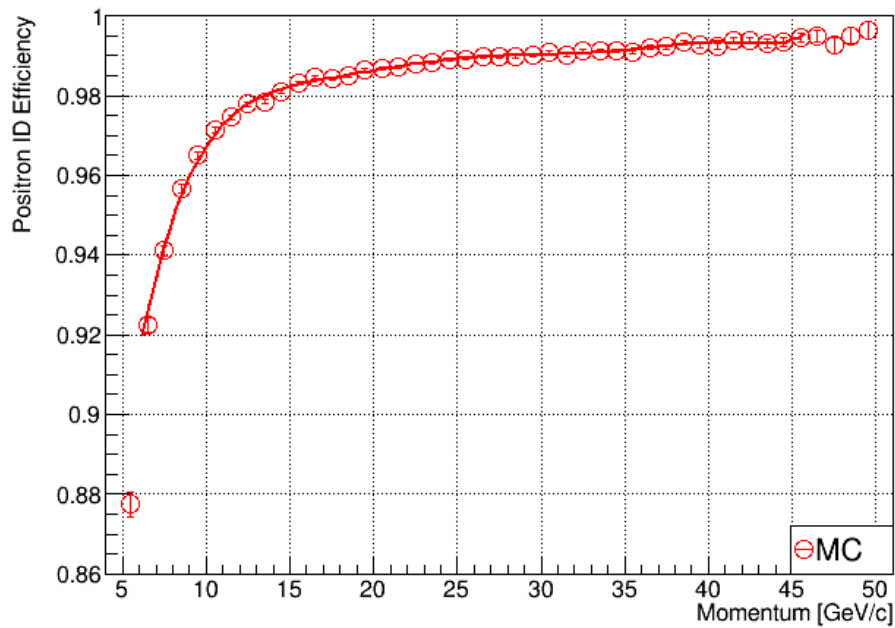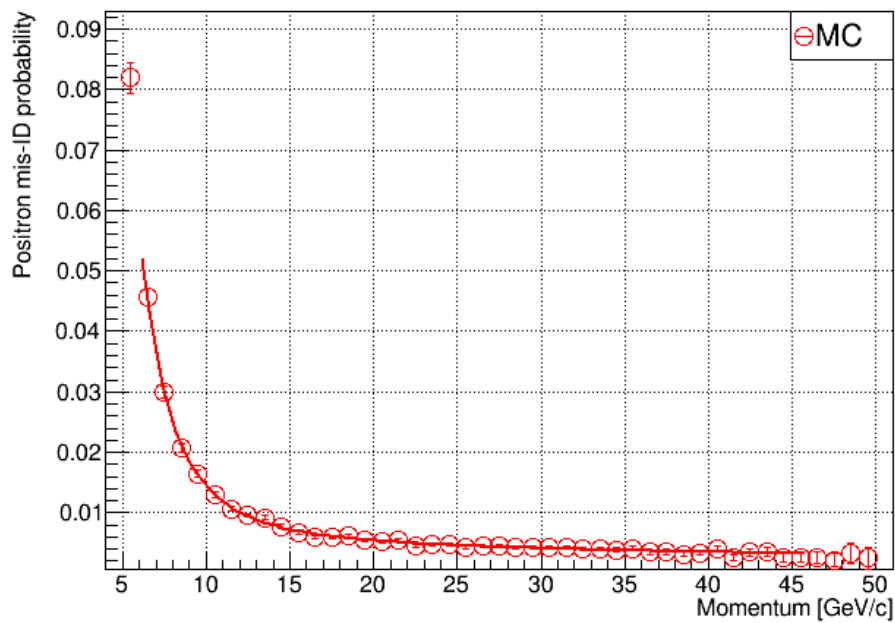
(a) $e^{\pm}$ identification efficiency

(b) $e^{\pm} \to \pi^{\pm}$ mis-identification probability

Figure 5.36: MC $e^{\pm}$ identification efficiency and $e^{\pm} \to \pi^{\pm}$ mis-identification probability measurements and the fits conducted. The fits are performed in the momentum range [6, 46] GeV/c.

An additional phenomenon that needs to be accounted for is the use of a random number generator (RNG) in the PID procedure[20]. We are comparing the $B(\pi_D^0)$ obtained using E/p from simulation and that from the fits to identification and mis-identification probabilities measured on MC in order to extract a systematic uncertainty estimate, and the latter uses a RNG when applying the PID procedure. A different RNG seed will hence result in a different systematic uncertainty estimate. To solve this, the $B(\pi_D^0)$ calculation obtained using the fits to the MC measurements was conducted 300 times and the mean $B(\pi_D^0)$ was used to calculate the systematic uncertainty. Only the deviation of the mean from the $B(\pi_D^0)$ calculated using E/p from simulation is important here; the variation about the mean is accounted for by the MC statistical uncertainty.

The distribution of $B(\pi_D^0)$, after repeating the procedure 300 times, each with a different RNG seed and using fits to the MC measurements for the PID, is shown in Figure 5.37. The mean and standard deviation are 1.095×10^{-2} and 0.256×10^{-2} respectively. The result obtained using E/p from simulation for the PID is $B(\pi_D^0 = (1.110 \pm 0.018) \times 10^{-2}$

The difference between the $B(\pi_D^0)$ obtained using E/p from simulation and the mean $B(\pi_D^0)$ from running the procedure 300 times using the identification and mis-identification probabilities measured on MC is taken as the systematic uncertainty on the measured $B(\pi_D^0)$ arising from the PID procedure:

$$\delta B(\pi_D^0)\big|_{\text{PID}} = 1.51 \times 10^{-4}. \tag{5.19}$$

This uncertainty is equivalent to a relative uncertainty of 1.3%.

---

[20]The CERN HTCondor batch system was used when running this analysis so the actual random number generator seed used was a function of the HTCondor job ID, meaning parallel jobs were not using the same random numbers but still produced reproducible results.
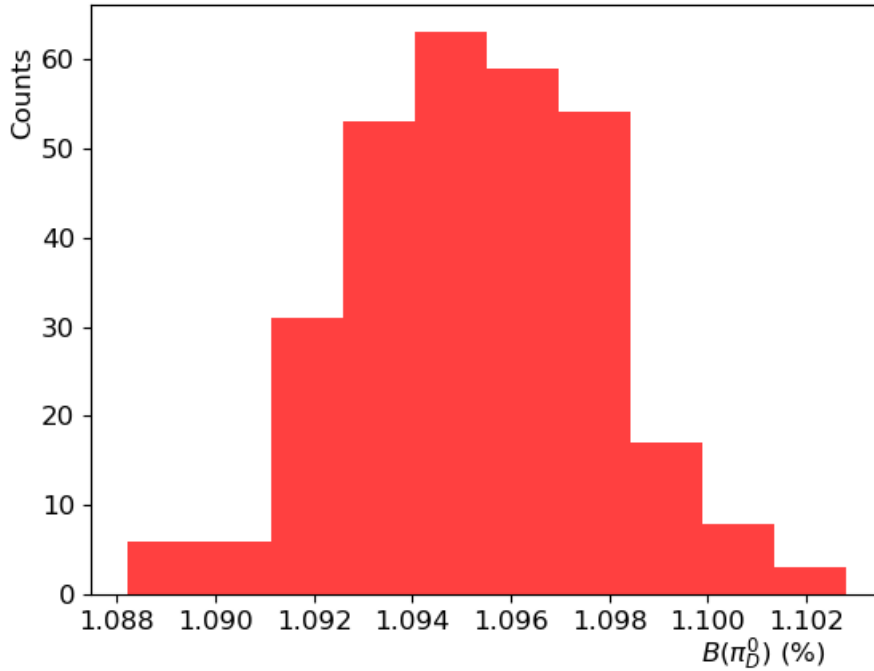
Figure 5.37: Distribution of $B(\pi_\mathrm{D}^0)$ when varying the seed used in the RNG. 300 iterations were used.

5.10.4 Beam momentum weighting uncertainty

The systematic uncertainty associated with the corrections made for the limited beam simulation via a weighting procedure, as described in Subsection 5.4.5, is not expected to be large due to the signal selection being a stricter version of the normalisation selection. It is evaluated by turning the weighting procedure off (or equivalently, setting all weights to 1). The difference between the measured $B(\pi_\mathrm{D}^0)$ with and without the weighting procedure is taken as a conservative systematic uncertainty, equal to

$$\delta B(\pi_\mathrm{D}^0)\big|_{\text{beam corr.}} = 3.5 \times 10^{-5}, \tag{5.20}$$

corresponding to a relative uncertainty of 0.31%.

5.10.5   Trigger efficiency

The one-track and three-track trigger efficiency measurements described in Section 5.8 each have a statistical uncertainty. These statistical uncertainties are treated as a systematic error on the $B(\pi_D^0)$ measurement. Due to the method by which the trigger efficiency measurements were conducted, the two measurements will be correlated. However, the uncertainty on the three-track efficiency is an order of magnitude larger than that on the one track efficiency. Furthermore, the three-track efficiency error is an order of magnitude smaller than the statistical error on $B(\pi_D^0)$ arising from data. It was thus decided that the uncertainty on the ratio between the three-track and one-track efficiencies (i.e. that used to correct the measured ϵ) would be taken as that on the three-track efficiency, neglecting the uncertainty on the one track efficiency and any correlation between the two measurements.

Taking the above into account, the correction made to ϵ_{data} to account for the trigger efficiency is

$$\frac{\eta_{1T}}{\eta_{3T}} = 0.9868 \pm 0.0004. \tag{5.21}$$

This results in a systematic error on $B(\pi_D^0)$, arising from the statistical error on the trigger efficiency, of

$$\delta B(\pi_D^0)\big|_{\text{trigger eff.}} = 4.7 \times 10^{-6}, \tag{5.22}$$

corresponding to a relative uncertainty of 0.04%.

This uncertainty does not account for the fact that a simulation of the trigger is not used within the analysis. This is discussed further in Subsection 5.12.

5.10.6   Stability with respect to selection cuts

To check the stability of the $B(\pi_D^0)$ result with respect to the cuts used in the signal selection, the cuts were independently varied. This allows for checks of potential issues or unaccounted for large systematics in the analysis. Figures 5.38 to 5.47 show the stability of the $B(\pi_D^0)$ result when varying cuts (within reasonable inter-

vals) applied in the signal selection. The default cut value is shown by the green dashed line. Each plot shows the full statistical uncertainty from data as well as the uncorrelated uncertainty, calculated via,

$$\sigma_{uncorr,i} \simeq \sqrt{|\sigma^2 - \sigma_i^2|}, \tag{5.23}$$

where σ is the statistical uncertainty from data from the $B(\pi_D^0)$ result presented in Subsection 5.9 and σ_i is the statistical uncertainty from data on the $B(\pi_D^0)$ result obtained after altering one of the selection cuts[21]. The MC statistical uncertainty is not shown but is equal to 0.0145% (absolute) and hence much larger than the error bars in each plot showing the data statistical uncertainty. Also shown is the number of events passing the signal selection (in data) as a function of the cut value used in each case. The cut on E/p is not varied due to the PID method used (see Subsection 5.4.4; the systematic uncertainty associated with this method was discussed in Subsection 5.10.3). The stability of the $B(\pi_D^0)$ result with respect to the cuts made in the common selection (i.e. that present in both the signal and normalisation selections) is expected to be stable due to cancellation in the signal/normalisation ratio and hence not shown here.

The $B(\pi_D^0)$ result is stable with respect to the signal selection cut variations in most cases (especially when the MC statistical uncertainty is also accounted for), with the exceptions being the cuts involving the CTRL trigger time and the minimum Z_{vtx}. These cases are discussed further below.

Figure 5.43, showing the stability of the $B(\pi_D^0)$ result with respect to the cut on the minimum Z_{vtx}, appears to be unstable as the cut is moved further into the decay volume. To test this further, the cut was varied to extremes, as shown in Figure 5.48. It can be seen that the $B(\pi_D^0)$ result varies by $\sim 3\%$ (absolute) as the

---

[21]This equation is derived in many high energy physics statistics textbooks/lecture series, for example Ref. [99]. Being an estimate, it does not always hold true exactly; this can be seen in the following plots where the uncorrelated uncertainty very occasionally decreases with respect to the default cut despite the correlation decreasing. The results are stable in all these cases however.
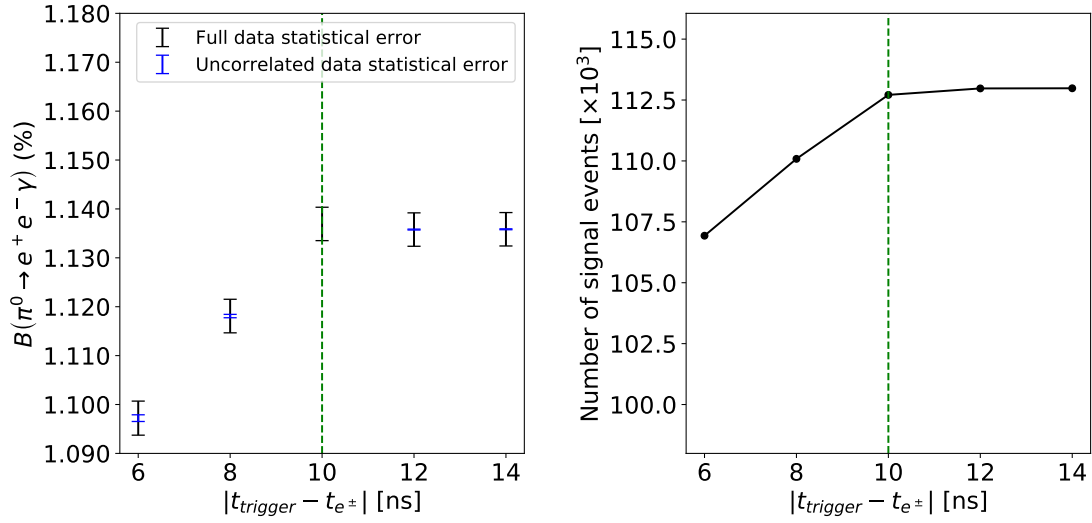
Figure 5.38: $B(\pi_D^0)$ result stability whilst varying the cut on $|t_{\text{trigger}} - t_{e^\pm}|$. The $e^\pm$ track time is given by the NA48-CHOD or CHOD time.
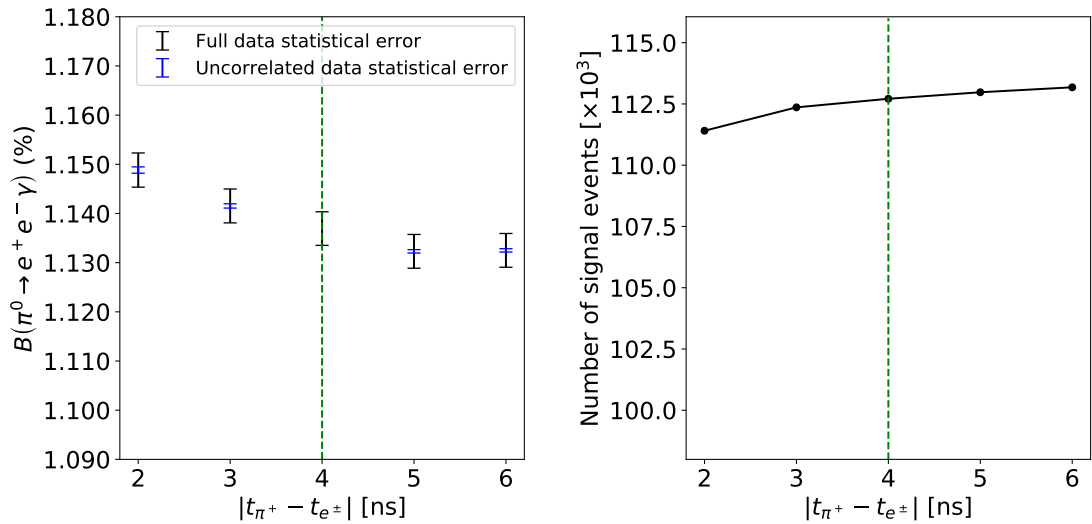
Figure 5.39: $B(\pi_D^0)$ result stability whilst varying the cut on $|t_{\pi^+} - t_{e^\pm}|$. Both track times are given by the NA48-CHOD or CHOD time.

Figure 5.40: $B(\pi^0_D)$ result stability whilst varying the cut on the $e^\pm$ track χ^2.
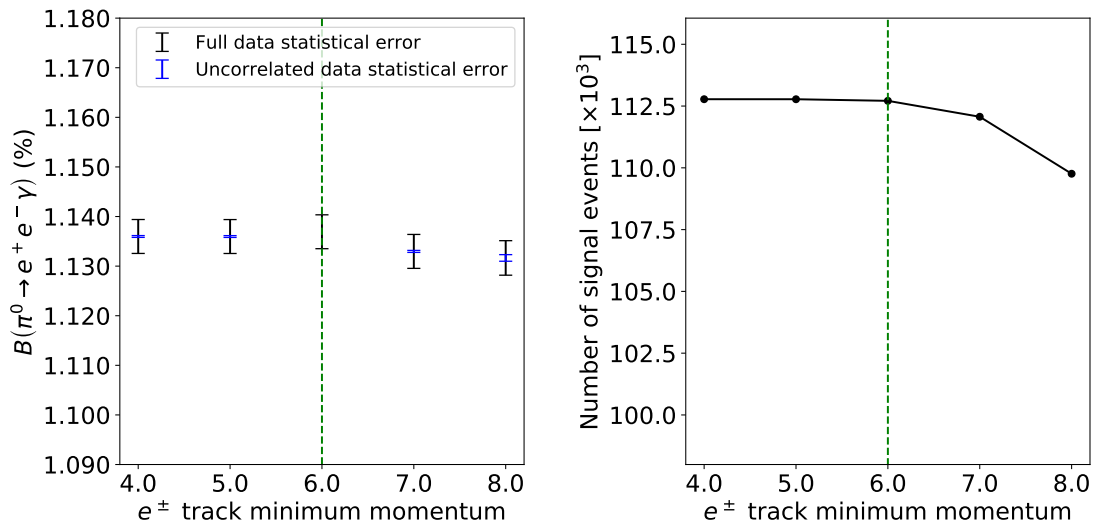
Figure 5.41: $B(\pi^0_D)$ result stability whilst varying the cut on the minimum $e^\pm$ track momentum.
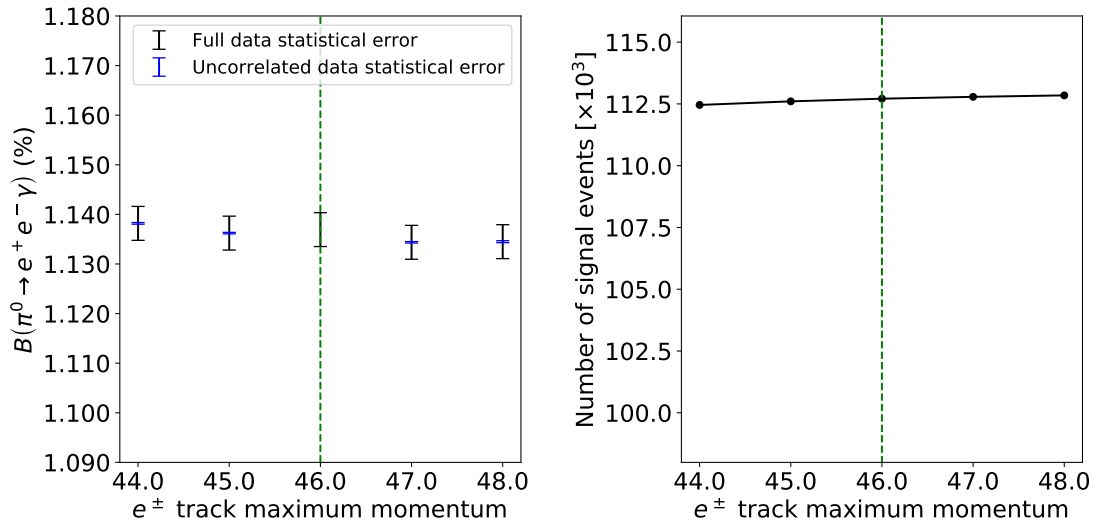
Figure 5.42: $B(\pi_D^0)$ result stability whilst varying the cut on the maximum $e^\pm$ track momentum.
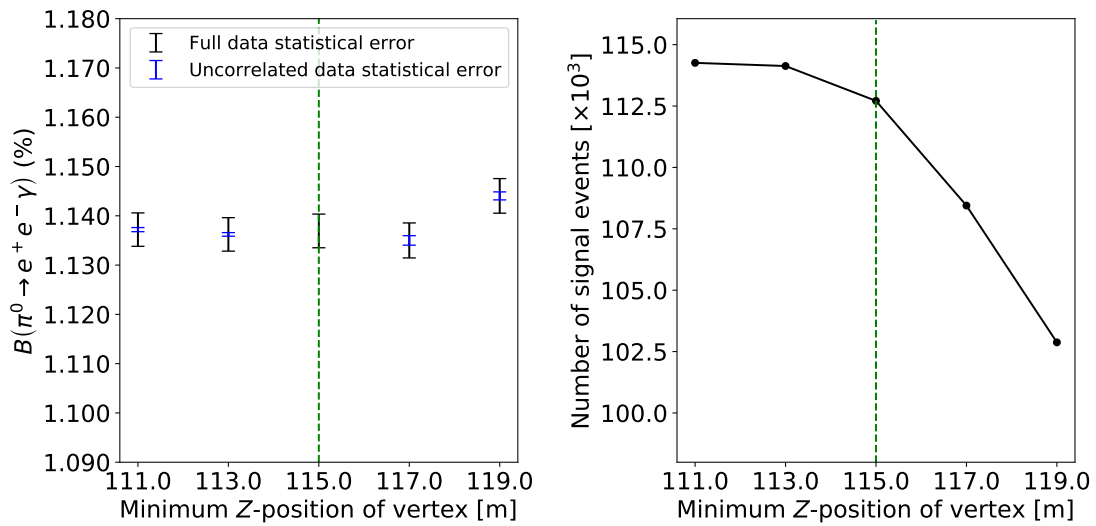
Figure 5.43: $B(\pi_D^0)$ result stability whilst varying the cut on the minimum Z_{vtx}.
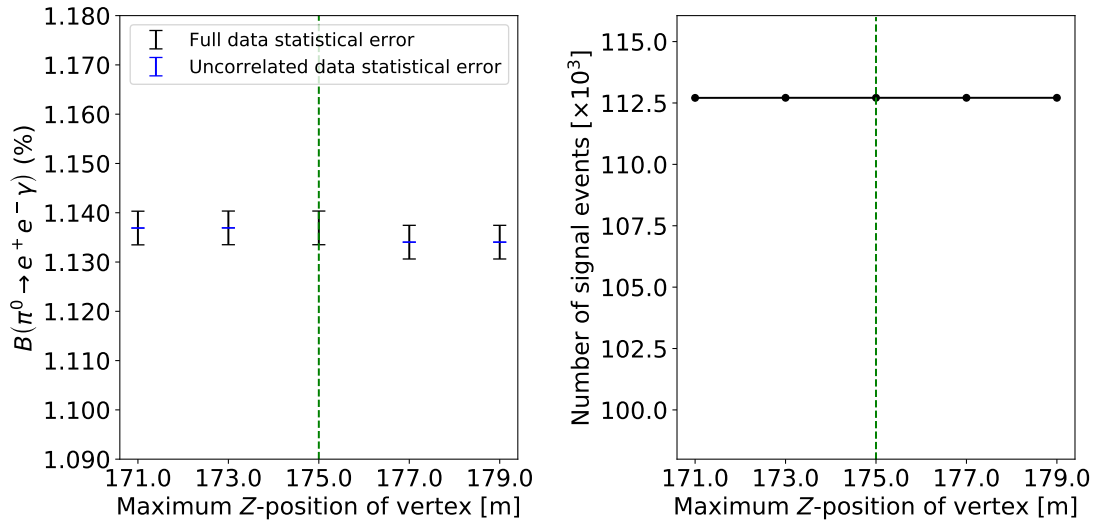
Figure 5.44: $B(\pi_D^0)$ result stability whilst varying the cut on the maximum Z_{vtx}.
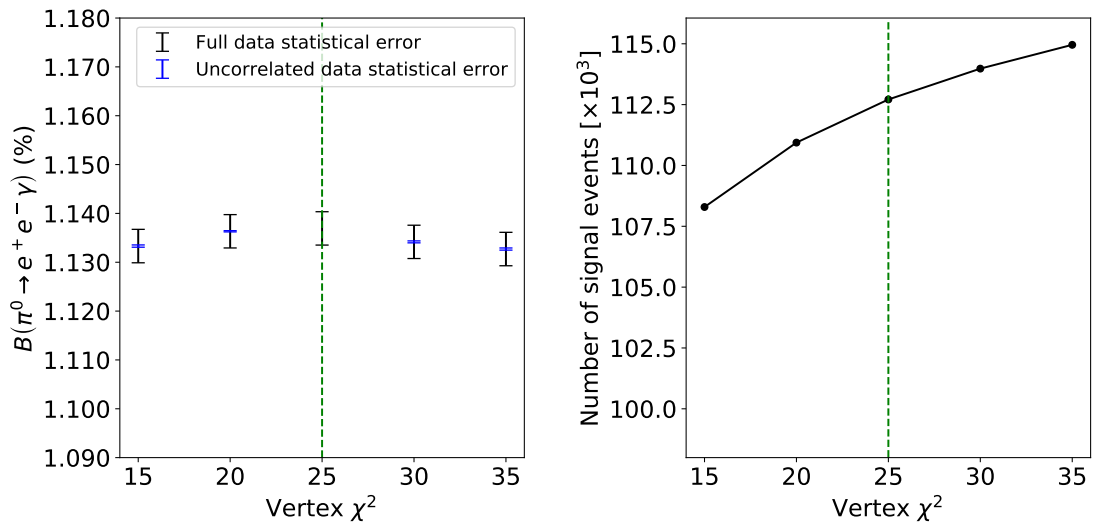
Figure 5.45: $B(\pi_D^0)$ result stability whilst varying the cut on the vertex χ^2.

175

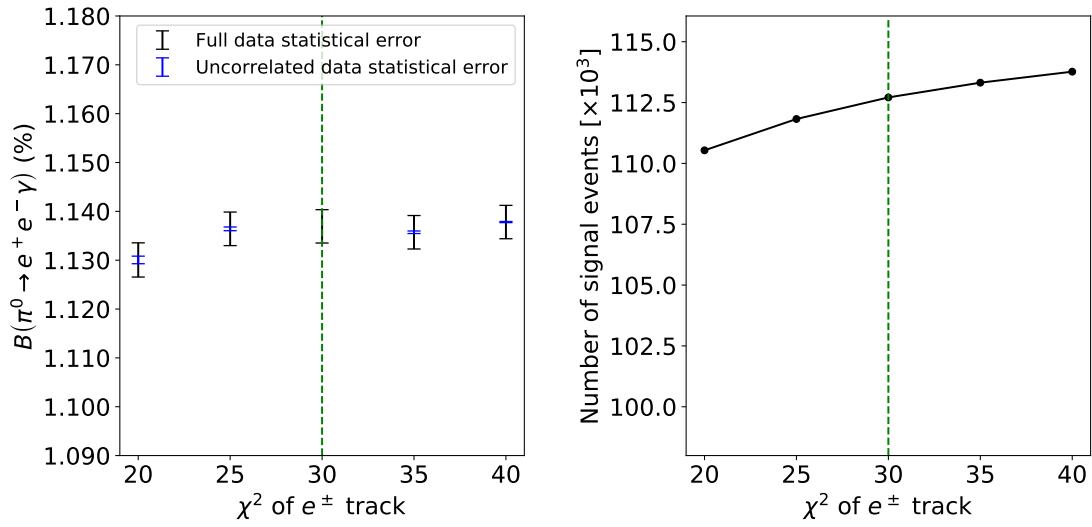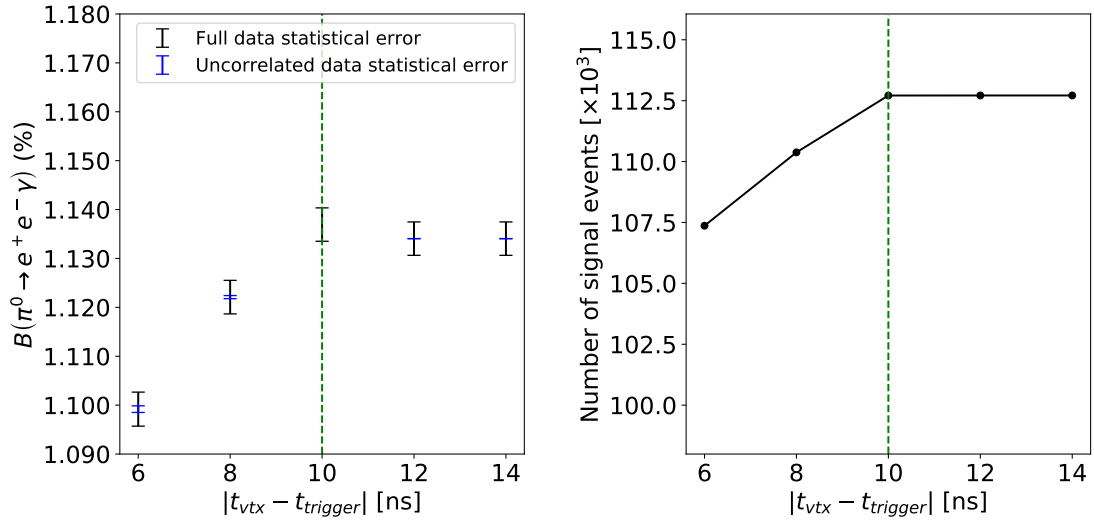Figure 5.46: $B(\pi_D^0)$ result stability whilst varying the cut on $|t_{\text{trigger}} - t_{\text{vtx}}|$.
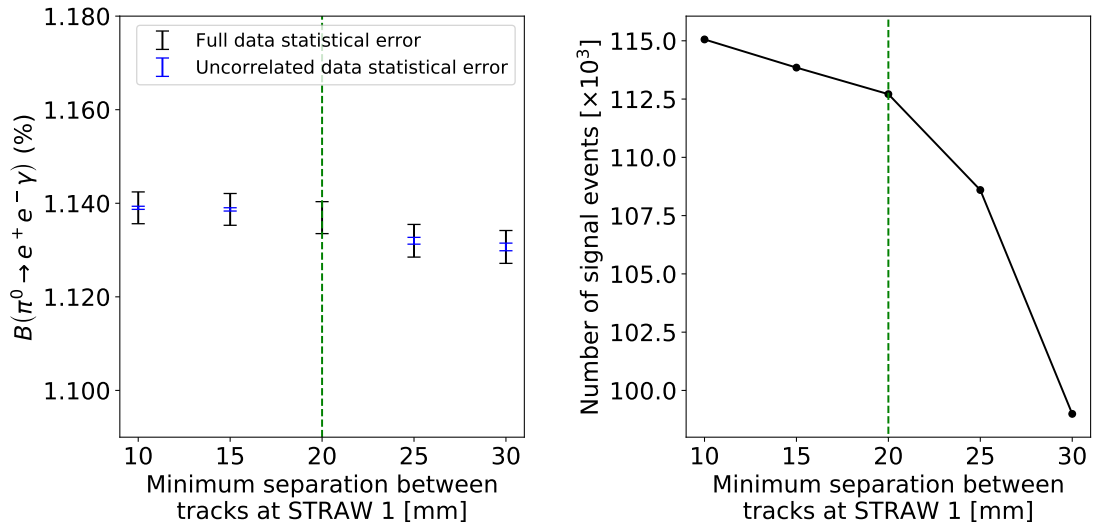
Figure 5.47: $B(\pi_D^0)$ result stability whilst varying the cut on the separation between the π^+, e^+ and e^- tracks at the first STRAW plane.
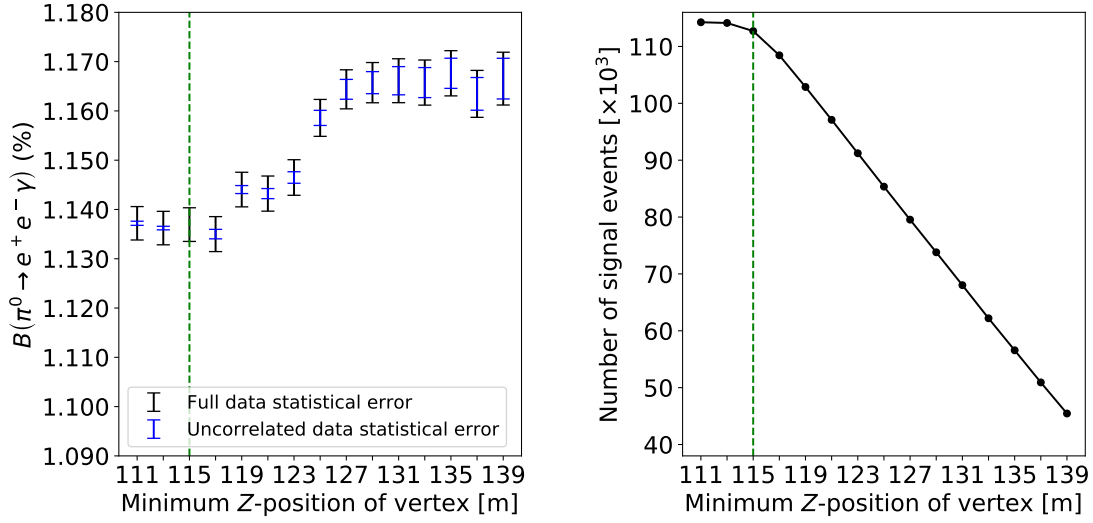
Figure 5.48: $B(\pi_D^0)$ result stability whilst varying the cut on the minimum Z_{vtx} to extremes.

cut on the minimum Z_{vtx} is increased but stable as the cut is decreased. The latter is due to the cut being correlated with the cut made on $Z_{vtx}^{\text{beam axis}}$ in the common selection, resulting in very little change in the number of events passing the signal selection as the Z_{vtx} cut is decreased.

As mentioned previously, the statistical error shown in Figure 5.48 is from data only and thus does not include the much larger systematic error arising from the limited MC statistics (Equation 5.15). Hence, the $\sim 3\%$ shift seen in the figure could be within the expected variation when the MC statistical uncertainty is included (see below). In addition, statistical variations in the region $115 \text{ m} \lesssim Z_{vtx} \lesssim 125 \text{ m}$, which is where the apparent instability lies, can be seen in the Z_{vtx} distribution and corresponding data/MC ratio plot shown in Figure 5.27. The limited sample size, causing local maxima and minima in the distribution, can be seen.

To test the hypothesis that the instability in Figure 5.48 is caused by statistical fluctuations, a χ^2 fit of the data/MC plot in Figure 5.27 was performed. The fit function used was a constant; the constant should be equal to 1 if perfect data/MC agreement is found. The fit was executed using two fit ranges, one that contained the low Z_{vtx} region and one that did not. These ranges, the resulting fit parameters

Table 5.9: Results from the two χ^2 fits to the Z_{vtx} data/MC distribution.

Fit range	Fit parameter	χ^2/ndf	p-value	Significance
[125 m, 160 m]	1.025 ± 0.015	0.74	0.870	0.16σ
[115 m, 160 m]	0.987 ± 0.013	1.55	0.011	2.54σ

as well as the χ^2 and p-values are shown in Table 5.9. The fit range that excluded the low Z_{vtx} region is consistent with the hypothesis that data agrees with MC within $< 1\sigma$, as one would expect. The fit range that included the low Z_{vtx} region (and thus contains the supposed statistical fluctuations), is consistent with the hypothesis that data agrees with MC within 2.54σ. Hence, the hypothesis that the variations seen in Figure 5.27, as well as the instability in Figure 5.48, are purely statistical should hence be rejected. This is discussed further when describing the next steps of the analysis in Section 5.12.

The other cuts causing instability of the $B(\pi_D^0)$ result are those involving the CTRL trigger time, as shown in Figures 5.38 and 5.46. In both of these plots, the $B(\pi_D^0)$ result appears to be stable as the cut value is increased (i.e. loosened). However, this cut is correlated with, for example, the cut made on the π^+ time with respect to the trigger time and thus loosening the cut has very little impact on the $B(\pi_D^0)$ result. Varying all timing cuts at the same time (to avoid this correlation effect) results in the same trend, as that seen when the cut is tightened, continuing.

The instability as the cut value is decreased (i.e. tightened) is expected and is caused by the lack of corrections within the CTRL trigger hardware that account for the time taken for signals to traverse the NA48-CHOD slabs. These corrections are not included because, online at the trigger level, it is not possible to combine both NA48-CHOD hits in the vertical and horizontal slabs and apply a correction to account for the signal propagation down the slabs. An offline correction cannot be introduced at the reconstruction/analysis level because it is not known which track caused the firing of the trigger. This leads to a large discrepancy between the timing distributions between data and MC, as demonstrated in Figure 5.49 which
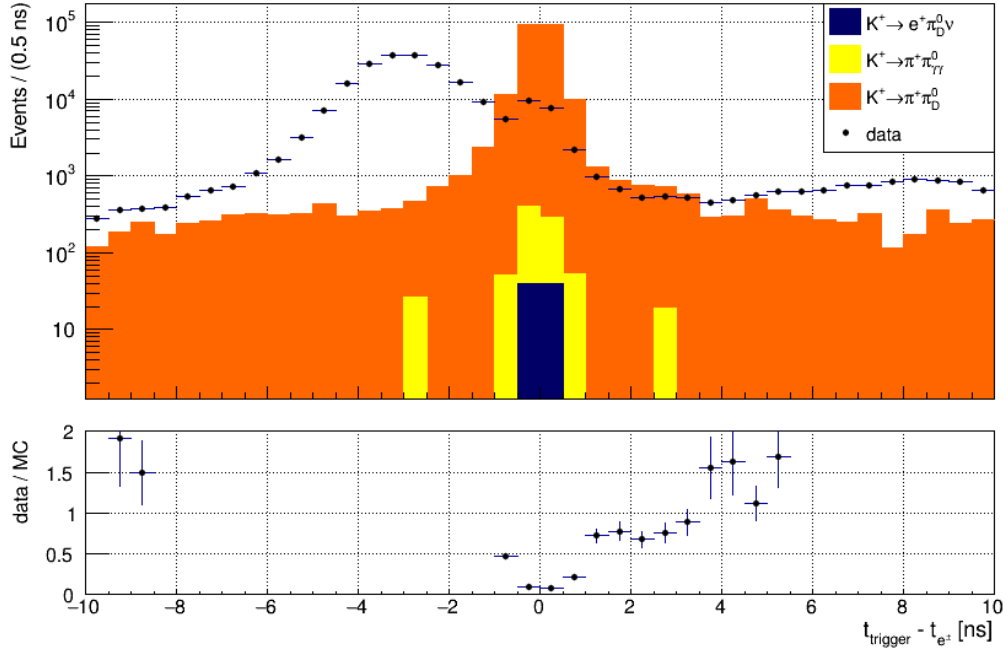
Figure 5.49: CTRL trigger time with respect to the $e^\pm$ track time (NA48-CHOD or CHOD), produced after application of the signal selection.

shows $\delta t = t_{\text{trigger}} - t_{e^\pm}$, where t_{trigger} is the CTRL trigger time and $t_{e^\pm}$ is the $e^\pm$ track NA48-CHOD time (or CHOD time if the NA48-CHOD time does not exist). This was produced after application of the signal selection. Any variation of the cut used on δt will thus affect data and MC differently, producing a large variation in $B(\pi_D^0)$.

The data distribution in Figure 5.49 has a second peak at zero. This is caused by events in which a physics trigger (i.e. a non-CTRL trigger) fired alongside the CTRL trigger. The physics trigger time takes priority over the CTRL trigger time. The physics triggers use the RICH detector to measure the trigger time meaning these events do not suffer from the same timing issues as events in which only a CTRL trigger is present.

There are three options that could be pursued in order to partially fix/solve the timing cut instability. The first is a simple 3 ns shift of the trigger time in data in order to align the peaks of the data and MC distributions shown in Figure 5.49. This was tested and it actually worsened the $B(\pi_D^0)$ instability. It was thus concluded

that this was too simple an approach. The second option is the production of a full, complete, CTRL trigger emulator. This would improve the agreement between the data and MC distributions shown in Figure 5.49 which could resolve the instability. This will not solve the issue of the poor and unreliable CTRL trigger timing distribution however. The third option is to use more recent data. The Run 1 data used in this analysis was taken in 2018 and the CTRL trigger used the NA48-CHOD detector. Run 2 at NA62 started in 2021 and is continuing in 2022. In Run 2, the detector(s) used for the CTRL trigger were changed, in part due to the unreliable NA48-CHOD timing measurements. The new CTRL trigger instead requires a signal in the RICH as well as in the CHOD. The trigger time is given by the RICH time and is hence more reliable than that of the NA48-CHOD. By switching to Run 2 data, the $B(\pi_D^0)$ measurement will not suffer from the trigger timing instability. This work is not presented in this thesis and is the subject of future research.

5.11   The $B(\pi_D^0)$ result

The branching ratio of the π^0 Dalitz decay is measured to be

$$B(\pi_D^0) = (1.137 \pm 0.003_{\text{stat}} \pm 0.022_{\text{syst}}) \times 10^{-2}. \qquad (5.24)$$

Table 5.10 shows the full statistical and systematic error budget. The final uncertainty is dominated by the systematic uncertainty associated with the PID procedure and the MC statistical error.

A comparison of the result in Equation 5.24 with previous measurements and theoretical calculations is shown in Figure 5.50[22]. As further steps are required to complete the measurement, numerical comparisons to the Standard Model and previous experimental measurements are not made. These further steps are described

---

[22]The values and associated uncertainties for each measurement/calculation are shown in Table 1.7.

Table 5.10: The statistical and systematic uncertainties on $B(\pi_{\mathrm{D}}^0)$. Note that this is not the final result, as will be discussed in Section 5.12.

Source	Uncertainty	Relative uncertainty
Statistical (data)	0.34×10^{-4}	0.30%
Statistical (MC)	1.45×10^{-4}	1.27%
STRAW reco. efficiency	0.49×10^{-4}	0.43%
Data-driven LKr PID	1.51×10^{-4}	1.33%
Trigger efficiency (stat. only)	0.05×10^{-4}	0.04%
Beam momentum weighting	0.35×10^{-4}	0.31%
Total	2.20×10^{-4}	1.94%
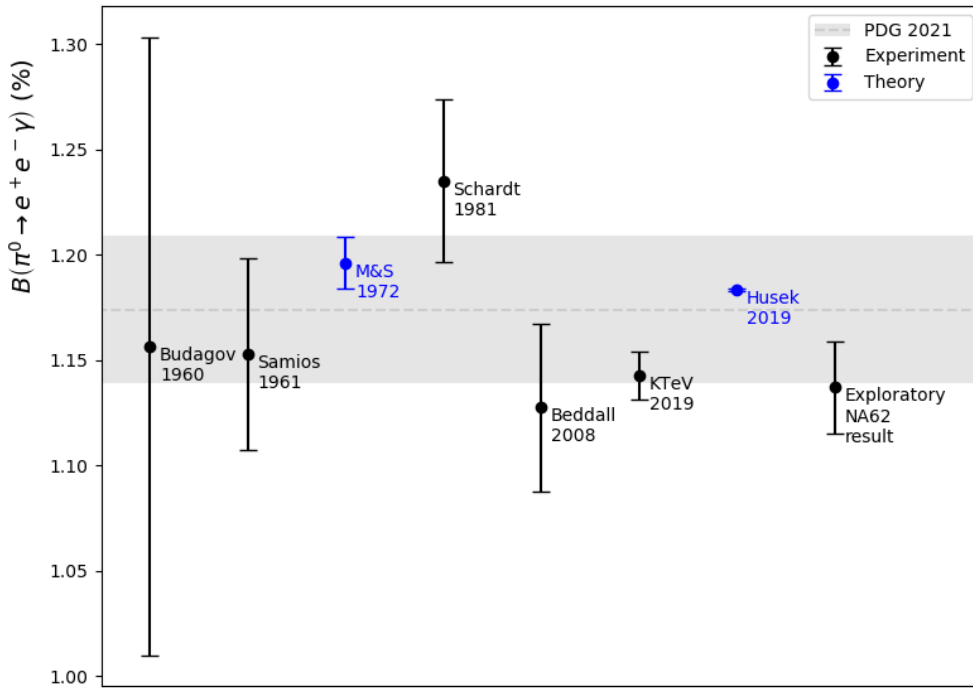
Figure 5.50: The $B(\pi_{\mathrm{D}}^0)$ result presented in this thesis compared with previous measurements and theoretical calculations. As discussed in Subsection 1.3.2, the previous measurements were all of $B(\pi_{\mathrm{D}}^0)/B(\pi_{\gamma\gamma}^0)$ but have been converted to $B(\pi_{\mathrm{D}}^0)$ for this comparison.

in the following section.

5.12   Next steps

As mentioned in the previous sections, the measurement described in this chapter requires further steps before completion. The first step forward should be a switch to NA62 Run 2 data, taken during 2021 and 2022 (and continuing in 2025). The main advantage this will bring is an improved minimum bias (CTRL) trigger that uses the RICH and CHOD detectors instead of the NA48-CHOD. The poor trigger time measurements observed in the Run 1 dataset (see for example, Figure 5.49) will be replaced with the time obtained from the RICH detector which does not suffer from the same issues. Alongside the switch to a different CTRL trigger, a full trigger emulator should be implemented within the analysis (as well as a method to estimate the systematic uncertainty associated with said emulator). This emulator has already been developed for the Run 2 CTRL trigger and should improve the agreement observed in the distributions involving the trigger time between data and MC. Using the new trigger and emulator, the $B(\pi_D^0)$ instability observed when cuts involving the trigger time are varied should also disappear.

As well as a switch to Run 2 data, switching to standard, as opposed to mixed, MC samples would reduce the systematic uncertainty on the measured $B(\pi_D^0)$ as a result of the MC statistical error. To do this, a MC weighting procedure needs to be included within the analysis which ensures that the samples are present in the correct proportions.

In addition, the fluctuations observed in the Z_{vtx} distribution and their effect on the stability of the $B(\pi_D^0)$ result should be understood. It may be that switching to Run 2 data, including a trigger emulator and/or switching to standard MC samples affect the issues observed so a study should be completed regarding this.

Finally, some stability checks have been performed but additional ones, such as the $B(\pi_D^0)$ stability as a function of the data taking period should also be evaluated. Checks for systematic uncertainties not accounted for in this chapter should also be made.

Conclusions

Two solutions have been presented for a KTAG upgrade that uses a CEDAR filled with hydrogen rather than nitrogen. One of these was used to continue the studies and the new CEDAR is currently being built. It is due to be tested, using a test beam at CERN, in October 2022, followed by installation on the NA62 beam line in January 2023.

In addition, an exploratory branching ratio measurement of the $\pi^0 \rightarrow e^+e^-\gamma$ decay has been performed using the NA62 2018 dataset. This measurement is the dominant uncertainty on a number of kaon and neutral pion measurements. An improvement on the $\sim 3\%$ PDG precision will thus have a large impact. Furthermore, there have been no $B(\pi_D^0)$ measurements that include the most up to date SM calculations of the π_D^0 radiative corrections. For these reasons, a new $B(\pi_D^0)$ measurement is needed. The $B(\pi_D^0)$ result presented in this thesis was

$$B(\pi_D^0) = (1.137 \pm 0.003_{\text{stat}} \pm 0.022_{\text{syst}}) \times 10^{-2}, \tag{5.25}$$

where the systematic error dominates the overall uncertainty of 1.94%. The largest systematic errors are from the particle identification procedure and the limited MC sample size, together resulting in a systematic uncertainty of 0.021×10^{-2}. To conduct the measurement, it was necessary to improve and add features to the NA62 Monte Carlo simulation, in particular those related to pileup and the production method.

The $B(\pi_D^0)$ measurement will benefit from switching to NA62 Run 2 data due to

the improved control trigger. Furthermore, adapting the procedure to use the standard MC samples (as opposed to mixed MC) will reduce the systematic uncertainty due to the larger signal MC sample available. Once complete, NA62 should be able to improve upon the current PDG uncertainty.

Appendix A

CEDAR and KTAG studies

A.1 The CEDAR detector

Figure A.1 shows a more detailed diagram of the optical components inside a CEDAR detector (the dimensions shown here are for a CEDAR-N but the components are the same in a CEDAR-W). The beam is in the direction of the optical axis and the diaphragm is located slightly upstream of the condensers. The windows shown are those at the upstream edge of the CEDAR vessel.

As part of the work to upgrade a CEDAR for use with hydrogen (see Section 3.3), the CERN engineering department opened a CEDAR vessel for examination. A photograph, taken during this procedure, is shown in Figure A.2. The diaphragm and Chromatic Corrector can be seen in the foreground.
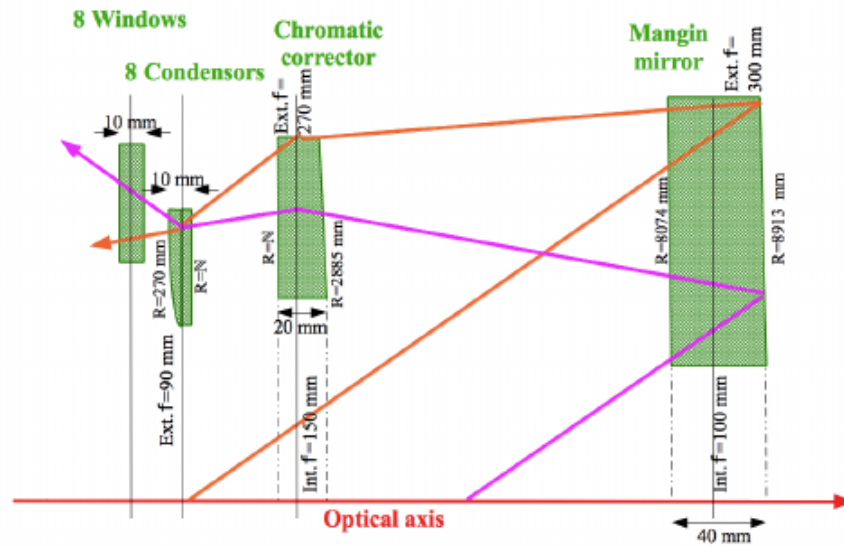
Figure A.1: Schematic drawing of the original CEDAR vessel and its optical components [74].

Figure A.2: An opened CEDAR (photograph taken by Serge Mathot (CERN)).

A.2   KTAG and CEDAR geometrical parameters

The definitions of certain parameters are shown in Table A.1. Table A.2 shows a list

of parameters used in the simulations. All units are in mm unless otherwise stated.

Table A.1: List of parameter definitions.

Parameter	Definition
Z	Axial position (surface is specified in the table).
R	Radius of curvature.
Central thickness	Thickness of material in the axial direction at the inner radius.
Thickness	Thickness of material in the axial direction (unless otherwise specified).
Central angle	Angle, relative to the z-axis, at which the normal to the spherical mirror cap centre lies.
Light guide diameter	Axial distance between the edges of the outer PMT rows.
Radial offset	Radial position relative to the z-axis.

Table A.2: Full list of parameters used in the CEDAR simulations. The parameters discussed in Subsections 3.2.2 and 3.2.3 are shown under CEDAR-N (optimised) and CEDAR (custom) respectively. The double horizontal line shows the point at which the photons leave the CEDAR. All units are in mm unless otherwise stated.

CEDAR type		CEDAR-N (standard)	CEDAR-W (standard)	CEDAR-N (optimised)	CEDAR (custom)
Gas		*He*	*N₂*	*H₂*	*H₂*
Pressure (bar)		10.74	1.71	4.10	4.06
Front vessel (upstream vessel)	Length	339.0	339.0	339.0	339.0
	Inner radius	139.0	139.0	139.0	139.0
	Outer radius	150.0	150.0	150.0	150.0
Main vessel (downstream vessel)	Length	4,457.0	4,457.0	4,457.0	4,457.0
	Inner radius	267.0	267.0	267.0	267.0
	Outer radius	279.0	279.0	279.0	279.0
Chromatic corrector	Z (upstream surface)	2,234.0	2,234.0	1,651.0	2,234.0
	R	2,885.0	1,385.0	583.0	1,185.0
	Central thickness	20.0	20.0	20.0	20.0
	Hole diameter	150.0	150.0	150.0	150.0
	Diameter	270.0	320.0	330.0	320.0-360.0
Mangin mirror	Z (upstream surface)	5,732.0	5,732.0	5,732.0	5,732.0
	R (refracting)	8,074.0	6,615.0	8,074.0	6,080.0
	R (reflecting)	8,913.0	8,610.0	8,913.0	8,470.0
	Central thickness	40.0	40.0	40.0	40.0
	Hole diameter	100.0	100.0	100.0	100.0
	Diameter	300.0	300.0	300.0	300.0
Diaphragm	Z (centre)	1,251.0	1,251.0	1,251.0	1.251.0
	Radial position of aperture	100.0	100.0	100.0	100.0
	Aperture diameter	2.0	2.0	2.0	2.0
Condensers	Z (downstream surface)	1,221.0	1,221.0	1,221.0	1,221.0
	Max thickness	10.0	10.0	10.0	10.0
	R	270.0	300.0	270.0	270.0/300.0
Concave lens (new)	Z (downstream surface)	-	-	1,170.0	-
	R	-	-	420.0	-
	Thickness (at outer radius)	-	-	20.0	-
	Hole diameter	-	-	130.0	-
	Diameter	-	-	260.0	-
Quartz windows	Z (upstream surface)	851.0	851.0	851.0	851.0
	Thickness	10.0	10.0	10.0	10.0
	Diameter	50.0	50.0	50.0	50.0
	Radial offset (of centre)	103.0	103.0	103.0	103.0
Optical caps	Z (upstream surface)	-	829.0	829.0	829.0
	Minimum thickness	-	4.24	4.24	4.24
	R	-	114.62	91.69	114.62
	Diameter	-	50.0	50.0	50.0
	Radial offset (of centre)	-	103.0	103.0	103.0
Spherical mirrors	R	-	51.68	51.68	51.68
	Diameter	-	50.00	50.0	50.0
	Central angle (deg)	-	45.00	45.0	45.0
	Radial offset (of cap centre)	-	106.0	106.0	104.0
	Z (of cap centre)	-	701.0	701.0	701.0
Light guide	Z (of centre)	-	701.0	701.0	701.0
	Radial offset (of centre)	-	335.0	335.0	335.0
	Diameter	-	129.6	129.6	129.6

References

[1] C. N. Yang and R. L. Mills. "Conservation of Isotopic Spin and Isotopic Gauge Invariance". In: *Physical Review* 96.1 (Oct. 1, 1954). Publisher: American Physical Society, pp. 191–195. DOI: 10.1103/PhysRev.96.191. URL: https://link.aps.org/doi/10.1103/PhysRev.96.191 (visited on 06/02/2021).

[2] Sheldon L. Glashow. "Partial-symmetries of weak interactions". In: *Nuclear Physics* 22.4 (Feb. 1, 1961), pp. 579–588. ISSN: 0029-5582. DOI: 10.1016/0029-5582(61)90469-2. URL: https://www.sciencedirect.com/science/article/pii/0029558261904692 (visited on 06/02/2021).

[3] Peter W. Higgs. "Broken Symmetries and the Masses of Gauge Bosons". In: *Physical Review Letters* 13.16 (Oct. 19, 1964). Publisher: American Physical Society, pp. 508–509. DOI: 10.1103/PhysRevLett.13.508. URL: https://link.aps.org/doi/10.1103/PhysRevLett.13.508 (visited on 06/02/2021).

[4] G. Arnison et al. "Experimental observation of lepton pairs of invariant mass around 95 GeV/c^2 at the CERN SPS collider". In: *Physics Letters B* 126.5 (July 7, 1983), pp. 398–410. ISSN: 0370-2693. DOI: 10.1016/0370-2693(83)90188-0. URL: https://www.sciencedirect.com/science/article/pii/0370269383901880 (visited on 06/02/2021).

[5] G. Arnison et al. "Experimental observation of isolated large transverse energy electrons with associated missing energy at $s = 540$ GeV". In: *Physics Letters B* 122.1 (Feb. 24, 1983), pp. 103–116. ISSN: 0370-2693. DOI: 10.1016/0370-2693(83)91177-2. URL: https://www.sciencedirect.com/science/article/pii/0370269383911772 (visited on 06/02/2021).

[6] M. Banner et al. "Observation of single isolated electrons of high transverse momentum in events with missing transverse energy at the CERN pp collider". In: *Physics Letters B* 122.5 (Mar. 17, 1983), pp. 476–485. ISSN: 0370-2693. DOI: 10.1016/0370-2693(83)91605-2. URL: https://www.sciencedirect.com/science/article/pii/0370269383916052 (visited on 06/02/2021).

[7] P. Bagnaia et al. "Evidence for $Z^0 \rightarrow e^+e^-$ at the CERN $\bar{p}p$ collider". In: *Physics Letters B* 129.1 (Sept. 15, 1983), pp. 130–140. ISSN: 0370-2693. DOI: 10.1016/0370-2693(83)90744-X. URL: https://www.sciencedirect.com/science/article/pii/037026938390744X (visited on 06/02/2021).

[8] Makoto Kobayashi and Toshihide Maskawa. "CP-Violation in the Renormalizable Theory of Weak Interaction". In: *Progress of Theoretical Physics* 49.2 (Feb. 1, 1973), pp. 652–657. ISSN: 0033-068X. DOI: 10.1143/PTP.49.652. URL: https://doi.org/10.1143/PTP.49.652 (visited on 10/05/2021).

[9] CDF Collaboration et al. "Observation of Top Quark Production in $\bar{p}p$ Collisions with the Collider Detector at Fermilab". In: *Physical Review Letters* 74.14 (Apr. 3, 1995). Publisher: American Physical Society, pp. 2626–2631. DOI: 10.1103/PhysRevLett.74.2626. URL: https://link.aps.org/doi/10.1103/PhysRevLett.74.2626 (visited on 06/03/2021).

[10] D0 Collaboration et al. "Observation of the Top Quark". In: *Physical Review Letters* 74.14 (Apr. 3, 1995). Publisher: American Physical Society, pp. 2632–2637. DOI: 10.1103/PhysRevLett.74.2632. URL: https://link.aps.org/doi/10.1103/PhysRevLett.74.2632 (visited on 06/03/2021).

[11] Jun Cao and Miao He. "Neutrino oscillation: discovery and perspectives". In: *Science Bulletin* 61.1 (Jan. 1, 2016), pp. 48–51. ISSN: 2095-9281. DOI: 10.1007/s11434-015-0969-7. URL: https://doi.org/10.1007/s11434-015-0969-7 (visited on 06/03/2021).

[12] Andrei D. Sakharov. "Violation of CP invariance, C asymmetry, and baryon asymmetry of the universe". In: *Soviet Physics Uspekhi* 34.5 (May 31, 1991). Publisher: IOP Publishing, p. 392. ISSN: 0038-5670. DOI: 10.1070/PU1991v034n05ABEH002497. URL: https://iopscience.iop.org/article/10.1070/PU1991v034n05ABEH002497/meta (visited on 06/03/2021).

[13] V. C. Rubin, W. K. Ford Jr., and N. Thonnard. "Rotational properties of 21 SC galaxies with a large range of luminosities and radii, from NGC 4605 ($R = 4\text{kpc}$) to UGC 2885 ($R = 122\text{kpc}$)". In: *The Astrophysical Journal* 238 (June 1, 1980), pp. 471–487. ISSN: 0004-637X. DOI: 10.1086/158003. URL: http://adsabs.harvard.edu/abs/1980ApJ...238..471R (visited on 06/03/2021).

[14] G. Aad et al. "Observation of a new particle in the search for the Standard Model Higgs boson with the ATLAS detector at the LHC". In: *Physics Letters B* 716.1 (Sept. 17, 2012), pp. 1–29. ISSN: 0370-2693. DOI: 10.1016/j.physletb.2012.08.020. URL: https://www.sciencedirect.com/science/article/pii/S037026931200857X (visited on 06/03/2021).

[15] S. Chatrchyan et al. "Observation of a new boson at a mass of 125 GeV with the CMS experiment at the LHC". In: *Physics Letters B* 716.1 (Sept. 17, 2012), pp. 30–61. ISSN: 0370-2693. DOI: 10.1016/j.physletb.2012.08.021. URL: https://www.sciencedirect.com/science/article/pii/S037026931200858 1 (visited on 06/03/2021).

[16] Michael E. Peskin and Daniel V. Schroeder. *An Introduction to Quantum Field Theory*. CRC, Sept. 11, 2019. 866 pp. ISBN: 978-0-367-32056-0.

[17] W. N. Cottingham and D. A. Greenwood. *An Introduction to the Standard Model of Particle Physics*. Cambridge University Press, Feb. 22, 2007. 293 pp. ISBN: 978-1-139-46221-1.

[18] Nicola Cabibbo. "Unitary Symmetry and Leptonic Decays". In: *Physical Review Letters* 10.12 (June 15, 1963). Publisher: American Physical Society, pp. 531–533. DOI: 10.1103/PhysRevLett.10.531. URL: https://link.aps.org/doi/10.1103/PhysRevLett.10.531 (visited on 10/05/2021).

[19] Ling-Lie Chau and Wai-Yee Keung. "Comments on the Parametrization of the Kobayashi-Maskawa Matrix". In: *Physical Review Letters* 53.19 (Nov. 5, 1984). Publisher: American Physical Society, pp. 1802–1805. DOI: `10.1103/Ph ysRevLett.53.1802`. URL: `https://link.aps.org/doi/10.1103/PhysRev Lett.53.1802` (visited on 10/05/2021).

[20] P. A. Zyla et al. (Particle Data Group). "Particle Listings". In: *Prog. Theor. Exp. Phys* 083C01 (2021). DOI: `https://doi.org/10.1093/ptep/ptaa104`. URL: `https://pdg.lbl.gov/2021/listings/contents_listings.html`.

[21] J. Beacham et al. "Physics beyond colliders at CERN: beyond the Standard Model working group report". In: *Journal of Physics G: Nuclear and Particle Physics* 47.1 (Dec. 2019). Publisher: IOP Publishing, p. 010501. ISSN: 0954-3899. DOI: `10.1088/1361-6471/ab4cd2`. URL: `https://doi.org/10.1088/1 361-6471/ab4cd2` (visited on 09/15/2021).

[22] G. D. Rochester and C. C. Butler. "Evidence for the Existence of New Unstable Elementary Particles". In: *Nature* 160.4077 (Dec. 1947). Number: 4077 Publisher: Nature Publishing Group, pp. 855–857. ISSN: 1476-4687. DOI: `10.1 038/160855a0`. URL: `https://www.nature.com/articles/160855a0` (visited on 06/03/2021).

[23] R. Brown et al. "Observations with Electron-Sensitive Plates Exposed to Cosmic Radiation*". In: *Nature* 163.4133 (Jan. 1949), pp. 82–87. ISSN: 1476-4687. DOI: `10.1038/163082a0`. URL: `https://www.nature.com/articles/163082 a0/figures/` (visited on 10/06/2021).

[24] A. Pais. "Some Remarks on the *V*-Particles". In: *Physical Review* 86.5 (June 1, 1952). Publisher: American Physical Society, pp. 663–672. DOI: `10.1103/Phy sRev.86.663`. URL: `https://link.aps.org/doi/10.1103/PhysRev.86.663` (visited on 10/06/2021).

[25] M. Gell-Mann. "Isotopic Spin and New Unstable Particles". In: *Physical Review* 92.3 (Nov. 1, 1953). Publisher: American Physical Society, pp. 833–834. DOI: `10.1103/PhysRev.92.833`. URL: `https://link.aps.org/doi/10.1103 /PhysRev.92.833` (visited on 10/06/2021).

[26] A. Pais. "On the Baryon-meson-photon System*". In: *Progress of Theoretical Physics* 10.4 (Oct. 1, 1953), pp. 457–469. ISSN: 0033-068X. DOI: `10.1143 /PTP.10.457`. URL: `https://doi.org/10.1143/PTP.10.457` (visited on 10/06/2021).

[27] Tadao Nakano and Kazuhiko Nishijima. "Charge Independence for V-particles". In: *Progress of Theoretical Physics* 10.5 (Nov. 1, 1953), pp. 581–582. ISSN: 0033-068X. DOI: `10.1143/PTP.10.581`. URL: `https://doi.org/10.1143 /PTP.10.581` (visited on 10/06/2021).

[28] J. H. Christenson et al. "Evidence for the 2π Decay of the K_2^0 Meson". In: *Physical Review Letters* 13.4 (July 27, 1964). Publisher: American Physical Society, pp. 138–140. DOI: `10.1103/PhysRevLett.13.138`. URL: `https://li nk.aps.org/doi/10.1103/PhysRevLett.13.138` (visited on 06/03/2021).

[29]   *The Nobel Prize in Physics 1980.* NobelPrize.org. URL: `https://www.nobelp rize.org/prizes/physics/1980/summary/` (visited on 10/06/2021).

[30]   G. D. Barr et al. "A new measurement of direct CP violation in the neutral kaon system". In: *Physics Letters B* 317.1 (Nov. 4, 1993), pp. 233–242. ISSN: 0370-2693. DOI: `10.1016/0370-2693(93)91599-I`. URL: `https://www.s ciencedirect.com/science/article/pii/037026939391599I` (visited on 06/03/2021).

[31]   V. Fanti et al. "A new measurement of direct CP violation in two pion decays of the neutral kaon". In: *Physics Letters B* 465.1 (Oct. 21, 1999), pp. 335–348. ISSN: 0370-2693. DOI: `10.1016/S0370-2693(99)01030-8`. URL: `https://ww w.sciencedirect.com/science/article/pii/S0370269399010308` (visited on 06/03/2021).

[32]   KTeV Collaboration et al. "Observation of Direct CP Violation in $K_{S,L} \to \pi\pi$ Decays". In: *Physical Review Letters* 83.1 (July 5, 1999). Publisher: American Physical Society, pp. 22–27. DOI: `10.1103/PhysRevLett.83.22`. URL: `ht tps://link.aps.org/doi/10.1103/PhysRevLett.83.22` (visited on 06/03/2021).

[33]   Andrzej J. Buras et al. "$K^+ \to \pi\nu\nu$ and $K_L \to \pi^0\nu\nu$ in the Standard Model: Status and Perspectives". In: *Journal of High Energy Physics* 2015.11 (Nov. 2015), p. 33. ISSN: 1029-8479. DOI: `10.1007/JHEP11(2015)033`. arXiv: `1503 .02693`. URL: `http://arxiv.org/abs/1503.02693` (visited on 09/24/2019).

[34]   Andrzej J. Buras and Elena Venturini. "Searching for New Physics in Rare K and B Decays without V_{cb} and V_{ub} Uncertainties". In: *arXiv:2109.11032 [hep-ex, physics:hep-lat, physics:hep-ph]* (Oct. 5, 2021). arXiv: `2109.11032`. URL: `http://arxiv.org/abs/2109.11032` (visited on 10/07/2021).

[35]   Hideki Yukawa. "On the Interaction of Elementary Particles. I". In: *Proceedings of the Physico-Mathematical Society of Japan. 3rd Series* 17 (1935), pp. 48–57. DOI: `10.11429/ppmsj1919.17.0_48`.

[36]   Hideki Yukawa, Shoichi Sakata, and Mitsuo Taketani. "On the Interaction of Elementary Particles. III". In: *Proceedings of the Physico-Mathematical Society of Japan. 3rd Series* 20 (1938). Publisher: THE PHYSICAL SOCIETY OF JAPAN , The Mathematical Society of Japan, pp. 319–340. ISSN: 0370-1239, 2185-2707. DOI: `10.11429/ppmsj1919.20.0_319`.

[37]   N. Kemmer. "The charge-dependence of nuclear forces". In: *Mathematical Proceedings of the Cambridge Philosophical Society* 34.3 (July 1938). Publisher: Cambridge University Press, pp. 354–364. ISSN: 1469-8064, 0305-0041. DOI: `10.1017/S0305004100020296`. URL: `https://www.cambridge.org/core/jo urnals/mathematical-proceedings-of-the-cambridge-philosophical- society/article/chargedependence-of-nuclear-forces/6FF2BF23B8241 82B5FAE8D5197A033FC#` (visited on 09/20/2021).

[38] Shoichi Sakata and Yasutaka Tanikawa. "The Spontaneous Disintegration of the Neutral Mesotron (Neutretto)". In: *Physical Review* 57.6 (Mar. 15, 1940). Publisher: American Physical Society, pp. 548–548. DOI: 10.1103/PhysRev.57.548. URL: https://link.aps.org/doi/10.1103/PhysRev.57.548 (visited on 09/20/2021).

[39] C. Y. Chao. "Mixed Cosmic-Ray Showers at Sea Level". In: *Physical Review* 75.4 (Feb. 15, 1949). Publisher: American Physical Society, pp. 581–590. DOI: 10.1103/PhysRev.75.581. URL: https://link.aps.org/doi/10.1103/PhysRev.75.581 (visited on 09/20/2021).

[40] W. B. Fretter. "Penetrating Showers". In: *Physical Review* 76.4 (Aug. 15, 1949). Publisher: American Physical Society, pp. 511–517. DOI: 10.1103/PhysRev.76.511. URL: https://link.aps.org/doi/10.1103/PhysRev.76.511 (visited on 09/20/2021).

[41] R. Bjorklund et al. "High Energy Photons from Proton-Nucleon Collisions". In: *Physical Review* 77.2 (Jan. 15, 1950). Publisher: American Physical Society, pp. 213–218. DOI: 10.1103/PhysRev.77.213. URL: https://link.aps.org/doi/10.1103/PhysRev.77.213 (visited on 09/20/2021).

[42] R. H. Dalitz. "On an Alternative Decay Process for the Neutral -Meson". In: *Proceedings of the Physical Society. Section A* 64.7 (July 1951). Publisher: IOP Publishing, pp. 667–669. ISSN: 0370-1298. DOI: 10.1088/0370-1298/64/7/115. URL: https://doi.org/10.1088/0370-1298/64/7/115 (visited on 09/20/2021).

[43] L. G. Landsberg. "Electromagnetic decays of light mesons". In: *Physics Reports* 128.6 (Nov. 1, 1985), pp. 301–376. ISSN: 0370-1573. DOI: 10.1016/0370-1573(85)90129-2. URL: https://www.sciencedirect.com/science/article/pii/0370157385901292 (visited on 09/21/2021).

[44] Tomáš Husek, Karol Kampf, and Jiří Novotný. "Radiative corrections to the Dalitz decay $\pi^0 \to e^+e^-\gamma$ revisited". In: *Physical Review D* 92.5 (Sept. 23, 2015). Publisher: American Physical Society, p. 054027. DOI: 10.1103/PhysRevD.92.054027. URL: https://link.aps.org/doi/10.1103/PhysRevD.92.054027 (visited on 09/22/2021).

[45] D. W. Joseph. "Electron pair creation in π^+p capture reactions from rest". In: *Il Nuovo Cimento (1955-1965)* 16.6 (June 1, 1960), pp. 997–1013. ISSN: 1827-6121. DOI: 10.1007/BF02860383. URL: https://doi.org/10.1007/BF02860383 (visited on 09/21/2021).

[46] B. E. Lautrup and J. Smith. "Radiative Corrections to Decays with a Dalitz Pair". In: *Physical Review D* 3.5 (Mar. 1, 1971). Publisher: American Physical Society, pp. 1122–1135. DOI: 10.1103/PhysRevD.3.1122. URL: https://link.aps.org/doi/10.1103/PhysRevD.3.1122 (visited on 09/21/2021).

[47] K. O. Mikaelian and J. Smith. "Radiative Corrections to the Decay $\pi^0 \to \gamma e^+e^-$". In: *Physical Review D* 5.7 (Apr. 1, 1972). Publisher: American Physical Society, pp. 1763–1773. DOI: 10.1103/PhysRevD.5.1763. URL: https://link.aps.org/doi/10.1103/PhysRevD.5.1763 (visited on 09/21/2021).

[48] C. Lazzeroni et al. "Measurement of the π^0 electromagnetic transition form factor slope". In: *Phys.Lett.* B768 (May 10, 2017), pp. 38–45. DOI: `10.1016/j.physletb.2017.02.042`.

[49] Tomáš Husek, Evgueni Goudzovski, and Karol Kampf. "Precise Determination of the Branching Ratio of the Neutral-Pion Dalitz Decay". In: *Physical Review Letters* 122.2 (Jan. 18, 2019). Publisher: American Physical Society, p. 022003. DOI: `10.1103/PhysRevLett.122.022003`. URL: `https://link.aps.org/doi/10.1103/PhysRevLett.122.022003` (visited on 09/22/2021).

[50] Y. A. Budagov et al. "Internal conversion pairs in the decay of neutral 1T mesons". In: *SOVIET PHYSICS JETP* 11 (1960).

[51] N. P. Samios. "Dynamics of Internally Converted Electron-Positron Pairs". In: *Physical Review* 121.1 (Jan. 1, 1961). Publisher: American Physical Society, pp. 275–281. DOI: `10.1103/PhysRev.121.275`. URL: `https://link.aps.org/doi/10.1103/PhysRev.121.275` (visited on 09/23/2021).

[52] M. A. Schardt et al. "New measurement of the Dalitz-decay branching ratio of the π^0". In: *Physical Review D* 23.3 (Feb. 1, 1981). Publisher: American Physical Society, pp. 639–648. DOI: `10.1103/PhysRevD.23.639`. URL: `https://link.aps.org/doi/10.1103/PhysRevD.23.639` (visited on 09/23/2021).

[53] A. Beddall and A. Beddall. "Measurement of the Dalitz-decay branching ratio of the π^0". In: *The European Physical Journal C* 54.3 (Apr. 1, 2008), pp. 365–370. ISSN: 1434-6052. DOI: `10.1140/epjc/s10052-008-0539-0`. URL: `https://doi.org/10.1140/epjc/s10052-008-0539-0` (visited on 09/23/2021).

[54] E. Abouzaid et al. "A Measurement of the Branching Ratio of π^0 Dalitz Decay using $K_L \rightarrow \pi^0\pi^0\pi^0$ Decays". In: *arXiv:1902.01375 [hep-ex]* (Feb. 4, 2019). arXiv: `1902.01375`. URL: `http://arxiv.org/abs/1902.01375` (visited on 02/06/2019).

[55] KTeV Collaboration et al. "Determination of the Parity of the Neutral Pion via Its Four-Electron Decay". In: *Physical Review Letters* 100.18 (May 6, 2008). Publisher: American Physical Society, p. 182001. DOI: `10.1103/PhysRevLett.100.182001`. URL: `https://link.aps.org/doi/10.1103/PhysRevLett.100.182001` (visited on 09/24/2021).

[56] E. Abouzaid et al. "Measurement of the rare decay $\pi^0 \rightarrow e^+e^-$". In: *Physical Review D* 75.1 (Jan. 11, 2007). Publisher: American Physical Society, p. 012004. DOI: `10.1103/PhysRevD.75.012004`. URL: `https://link.aps.org/doi/10.1103/PhysRevD.75.012004` (visited on 09/24/2021).

[57] J. R. Batley et al. "Precise measurement of the $K^\pm \rightarrow \pi^\pm e^+e^-$ decay". In: *Physics Letters B* 677.5 (June 29, 2009), pp. 246–254. ISSN: 0370-2693. DOI: `10.1016/j.physletb.2009.05.040`. URL: `https://www.sciencedirect.com/science/article/pii/S0370269309006169` (visited on 09/24/2021).

[58] J. R. Batley et al. "First observation and study of the $K^\pm \rightarrow \pi^\pm\pi^0 e^+e^-$ decay". In: *Physics Letters B* 788 (Jan. 10, 2019), pp. 552–561. ISSN: 0370-2693. DOI: `10.1016/j.physletb.2018.11.046`. URL: `https://www.sciencedirect.com/science/article/pii/S037026931830892X` (visited on 09/24/2021).

[59] The NA48 Collaboration. "Investigation of $K_{L,S} \to \pi^+\pi^-e^+e^-$ decays". In: *The European Physical Journal C - Particles and Fields* 30.1 (Sept. 1, 2003), pp. 33–49. ISSN: 1434-6052. DOI: 10.1140/epjc/s2003-01252-y. URL: https://doi.org/10.1140/epjc/s2003-01252-y (visited on 09/24/2021).

[60] Alexander E. Dorokhov and Mikhail A. Ivanov. "Rare decay $\pi^0 \to e^+e^-$: Theory confronts KTeV data". In: *Physical Review D* 75.11 (June 20, 2007). Publisher: American Physical Society, p. 114007. DOI: 10.1103/PhysRevD.75.114007. URL: https://link.aps.org/doi/10.1103/PhysRevD.75.114007 (visited on 12/08/2021).

[61] Yonatan Kahn, Michael Schmitt, and Tim Tait. "Enhanced Rare Pion Decays from a Model of MeV Dark Matter". In: *Physical Review D* 78.11 (Dec. 2, 2008), p. 115002. ISSN: 1550-7998, 1550-2368. DOI: 10.1103/PhysRevD.78.115002. arXiv: 0712.0007. URL: http://arxiv.org/abs/0712.0007 (visited on 12/08/2021).

[62] M. Leventhal, C. J. MacCallum, and P. D. Stang. "Detection of 511 keV positron annihilation radiation from the galactic center direction." In: *The Astrophysical Journal* 225 (Oct. 1, 1978). ADS Bibcode: 1978ApJ...225L..11L, pp. L11–L14. ISSN: 0004-637X. DOI: 10.1086/182782. URL: https://ui.adsabs.harvard.edu/abs/1978ApJ...225L..11L (visited on 12/08/2021).

[63] NA62 Collaboration. "Searches for lepton number violating K^+ decays". In: *Physics Letters B* 797 (Oct. 10, 2019), p. 134794. ISSN: 0370-2693. DOI: 10.1016/j.physletb.2019.07.041. URL: http://www.sciencedirect.com/science/article/pii/S0370269319304988 (visited on 09/25/2019).

[64] NA62 collaboration. "Search for production of an invisible dark photon in π^0 decays". In: *Journal of High Energy Physics* 2019.5 (May 28, 2019), p. 182. ISSN: 1029-8479. DOI: 10.1007/JHEP05(2019)182. URL: https://doi.org/10.1007/JHEP05(2019)182 (visited on 09/25/2019).

[65] E. Cortina Gil et al. "Search for heavy neutral lepton production in K^+ decays to positrons". In: *Physics Letters B* 807 (Aug. 10, 2020), p. 135599. ISSN: 0370-2693. DOI: 10.1016/j.physletb.2020.135599. URL: https://www.sciencedirect.com/science/article/pii/S0370269320304032 (visited on 06/07/2021).

[66] E. Cortina Gil et al. "Search for K^+ decays to a muon and invisible particles". In: *Physics Letters B* 816 (May 10, 2021), p. 136259. ISSN: 0370-2693. DOI: 10.1016/j.physletb.2021.136259. URL: https://www.sciencedirect.com/science/article/pii/S0370269321001994 (visited on 06/07/2021).

[67] NA62 collaboration. "The beam and detector of the NA62 experiment at CERN". In: *Journal of Instrumentation* 12.5 (May 31, 2017), P05025–P05025. ISSN: 1748-0221. DOI: 10.1088/1748-0221/12/05/P05025. arXiv: 1703.08501. URL: http://arxiv.org/abs/1703.08501 (visited on 09/24/2019).

[68] R. Ammendola et al. "The integrated low-level trigger and readout system of the CERN NA62 experiment". In: *Nuclear Instruments and Methods in Physics Research A* 929 (June 11, 2019), pp. 1–22. ISSN: 0168-9002. DOI: `10.1016/j.nima.2019.03.012`. URL: `https://www.sciencedirect.com/science/article/pii/S0168900219303055` (visited on 12/28/2021).

[69] M. Fiorini et al. "High rate particle tracking and ultra-fast timing with a thin hybrid silicon pixel detector". In: *Nuclear Instruments and Methods in Physics Research A* 718 (2013), pp. 270–273. DOI: `10.1016/j.nima.2012.10.108`. URL: `https://inspirehep.net/literature/1250571` (visited on 06/11/2021).

[70] A. Sergi. "NA62 Spectrometer: A Low Mass Straw Tracker". In: *Physics Procedia*. Proceedings of the 2nd International Conference on Technology and Instrumentation in Particle Physics (TIPP 2011) 37 (Jan. 1, 2012), pp. 530–534. ISSN: 1875-3892. DOI: `10.1016/j.phpro.2012.03.713`. URL: `https://www.sciencedirect.com/science/article/pii/S1875389212017348` (visited on 06/11/2021).

[71] E. Goudzovski et al. "Development of the kaon tagging system for the NA62 experiment at CERN". In: *Nuclear Instruments and Methods in Physics Research A* 801 (Nov. 2015), pp. 86–94. ISSN: 01689002. DOI: `10.1016/j.nima.2015.08.015`. arXiv: `1509.03773`. URL: `http://arxiv.org/abs/1509.03773` (visited on 09/17/2019).

[72] C. Bovet, S. Milner, and A. Placci. "Cerenkov Differential counters with Achromatic Ring focus". In: *CERN Libraries* (1975).

[73] C. Bovet et al. "The Cedar counters for particle identification in the SPS secondary beams: A description and an operation manual". In: *CERN Libraries* (1982), p. 45.

[74] NA62 Collaboration. *NA62 Technical Design Document.* NA62-10-07. Dec. 2010. URL: `http://na62.web.cern.ch/na62/Documents/TD_Full_doc_v10.pdf` (visited on 04/01/2019).

[75] B. Angelucci et al. "Pion-muon separation with a RICH prototype for the NA62 experiment". In: *Nuclear Instruments and Methods in Physics Research A* 621 (2010), pp. 205–211. DOI: `10.1016/j.nima.2010.05.062`. URL: `https://inspirehep.net/literature/874856` (visited on 06/11/2021).

[76] V. Fanti et al. "The beam and detector for the NA48 neutral kaon CP violation experiment at CERN". In: *Nuclear Instruments and Methods in Physics Research A* 574.3 (May 11, 2007), pp. 433–471. ISSN: 0168-9002. DOI: `10.1016/j.nima.2007.01.178`. URL: `https://www.sciencedirect.com/science/article/pii/S0168900207002719` (visited on 06/09/2021).

[77] S. A. Fedotov, A. A. Kleymenova, and A. N. Khotjantsev. "New CHOD detector for the NA62 experiment at CERN". In: *Physics of Particles and Nuclei* 49.1 (Jan. 1, 2018), pp. 26–29. ISSN: 1531-8559. DOI: `10.1134/S1063779618010094`. URL: `https://doi.org/10.1134/S1063779618010094` (visited on 06/11/2021).

[78] F. Ambrosino et al. "The Large-Angle Photon Veto System for the NA62 Experiment at CERN". In: IEEE Nuclear Science Symposium and Medical Imaging Conference (NSS/MIC 2011). 2011. DOI: `10.1109/NSSMIC.2011.6 154594`. URL: `https://inspirehep.net/literature/946499` (visited on 06/11/2021).

[79] A. Ceccucci et al. "The NA62 liquid Krypton calorimeter new readout system". In: *Journal of Instrumentation* 9.1 (Jan. 2014). Publisher: IOP Publishing, pp. C01047–C01047. ISSN: 1748-0221. DOI: `10.1088/1748-0221/9/01/C010 47`. URL: `https://doi.org/10.1088/1748-0221/9/01/c01047` (visited on 06/11/2021).

[80] F. Ambrosino et al. "CHANTI: a fast and efficient charged particle veto detector for the NA62 experiment at CERN". In: *Journal of Instrumentation* 11.3 (Mar. 2016). Publisher: IOP Publishing, P03029–P03029. ISSN: 1748-0221. DOI: `10.1088/1748-0221/11/03/P03029`. URL: `https://doi.org/10.1088 /1748-0221/11/03/p03029` (visited on 06/11/2021).

[81] M. B. Golubeva et al. "Forward hadron calorimeter for measurements of projectile spectators in heavy-ion experiment". In: *Phys. At. Nucl.* (2012).

[82] D. Soldi and S. Chiozzi. "Level Zero Trigger Processor for the NA62 experiment". In: *Journal of Instrumentation* 13.5 (May 2018), P05004–P05004. ISSN: 1748-0221. DOI: `10.1088/1748-0221/13/05/P05004`. URL: `https://doi.org /10.1088%2F1748-0221%2F13%2F05%2Fp05004` (visited on 09/25/2019).

[83] B. G. Taylor. *TTC laser transmitter (TTCex, TTCtx, TTCmx) User Manual.* 2012. URL: `ttc.web.cern.ch/TTC/TTCtxManual.pdf` (visited on 11/28/2022).

[84] The NA62 Collaboration. *Performance of the NA62 trigger system.* Aug. 1, 2022. DOI: `10.48550/arXiv.2208.00897`. arXiv: `2208.00897[hep-ex,p hysics:physics]`. URL: `http://arxiv.org/abs/2208.00897` (visited on 08/05/2022).

[85] NA62 Collaboration. *NA62 Framework.* URL: `https://na62-sw.web.cern.c h/` (visited on 06/04/2021).

[86] S. Agostinelli et al. "Geant4—a simulation toolkit". In: *Nuclear Instruments and Methods in Physics Research Section A: Accelerators, Spectrometers, Detectors and Associated Equipment* 506.3 (July 1, 2003), pp. 250–303. ISSN: 0168-9002. DOI: `10.1016/S0168-9002(03)01368-8`. URL: `https://www.s ciencedirect.com/science/article/pii/S0168900203013688` (visited on 08/16/2022).

[87] K. L. Brown and F. C. Iselin. "Decay TURTLE (Trace Unlimited Rays Through Lumped Elements): A Computer Program for Simulating Charged Particle Beam Transport Systems, Including Decay Calculations". In: (Feb. 1974). DOI: `10.5170/CERN-1974-002`.

[88] ROOT team. *ROOT: analyzing petabytes of data, scientifically.* ROOT. URL: `https://root.cern/` (visited on 06/04/2021).

[89] R. Frühwirth. "Application of Kalman filtering to track and vertex fitting". In: *Nuclear Instruments and Methods in Physics Research Section A: Accelerators, Spectrometers, Detectors and Associated Equipment* 262.2 (Dec. 15, 1987), pp. 444–450. ISSN: 0168-9002. DOI: `10.1016/0168-9002(87)90887-4`. URL: `https://www.sciencedirect.com/science/article/pii/0168900287908874` (visited on 10/13/2021).

[90] P. Billoir, R. Frühwirth, and M. Regler. "Track element merging strategy and vertex fitting in complex modular detectors". In: *Nuclear Instruments and Methods in Physics Research Section A: Accelerators, Spectrometers, Detectors and Associated Equipment* 241.1 (Nov. 15, 1985), pp. 115–131. ISSN: 0168-9002. DOI: `10.1016/0168-9002(85)90523-6`. URL: `https://www.sciencedirect.com/science/article/pii/0168900285905236` (visited on 10/13/2021).

[91] NA62 Collaboration. "Measurement of the very rare $K^+ \to \pi^+\nu\bar{\nu}$ decay". In: *arXiv:2103.15389 [hep-ex]* (Mar. 29, 2021). arXiv: `2103.15389`. URL: `http://arxiv.org/abs/2103.15389` (visited on 06/07/2021).

[92] NA62 Collaboration. "First search for $K^+ \to \pi\nu\nu$ using the decay-in-flight technique". In: *Physics Letters B* 791 (Apr. 10, 2019), pp. 156–166. ISSN: 0370-2693. DOI: `10.1016/j.physletb.2019.01.067`. URL: `http://www.sciencedirect.com/science/article/pii/S0370269319301121` (visited on 09/25/2019).

[93] G. Ruggiero. "New Result on $K^+ \to \pi\nu\nu$ from the NA62 Experiment". In: KAON 2019, Perugia, 2019.

[94] J. Jackson. *Classical electrodynamics*. 3rd. John Wiley & Sons, Incorporated, 1999.

[95] NIST Engineering Metrology Toolbox. *Refractive index*. July 1, 2019. URL: `https://emtoolbox.nist.gov/Wavelength/Documentation.asp` (visited on 09/16/2019).

[96] Max J. Riedl. "The Mangin Mirror and Its Primary Aberrations". In: *Applied Optics* 13.7 (July 1, 1974). Publisher: Optical Society of America, pp. 1690–1694. ISSN: 2155-3165. DOI: `10.1364/AO.13.001690`. URL: `https://www.osapublishing.org/ao/abstract.cfm?uri=ao-13-7-1690` (visited on 11/11/2021).

[97] Eduardo Cortina Gil et al. *Searches for lepton number violating $K^+ \to \pi^-(\pi^0)$ e^+e^+ decays*. arXiv:2202.00331. Publication Title: CERN Document Server. CERN-EP-DRAFT-NA62-2021-002, Jan. 31, 2022. URL: `https://cds.cern.ch/record/2792406` (visited on 03/03/2022).

[98] Eduardo Cortina Gil et al. "A Measurement of the $K^+ \to \pi^+\mu^+\mu^-$ Decay". In: *Journal of High Energy Physics* 11 (Nov. 4, 2022). URL: `https://link.springer.com/article/10.1007/JHEP11(2022)011` (visited on 11/11/2022).

[99] Olaf Behnke et al. *Data Analysis in High Energy Physics: A Practical Guide to Statistical Methods*. Weinheim, GERMANY: John Wiley & Sons, Incorporated, 2013. ISBN: 978-3-527-65344-7. URL: `http://ebookcentral.proquest.com/lib/bham/detail.action?docID=1315866` (visited on 05/14/2019).